

Research Laboratory

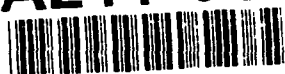
ington, DC 20375-5000

2



NRL Memorandum Report 6930

AD-A244 643



Spectroscopic Study of Neon Z-Pinch Plasma for Sodium-Neon Photopumping Experiments

B. L. WELCH,* F. C. YOUNG AND H. R. GRIEM*

*Pulsed Power Physics Branch
Plasma Physics Division*

**University of Maryland
College Park, MD 20742*

DTIC
ELECTE
JAN 31 1992
S D

January 6, 1992

92-02471



Approved for public release; distribution unlimited.

1 1 1

REPORT DOCUMENTATION PAGE			Form Approved OMB No. 0704-0188	
<small>Public reporting burden for this collection of information is estimated to average 1 hour per response, including the time for reviewing instructions, searching existing data sources, gathering and maintaining the data needed, and completing and reviewing the collection of information. Send comments regarding this burden estimate or any other aspect of this collection of information, including suggestions for reducing this burden, to Washington Headquarters Services, Directorate for Information Operations and Reports, 1215 Jefferson Davis Highway, Suite 1204, Arlington, VA 22202-4302, and to the Office of Management and Budget, Paperwork Reduction Project (0704-0188), Washington, DC 20503.</small>				
1. AGENCY USE ONLY (Leave blank)	2. REPORT DATE 1992 January 6	3. REPORT TYPE AND DATES COVERED Interim		
4. TITLE AND SUBTITLE Spectroscopic Study of Neon Z-Pinch Plasma for Sodium-Neon Photopumping Experiments		5. FUNDING NUMBERS PE — 63220C		
6. AUTHOR(S) B. L. Welch,* F. C. Young, H. R. Griem*				
7. PERFORMING ORGANIZATION NAME(S) AND ADDRESS(ES) Naval Research Laboratory Washington, DC 20375-5000		8. PERFORMING ORGANIZATION REPORT NUMBER NRL Memorandum Report 6930		
9. SPONSORING/MONITORING AGENCY NAME(S) AND ADDRESS(ES) Strategic Defense Initiative Organization T/IS Washington, DC 20301-7100		10. SPONSORING/MONITORING AGENCY REPORT NUMBER		
11. SUPPLEMENTARY NOTES *University of Maryland, College Park, MD 20742 This work was carried out at NRL by B.L. Welch as a part of the Ph.D thesis requirements at the University of Maryland. Dr. F. C. Young was the mentor for the work at NRL, and Professor H. R. Griem was the thesis advisor at the University of Maryland.				
12a. DISTRIBUTION/AVAILABILITY STATEMENT Approved for public release; distribution unlimited.		12b. DISTRIBUTION CODE A		
13. ABSTRACT (Maximum 200 words) Spectroscopic measurements were made of neon Z-pinch plasmas to establish conditions appropriate for sodium-neon photopumping. Emissions of soft X-rays, extreme ultraviolet (XUV), and near ultraviolet (NUV) were measured. Plasma electron temperatures and densities were determined by comparing measurements with steady-state and time-dependent atomic-physics models. Dependences of plasma emissions on the magnitude and risetime of the current and on the initial mass loading were investigated. Peak currents of 120 to 300 kA and 1-μs to 50-ns risetime were used to implode a 1-cm diameter neon gas puff. Mass loadings ranging from 1.2 to 3.6 μg/cm were varied by adjusting the gas-puff pressure. Adjustments of the current, current risetime, and mass loading can be used to produce an appropriate neon plasma for sodium-neon photopumping.				
11. (Continued) This work was supported in part by the Strategic Defense Initiative Organization under Job Title, "Ultra Short Wavelength Laser Research."				
14. SUBJECT TERMS Z-pinch, Neon plasma XUV and NUV spectroscopy Sodium/neon x-ray laser			15. NUMBER OF PAGES 285	
			16. PRICE CODE	
17. SECURITY CLASSIFICATION OF REPORT UNCLASSIFIED	18. SECURITY CLASSIFICATION OF THIS PAGE UNCLASSIFIED	19. SECURITY CLASSIFICATION OF ABSTRACT UNCLASSIFIED	20. LIMITATION OF ABSTRACT UL	

ABSTRACT

Title of Dissertation: SPECTROSCOPIC STUDY OF NEON Z-PINCH PLASMA FOR
SODIUM-NEON PHOTOPUMPING EXPERIMENTS

Benjamin Lawrence Welch, Doctor of Philosophy, 1991

Dissertation directed by: Hans R. Griem, Professor, Department of
Physics

Spectroscopic measurements were made of neon Z-pinch plasmas to establish conditions appropriate for sodium-neon photopumping. Emissions of soft X-rays, extreme ultraviolet (XUV), and near ultraviolet (NUV) were measured. Plasma electron temperatures and densities were determined by comparing measurements with steady-state and time-dependent atomic-physics models.

Temporal, spacial, and spectral resolutions were required to characterize the imploded plasmas. Two successive implosions are observed. At the first implosion, the plasma radiates soft X-rays from localized regions (< 0.5 mm diam) and XUV from a 1-mm diameter plasma with densities of $0.8 - 3 \times 10^{20} \text{ cm}^{-3}$. At the second implosion, Ne VIII lines (NUV) are emitted from a 3.5-mm diameter plasma with a density of $6 \times 10^{18} \text{ cm}^{-3}$. Temperatures determined from time-resolved Ne VII, Ne VIII, and Ne IX spectral measurements are 200 to 300 eV at the first implosion and 60 to 100 eV at the second

implosion. The absolute intensity and Stark-broadened width of the Ne VIII $1s^2 3s-1s^2 3p$ transitions were used to estimate a Ne IX ground-state fraction of 70% at the second implosion.

Dependences of plasma emissions on the magnitude and risetime of the current and on the initial mass loading were investigated. Peak currents of 120 to 300 kA and 1- μ s to 50-ns risetime were used to implode a 1-cm diameter neon gas puff. As the driving current is increased, the volume of plasma emitting soft X-rays increases, but this volume is only a small fraction of the total plasma, which radiates in the XUV. With a fast-risetime current, the soft X-ray-emitting volume decreases and a more uniform plasma is produced, albeit at lower temperature. Mass loadings ranging from 1.2 to 3.6 μ g/cm were varied by adjusting the gas-puff pressure. Increasing the mass loading decreased the temperature. Adjustments of the current, current risetime, and mass loading can be used to produce an appropriate neon plasma for sodium-neon photopumping.

Accession For	
NTIS CRA&I	<input checked="" type="checkbox"/>
DTIC TAB	<input type="checkbox"/>
Unannounced	<input type="checkbox"/>
Justification	
By	
Distribution/	
Availability Codes	
Dist	Availability for Special
A-1	



ACKNOWLEDGEMENTS

I would like to thank my advisor, Dr. Hans R. Griem, for his expert guidance in the moments of progress and his patience in the struggles between. I would also like to thank my mentor at the Naval Research Laboratory, Dr. Frank C. Young, for allowing me to shape the direction of this research and keeping me focused on that direction. The commitment of these individuals to the administrative responsibility of graduate research has made this effort possible.

I would like to thank my dissertation committee: Dr. Carroll Alley, Dr. George Goldenbaum, Dr. Julius Goldhar, and Dr. Adil Hassam for their time and effort in this educational process.

I would like to thank the many people that I have met at the University of Maryland who have offered advice and support. In particular, Dr. J.-S. Wang, Dr. Juan Moreno, and Dr. Enrique Iglesias have been a constant source of advice in atomic physics and spectroscopic measurements. I would also like to thank Dr. H.-J. Kunze and Dr. S. Goldsmith for helpful discussions on their visits to the University of Maryland.

I would like to take this opportunity to express my appreciation to the people at the Naval Research Laboratory (NRL) who have shared their time and resources with me. I would like to thank Dr. Gerald Cooperstein, Dr. Bob Comisso, Dr. Bruce Weber, Dr. Paul Ottinger, Dr. Steve Stephanakis, Dr. Dave Mosher, Dr. Jess Neri, Dr. Dave Hinshelwood, Mr. Ron Boller, Mr. John Shipman, Mr. Dave Rose, Mr. Phil Goodrich, and Mr. Vic Sherrer of the Pulsed Power Physics Branch. I worked with all of these individuals on a regular basis and the occasions in which they offered assistance are too numerous to

mention. I also appreciate the technical assistance and advice of Mr. George Langley, Mr. Walt Snider, Mr. Rick Fisher, Mr. John Fields, Mr. Frank Hollis, Mr. Tony Robinson, Mr. Kevin Britton, and Mr. Bruce Roberts.

I would like to thank Dr. John Apruzese of the Radiation Hydrodynamics Branch at NRL for his enthusiasm for this project and for theory support, particularly with CRE code calculations. I am grateful to Dr. Ray Elton, Mr. Edgar McLean, Dr. T.N. Lee, Dr. Charles Manka, Dr. Andrew Mostovych, and Dr. Stephen Obenschain of the Plasma Physics Division at NRL for assistance in using the grazing incidence spectrograph and the optical multichannel analyzer. These instruments were critical to the success of this work. I would like to thank Dr. Philip Burkhalter, Dr. G. Mehlman, and Mr. Dan Newman of the Condensed Matter and Radiation Sciences Division at NRL for the use of the crystal spectrograph and for help in reducing the films of soft X-ray spectra.

I am grateful to Dr. W. L. Wiese, Dr. W. C. Martin, and Dr. J. Z. Klose of the National Institute of Science and Technology in Gaithersburg, Maryland for readily providing informative atomic-physics data.

The friendship of Dr. Chris Deeney of Physics International Company and his enthusiasm for pulsed power X-ray laser studies is appreciated.

I appreciate the commitment and foresight of Dr. Sidney Ossakow, Superintendent of the NRL Plasma Physics Division, and Dr. Victor Granatstein, Director of the Laboratory for Plasma Research (LPR), in maintaining the LPR/NRL connection which has been responsible for the education of many graduate students in plasma physics.

The support of the Strategic Defense Initiative Organization (SDIO) in funding some of this research is appreciated. The efforts of Dr. Dwight Dustin of the SDIO Innovative Science and Technology Office and Dr. Jack Davis, the NRL Scientific and Technical Advisor to IST/SDIO, in promoting this research are acknowledged.

I am especially grateful to my family Sharon, Garrette, and Austin for their support.

This thesis is dedicated to my mother who encouraged me to begin my education and to my wife who encouraged me to finish my education.

Benjamin L. Welch

August 21, 1991

TABLE OF CONTENTS

Abstract.....	iii
Acknowledgements.....	v
Chapter 1 INTRODUCTION	1
1.1 Extreme Vacuum Ultraviolet Lasers	2
1.2 Pulsed Power	5
1.3 Motivation and Goals of the Present Work	6
1.3.1 Neon Implosions	8
1.3.2 Plasma Opening Switch	10
Chapter 2 XUV LASERS	13
2.1 Electron Collisional Excitation and Recombination	14
2.2 Resonant Photopumping	17
2.2.1 Neon Plasma	18
2.2.2 Sodium Plasma	31
2.2.3 Previous Experiments	35
Chapter 3 Z-PINCH PLASMAS	38
3.1 Z-Pinch Theory	40
3.2 Neon Z-Pinch Implosions	46
3.3 Sodium Z-Pinch Implosions	48
3.4 Sodium/Neon Photopumping Experiments	52
Chapter 4 EXPERIMENTAL GAS-PUFF Z-PINCH	53
4.1 Design Parameters	53
4.2 Inductive-Storage Generator	56
4.2.1 Capacitor Bank	58
4.2.2 Vacuum Inductor	58
4.2.3 Plasma Opening Switch	60
4.3 Neon Gas-Puff Source	63
4.4 Preionization	65
4.5 Electrical Measurements	70
4.5.1 Preionization	70
4.5.2 Z-Pinch	71
4.6 Spectroscopic Diagnostics	76
Chapter 5 SOFT X-RAY EMISSION	81
5.1 Spectral Measurements	82
5.2 Pinhole-Camera Images	86
5.3 X-Ray Diode Measurements	89
5.4 Analysis	92
5.4.1 Electron Density	92
5.4.2 Electron Temperature	94
Chapter 6 EXTREME VACUUM ULTRAVIOLET EMISSION	96
6.1 X-ray Diode Measurements	98
6.1.1 Current Variations	100
6.1.2 Mass-Load Variations	103
6.2 Pinhole-Camera Measurements	103
6.2.1 Current Variations	105

6.2.2 Mass-Load Variations	107
6.3 Grazing Incidence spectra	110
6.3.1 Current Variations	112
6.3.2 Mass-Load Variations	112
6.4 Extreme Vacuum Ultraviolet Monochromator	117
6.4.1 Current Variations	119
6.4.2 Mass-Load Variations	122
6.4.3 Various Ionization States	122
6.5 Analysis	129
6.5.1 Electron Density	129
6.5.2 Electron Temperature	129
Chapter 7 NEAR ULTRAVIOLET RADIATION	138
7.1 Near Ultraviolet Monochromator Measurements	140
7.1.1 Continuum Intensity Measurements	141
7.1.2 Line-Emission Measurements	144
7.2 NUV Optical- Multichannel-Analyzer Measurements	146
7.3 Analysis	149
7.3.1 Electron Temperature	153
7.3.2 Stark Broadening	158
7.3.3 Continuum Intensity	160
7.3.4 Ne VIII $1s^2 3p$ Level Population	161
Chapter 8 CONCLUSIONS	166
8.1 Neon IX Ground State Density	166
8.2 Neon Plasmas Produced by Slow-Risetime Currents	168
8.2.1 Time Histories of Electron Temperature and Density	168
8.2.2 Current Variations	171
8.2.3 Mass-Load Variations	173
8.3 Neon Plasmas Produced by Fast-Risetime Currents	174
8.3.1 Time Histories of Electron Temperature and Density	175
8.3.2 Current Variations	177
8.3.3 Mass-Load Variations	178
8.4 Imploded Neon Plasma as the Lasant for Photopumping ...	178
8.4.1 Mass-Load Control of the Temperature	179
8.4.2 Current Control of the Lasant Uniformity	180
8.4.3 Comparison with Photopumping Experiments	180
8.5 Suggestions for Future Work	181
Appendix A ATOMIC PHYSICS	185
A.1 Equilibrium Relations	186
A.2 Spectral Emission	193
A.2.1 Line Intensity	194
A.2.2 Line Broadening	195
A.2.3 Continuum Intensity	200
Appendix B MODELING OF DYNAMIC IMPLOSIONS	203
B.1 Applicability of the Original Code	203
B.2 Modification of the Code	208
B.3 Optimization	214
B.4 Conclusions	222

Appendix C PLASMA MODELING	225
C.1 Line Ratios from LTE Model	225
C.2 Line Ratios from Coronal Model	226
C.3 Rate-Dependent Model	231
Appendix D RADIATION DETECTORS	240
D.1 Detectors for Soft X-ray and XUV Emissions	240
D.1.1 Pinhole Camera	240
D.1.2 Vacuum Diodes	243
D.2 Grazing Incidence Spectrometer	247
D.2.1 Time-Integrated Spectra	247
D.2.2 Time-Resolving Monochromator	248
D.3 Near Ultraviolet Spectrometers	249
D.3.1 Monochromators	249
D.3.2 Optical Multichannel Analyzer	257
Bibliography	265

SPECTROSCOPIC STUDY OF NEON Z-PINCH PLASMA FOR SODIUM-NEON PHOTOPUMPING EXPERIMENTS

Chapter 1

INTRODUCTION

Light Amplification by Stimulated Emission of Radiation (LASER) was first demonstrated by Theodore Maiman in 1960 using an ultra-violet flashlamp and a ruby rod. The laser (a name commonly given to the source of this radiation) produces intense, coherent, monochromatic, and highly directional radiation. The variety of laser sources as well as their applications has grown steadily since that time. Early inventors of the laser could not have envisioned the numerous and diverse applications of this device. Today, we see lasers being used for applications ranging from exciting discoveries on the frontiers of scientific research to the monotonous task of reading bar codes at the grocery store.

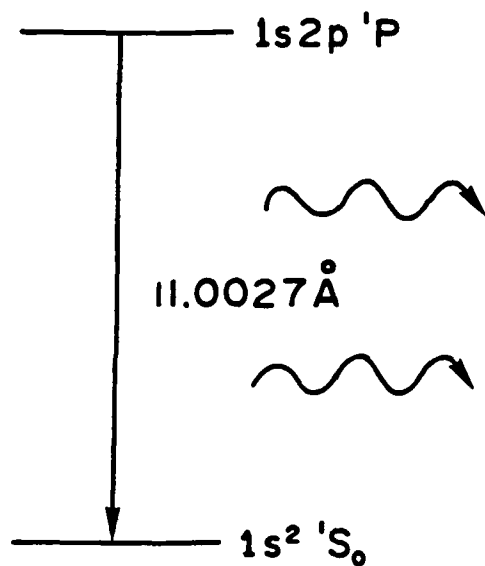
New applications of lasers can be expected if the energy of the lasing photons is increased. One application of extreme ultraviolet (XUV) laser radiation of particular interest is the microscopy of living biological cells. The penetrating characteristics of XUV radiation, as opposed to electrons, make possible the production of time-resolved, high-spatial-resolution images of cells in their natural fluid. Tailoring the energy of the radiation to that which would be absorbed by carbon but transmitted by oxygen in water (referred to as the water window) would permit high contrast imaging

of organic macromolecules. In addition, the coherence of an XUV laser would make it possible to produce three dimensional holograms of living biological samples.¹ Other potential applications for XUV lasers include lithography for integrated circuits of sub-micron dimensions, X-ray crystallography where phase information could be used to determine three dimensional electron distributions, and diagnostics for high-density inertial-confinement-fusion experiments.

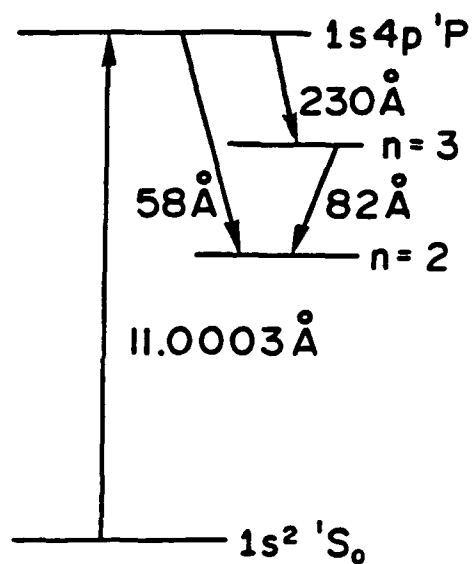
1.1 Extreme Vacuum Ultraviolet Lasers

The natural occurrence of an energy coincidence in characteristic radiation from helium-like sodium (Na X) and helium-like neon (Ne IX) provides an excellent opportunity to create a population inversion in the excited levels of Ne IX. (Refs. 2,3) A partial energy-level diagram describing this system is given in Fig. 1.1. If radiation from the $1s^2(^1S_0)-1s2p(^1P_1)$ transition of Na X at 11.0027 Å is provided in copious quantities, it can be used to photopump Ne IX ions from the ground state to the n=4 excited state by the $1s^2(^1S_0)-1s4p(^1P_1)$ transition at 11.0003 Å. (Ref. 4) This sodium flashlamp can create a population inversion in the n=4 levels of Ne IX relative to the n=2 and n=3 levels.⁵ Then this population inversion can lead to amplified stimulated emission of the $3d(^1D_2)-4f(^1F_3)$, $2p(^1P_1)-3d(^1D_2)$, and $2p(^1P_1)-4d(^1D_2)$ transitions at 230 Å, 82 Å, and 58 Å respectively, in an appropriately prepared neon plasma.⁶ The present investigation of neon Z-pinch implosions was carried out in order to create a high-temperature neon plasma suitable for such sodium-neon photopumping.

One requirement for generating XUV laser radiation is to produce



He - like Na
PUMP



He - like Ne
LASANT

FIG. 1.1. Partial energy-level diagram of the sodium-neon photopumping system.

and maintain a population inversion between the upper laser level (u) and the lower laser level (l) at a rate which allows stimulated emission to take place. As an estimate of the power required for stimulated emission, consider the relationship between the probability for spontaneous emission A_{ul} and the probability for stimulated emission B_{ul} given by:

$$\frac{A_{ul}}{B_{ul}} = \frac{8\pi h \nu^3}{c^3} \quad (1.1)$$

which was derived by Einstein from thermodynamic arguments. This expression states that the rate of spontaneous emission increases as the cube of the frequency (ν) relative to the corresponding rate of stimulated emission. Spontaneous emission is a competing process to stimulated emission in that it relaxes the inverted population distribution required for stimulated emission. This means that the rate required to create the population inversion necessary for lasing becomes increasingly larger, as the cube of the photon frequency. Combining this dependence with the photon energy of the transition ($h\nu$), we conclude that the power required to create and maintain an excited-state population for a laser scales as the fourth power of the photon energy. To illustrate the power levels involved, a visible light laser (3000 Å) may require a pump power of 100 kW to maintain a population inversion, while the required pumping power for an XUV laser (100 Å) may approach 100 GW. (Ref. 7)

The gigawatt power level required to produce substantial gain for an XUV laser necessitates the use of some type of pulsed system. Typically, existing XUV lasers use pulsed electrical energy to pump a visible or infrared laser, and this laser output is used to create an

XUV laser plasma. Here an electrical discharge drives a flashlamp, which produces population inversion in the visible (infrared) laser medium on a slow timescale, and a visible (infrared) laser pulse is produced on a short timescale by means of an optical switch. This approach has been used to produce up to 10 TW of power and to successfully drive XUV lasers.⁸ This approach has a rather low efficiency due to the various stages involved, and efforts are being made to couple electrical energy more directly to the XUV lasing medium.

1.2 Pulsed Power

One technique for coupling stored electrical energy more directly to a lasing medium is to use a Z-pinch discharge to produce soft X-rays which in turn directly photopump the lasing medium. Here, the electrical energy is delivered to a cylindrically symmetric load which implodes on axis due to the magnetic force on the load arising from the current carried by the load. For megampere level currents, resistive heating, implosion kinetic energy, and magnetic pressure on the load can produce a high-density high-temperature plasma and a large fraction of the energy coupled to the plasma can be converted into soft X-rays.⁹ For line-coincidence photopumping, high conversion efficiencies can be expected because every absorbed photon leads to an upper-level excited-state ion. If the electrical energy can be delivered in a sufficiently fast power pulse, stimulated emission will dominate radiative decay. In that case, the ratio of the lasing photon energy to the photopumping photon energy will be the efficiency with which the absorbed energy is converted into lasing energy.¹⁰

Pulsed power technology has been used to produce devices which are capable of tremendous electrical power pulses and hold the promise of becoming even more compact and efficient. The development of oil-filled Marx generators coupled to water-dielectric transmission lines has enabled electrical power pulses of 30 TW to be produced. Research in plasma opening switches is being carried out in hopes of producing inductive storage devices capable of similar level power pulses without massive oil- and water-filled systems.¹¹ Although still developmental, an inductive-storage generator coupled to a Z-pinch radiation source has the potential to be a compact and efficient power supply for a photopumped XUV laser.

1.3 Motivation and Goals of the Present Work

Experiments using the Gamble II pulsed power generator at the Naval Research Laboratory (NRL) have demonstrated sodium/neon photopumping.⁴ In these experiments a 1-MA main current pulse was used to implode a sodium-fluoride Z-pinch load, and a fraction of the current pulse returning to ground (about 200 kA) was used to implode a parallel neon gas-puff Z-pinch. A sodium pump power in this experiment of 25 GW was sufficient to observe an enhancement of the photopumped level in the nearby neon plasma.¹² A schematic diagram of the experiment is given in Fig. 1.2. To achieve amplified stimulated emission, research efforts are underway to improve both the sodium radiation source and the neon laser. Larger power for the 11-Å sodium line radiation is needed to achieve appreciable gain in the neon plasma. The sodium-fluoride source has been modified and fielded on a 3-MA pulsed power generator.¹³ Also a pure sodium source has

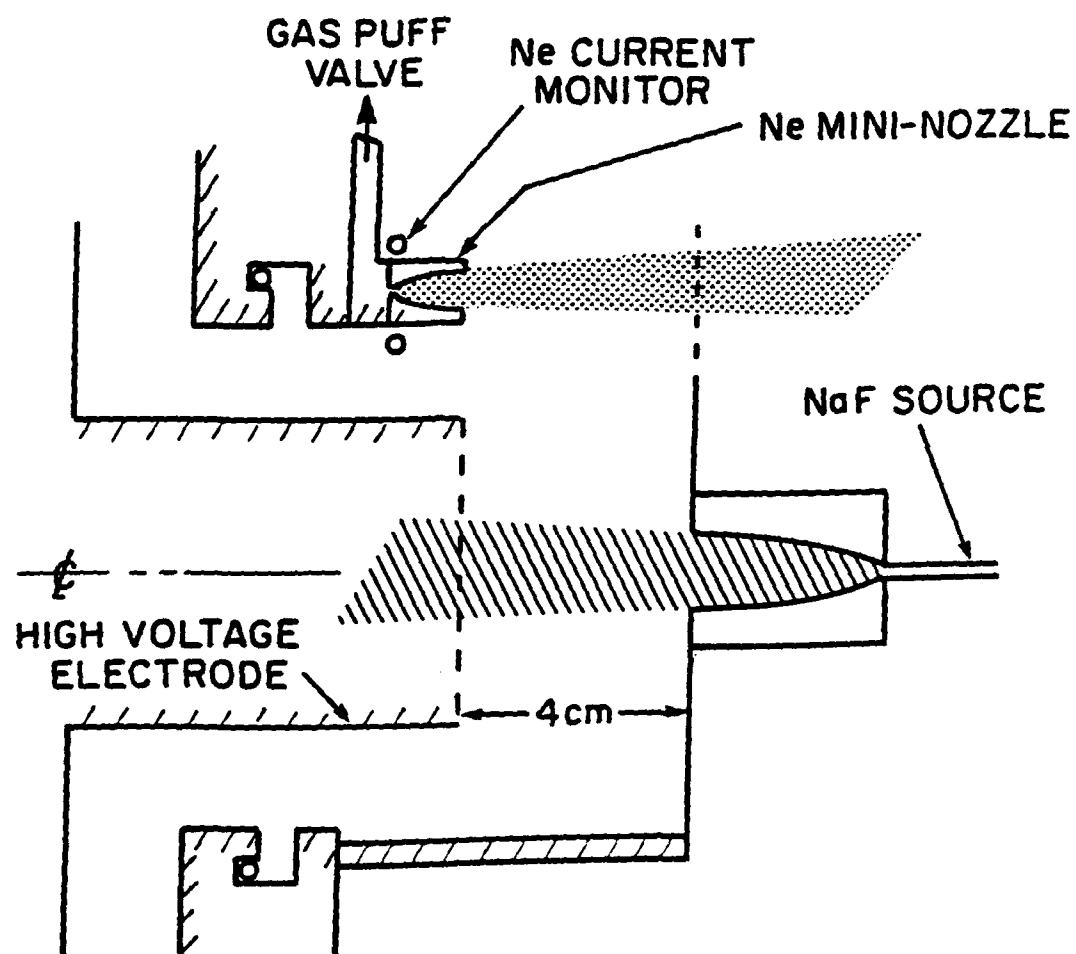


FIG. 1.2. Schematic diagram of the Gamble II photopumping experiment.

been developed and used on 3-MA and 10-MA generators.¹³⁻¹⁵ Power in the 11-Å sodium line exceeding 100 GW has been achieved at 3 MA and exceeding 200 GW at 10 MA.¹⁶

A quantitative investigation of neon gas-puff implosions is needed to determine the experimental parameters required to produce a neon plasma in a state appropriate for photopumping. The relatively slow repetition rate (1-4 shots/day) and harsh electromagnetic environment of large pulsed power devices makes it difficult to carry out detailed quantitative measurements on such a neon plasma. Also, the current required to produce an appropriate neon plasma is only a few hundred kiloamperes. Therefore, a small capacitor-discharge device was developed and used to study implosions of neon gas puffs as used in the sodium/neon photopumping experiments on Gamble II. A photograph of the experimental test stand is given in Fig. 1.3.

1.3.1 Neon Implosions

The objective of producing neon gas-puff Z-pinch implosions was to determine the neon plasma conditions present in the photopumping experiments on the Gamble II generator and to estimate the Ne IX ground-state population. In the sodium/neon photopumping experiments on Gamble II, indication that the sodium 11-Å radiation photopumped the neon was given by measurements of K-shell X-ray spectra from Ne IX. These spectra showed an enhancement of the 11-Å radiation from the $n=4$ level of neon when the sodium pump was present. For the 25-GW pump power, theoretical calculations predict various levels of enhanced radiation of the $n=4$ level of Ne IX, depending on the neon plasma conditions.⁴ The present investigation was carried out to

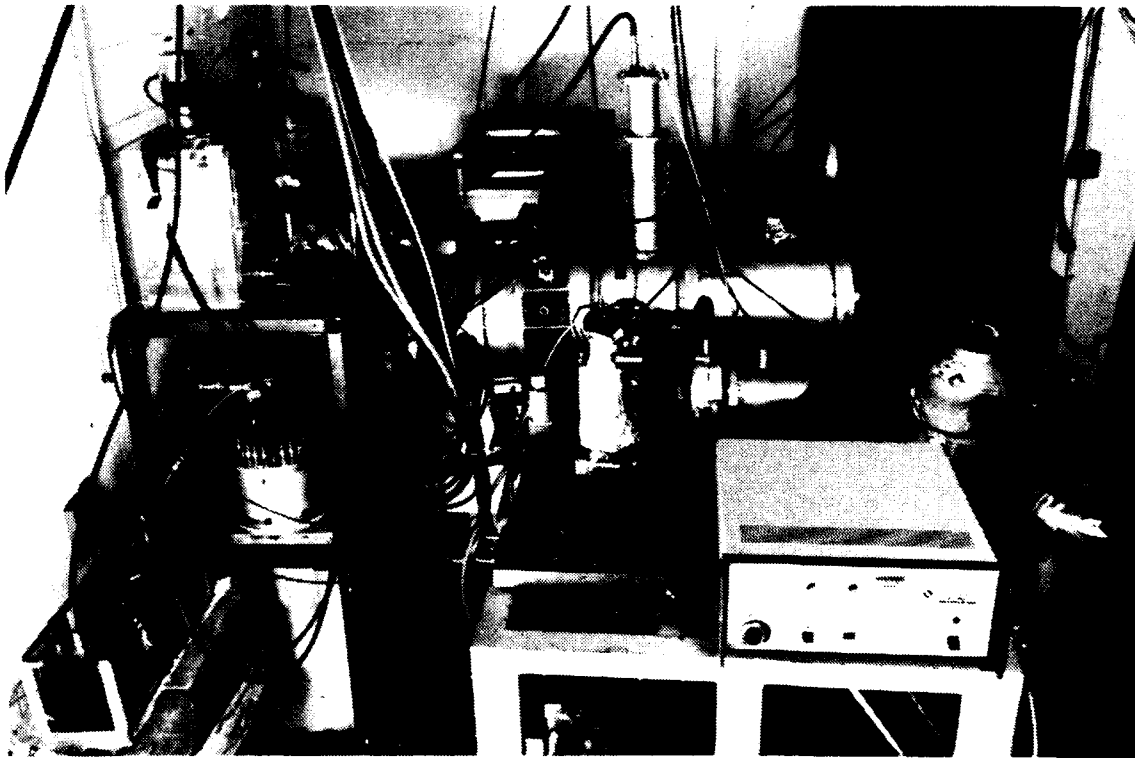


FIG. 1.3. Photograph of the experimental setup with capacitor banks on the left and the grazing incidence spectrograph in the foreground.

experimentally determine the conditions present in such a neon plasma.

Although radiation from Ne IX can be used to determine photopumping, radiation from Ne VIII is better suited for establishing the conditions required for photopumping. The excited states of Ne VIII are more closely coupled to the ground state of Ne IX than are the excited states of Ne IX. This can be seen from the energy-level diagram in Fig. 1.4. Optimum neon plasma conditions would maximize the population of the ground state of Ne IX and minimize the population of the excited states of Ne IX. Emission from excited states of Ne VIII would therefore be maximum and the emission from Ne IX would be minimal. Spectral, temporal, and spatially resolved measurements have been made of Ne VIII and Ne IX emissions from neon gas-puff Z-pinch implosions under various experimental conditions. These measurements are used to estimate the neon-plasma conditions and to predict optimum conditions for photopumping.

1.3.2 Plasma Opening Switch

A plasma opening switch (POS) was used to drive the neon gas-puff Z-pinch implosion in order to approximate the fast-risetime current pulse used in photopumping experiments on Gamble II. This switch was coupled with an inductive-storage circuit to produce a current pulse similar to that used to implode the neon gas puff in the Gamble II photopumping experiments. The inductive-storage/POS device provided a compact, high-repetition-rate test stand to produce the neon plasma; to measure the plasma properties of interest; and to study the effects of different experimental conditions upon the dynamics of the implosion and the properties of the plasma. Various nozzle designs,

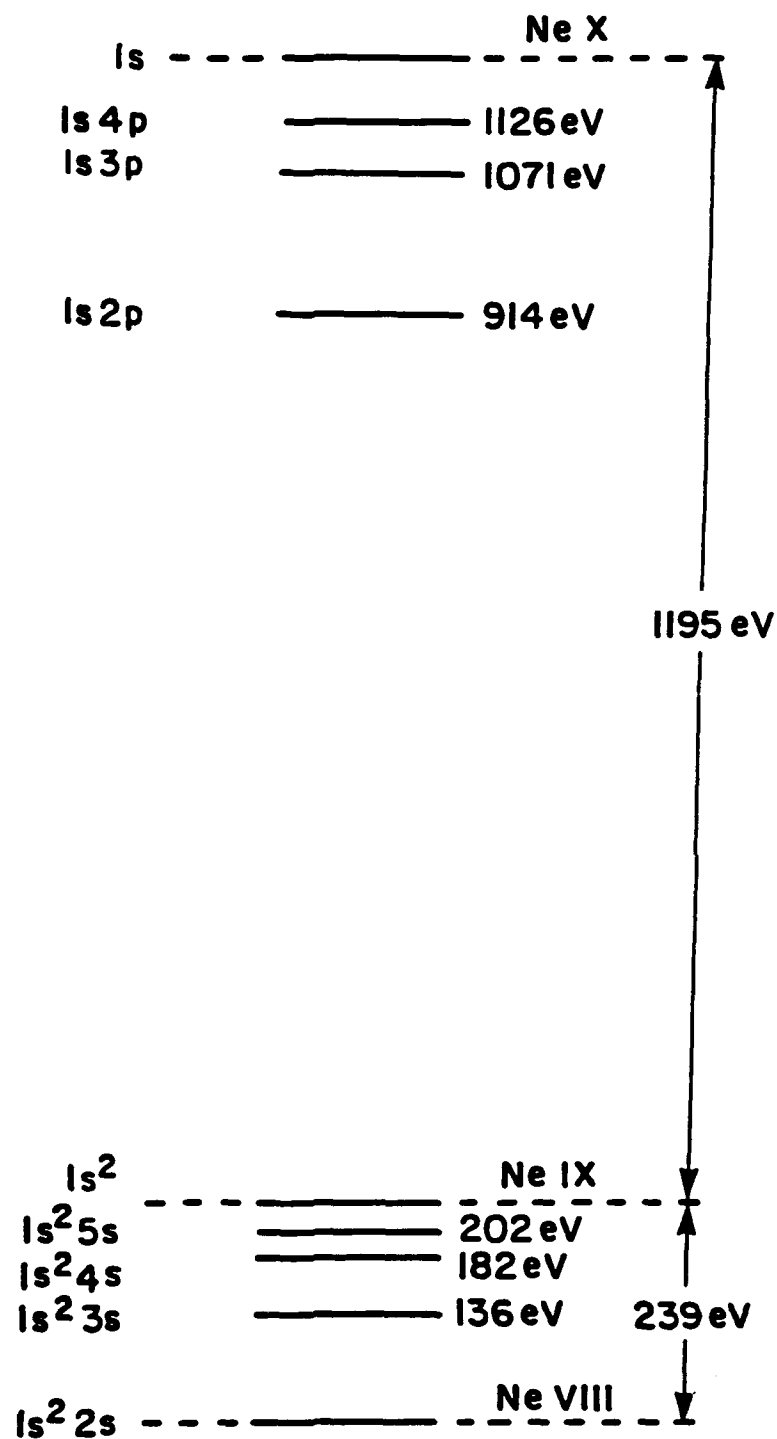


FIG. 1.4. Energy-level diagram of Ne IX and Ne VIII.

neon gas-puff pressures, and currents of different risetime and magnitude could be used.

Chapter 2

XUV LASERS

In order to achieve net gain over a length L in a lasing medium, a positive gain coefficient G is required. This gain coefficient represents the difference between the absorption and stimulated emission in the medium. If N_u and N_l represent the corresponding upper- and lower-level populations and σ_{ind} and σ_{abs} the induced emission and absorption cross sections, then the gain coefficient can be expressed as:

$$G = N_u \sigma_{ind} - N_l \sigma_{abs} = \pi r_0^2 c f \frac{g_l}{g_u} \cdot \frac{N_u}{\Delta \nu} \left(1 - \frac{N_l/g_l}{N_u/g_u} \right) \quad (2.1)$$

where r_0 is the classical electron radius, g_u and g_l are the upper- and lower-level statistical weights, f is the absorption oscillator strength, and $\Delta \nu$ is the (Lorentzian) line width in frequency units.¹⁷ For a medium exhibiting gain, the intensity increases as $\exp(GL)$. For lasers operating at visible wavelengths, partially reflecting mirrors are placed at the ends of the medium to define a resonant cavity for the lasing radiation. The effective length is determined by the number of passes the light makes before it exits the cavity. Because reflective materials become less efficient at higher photon energy, lasers operating in the XUV energy region usually do not use a

resonant cavity, and amplification occurs in a single pass. For this reason, the term Amplified Stimulated Emission (ASE) is used to describe this radiation. Progress has been made in producing mirrors for XUV radiation and research is ongoing to produce resonant XUV cavities.¹⁸

To insure a positive gain coefficient, the inversion criterion must be met:

$$N_u > \frac{g_u}{g_l} N_l. \quad (2.2)$$

Various techniques to achieve inversion have been proposed, and three such techniques will be discussed. A number of review articles and a text have been written giving details of these three techniques as well as others.^{19,20}

2.1 Electron Collisional Excitation and Recombination

Amplified stimulated emission has been achieved at XUV energies by irradiating targets with high-power pulsed optical lasers focused onto a line. These optical lasers produce a hot dense plasma at the interface where the laser strikes the target. Depending on the target material and the parameters of the incident laser pulse, population inversion is generally achieved in one of two ways. Electron collisional excitation can selectively populate one level relative to a lower level, or electron collisional recombination of a cooling plasma may over-populate upper levels of an ion relative to lower levels of the ion.

One of the most successful XUV laser schemes uses electron

collisional excitation to populate the $n=3$ levels of a neon-like ion. The 3s and 3d levels have allowed transitions to the 2p level, however the 3p level is metastable with respect to spontaneous decay to the 2p level. This provides a mechanism for an inversion of the 3p level relative to the 3s level. Although this technique could lead to inversions in all ions with a $2p^n$ ground state, neon-like ions are most attractive because their closed-shell configuration is relatively stable over a wide temperature range. Significant gain at 206.3 and 209.6 Å from 3s-3p transitions in neon-like selenium due to collisional-excitation pumping was demonstrated in 1985. [Ref. 8] Subsequently ASE was observed in neon-like ions of yttrium, molybdenum, and strontium.^{21,22} Other researchers have reported ASE in neon-like copper, germanium, zinc, gallium, and arsenic.^{23,24} An inversion in nickel-like ions by collisional excitation has also been used to produce ASE in nickel-like ytterbium, europium, tantalum, tungsten, and rhenium.²⁵

Another approach to achieve ASE at XUV energies uses electron collisional recombination to create a population inversion. Electron collisional recombination is a "three body" process involving an ion and two electrons. The second "spectator" electron is necessary to conserve energy since the recombination is radiationless. This causes an extra electron-density dependence in the recombination rate as opposed to radiative recombination. For high-density recombining plasmas, collisional recombination can exceed radiative recombination. Collisional recombination leads to higher-level quantum states as opposed to radiative recombination. Consequently, population inversion can be created by collisional recombination in dense recombining plasmas. To understand this pumping mechanism, it is

convenient to recall the energy level n' referred to as the "collision limit". (See Eq. A.13.) For states above this level, collisional excitation is more likely than radiative decay, and these levels are closely coupled to the next higher ionization stage. For levels below this level, radiative decay is more likely, and these levels are coupled to the ground state of the ion. For recombination into levels above the collision limit, collisional mixing exceeds radiative decay; therefore these levels are continuously repopulated by collisions. For levels below the collision limit, radiative decay dominates and tends to depopulate the lower laser level.

Electron collisional recombination pumping has been used to achieve ASE in plasmas that are produced with a short laser pulse and then allowed to expand freely and cool quickly. Evidence of population inversion and gain due to collisional recombination has been reported by several laboratories.⁷ Gain has been measured for $n=3$ to $n=2$ transitions in hydrogen-like carbon, oxygen and fluorine.²⁶⁻³² Gain has also been measured for $n=4$ to $n=3$ transitions in lithium-like oxygen, aluminum, silicon, and chlorine.³³⁻³⁶ Gain has been reported for higher-energy transitions from $n=5$ to $n=3$ levels in lithium-like ions of aluminum and sulfur.^{37,38} One notable exception to the use of short-pulse lasers is the technique developed at Princeton University.³⁹ Here, a long pulse CO_2 laser is used to heat a carbon plasma through the hydrogen-like state; then the plasma is allowed to cool as it is confined in a theta pinch. As the plasma recombines, cascading electrons populate the 3d level prior to the 2p level thereby producing an inversion. ASE of the 2p-3d transition in hydrogen-like carbon at 182 Å has been reported.

2.2 Resonant Photopumping

Another method to produce population inversion is to selectively populate an upper level relative to a lower level by photopumping electrons from a third even lower level.⁴⁰⁻⁴² Several coincidences of characteristic X-ray energies and energy-level differences in particular ions have been proposed for resonant photopumping.^{1,43} One attractive coincidence is the Na X $1s^2-1s2p$ (1P_1) transition at 11.0027 Å and the Ne IX $1s^2-1s4p$ (1P_1) transition at 11.0003 Å. This match is particularly attractive for three reasons. First, the energy match is excellent (2 parts in 10^4). Broadening of the sodium pump line is expected to be larger than this energy difference so that the pump line profile should include the Ne IX absorption line profile. Second, the pump line is the resonance line of Na X (helium-like sodium). It is therefore the strongest line in the Na X spectrum, and that ionization state is present over a large temperature range. Third, photopumping of Ne IX by this technique can lead to overpopulation of the $n=4$ level relative to the $n=2$ and $n=3$ levels, which depopulate rapidly to the $n=1$ level. This provides a mechanism by which population inversion can be sustained.

The sodium/neon photopumping scheme requires an intense source of the 11-Å sodium radiation, analogous to the "flashlamp" in the ruby laser. The sodium plasma must be produced under conditions which optimize the intensity of the sodium pump radiation in the energy region of the Ne IX absorption. Also a neon lasing must be produced simultaneously in close proximity to the sodium pump. The neon plasma conditions must be adjusted to optimize absorption of the 11-Å sodium pump radiation and to minimize the Ne IX excited-state populations,

thereby achieving maximum population inversion when the neon plasma is photopumped. Extensive theoretical analysis has been devoted to establishing the appropriate conditions for these plasmas.^{5,44-47} These analyses place restrictions on the temperature, density, and dimensions of the two plasmas. Since the conditions required for the sodium and neon plasmas are quite different, they will be discussed separately. Then comparisons will be made with previous analyses.

2.2.1 Neon Plasma

For the neon plasma, the temperature is constrained by the requirement that the Ne IX ground-state population be maximum while the Ne IX excited-level populations be as small as possible, particularly the $n=2$ and $n=3$ levels. The atomic-physics model most appropriate for determining the level populations depends on the density of the plasma. The relationship between the principal quantum number and the minimum electron density for partial LTE (Eq. A.11) is plotted in Fig. 2.1, along with a similar plot of the collision limit (Eq. A.13) for a neon plasma at a temperature of 75 eV. If the electron density is above $6 \times 10^{19} \text{ cm}^{-3}$, then the $n=4$ level of Ne IX can be expected to be in partial LTE with respect to all higher levels and collisions dominate the rate processes. For densities between 6×10^{19} and 10^{20} cm^{-3} , both collisional and radiative processes influence the level populations, and both must be included by invoking a collisional-radiative-equilibrium (CRE) model. For plasmas with an electron density below 10^{20} cm^{-3} , collisional excitation is balanced by radiative decay, and the $n=4$ level can be expected to be in coronal equilibrium with respect to the ground state.

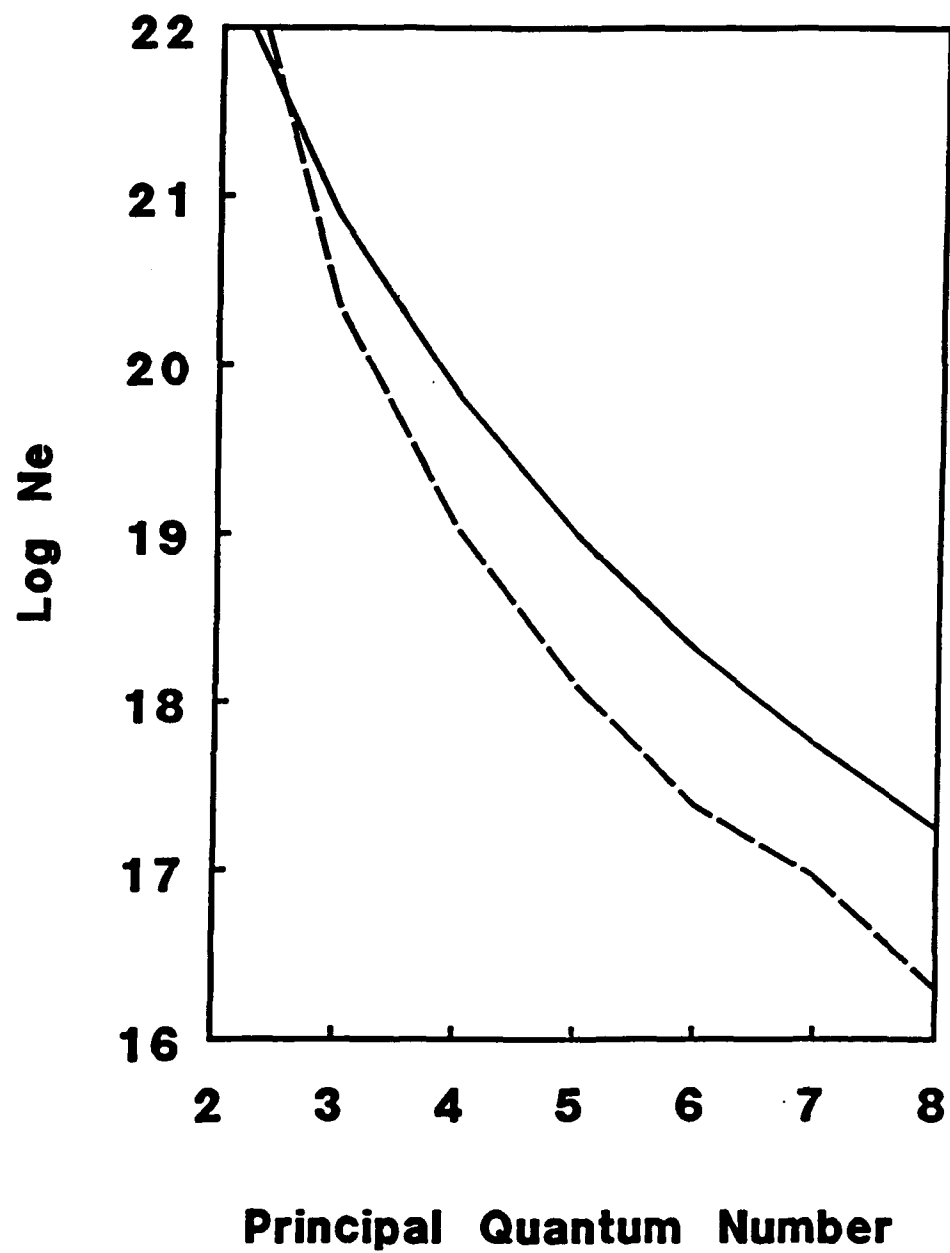


FIG. 2.1. Condition for partial LTE (solid) and collision limit (dashed) for Ne IX at 75 eV.

For a coronal equilibrium model, the temperature dependence of the fractional abundance of the various ionization states is presented in Fig. 2.2.[Ref. 48] Here, electron collisional ionization is balanced with radiative and dielectronic recombination. As the temperature increases, the population fraction of successingly higher ionization stages is maximized. The Ne IX ion exists over a relatively large temperature range because the energy difference between the ground state ($n=1$) and the $n=2$ level of Ne IX is much larger than the ionization energy of Ne VIII. At a temperature of 50 eV, the fractional abundances of Ne VI, Ne VII, Ne VIII, and Ne IX are approximately 25% for all four ionization states. For temperatures above 75 eV the population fraction of Ne IX is 90% and remains above 90% until the temperature exceeds 200 eV. Above 300 eV the fractional abundance of Ne X begins to dominate. The upper limit on the temperature of the neon plasma is not determined by the fractional abundance of the Ne IX ions, but by excitation of the $n=2$ and $n=3$ levels of Ne IX. Excitation of these levels reduces the inversion ratio. Since collisional excitations are balanced by radiative decay, populations of the excited levels can be determined from the ratio of the collisional excitation rate and the radiative rate according to Eq. A.15. The temperature dependence of the ratios of the populations of the 2p, 3p, and 4p levels of Ne IX to the Ne IX ground-state population is given in Fig. 2.3 for an electron density of 10^{19} cm^{-3} . The relative population of the 2p level increases by three orders of magnitude from 50 to 175 eV. This increase puts an upper limit on the temperature for an optimum neon plasma.

For higher-density plasmas, ($> 6 \times 10^{19} \text{ cm}^{-3}$) the ionization balance is determined by a combination of the Saha equation (Eq. A.8)

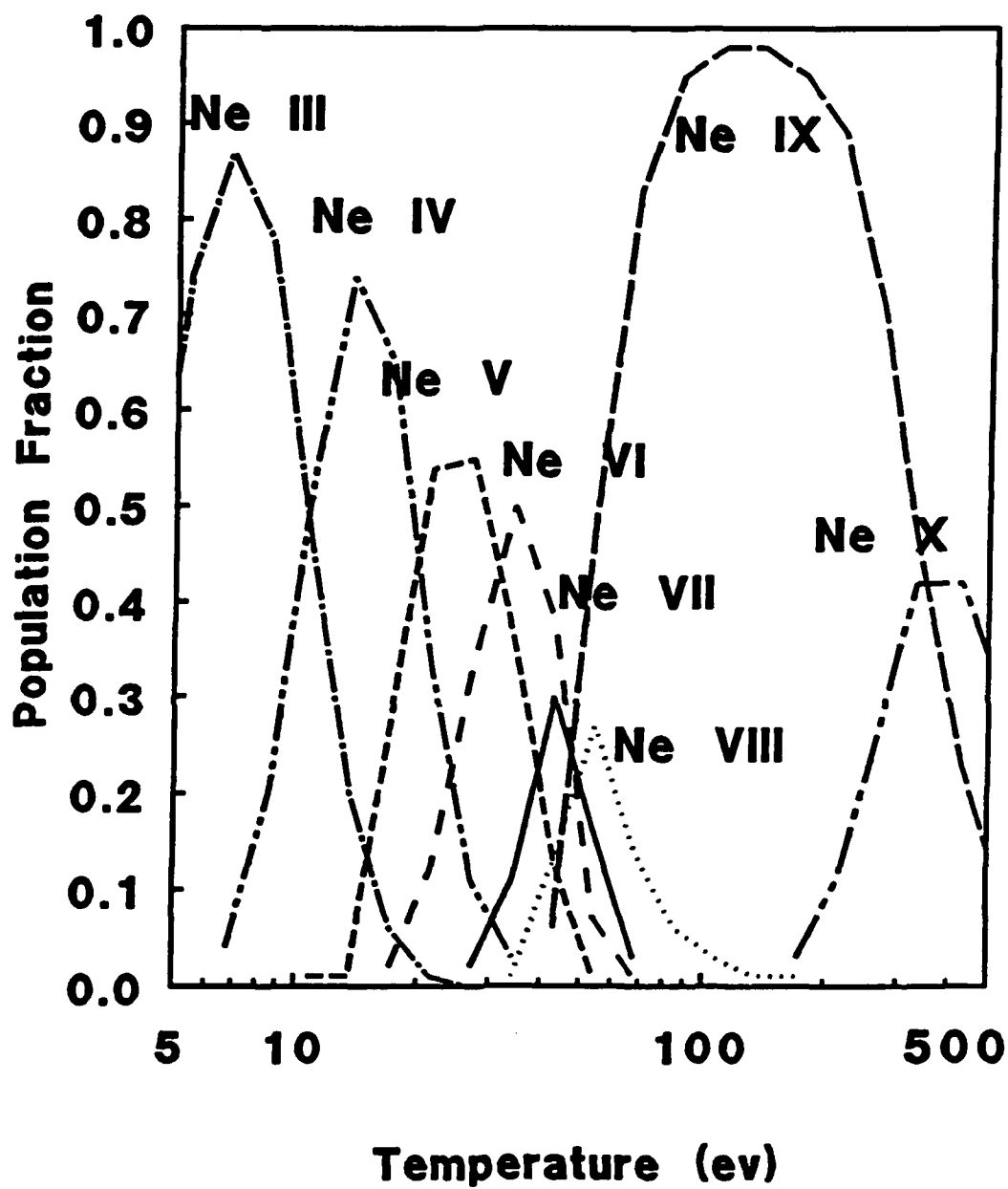


FIG. 2.2. Neon ionization-state fractions from the coronal equilibrium model. Population fractions for Ne III through Ne X are given as a function of temperature.

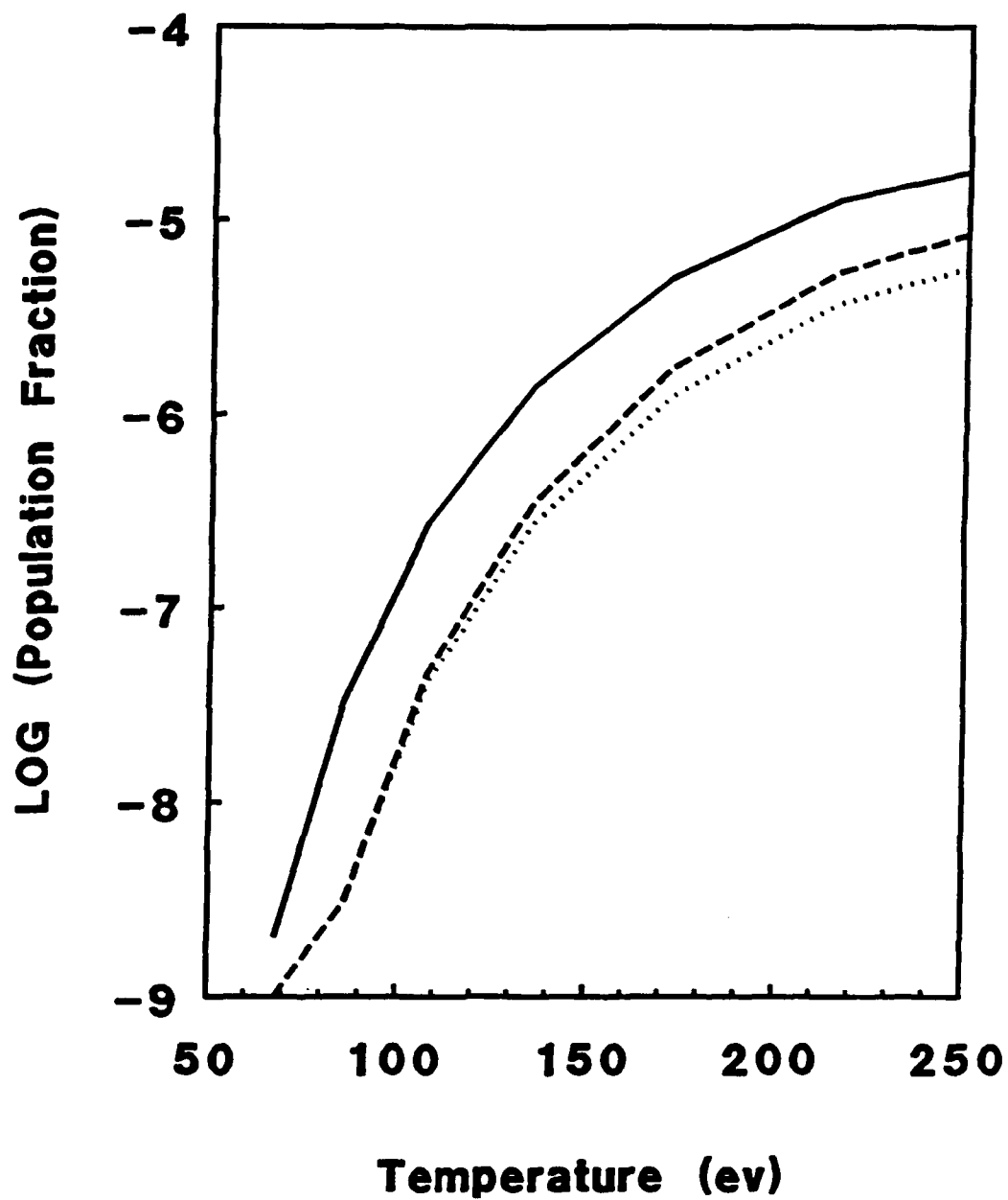


FIG. 2.3. Temperature dependence of Ne IX excited state population fractions from coronal equilibrium model (1s2p-solid, 1s3p-dotted, and 1s4p-dashed).

and charge neutrality. The Saha equation is used to relate one ionization state to the next higher ionization state. Charge neutrality relates the various ionization-state populations to the electron density. The graph in Fig. 2.4 illustrates the temperature dependence of the ratio of the Ne IX to Ne VIII populations, for an electron density of $6 \times 10^{19} \text{ cm}^{-3}$. At this density, the $n=4$ level of Ne IX is expected to be in partial LTE with respect to all higher levels. The Ne IX and Ne VIII populations are approximately the same at about 30 eV, while above 50 eV the plasma is over 90% Ne IX. The ratio of the Ne IX to Ne VIII populations continues to increase with temperature because the Ne VIII population decreases. To determine an upper limit on the temperature which maximizes the Ne IX fraction the ratio of Ne X to Ne IX is needed. However, this ratio does not determine the upper limit on the neon temperature for photopumping a neon plasma. This temperature is limited by collisional excitation of excited levels of Ne IX which tends to reduce any inversion by populating the lower lasing levels directly and by reducing the ground-state fraction and thereby the ions to be photopumped. The relative population of Ne IX excited levels compared with the total Ne IX population can be determined from the Boltzmann relation (Eq. A.6). The temperature dependence of the 2p, 3p, and 4p levels of Ne IX relative to the total Ne IX population is given in Fig. 2.5 for an electron density of $6 \times 10^{19} \text{ cm}^{-3}$. The population fraction of the 2p level increases more than two orders of magnitude from 70 to 135 eV. Temperatures below this increase are preferred for photopumping.

The density of the neon plasma is constrained by collisional mixing of the photopumped level. The upper limit must not be so large as to cause collisional mixing of the $n=4$ level with higher levels of

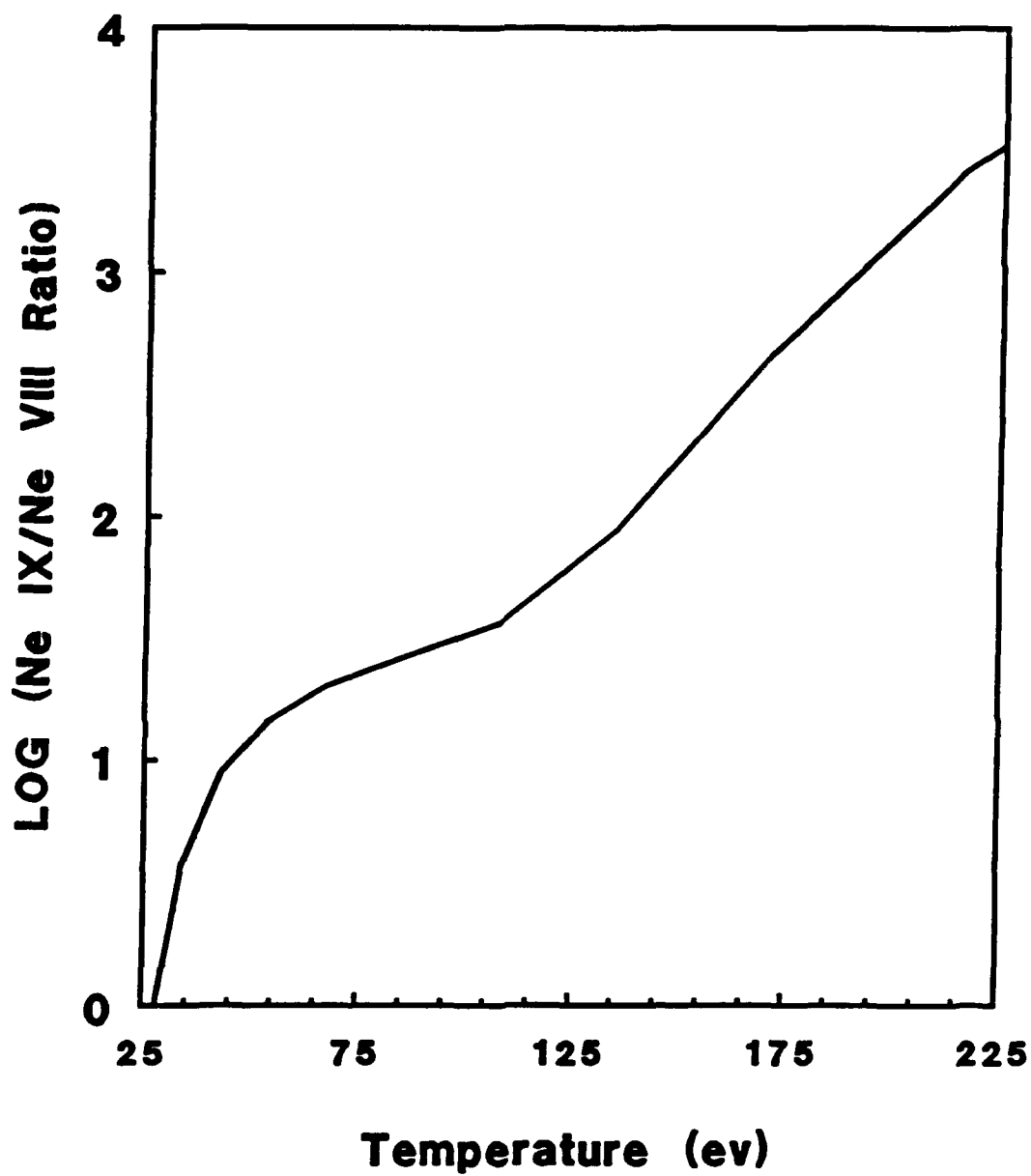


FIG. 2.4. Ratio of Ne IX/Ne VIII populations from the Saha equation for an electron density of $6 \times 10^{19} \text{ cm}^{-3}$.

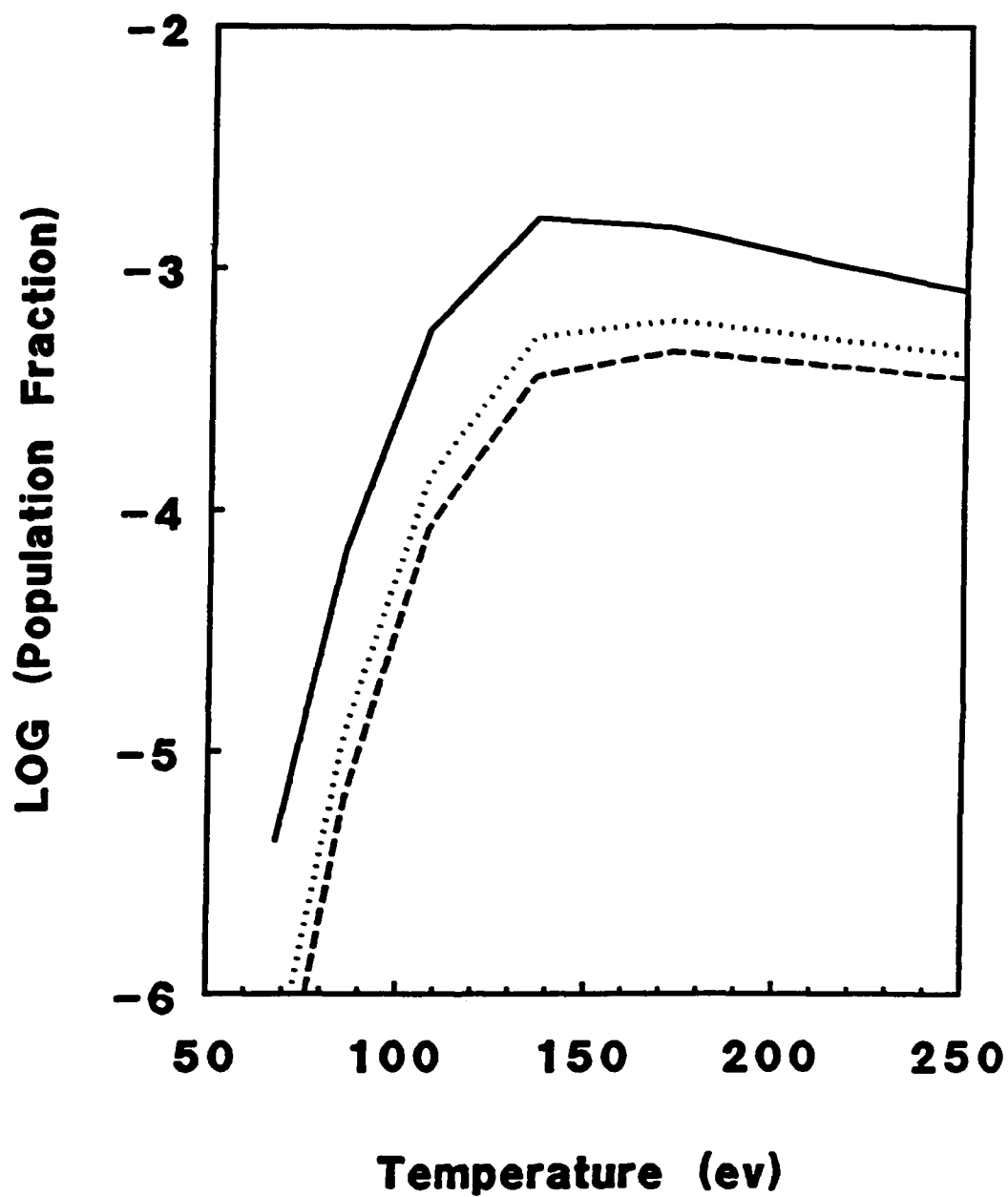


FIG. 2.5. Temperature dependence of Ne IX excited-state-population fractions from the Boltzmann relation for an electron density of $6 \times 10^{19} \text{ cm}^{-3}$ (1s2p-solid, 1s3p-dotted, and 1s4p-dashed).

Ne IX and thereby destroy the inversion. The density for which collisions dominate the population processes between the $n=4$ level and higher levels can be estimated from the condition for partial LTE. Referring to Fig. 2.1, we see that partial LTE exists for the $n=4$ level for an electron density greater than $6 \times 10^{19} \text{ cm}^{-3}$. Above this density considerable depopulation of the photopumped level by collisions to higher levels is expected. For electron densities above $8 \times 10^{20} \text{ cm}^{-3}$ the $n=3$ level is in partial LTE. These densities serve as upper limits for the neon plasma density to maintain population inversion in the corresponding levels. However, collisions among the $n=4$ levels are desirable since electrons pumped to the $1s4p$ level must be collisionally transferred to the $1s4d$ and $1s4f$ levels for lasing to occur. The collisional excitation rate between different $n=4$ levels can be estimated using Eq. A.16. For the $1s4s$ - $1s4p$ transition, an oscillator strength of $f=0.13$ and an energy difference of 0.8 eV is used to determine this rate.^{49,50} For temperatures of 50 to 150 eV , the collisional rate coefficient is $2 - 3.5 \times 10^{-7} \text{ cm}^3/\text{s}$. For an electron density of 10^{19} cm^{-3} , the collisional excitation rate is $2 - 3.5 \times 10^{12} \text{ s}^{-1}$. This rate is a factor of ten larger than the collisional excitation rate to the $n=5$ level ($2 \times 10^{11} \text{ s}^{-1}$) or the radiative decay rate to the $1s^2$ level ($2 \times 10^{11} \text{ s}^{-1}$). Collisional transfer among the $n=4$ levels occurs at a much faster rate than collisional transfer to the $n=5$ level. For electron densities below 10^{19} cm^{-3} , spontaneous decay begins to compete with collisional transfer between the $n=4$ levels.

A restriction on the product of the density and depth of the neon plasma is that it be large enough so that the pump radiation is absorbed but not so large that there is trapping of the $1s^2$ - $1s2p$ and

$1s^2-1s3p$ radiations which inhibits depopulation of the 2p and 3p levels. By combining this restriction with the limits on the density from collisional mixing, limits on the physical depth (or diameter) of the neon plasma can be determined. The optical depth is calculated from Eq. A.18 for oscillator strengths of 0.72, 0.15, and 0.056 for the $1s^2-1s2p$, $1s^2-1s3p$, $1s^2-1s4p$ transitions, respectively.⁵⁰ The physical depth corresponding to an optical depth of unity (at an ion density of 10^{18} cm^{-3}) is plotted as a function of temperature in Fig. 2.6 for these transitions. For a temperature of 75 eV, the $1s^2-1s4p$ transition has an optical depth of unity for a physical depth of 300 μm . An optical depth of five is acceptable for the $1s^2-1s2p$ and $1s^2-1s3p$ transitions.⁵¹ Then, plasma diameters of 400 μm and 2400 μm are allowed. Thermal gradients and streaming velocities could relax these restrictions and allow larger maximum depth.^{44,52,53}

For a Z-pinch with constant mass per unit length, the scaling of the optical depth depends on the relative importance of Doppler broadening and Stark broadening (see Appendix A.2.2). For a cylindrical geometry with constant mass per unit length, the density is inversely proportional to the square of the radius ($1/r^2$), and the density-radius product is inversely proportional to the radius ($1/r$). For a Doppler broadened line, the peak intensity of a normalized line-shape function is independent of density; therefore the optical depth at line center is inversely proportional to the radius ($1/r$). For a Stark-broadened line, the peak intensity of a normalized line-shape function is approximately inversely proportional to the line width. In situations where the Stark broadened line-width is linearly proportional to the electron density, the optical depth scales linearly with radius and is independent of density. Therefore,

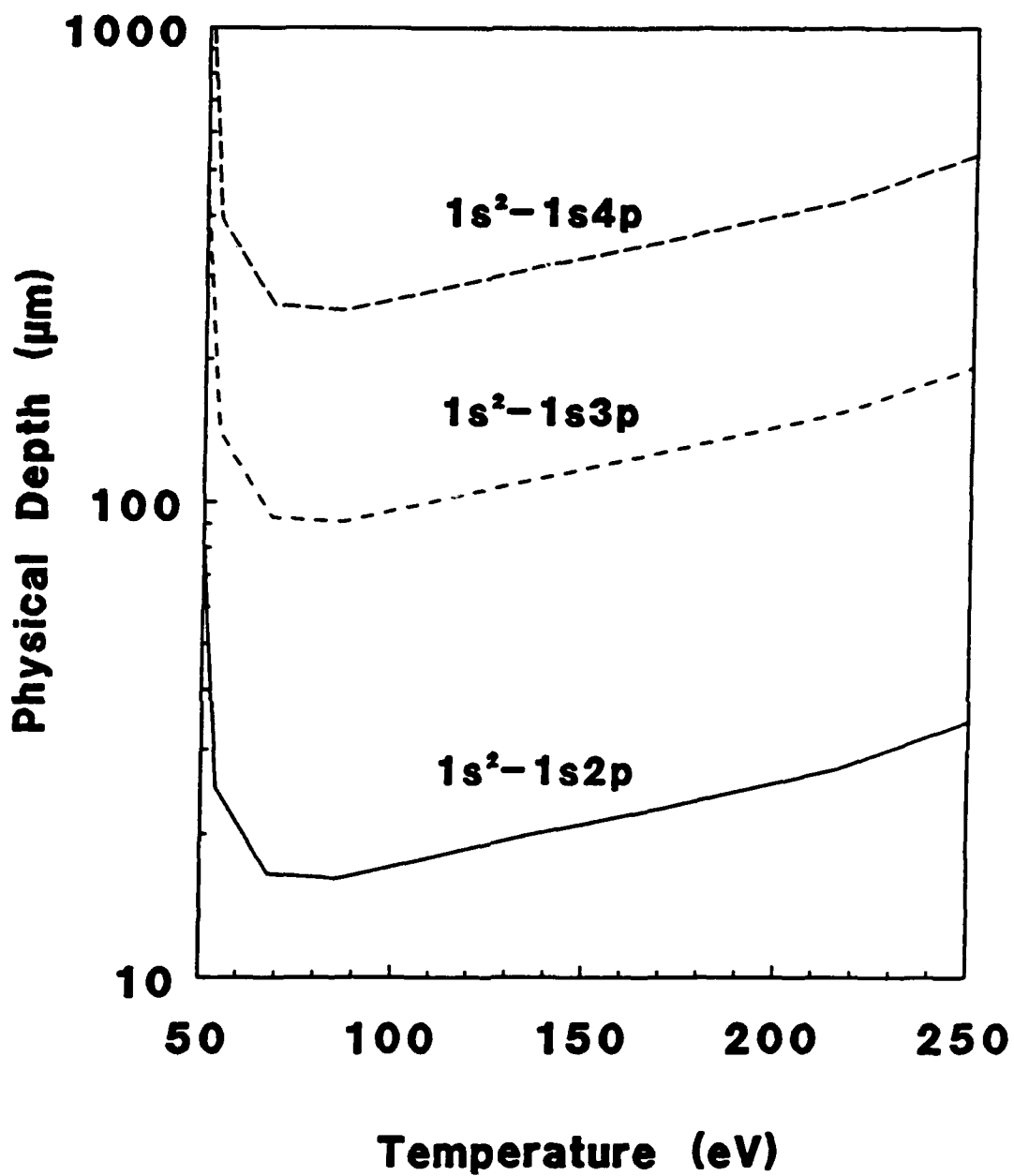


FIG. 2.6. Physical depth of a neon plasma at an ion density of 10^{18} cm^{-3} for an optical depth of unity for transitions in Ne IX.

until Stark broadening exceeds Doppler broadening, the optical depth increases with decreasing radius as $1/r$ and then decreases linearly with radius for small radius. To estimate the density at which the change in scaling with radius occurs, Doppler and Stark broadening widths must be determined. The Doppler full-width at half-maximum (FWHM) of the $1s^2-1s2p$ transition for a neon ion at 100 eV is 0.15 eV based on Eq. A.19. Stark widths of Ne IX transitions were estimated by scaling Stark-profile calculations of the resonance lines of helium-like argon.⁵⁴ These profiles result in a 0.7-eV Stark FWHM of the $1s^2-1s2p$ transition due to quasistatic ion fields and electron collisions at a density of 10^{24} cm^{-3} . The Stark width was determined by unfolding a Doppler width of 1.1 eV from a total width of 1.5 eV for the argon transition. A semiclassical estimate of Stark broadening indicates that the width scales inversely with the square of the ion charge.⁵⁴ Scaling from argon ($Z=17$) to neon ($Z=9$) gives a FWHM of 2.5 eV for the Ne IX $1s^2-1s2p$ transition at 10^{24} cm^{-3} . This width is more than an order of magnitude larger than the Doppler width (0.15 eV). The Stark width scales as N_e or $N_e^{2/3}$, where N_e is the electron density, depending on the importance of electron-collisional and quasistatic ion-field contributions.⁵⁴ These scalings indicate that electron densities of $2 - 6 \times 10^{22} \text{ cm}^{-3}$ produce a Stark width equal to the Doppler width for a temperature of 100 eV. According to the argon calculations,⁵⁴ the width of the $1s^2-1s4p$ transition is similar to the width of the $1s^2-1s2p$ transition if the electron density is a factor of 20 smaller. Therefore, for electron densities appropriate for the neon laser, i.e., less than 10^{21} cm^{-3} , Doppler broadening dominates the line widths of the $1s^2-1s2p$ and $1s^2-1s4p$ transitions. For the $1s^2-1s3p$ transition, the Stark width scales as

$N_e^{2/3}$ (Ref. 54) and is equal to the Doppler width for an even lower electron density of $5 \times 10^{19} \text{ cm}^{-3}$.

Calculations using a collisional-radiative equilibrium (CRE) model have established the plasma conditions necessary for optimal gain for the sodium/neon system.⁵ The sodium pump line intensity was assumed to be similar to that measured in experiments at the University of Rochester, namely the equivalent of a 227-eV blackbody. The neon plasma was assumed to be small enough that photon trapping into the lower lasing level was not a problem. For the $1s^2-1s2p$ transit on this required a depth d of neon such that:

$$d(\mu\text{m}) \leq \frac{3.6 \times 10^{20}}{N_I(\text{cm}^{-3})}, \quad (2.3)$$

where N_I is the ion density. This depth could be six times larger for the $1s^2-1s3p$ transition. The radiative transport and rate equations are then solved for steady-state conditions. Gain coefficients of over 100 cm^{-1} were determined from the computed densities of the upper and lower states. The density dependence of the gain coefficient was calculated for the $3d(^1D)-4f(^1F)$ transition at 230 Å, for the $2p(^1P)-4d(^1D)$ transition at 58 Å, and for the $2p(^1P)-3d(^1D)$ transition at 82 Å. In all cases the gain is less than a purely radiative plasma because with collisions, there is increased ionization of Ne IX from the $n=4$ level, which is only 69 eV from the Ne X ground state. For a temperature of 65 eV, peak gain coefficients for these three transitions occur at ion densities of 10^{19} cm^{-3} , $5 \times 10^{19} \text{ cm}^{-3}$, and 10^{20} cm^{-3} , respectively. For higher densities collisional mixing begins to spoil the inversion of the $n=4$ to $n=3$ level first, then the $n=4$ to $n=2$ level, and last the $n=3$ to $n=2$ level. Abrupt decreases in

the gain for these transitions occur at ion densities greater than 2×10^{19} , 10^{20} , and $2 \times 10^{20} \text{ cm}^{-3}$, respectively. The temperature dependence of the gain coefficient was calculated for the 82-Å transition for an ion density of 10^{20} cm^{-3} . Peak gain is achieved at a temperature of 50 eV. This temperature is much less than the temperature for maximum Ne IX fractional population, as shown in Fig. 2.2, because with collisions there is increased ionization from the $n=4$ photopumped level. This can be seen in Fig. 2.7, where the population fractions for Ne IX, Ne X, and Ne XI obtained from the model which includes photopumping are compared with those from the coronal model.

2.2.2 Sodium Plasma

The plasma conditions for the sodium flashlamp require maximum emission of the Na X $1s^2-1s2p$ transition in the region of neon absorption. This emission is maximum for a sodium plasma temperature corresponding to maximum population of the Na X $1s2p$ excited-state population. As previously discussed, the helium-like state is relatively stable over a large temperature range. Coronal equilibrium calculations for neon indicate that temperatures ranging from 55 to 325 eV produce a plasma with greater than 50% helium-like ions, and for temperatures in the 75 to 200 eV range the helium-like fraction is greater than 90%. A similar behavior is expected for sodium except the temperatures are slightly higher due to the higher charge state. Excitation of the Na IX $1s2p$ level is estimated from either coronal and Saha relations depending on the density. For electron densities below the collision limit of the $n=2$ level of Na X (ie. 10^{22} cm^{-3}),

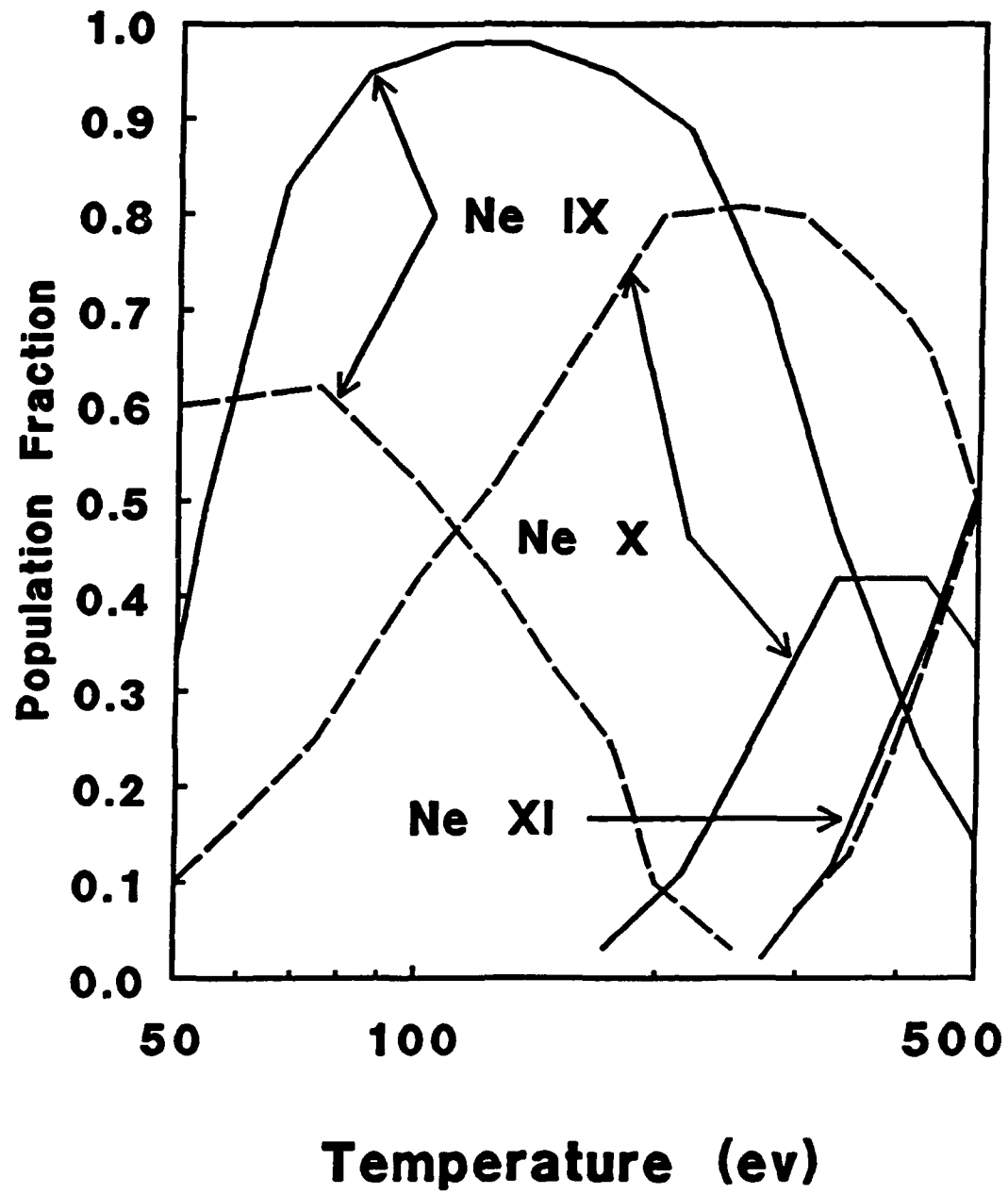


FIG. 2.7. Ionization-state fractions for Ne IX, Ne X, and Ne XI with (dashed) and without (solid) photopumping.

coronal equilibrium should be used to estimate the population of the $1s2p$ level. The increase in the excitation rate of the Na X $1s^2-1s2p$ level with temperature is partially cancelled by the decrease in ionization-state fraction above 200 eV, and the Na X $1s2p$ level population rises slowly up to this temperature.

The major restriction on the density of the sodium plasma arises from line broadening of the Na X $1s^2-1s2p$ transition. Some broadening is desirable to account for the energy mismatch (0.25 eV) between the sodium and neon transitions. However, increasing the sodium density so that the half-width at half-maximum of the pump line is larger than the energy mismatch exceeds the point of increasing returns. An estimate of the Stark width of the Na X $1s^2-1s2p$ transition can be made by scaling the calculations for argon.⁵⁴ For a Stark width equal to the energy mismatch, an electron density greater than 10^{23} cm^{-3} is required. Below this density, the shape of the pump line is determined by Doppler broadening, which gives a 0.3-eV full-width at half-maximum (at 300 eV).

Line broadening also limits the depth of the sodium plasma due to opacity. An optical depth greater than unity is acceptable, if not desirable in order to account for the energy mismatch. However, if the optical depth, which depends on the density-depth product is too large, the radiated power is dispersed into energies other than the energy of absorption for the Ne IX. With both a Doppler broadening of 0.3 eV and opacity broadening, an optical depth of four gives a half-width at half-maximum equal to the energy mismatch (based on Eq. A.20). Larger optical depths can be tolerated before the pump line saturates at the energy that matches the Ne IX absorption. For example, an optical depth of 20 implies a sodium geometric depth of 5

mm for an ion density of $2 \times 10^{17} \text{ cm}^{-3}$. In cylindrical geometry this implies a mass loading of $1.5 \text{ } \mu\text{g/cm}$. Larger mass loadings would lead to even larger optical depths.

A collisional-radiative equilibrium (CRE) model including radiative transport has been used to determine the plasma conditions necessary to optimize the output of the $11\text{-}\text{\AA}$ transition of Na X.⁴⁵ The pump flux is determined as a function of temperature, density, and diameter of the sodium plasma. The pump flux increases slightly with temperature for temperatures from 200 to 500 eV. This behavior results from combining the increasing $1s2p$ level population with the decreasing helium-like ion population as the temperature is increased. The pump flux increases with density although somewhat less than linear for ion densities above 10^{19} cm^{-3} . The pump flux also increases with plasma diameter up to about 5 mm and then becomes constant. The pump flux scales less than linearly with density or diameter because the optical depth increases as the density or diameter is increased, and larger Na X excited-level populations are produced due to re-absorption of emitted radiation. Since the ionization rate coefficient is larger for the excited levels, increased population of the upper levels leads to an effective larger ionization rate for the ion. This reduces the helium-like fraction, which produces a less than linear increase of pump flux with density or depth.

Other requirements on the geometry are: (1) The separation of the sodium and neon plasmas should be as small as possible so that the neon plasma subtends an appreciable solid angle of the sodium pump radiation. (2) The neon plasma must be uniform and straight so that its spontaneous emission may be amplified over an appreciable length.

(3) The neon lasing radiation should not be absorbed by colder plasma at the end of the lasing plasma.

2.2.3 Previous Experiments

Plasmas containing sodium and neon have been produced in experiments at three different laboratories using high power optical and infrared lasers. A discussion of these experiments will be presented and significant results relevant to the sodium/neon photopumping scheme will be summarized.

Soft X-ray spectra of Na X and Ne IX were observed simultaneously from the implosion of neon-filled microballoons using the Delta laser at the University of Rochester.⁵⁵ A 0.2-TW, 40-ps laser pulse was used to implode a 65- μm diameter glass microballoon filled with neon at a pressure of 8.6 atm. The sodium spectrum was a result of sodium impurities in the glass microballoon. An electron temperature of 300 eV was estimated from Ne IX and Ne X line ratios, and an electron density of $7 \times 10^{22} \text{ cm}^{-3}$ was estimated from the width of the Lyman- γ line of neon. For a compressed diameter of 19 μm , an optical depth of 100 was estimated for this line of neon. With this optical depth the Lyman- α line appeared constant over an energy range of 6 eV, with a full-width at half-maximum of 12 eV. This spectrum not only showed the energy coincidence of the sodium and neon radiations but also demonstrated line radiation that is flat-topped over a considerable energy region due to opacity broadening. Subsequent analysis by another group using a collisional-radiative-equilibrium model indicated a temperature of 380 eV and an ion density of $4 \times 10^{21} \text{ cm}^{-3}$, as compared with an ion density of $8 \times 10^{21} \text{ cm}^{-3}$ determined by

Rochester.⁵⁶ An optical depth of 200 was estimated for the neon Lyman- α line from a compressed plasma of 23- μ m diameter.

Experiments were performed at the Central Laser Facility of the Rutherford Appleton Laboratory to investigate sodium-neon photopumping.⁵⁷ A 0.1- μ m layer of sodium fluoride was coated onto a 3- μ m thick aluminum foil. Neon was ion-implanted into the other side of the foil to a depth of 0.14 μ m. This target was irradiated with two beams of a frequency-doubled neodymium glass laser. The neon was irradiated with 6 J of laser energy in a 100-ps pulse focused to 220- μ m diameter. This provided an irradiance of 2×10^{14} W cm⁻². The sodium fluoride was irradiated with 10 J of laser energy with a similar pulse width and focal spot size, but delayed for 300 ps from the neon pulse. An electron temperature of 210 eV and electron density of 10^{22} cm⁻³ were estimated from measured neon spectra. The spectra showed Ne IX lines, but no clear indication of photopumping was observed, possibly due to the lack of spacial resolution.⁵⁸ In other experiments with similar targets 0.8 J of 1.06- μ m laser energy was focused to 50- μ m diameter to produce an irradiance of 4×10^{14} W cm⁻². Time-resolved spectra of the Na X $1s^2$ (¹S)- $1s2p$ (¹P) transition indicated a peak absolute spectral brightness of this line in the photopumping experiments equivalent to a 157-eV blackbody. At the time of maximum spectral brightness the spectral half-width of this opacity-broadened line was 26 mÅ (2.7 eV).

A technique was developed at the Naval Research Laboratory to prepare frozen neon samples which could be used in laser plasma experiments.⁵⁹ An 8-J, 4-ns neodymium glass laser focused to 10^{12} W cm⁻² was used to irradiate the frozen neon samples. Grazing incidence spectra of extreme ultraviolet radiation were measured, and line

radiation from Ne IX and Ne VIII indicate that this technique can produce a lasant plasma for sodium/neon photopumping.⁶⁰ Experiments were also performed to produce the 11-Å sodium pump by irradiating a sodium fluoride target with 100 J of 1.06-μm radiation in a 4-ns pulse focused to $5 \times 10^{14} \text{ W cm}^{-2}$. The Na X radiation was measured with an absolutely calibrated crystal spectrograph, and a power of 25 MW of the 11-Å radiation emitted into 4π was estimated. Techniques to improve the sodium radiation were suggested, however photopumping experiments were never performed.⁶¹

Chapter 3

Z-PINCH PLASMAS

Two major problems in producing high-power electrical pulses from a given energy storage system are inductive restrictions that occur with time-varying currents and electrical breakdown that occurs with extremely high voltages. The development of oil-filled Marx generators coupled to water-dielectric transmission lines has helped to solve these problems. In Marx generators, capacitors are charged slowly at low voltage in parallel and then rapidly switched to high voltage in series and discharged into a water-dielectric transmission line before breakdown can occur. The transmission line not only can sustain the high voltage on a relatively short time-scale but can have low inductance compared with the Marx generator primarily due to the large dielectric constant of water. This power pulse is compressed in time and transferred to the load by closing switches in series with the load. Up to 10 TW of electrical power can be delivered to a load with this technique. The major drawbacks to such systems are the large physical dimensions of the generator and the massive oil and water tanks required.

Recent developments with plasma opening switches (POS) have opened up the possibility of using inductive storage systems to produce power levels similar to Marx-generator/water-capacitor

systems.^{11,62} In an inductive storage system, a relatively low voltage capacitor bank is used to current charge a large vacuum inductor in series with a POS. Near the peak of the charging current, the POS opens and the current is diverted to the load by a parallel current path. The change in inductance between the two current paths produces a voltage that is proportional to the product of the current and the rate at which the current is diverted between the two inductive paths. This can produce a voltage spike in excess of the initial capacitor voltage and, since it occurs near peak current, a corresponding power pulse. Inductive storage systems can provide considerable savings in size over Marx-generator/water-capacitor systems. Although still developmental, an inductive-storage generator coupled to a Z-pinch radiation source has the potential to be a compact and efficient power supply for a photopumped XUV laser.

Previous studies of Z-pinch plasmas have been carried out for various applications including fusion energy research, atomic-physics studies, and plasma-radiation-source (PRS) development. Experiments with CD_2 fibers, frozen deuterium fibers, and deuterium gas have been used to study plasmas capable of producing thermonuclear neutrons.⁶³⁻⁶⁵ Extensive theoretical modeling of the stability of these plasmas has guided this work.⁶⁶ An imploding-liner Z-pinch has been used extensively to study basic atomic physics, particularly the Stark broadening of spectral lines in high density plasmas.⁶⁷ With the development of large pulsed power devices, the Z-pinch plasma has become widely used as a high-power source of characteristic soft X-rays for materials testing.⁶⁸⁻⁷³ The various applications of the Z-pinch plasma place different requirements on the parameters of the plasma. Applications of Z-pinch plasmas have been reviewed by various

authors and conferences devoted to the subject of dense Z-pinches provide a wealth of information on the subject.^{9,74,75} The purpose here is to discuss Z-pinch plasmas as applied to producing a sodium/neon photopumped XUV laser. The basic theory of the equilibrium relations in a Z-pinch as well as situations where these are expected to be violated will be discussed. Examples of experiments carried out with neon and sodium Z-pinch plasmas will be presented. Finally, the results of experiments to demonstrate resonant photopumping of a neon plasma by radiation from a sodium plasma will be discussed.

3.1 Z-Pinch Theory

In 1934, W.H. Bennett derived the equilibrium conditions for a current channel.⁷⁶ He developed the relationship between the current, the charge per unit length, and the temperature for a Z-pinch discharge. This "Bennett pinch" relationship is:

$$I^2 = N c^2 2k(T_e + T_i) \quad (3.1)$$

where I is the total current (Gaussian units), N is the number of electrons or positive charges per unit length, T_e is the electron temperature, and T_i is the ion temperature. For a given current, the temperature is determined by the charge per unit length. This expression is a consequence of balancing the magnetic pressure of the current against the internal pressure of the plasma. It is an equilibrium relationship and does not describe the dynamics associated with implosions or instabilities. Also it does not determine the final radius of the pinch. Since the dependence of the magnetic

pressure on radius is identical to the dependence of the particle density on radius, the final radius or density is not specified by Eq. 3.1. This expression can be used to estimate the current required to produce a neon laser plasma appropriate for photopumping. For an effective charge of $Z=8$ (Ne IX) and for $T_e = T_i$, Eq. 3.1 can be written in the form:

$$I^2(\text{kA}) = 160 M(\mu\text{g/cm}) \times kT(\text{eV}) \quad (3.2)$$

where I is the current, kT is the temperature, and M is the neon mass load. This relationship is shown in Fig. 3.1 for temperatures of 50 and 100 eV. To produce a 75-eV plasma, currents of 100 to 250 kA and mass loadings of 1 to 6 $\mu\text{g/cm}$ are required.

The Bennett-pinch describes an equilibrium condition where magnetic pressure is balanced by internal pressure, but resistive and radiative effects are not included. Pease and Braginskii included these effects in an estimate of the maximum current required to maintain an equilibrium.⁷⁷ They assumed a hydrogen plasma for fusion applications. In this case, joule heating is balanced by bremsstrahlung losses for a current of 1.7 MA. For larger currents, radiative losses exceed resistive heating and the pinch collapses. For smaller currents, resistive heating dominates and the pinch expands. For an atomic species other than hydrogen, the maximum current for equilibrium is reduced by the factor $(Z+1)/2Z$ for ions of a charge Ze . For a plasma consisting primarily of Ne IX, this factor is 0.56, and the equilibrium current is 0.95 MA. This calculation includes bremsstrahlung radiation but does not consider characteristic radiation. A similar calculation including the effects of characteristic radiation indicates that far lower currents are

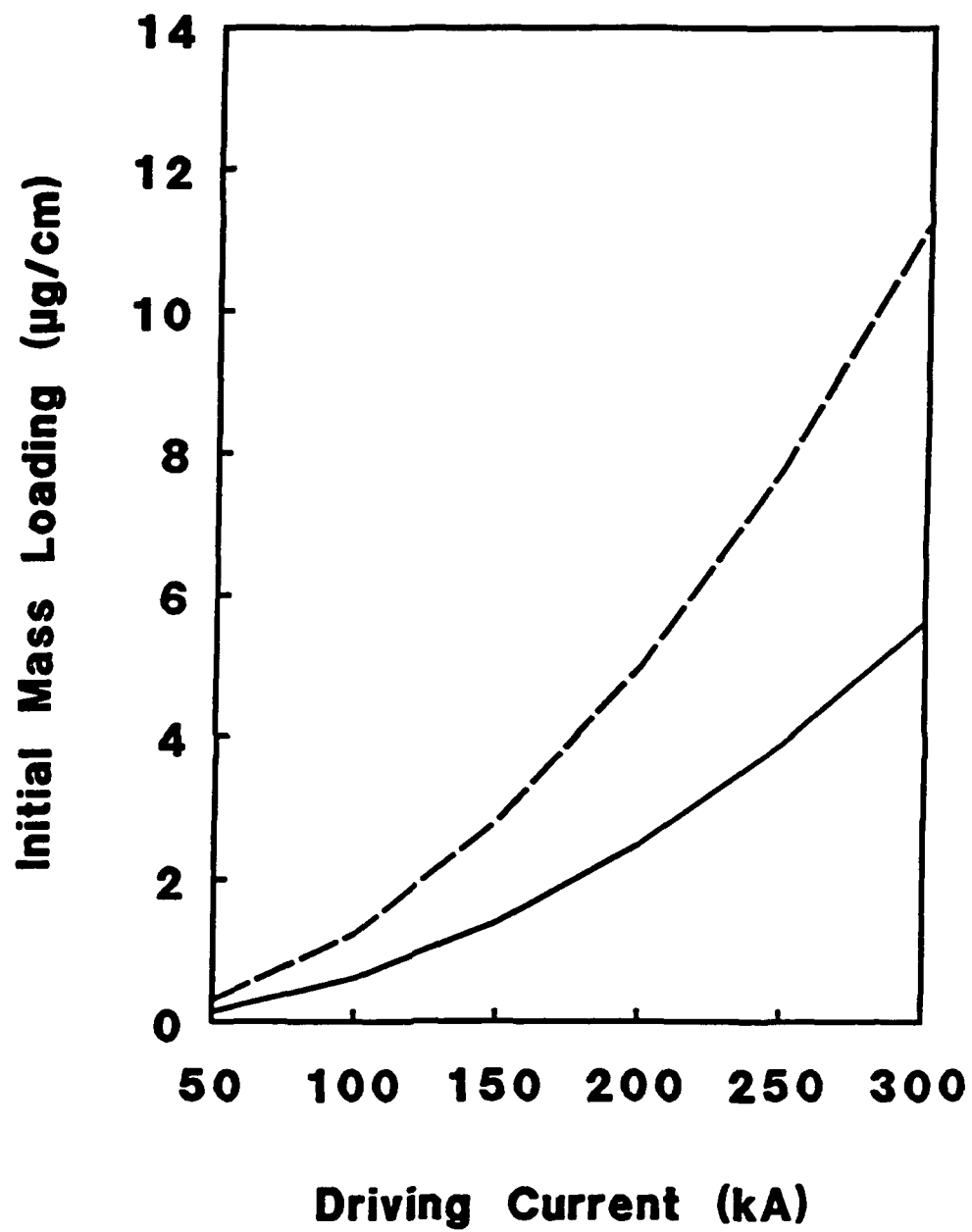


FIG. 3.1. Bennett-pinch condition for temperatures of 50 eV (dashed) and 100 eV (solid).

required to balance radiative losses against resistive heating.⁷⁸ An expression for the Pease-Braginskii current including characteristic radiation losses is:

$$I(\text{MA}) = 1.83 \times 10^{-16} \left(\frac{\ln \Lambda}{R(N_I, T)} \right)^{1/2} (1+Z) T^{1/4} (\text{keV}) \quad (3.3)$$

where $\ln \Lambda$ is the Coulomb logarithm, and $R(N_I, T)$ is the cooling coefficient (W-cm^3). The Coulomb logarithm can be estimated by:

$$\ln \Lambda = 24 - \ln \left(N_e^{1/2} T_e^{-1} \right) \quad (3.4)$$

where N_e is the electron density in cm^{-3} and T_e is the electron temperature in eV.⁷⁹ The calculations of either Terry et al. (in Ref. 80) or Post et al. (Ref. 81) were used to estimate the cooling coefficient and the effective charge. Values of these quantities, along with Pease-Braginskii currents based on Eqs. 3.3 and 3.4, are presented in Table 3.1 for a neon plasma. The cooling-coefficient and effective-charge values are for an ion density of 10^{18} cm^{-3} and for temperatures of 40, 50, 100, and 400 eV. The 40 and 400 eV temperatures were chosen because they correspond to peaks in the cooling coefficient. The 40-eV peak is due primarily to radiation greater than 50 Å (< 250 eV) from L-shell transitions. The calculation of the cooling-coefficient by Terry et al. includes effects of opacity which result in a value of the cooling-coefficient considerably less than that of Post et al. for the 40-eV peak. The 400-eV peak is due primarily to radiation less than 15 Å (> 850 eV) from K-shell transitions. The temperatures of 50 eV and 100 eV were chosen because of their relevance to the neon lasing problem. As can be seen from Table 3.1, the Pease-Braginskii currents are much less when characteristic radiation is included.

Temp. (eV)	Avg. Z	R (10^{-28} W cm ³)	I _{pe} (kA)
Post			
40	5.5	800	4.5
50	6.5	600	7.0
100	8.0	20	54
400	9.0	20	92
Terry			
40	6.5	28	28
50	7.0	20	38
100	8.0	6	98
400	9.0	19	94

Table 3.1. Effective charge, radiation coefficient (for ion density of 10^{18} cm⁻³), and Pease-Braginskii current for neon plasmas of different temperature.

For a Z-pinch driven by a rapidly rising current, the kinetic energy of the implosion is a significant fraction of the total energy, and this kinetic energy can be thermalized to add to the heating of the pinch.⁸² As the current in the pinch rises and the pinch implodes, magnetic energy is stored in the changing inductance of the load. Since the plasma is confined by the magnetic field, the kinetic energy of the implosion is added to the internal energy of the plasma. Significant amounts of electrical energy can be transferred to the load in this way. Because the Z-pinch plasma is a part of the electrical circuit, its impedance can affect the dynamics of the circuit.⁸³ The internal resistance and inductance of the Z-pinch load must be considered if low impedance power supplies are used or if the loading of the circuit due to the imploding plasma becomes large. In an imploding plasma load, both the inductance and resistance increase with decreasing radius. For a small radius Z-pinch, both contributions can be important and can effect the behavior of the electrical circuit.⁸⁴ A calculation which includes the dynamics of the neon plasma as an imploding load and the interaction of this load with the electrical circuit was used in designing the present experiment. The results will be discussed in Chapter 4.

The previous discussion was limited to ideal equilibrium conditions. In reality, the onset of nonlinear plasma instabilities can cause the plasma to break up or collapse. The most common instabilities are described by their azimuthal symmetries. The $m=0$ instability is symmetric with respect to the azimuthal angle and is known as the sausage instability. It produces localized pinches along the axis with smaller radius than the bulk of the plasma. The plasma is envisioned as a series of sausage links with the pinches at the

connection of the sausages, hence the name sausage instability. The growth rate of these instabilities has been the subject of a great deal of theoretical modeling.⁸⁵ The $m=1$ instability is referred to as the kink instability because it appears as a kink along a linear Z-pinch. This pinch has also been modeled extensively and some methods of stabilization have been suggested.⁸⁶

3.2 Neon Z-Pinch Implosions

Neon gas-puff Z-pinch implosions have been studied on numerous pulsed power generators by recording spectra of soft X-rays from Ne IX and Ne X. Extensive theoretical modeling has been carried out to interpret these spectra. Although inappropriate for use as a neon laser, these plasmas are interesting in the present context for two reasons. First, the spectra and their interpretation provide a basis for comparison with spectra obtained in neon-laser experiments. Second, empirical scaling laws of the radiation from these plasmas may be used to optimize the 11-Å Na X pump radiation. For these reasons, results of neon gas-puff Z-pinch experiments are discussed here.

A detailed investigation of neon gas-puff Z-pinch implosions was carried out on the 1-MA Gamble II generator at the Naval Research Laboratory. Variations in current, mass loading, initial gas-puff radius, and current risetime were investigated. The figure of merit for these investigations was the K-shell X-ray yield from Ne IX and Ne X.^{87,88} An optimum mass loading (linearly proportional to the gas-puff plenum pressure) was determined for several peak currents between 0.94 and 1.45 MA for a 2.5-cm initial gas-puff diameter. The maximum X-ray yield was achieved for mass loadings ranging from 15 to 45

$\mu\text{g}/\text{cm}$. This optimum yield scaled as the fourth power of the peak current.⁸⁹ Comparisons with yields from larger pulsed power generators are consistent with this scaling.⁹ Modeling of this scaling indicates an eventual transition to a quadratic scaling at larger current consistent with conservation of energy.⁹⁰ As the initial gas-puff radius was decreased, the implosion occurred closer to the peak of the current and the measured yield increased.⁹¹ Modeling of this radius scaling agreed with experiment. Up to 2.5 kJ of radiation in the range from 0.9 keV to 1.6 keV was produced with a 2.5-cm diameter nozzle and a peak current of 1.2 MA.⁸⁸ This yield increased to about 7 kJ for a 1.75-cm diameter nozzle.⁹¹ The K-shell yield increased as the current risetime was reduced from 60 to 20 ns with a plasma opening switch (POS).⁸⁹ With the POS, an axially more uniform plasma was indicated by X-ray pinhole-camera images and spatially resolved X-ray spectra. Axial non-uniformities in the spectra may be associated with a zippering effect in these implosions due to flaring of the cold neon gas from the nozzle. Zippering is predicted in modeling the effect on the implosion of an axial variation in the initial gas distribution.⁹² Spectroscopic measurements indicated that approximately 75% of the soft X-ray emission was contained in the Ne IX resonance transition and Lyman- α line for the plasma produced using the POS. Without the POS, only 45% of the X-ray emission was contained in these lines. The ratio of the Ne IX resonant transition to the Lyman- α line varied from 0.2 to 0.9 along the axis of the pinch for the implosions without the POS, while with the POS a variation of less than 10% from a value of 1.1 was observed. Estimates of plasma temperatures based on a collisional-radiative equilibrium (CRE) model are 150 eV without the POS and 185

eV with the POS. Mass loadings of 34 $\mu\text{g}/\text{cm}$ (without the POS) and 29 $\mu\text{g}/\text{cm}$ (with the POS), combined with a measured diameter of 1.8 mm, indicate an ion density of $3 - 4 \times 10^{19} \text{ cm}^{-3}$.

Larger pulsed power machines with higher currents have produced larger neon K-shell X-ray yields. The Double EAGLE generator at Physics International Company delivers 4 MA (6 TW) and has produced 15 kJ of neon K-shell X-rays.⁹³ Spectra of the Ne IX and Ne X K-shell transitions indicate that the Lyman- α line is three to six times more intense than the Ne IX resonant transition. The SATURN generator at Sandia National Laboratories delivers 10 MA (32 TW) and has produced 100 kJ of neon K-shell X-rays.⁹⁴ In this case, the ratio of the Lyman- α line to the Ne IX resonant transition is 2.3. A comparison of relevant parameters for these generators is given in Table 3.2.

3.3 Sodium Z-Pinch Implosions

To produce an imploding Z-pinch containing sodium for photopumping experiments, a sodium-fluoride (NaF) capillary-discharge source was developed.⁹⁵ This source was produced by discharging current from a charged capacitor through a 0.5-mm diameter capillary drilled in packed NaF powder. The NaF was heated by the current, and plasma was ejected through a nozzle to produce a cylindrically symmetric plasma column. Implosions of the plasma from this source with a 1-MA current pulse produced an intense 20-ns pulse of sodium K-shell X-rays. The total sodium K-shell peak power was 70 GW, and the peak power of the Na X resonant line at 11 Å was 25 GW.⁹⁶ K-shell X-ray spectra indicated the ratio of the Lyman- α line to the Na X resonant transition ranged from 0.7 to 1.2.⁹⁷ Temperatures of 250-500

	GAMBLE II	Double EAGLE	SATURN
Total K-shell (kJ)	4	15	100
Pulse Width (ns)	23	22	20
Ne X/Ne IX	0.2-0.9	3.2-6.5	2.3
Temperature (eV)	150-185	1300	>300
N_e Density (10²⁰ cm⁻³)	3.4	1.6	1
Final Radius (mm)	0.9	-	2.2
Mass Loading (μg/cm)	29-34	-	1000

Table 3.2. Summary of the characteristics of neon implosions on the Gamble II, Double EAGLE, and SATURN generators.

eV and an electron density of 10^{20} cm^{-3} were estimated using a collisional-radiative equilibrium (CRE) model.⁹⁸ Recently, a higher-current version of this source was modified and used on the Double-EAGLE generator to produce more than 100 GW of the Na X 11-Å pump radiation.⁹⁹

The sodium pump power may be increased by replacing the NaF plasma with a pure sodium plasma. To this end, an array of sodium wires, produced by extruding pure sodium through pinholes, was imploded on the Double-EAGLE generator to produce 150 GW of 11-Å sodium pump radiation.¹⁰⁰ A similar technique was used on the SATURN generator to produce considerable Na K-shell radiation.¹⁰¹ Properties of these sources are given in Table 3.3.

Several other techniques have been investigated in an effort to produce a sodium source for photopumping experiments. Metal vapor sources were studied at NRL based on the work of Doucet.¹⁰² In this source, an annular puff of sodium plasma is produced by a radial electrical discharge across a sodium foil. Alternatively, the electrically driven explosion of a sodium wire confined in a space, analogous to the capillary discharge, was developed and tested. Implosions on the Gamble II generator with both of these sources produced modest powers of 11-Å sodium radiation.¹⁰³ An annular sodium-chloride plasma produced with a radial discharge source, was imploded on the PITHON generator to produce 50 GW of 11-Å sodium radiation.¹⁰⁰ The Proto II generator was used to implode an annular neon gas puff onto a sodium-fluoride coated paralyene cylinder to produce sodium radiation.⁷³ Peak powers of up to 100 GW of 11-Å sodium radiation were produced with this technique.

	GAMBLE II NaF	Double NaF	EAGLE Na	SATURN Na
Total K-shell (kJ)	1.7	14	35	(350)
Pulse Width (ns)	20	26	53	35
Na XI/Na X	0.7	2-4	2	2
Temperature (eV)	240	<560	360	-
N_e Density (10²⁰ cm⁻³)	3.6	6	2-5	-
Final Radius (mm)	1.0	1.5-2.0	1.2-2.4	4
Mass Loading (μg/cm)	93	300	170	-
11-Å[•] Power (GW)	25	130	150	200
11-Å[•] Energy (kJ)	0.6	3.4	8	(4)

Table 3.3. Summary of sodium implosions on the Gamble II, Double EAGLE, and SATURN generators using sodium wire arrays and NaF capillary discharges.

3.4 Sodium/Neon Photopumping Experiments

Simultaneous implosions of parallel sodium fluoride (NaF) and neon Z-pinchs were used in experiments to measure photopumping of the Ne IX $1s^2-1s4p$ transition.^{12,104,105} The NaF Z-pinch was produced on the axis of the Gamble II generator by the main current pulse. The neon Z-pinch was produced 5 cm off axis by driving a fraction of the generator current through a neon gas puff. Up to 30 GW of 11-Å sodium pump power was measured from the NaF plasma imploded by a 1-MA current. Currents of 100 to 150 kA were used to implode the neon. The neon implosion occurred zero to 25 ns after the peak of the 80-ns risetime current pulse as indicated by filtered vacuum diodes. Comparisons of the ratio of the intensities of the Ne IX $1s^2-1s4p$ (11.0 Å) transition and the Ne IX $1s^2-1s3p$ (11.5 Å) transition were made for neon implosions with and without the sodium source. This ratio was 0.6 when the NaF plasma was replaced with a metal rod or a magnesium-fluoride plasma. This ratio was increased to 0.9 for neon spectra when the sodium radiation was present and coincident with the neon implosion.

Recently, experiments have been performed at Sandia National Laboratories using the SATURN generator to demonstrate photopumping. Neon gas was contained in a chamber and enclosed by a window material that is transparent to 11-Å sodium radiation. The neon was heated to the Ne IX state by the photon flux from a sodium wire-array implosion.¹⁰⁶ An enhancement of the intensity of the Ne IX $1s^2-1s4p$ (11 Å) transition relative to the Ne IX $1s^2-1s3p$ (11.5 Å) transition was observed at the time of the 11-Å sodium radiation.

Chapter 4

EXPERIMENTAL GAS-PUFF Z-PINCH

The criteria for the design of this experiment were determined by the required neon plasma conditions and by the experimental parameters of the neon lasant in the sodium/neon photopumping experiments on the Gamble II generator. The neon plasma conditions were discussed in Chapter 2. In the sodium/neon experiments a portion of the Gamble II current pulse was used to implode a neon gas puff. It is therefore desirable to use a current waveshape similar to that of Gamble II so that results of this experiment can be applied directly to the sodium/neon experiments on Gamble II.

4.1 Design Parameters

The previous discussion of the neon plasma in Sec. 2.2.1 provides guidelines for the design of the current source for the neon Z-pinch in this experiment. An electron temperature of 75 eV, an ion density of 10^{19} cm^{-3} and an imploded plasma diameter less than 0.5 mm were determined to be appropriate for the neon lasant plasma. Based on this density and diameter, a linear mass loading less than 0.65 $\mu\text{g/cm}$ is required. The Bennett pinch condition (Eq. 3.2) gives a current of 90 kA for a temperature of 75 eV, as can be seen from Fig. 3.1.

However, this estimate is for a steady-state condition and does not consider the dynamics of the implosion.

A code developed to model the radiation output of a Z-pinch on the Gamble II generator was used to evaluate the dynamic effects of this neon implosion (see Appendix B). This code incorporates a transmission-line model of the electrical circuit and treats the Z-pinch as a circuit element with a variable resistance and inductance. The inductance is determined by the pinch radius, and the resistance is determined by Spitzer resistivity. The plasma temperature is determined by joule heating, magnetic compression, thermalization of the implosion kinetic energy, and radiation losses. Radiation losses are determined by a temperature-dependent radiation coefficient. Effects of opacity can be included by reducing the radiation coefficient. Input parameters are the initial plasma radius, the linear mass loading, and the voltage waveshape. The Gamble II open-circuit waveshape was used with the peak voltage as an input parameter. The peak imploded plasma temperature and density were determined for various input parameters. Details of this design study are given in Appendix B and the results are summarized in Fig. 4.1. Here, the relation between the peak current and mass loading for final neon plasma temperatures of 50 to 100 eV is given by the shaded area. Compared with results from the Bennett pinch condition (Fig. 3.1), a higher mass loading can be heated to 50 to 100 eV when dynamic effects are included. Alternatively, less current is required to heat a given mass than the Bennett pinch condition predicts when dynamic effects are included. The reasons for this difference are discussed in Appendix B. The peak ion density as a function of the peak current for a 50- to 100-eV plasma is also plotted in Fig. 4.1. For example,

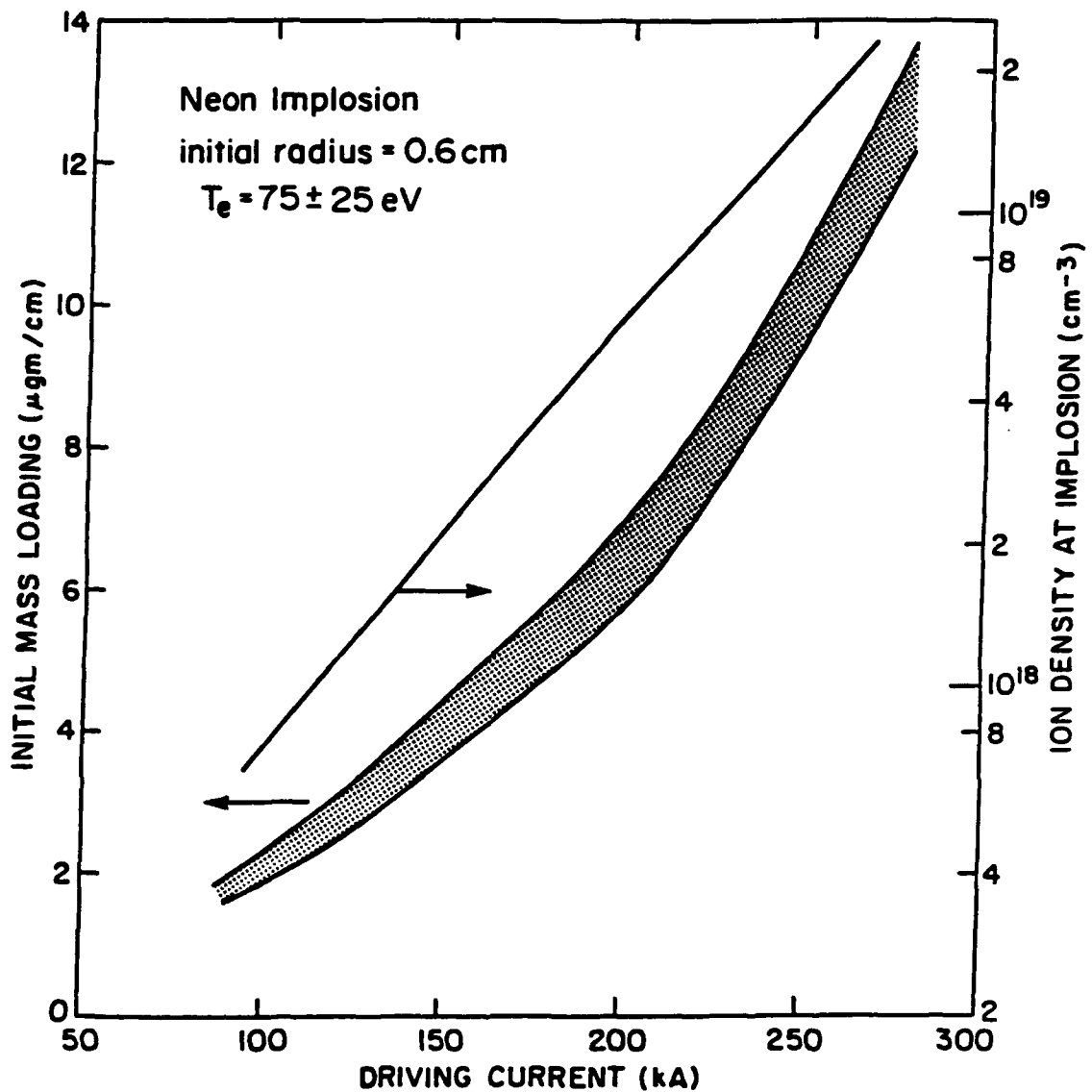


FIG. 4.1. The relation between driving current and mass loading for a 50- to 100-eV plasma (shaded area), and the relation between driving current and imploded neon ion density for a 50- to 100-eV plasma (curve).

a current of 150 kA is required to produce a 50- to 100-eV plasma for an initial neon mass loading of 4 $\mu\text{g}/\text{cm}$. The corresponding peak ion density for a current of 150 kA is $2 \times 10^{18} \text{ cm}^{-3}$. These results indicate that current levels below 150 kA are sufficient to produce the appropriate neon plasma.

4.2 Inductive-Storage Generator

To reproduce the neon plasma conditions used in the photopumping experiments on Gamble II, a 250-kA peak current pulse with a 100-ns risetime is required. A small inductive-storage generator with a high repetition rate was used to provide this current. Previously, this generator had been used to drive an electron beam diode in a proof-of-principle inductive-storage experiment.^{107,108} This generator consists of a capacitor bank, a low inductance feed to a coaxial vacuum inductor, and a plasma opening switch (POS). This system can produce both slow risetime (1 μs) and fast risetime (100 ns) current pulses by adjusting the POS. The source for the POS plasma was driven by a separate capacitor discharge so that the POS could be used simply by charging those capacitors, while other elements of the system were unchanged. An equivalent circuit of this generator and Z-pinch load is given in Fig. 4.2. The gas-puff load is represented as a circuit element with time-varying resistance and inductance. With this system it was possible to investigate the effects of current risetime variations on neon Z-pinch implosions.

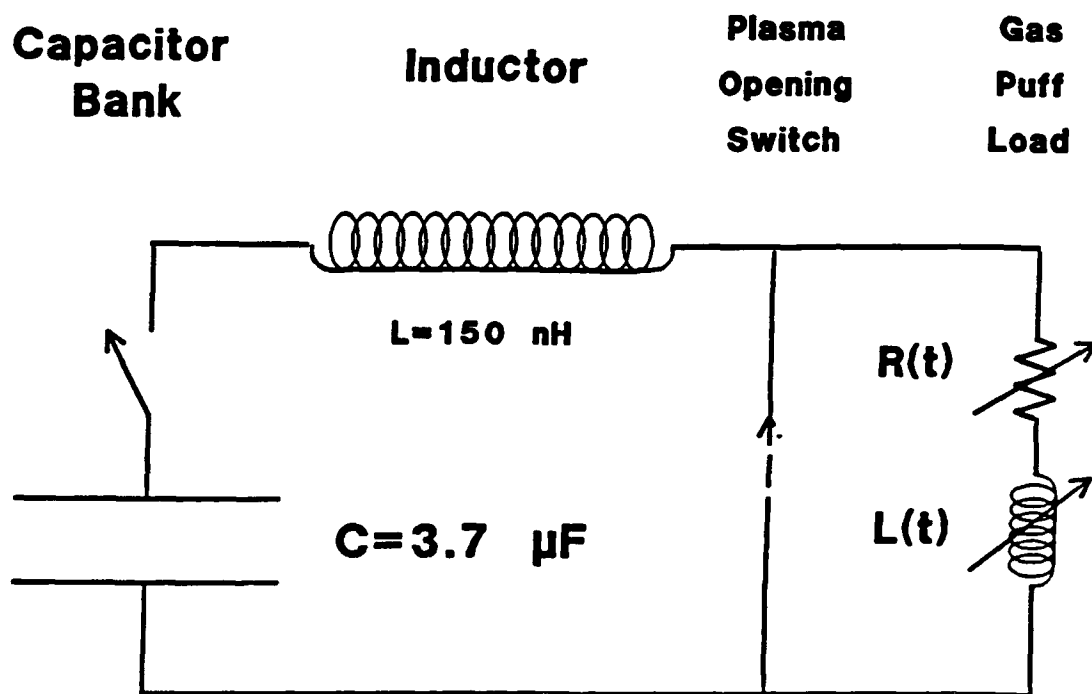


FIG. 4.2. Equivalent circuit of the inductive-storage generator with a Z-pinch load.

4.2.1 Capacitor Bank

The primary energy storage for this generator were two 1.85- μ F capacitors connected in parallel. Charged to 50 kV, the capacitors provided a stored energy of 5 kJ. The current was transferred from the capacitors to the vacuum coaxial inductor chamber through 36 (RG 213/U) cables approximately 1 meter in length. These cables were connected via a common vacuum interface to the coaxial vacuum inductor. The opposite end of the center conductor of the coaxial vacuum inductor served as the cathode of the Z-pinch load. Each capacitor was switched independently, and a common trigger was used for both switches. The capacitor charging circuit, switches, and RG 213/U connections were mounted atop each capacitor and submerged in oil. A schematic diagram of the charge and trigger circuit is given in Fig. 4.3. The current monitor (I_1), shown in Fig. 4.3, was used to record the preionization current, and will be discussed in Sec. 4.3.1.

4.2.2 Vacuum Inductor

The center conductor of the coaxial vacuum inductor consisted of a 5-cm diameter brass tube, initially 12 cm in length, and later changed to 50 cm when the POS was added. One end of this center conductor was connected to the capacitor bank through a vacuum interface. The other end served as the cathode for the neon gas puff via an array of 12 brass wires strung across the diameter of the tube. The neon gas puff was directed toward the wire array and the interior of the brass tube acted as a gas dump. Initially, various screens were used as the cathode, but they did not survive the discharge. The

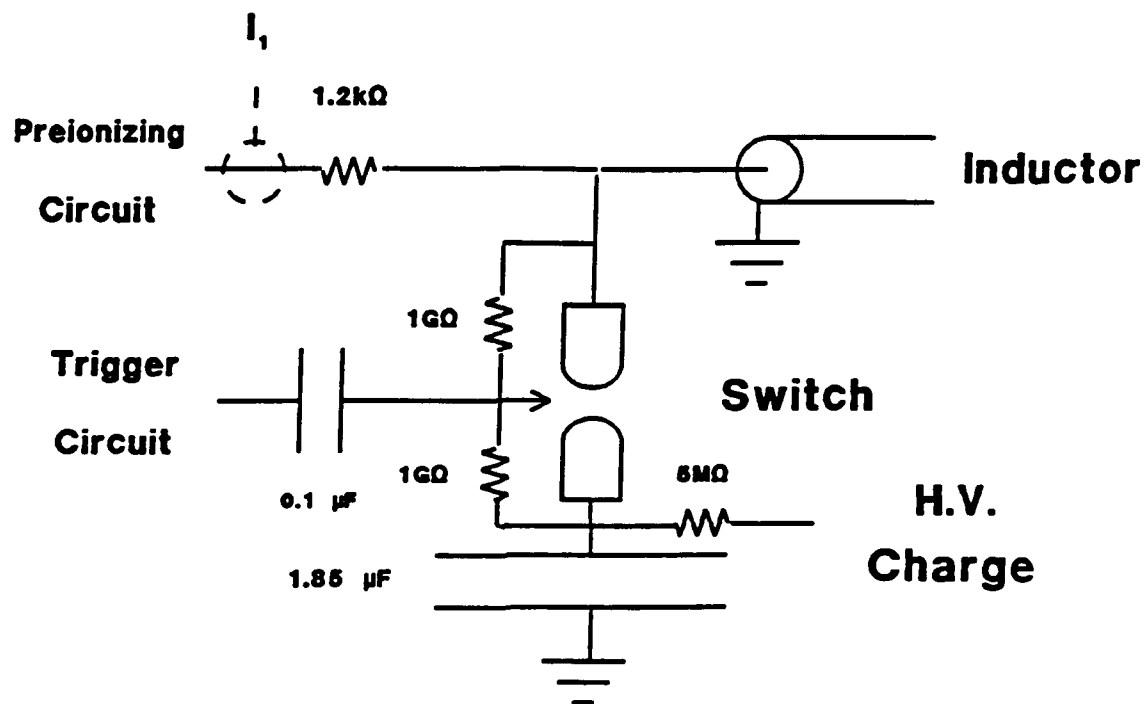


FIG. 4.3. Charge and trigger circuit for the Z-pinch capacitors.

brass wires did survive numerous discharges before being damaged. The current-return path of the coaxial vacuum inductor were 12 rods, each 3-mm in diameter, equally spaced on a 10-cm diameter. This geometry provided a transparent, coaxial current-return path through which the POS plasma was injected. The center conductor and 12 current-return rods (along with the cables from the capacitor bank to the vacuum interface) made up an inductor that could be current charged when the capacitors were triggered. Three current monitors, mounted in the current-return support structure, measured the axial current. One current monitor (I_2) was located between the vacuum interface and the POS region. A second monitor (I_3) was located between the POS region and the load. A third monitor (I_4) surrounded the nozzle and measured the current through the neon gas puff. A schematic of the inductive-storage generator is given in Fig. 4.4.

4.2.3 Plasma Opening Switch

The opening switch plasma was produced by six plasma guns driven by two capacitor banks.¹⁰⁹ The guns were equally spaced around the coaxial vacuum inductor and injected low-density plasma radially inward toward the center conductor through the return-current rods. Each capacitor bank contained three 0.6- μ F capacitors which were charged to 25 kV providing a stored energy of 155 J per gun or approximately 1-kJ total. A diagram of the plasma-gun circuit is given in Fig. 4.5(a), and a diagram of the plasma gun is given in Fig. 4.5(b). When the main capacitor bank is triggered, the POS plasma initially provides a short-circuit that isolates the gas-puff from the current source. This plasma acts as a current path between the

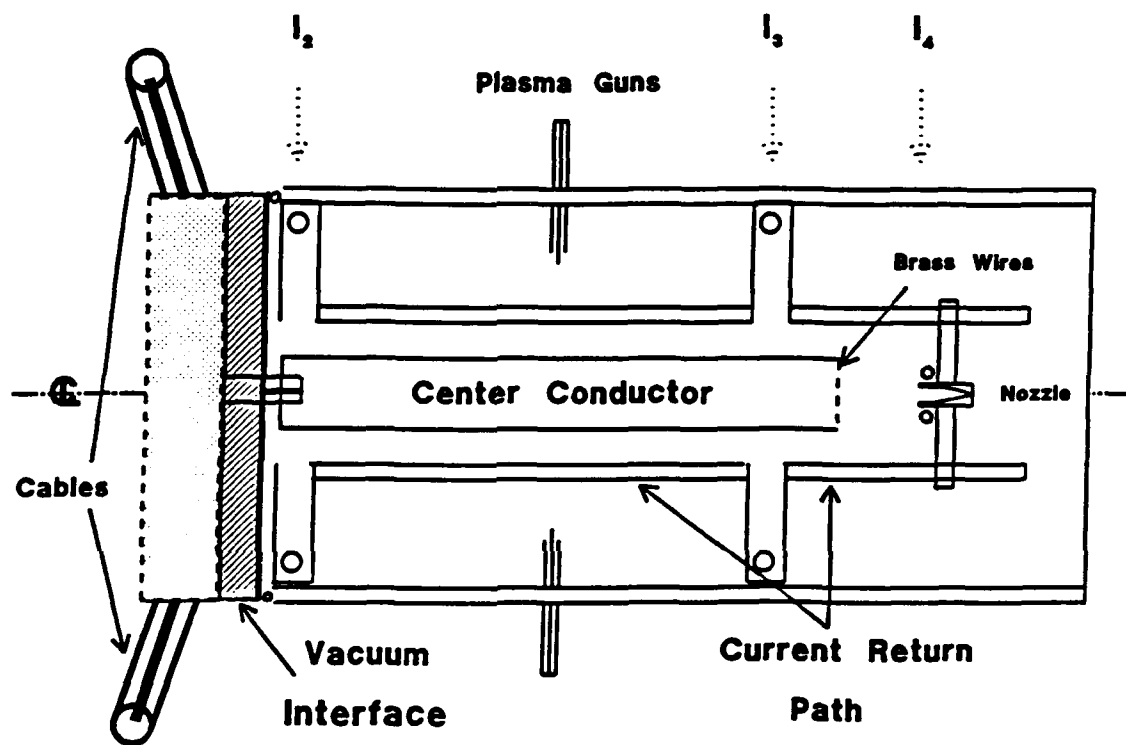


FIG. 4.4. Schematic of inductive-storage generator with a gas-puff load.

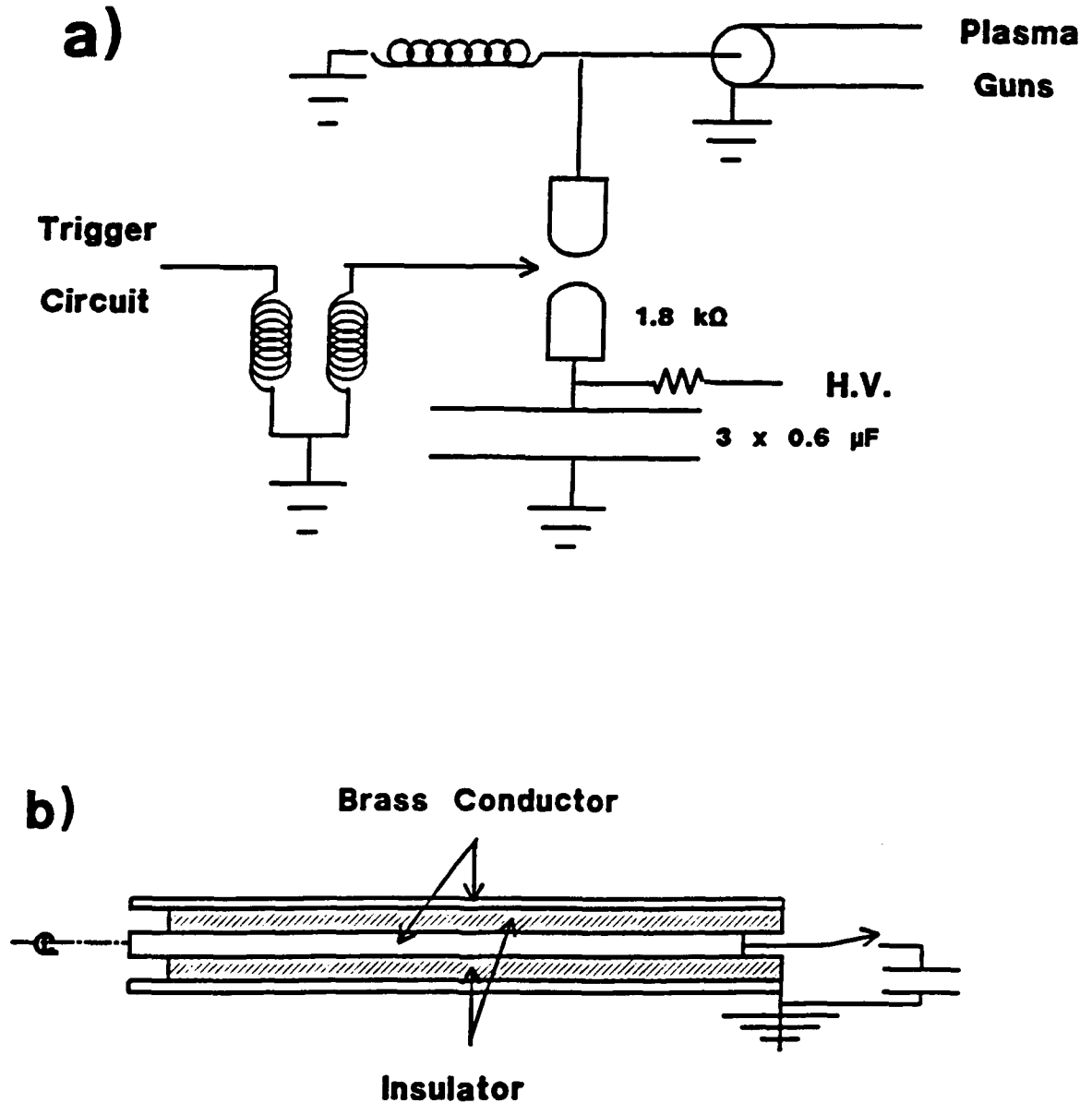


FIG. 4.5. a) Charge and trigger circuit for the POS plasma guns and b) schematic of a POS plasma source.

center conductor and the current-return rods (see Fig. 4.6(a)) until a threshold current level is exceeded. Then a vacuum gap opens between the center conductor and current return rods in the POS region, and current is abruptly switched to the gas-puff load (see Fig. 4.6(b)). The larger inductance associated with this new current path produces a voltage on the load proportional to the rate that the current is interrupted.

4.3 Neon Gas-Puff Source

To achieve neon plasma conditions similar to those in the photopumping experiment on Gamble II, the same neon gas-puff hardware was used. Neon from a high-pressure tank was fed to a fast opening valve which was connected to a small nozzle. The hardware could be mounted either on the test stand with the inductive storage generator or on Gamble II without any alterations; thereby assuring the same mass loading in either experiment.

The fast opening valve,¹¹⁰ a commercially available design, was previously used in fast Z-pinch experiments on Gamble II. The valve is operated by a current pulse from a capacitor discharged through a solenoid. A magnetic hammer concentric with the bore of the solenoid is accelerated by the rising magnetic field. Once accelerated, the hammer strikes a lexan drum which separates the high-pressure plenum from the vacuum. The drum is displaced from its position in contact with an O-ring seal, and high-pressure gas is allowed to expand into the vacuum. The drum is designed so that forces that arise from a pressure differential between the plenum and the ambient pressure are perpendicular to the direction of motion of the drum. The

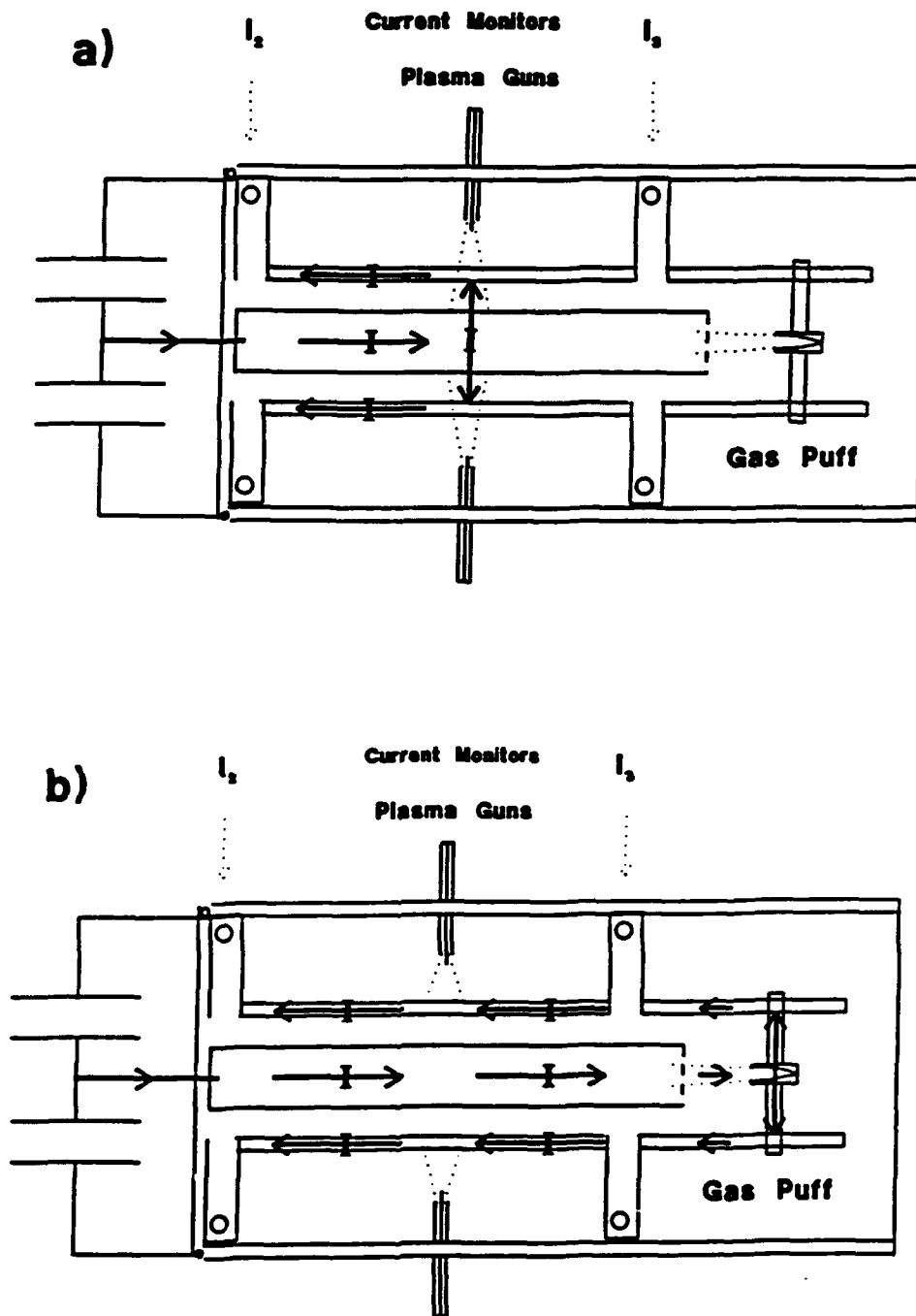


FIG. 4.6. Inductive-storage generator a) with the POS closed and b) with the POS open and coupled to the gas-puff load.

acceleration of the drum is therefore independent of the pressure differential, and the time required for the drum to open is independent of the plenum pressure. The fast-opening-valve hardware was adapted to connect the valve to a small brass nozzle through a 1-cm inner diameter, 12-cm long flexible tube. The nozzle had a 1.7-mm diameter throat and a 3-cm long contoured-taper opening to an exit diameter of 1 cm. This provided a ratio of 1:35 for the entrance and exit cross-sectional areas of the nozzle. The valve was typically operated with plenum pressures between 50 and 150 psi. A diagram of the valve and nozzle is given in Fig. 4.7.

4.4 Preionization

In an effort to achieve a reproduceable discharge across the neon gas puff, the gas was preionized by a small capacitor discharge in parallel with the main discharge. Experiments have demonstrated that the initial degree of ionization influences the dynamics of a gas-puff implosion¹¹¹⁻¹¹³. Experiments on Gamble II and other pulsed power machines typically use ultraviolet radiation from flashboards to provide a small degree of preionization. Efforts in the present experiment to implode the neon without preionization proved unsuccessful. Therefore, the capacitor discharge circuit shown in Fig. 4.8 was incorporated to preionize the neon gas.

The preionization discharge provided a technique to visualize the spatial extent of neon gas exiting the nozzle at various times. Neon was puffed through the nozzle toward the brass wires on the center conductor, which was connected to the high voltage of the preionizing circuit. A voltage pulse of 1.0 to 1.5 kV from this circuit broke

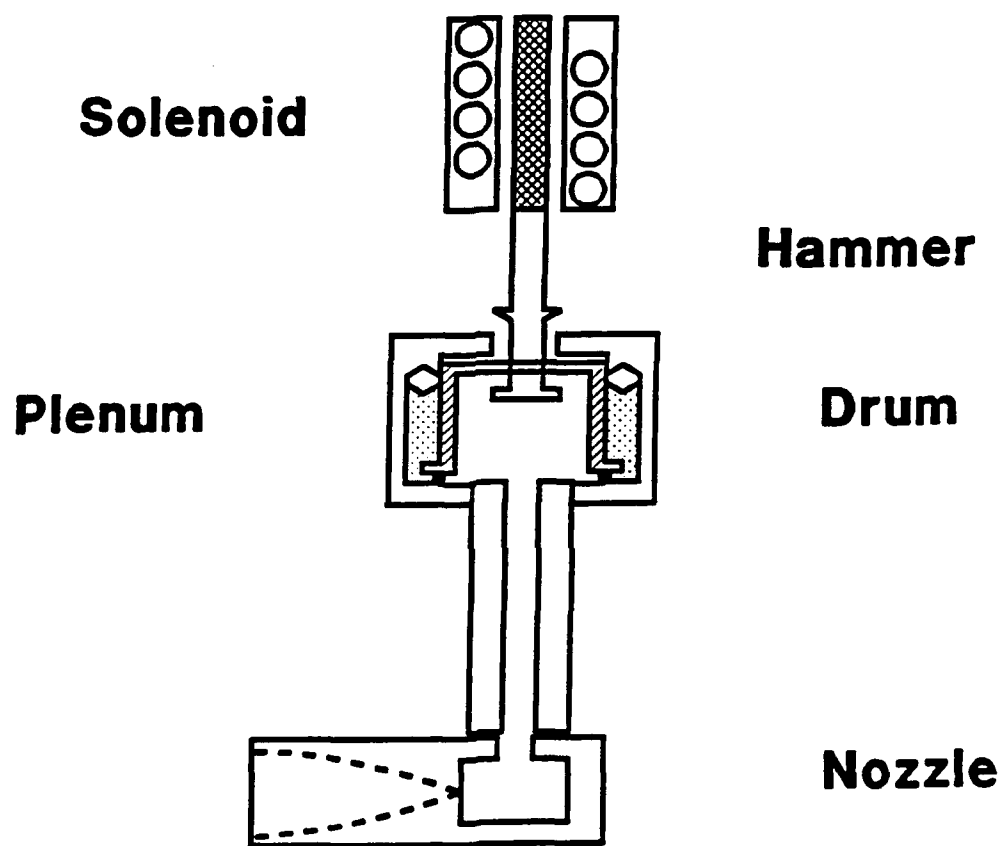


FIG. 4.7. Schematic of the fast-valve and nozzle assembly.

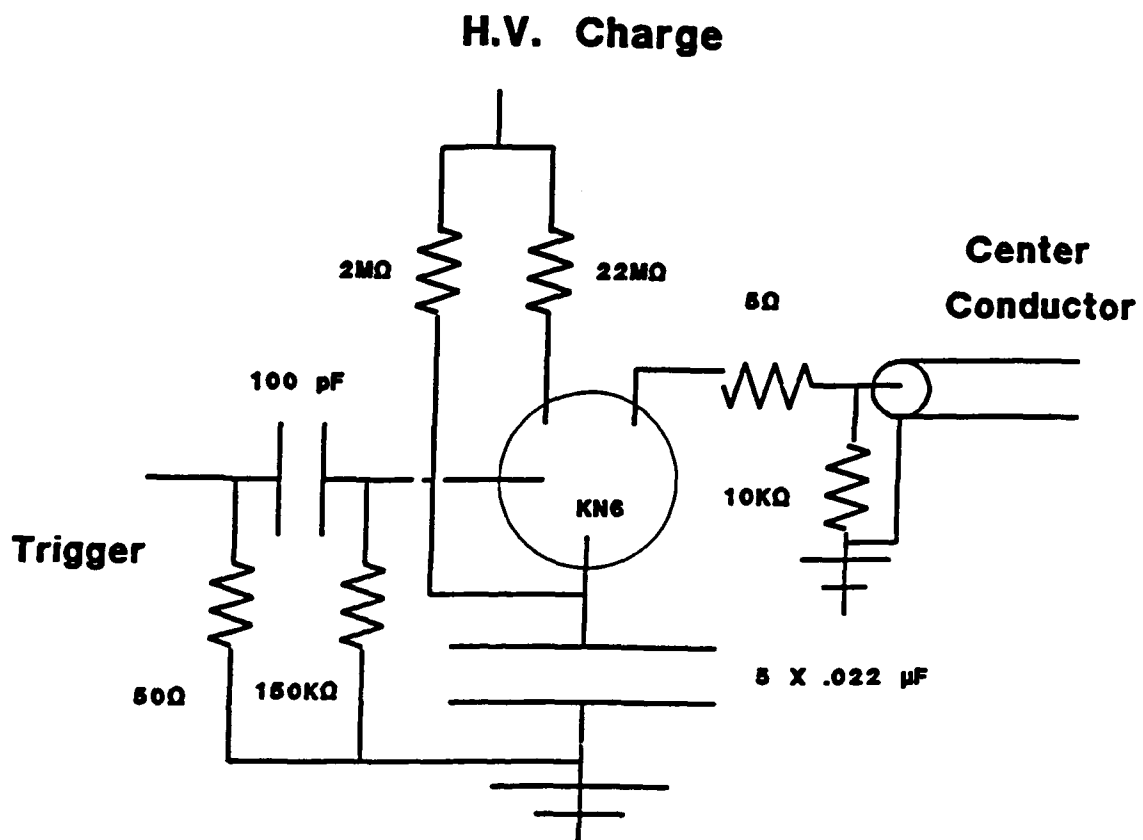


FIG. 4.8. Charge and trigger circuit for neon gas preionization.

down the neon gas, and the capacitor in the preionizing circuit was discharged through the neon. This current pulse partially ionized the neon, and light was emitted throughout the volume of the gas. An open-shutter photograph of this discharge provided an image of the light-emitting neon distribution. This 200-ns current pulse is short compared with the timescale of the gas flow so that images of the neon at various delay times could be recorded. The images in Fig. 4.9(a) correspond to delays between the fast-opening-valve trigger and the preionizing-circuit trigger of 3.05, 3.10, 3.15, and 3.25 ms, respectively. A pressure sensor located at the center conductor was used to determine the time delay between the trigger signal for the fast-valve circuit and the arrival of gas at the cathode. No signal was observed for the first 3 ms. This time delay is primarily associated with acceleration of the magnetic hammer. An example of the pressure-sensor signal after a time delay of 3 ms is given in Fig. 4.9(b). The times at the bottom of the figure correspond to the photographs in Fig. 4.9(a).

Initial photopumping experiments on the Gamble II generator were carried out with the fast valve connected to a 1-cm diameter guide tube.^{4,103,104} Measurements of the spacial distribution of the neon with the preionizing discharge indicated that the gas distribution from this guide tube was grossly nonuniform. The nozzle, described above, was constructed to provide a more cylindrical distribution. This nozzle produced a much more uniform gas distribution and was used in subsequent photopumping experiments.¹² The measurements in Fig. 4.9 were made with this nozzle.

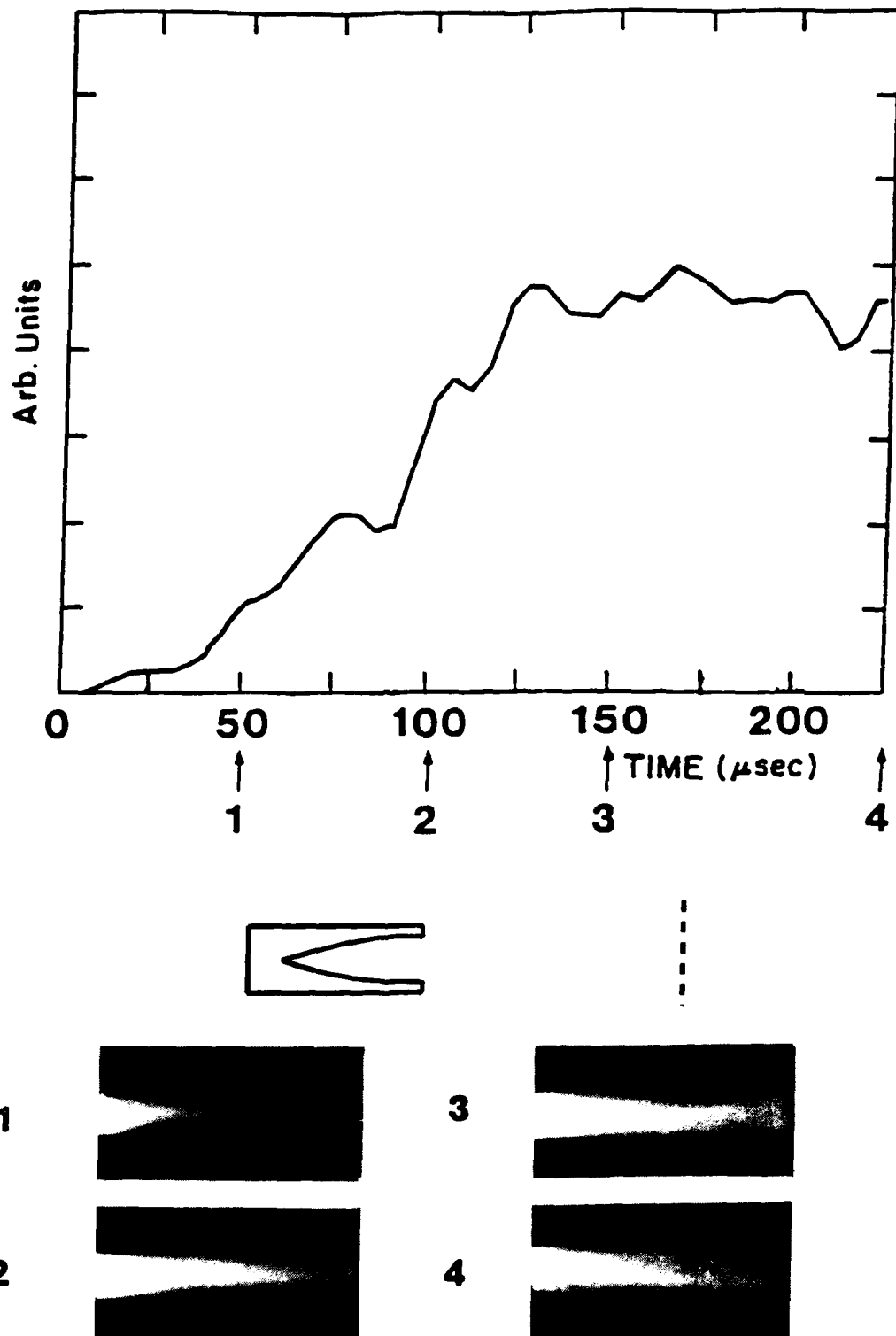


FIG. 4.9. a) Open shutter photographs (bottom) and b) pressure sensor signal (top) of neon gas puff. The numbers indicate timing.

4.5 Electrical Measurements

Electrical measurements for the neon Z-pinch experiment consisted of four current monitors at different locations as indicated in Figs. 4.3 (I_1) and Fig. 4.4 (I_2 , I_3 , and I_4). The monitor I_1 is on the preionizing circuit; monitor I_4 is on the nozzle; and monitors I_2 and I_3 are upstream and downstream of the POS in the coaxial vacuum inductor. Typically, all four currents were recorded on each shot.

4.5.1 Preionization

The current monitors on the preionizing circuit (I_1) and on the nozzle (I_4) provided a measure of the time required to break down the neon gas in the diode gap. An example of these two monitor signals is given in Fig. 4.10. The initial rise in the preionizing-circuit current (I_1) occurs 600 ns after the circuit is triggered. A corresponding signal is not recorded by the nozzle monitor (I_4) because the voltage across the neon gas puff has not achieved a value sufficient to breakdown the gas. The accumulation of charge between these two current monitors, indicated by the decay of I_1 , is understood as current from the preionizing circuit charging the capacitance of the cables and the cathode. As this current decays, the voltage on the cathode increases. When the cathode voltage is sufficient to break down the neon, a signal is recorded by the nozzle monitor (I_4). At this time, current is also recorded by I_1 because current flows to recharge the cathode. The time delay between the preionization-capacitor discharge and breakdown of the gas-filled gap between the center conductor and the nozzle (δt) proved to be a

sensitive function of the delay (T_0) between the opening of the gas-puff valve and triggering the preionizing circuit. This delay (T_0) is 3.0 ms in Fig. 4.10 . The time delay (δt) between triggering the preionizing circuit and gas-breakdown is 6 μ s. The relationship between these two delays (T_0 and δt) was investigated for various plenum pressures, and the results are presented in Fig. 4.11. The delay δt decreases sharply with increasing T_0 to a value of 6 to 8 μ s at different values of T_0 , depending on the pressure. The sharp decrease in δt is correlated with the sharp increase in gas pressure at the cathode (see Fig. 4.9). The limit of 6 μ s is imposed by the time required for the cathode voltage to increase to the breakdown voltage of the neon gas puff. This voltage risetime is determined by the RC time-constant of the preionizer circuit.

4.5.2 Z-Pinch

The main current pulse was measured with current monitor I_2 between the vacuum interface and the POS region and with current monitor I_3 between the POS region and the load. The relative calibration of these two monitors was made with a short-circuit load. The absolute calibration of these monitors was made with a low-current discharge through a resistive shunt of known resistance. An example of the current waveshape for these monitors without the POS plasma is given in Fig. 4.12. The current increases to a peak value of 270 kA in a quarter-period of 1 μ s. An example of the current waveshape of the two monitors with the POS is given in Fig. 4.13. The upstream monitor I_2 measured the current flowing into the POS region and the downstream monitor I_3 measured the current flowing from the switch

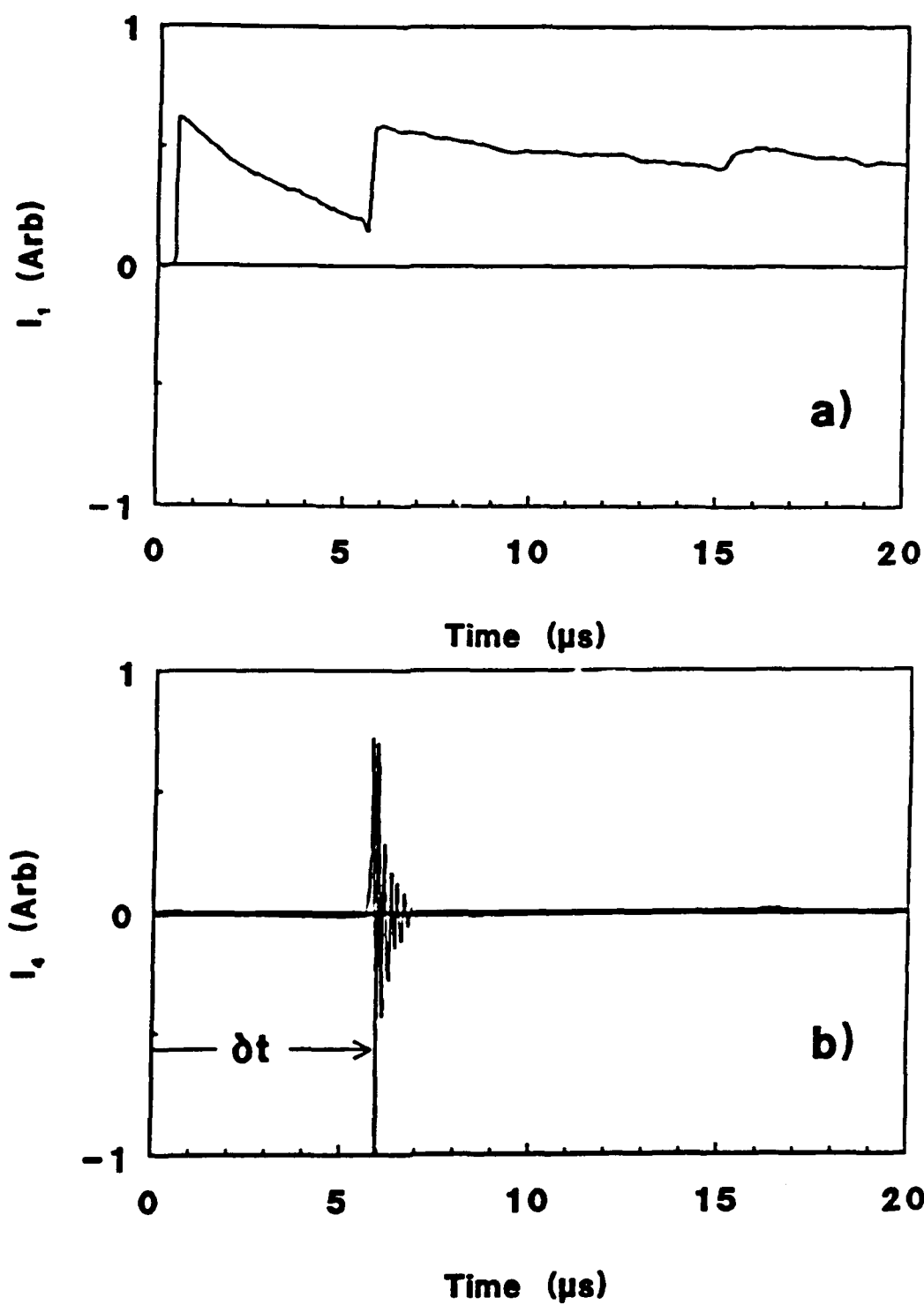


FIG. 4.10. a) Preionizer current (I_1) and b) nozzle current (I_4) signals for a gas-puff to preionization delay of 3 ms.

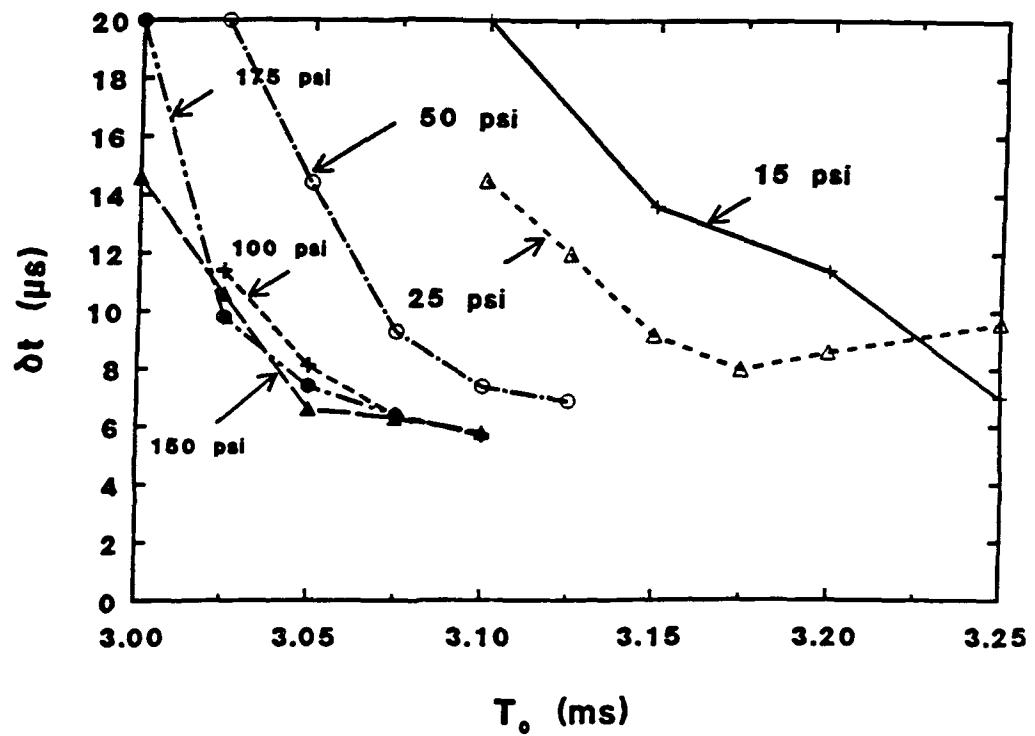


FIG. 4.11. Relation between fast-valve to preionizer delay (T_0) and preionizer to breakdown delay (δt) for various plenum pressures.

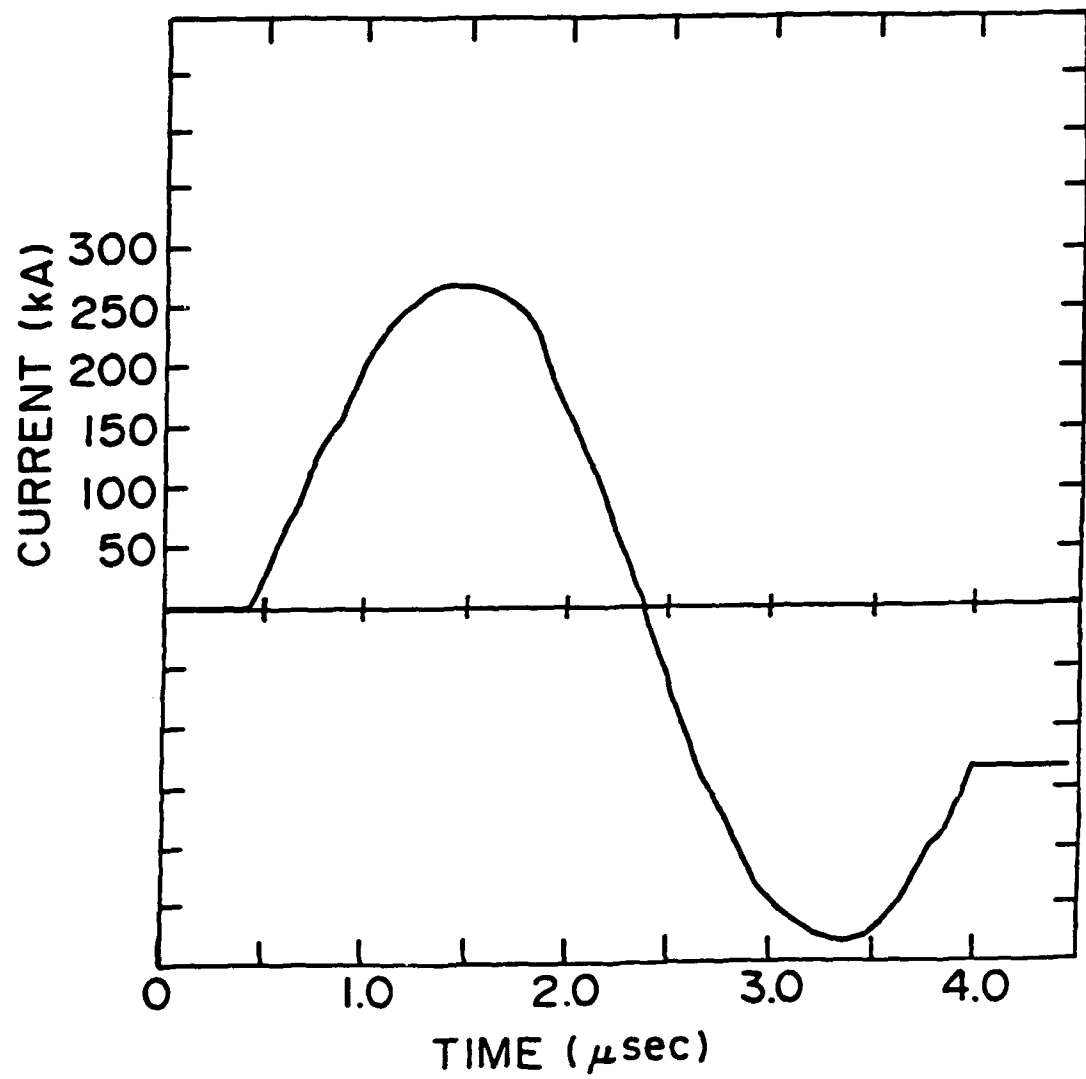


FIG. 4.12. The current waveshape for a 48-kV short-circuit discharge.

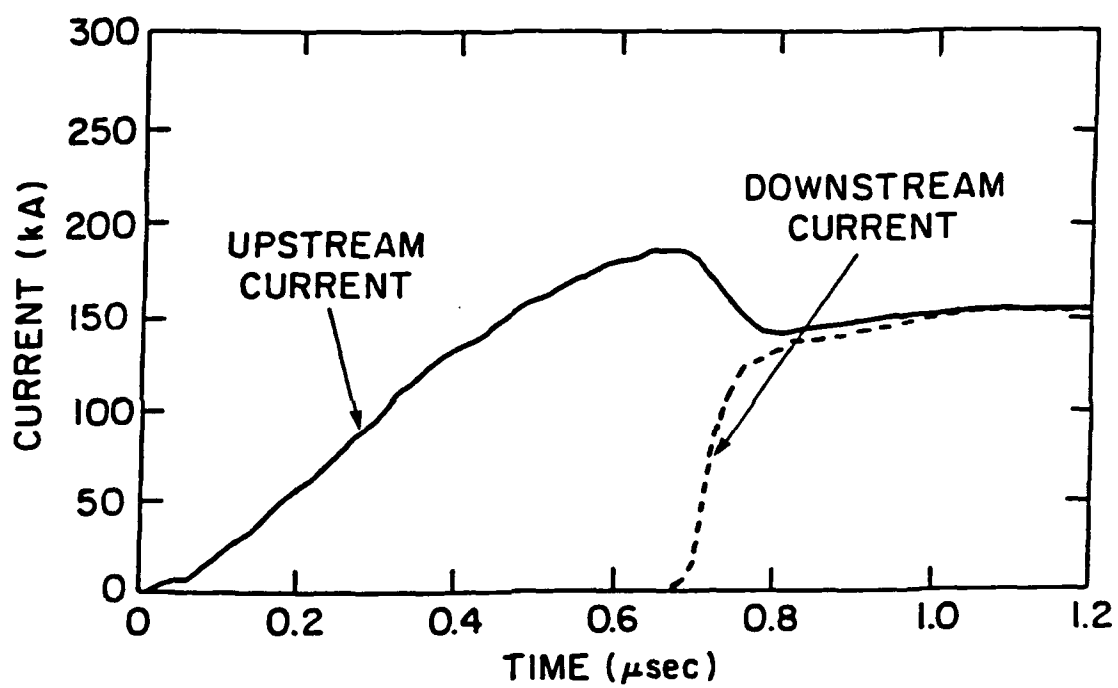


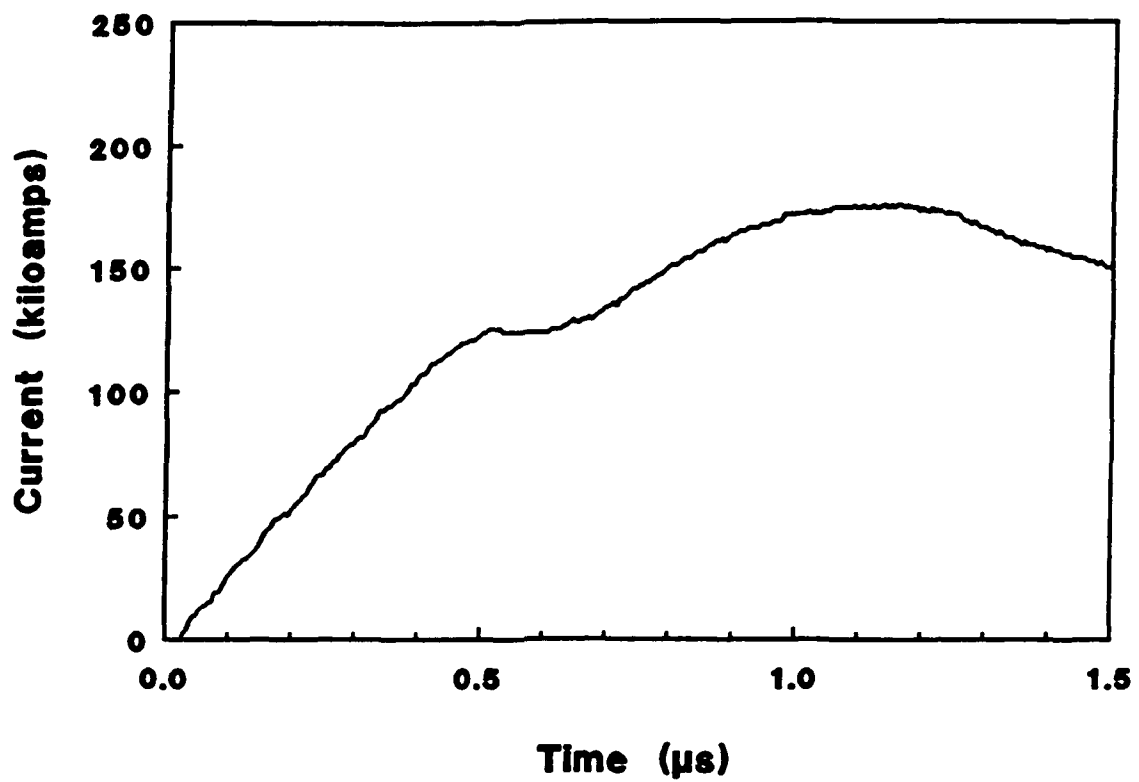
FIG. 4.13. Upstream (I_2) and downstream (I_3) currents for a 35-kV short-circuit discharge with the POS.

region to the load. The decrease of the upstream current as the downstream current increases is due to the added inductive load caused by the rapid switching from one current path to the other. The downstream current rises to 140 kA in less than 100 ns.

Examples of the current waveshapes for monitors I_2 and I_3 with the short circuit replaced by a neon gas-puff load are given in Figs. 4.14 and 4.15 for a charging voltage of 35 kV. Without the POS (Fig. 4.14(a)), the current rises monotonically to 125 kA in 500 ns as the neon gas puff is heated and imploded. The current waveshape then exhibits an abrupt change in slope for a period of 150 ns. The current then continues to increase to its peak value in 1.1 μ s. The changes in the slope of the current signal are indicative of the gas-puff impedance significantly loading the generator. An open-shutter photograph of the imploded neon plasma, similar to those of Fig. 4.9 (with considerable attenuation), is given in Fig. 4.14(b). With the POS (Fig. 4.15(a)), the upstream current I_2 increased to 200 kA in 0.5 μ s before current was switched to the load. The downstream current I_3 increased to a peak of 150 kA in 50 ns. Most of the upstream current was switched to the load. Inductive loading is also apparent in the downstream current. An open shutter photograph of the imploded plasma is given in Fig. 4.15(b).

4.6 Spectroscopic Diagnostics

Measurements of soft X-ray, extreme ultraviolet, and near ultraviolet radiation were used to diagnose the neon Z-pinch implosion. Soft X-ray emissions from Ne IX and Ne X ions were recorded with a curved-crystal spectrograph, filtered vacuum diode,

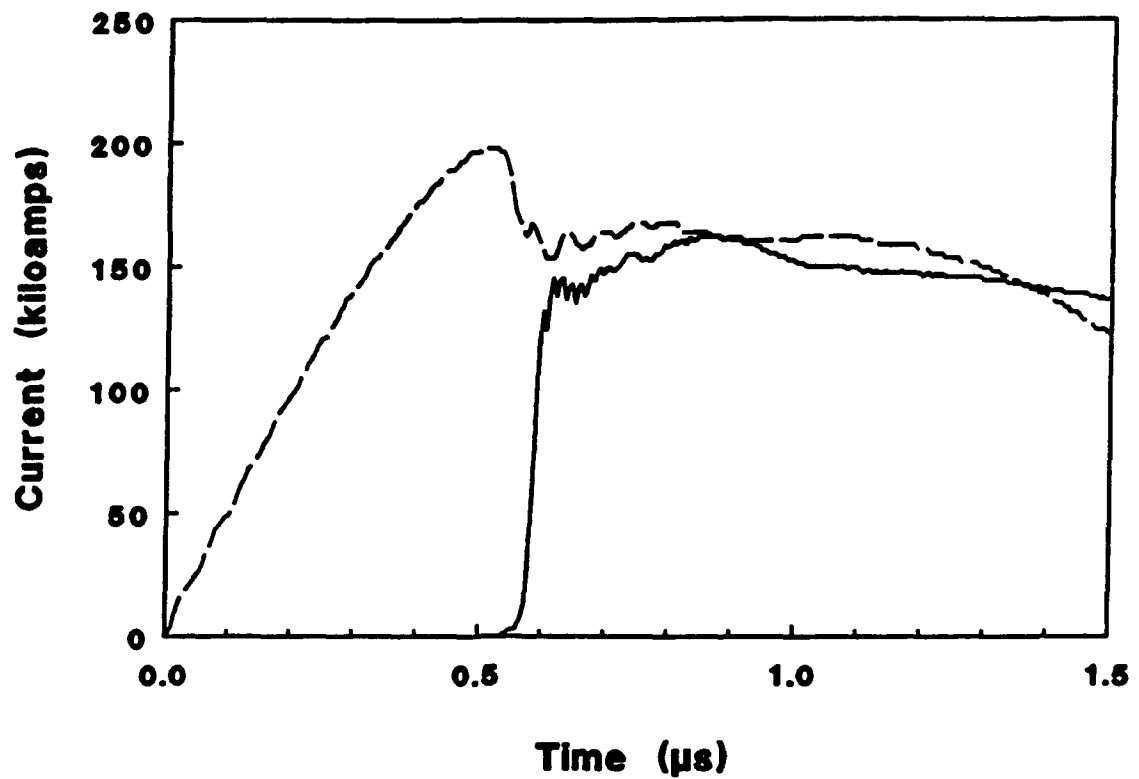


WITHOUT POS



VISIBLE LIGHT

FIG. 4.14. a) Current waveshape (top) and b) open-shutter photograph (bottom) for a neon gas-puff implosion.



WITH POS



VISIBLE LIGHT

FIG. 4.15. a) Upstream (I_2) and downstream (I_3) currents (top) and b) open-shutter photograph (bottom) for a neon gas-puff implosion with the POS.

and filtered pinhole camera. These diagnostics are similar to those used in the photopumping experiments on the Gamble II generator and direct comparisons can therefore be made. Time-integrated and time-resolved extreme ultraviolet (XUV) emissions were also recorded with a grazing-incidence vacuum spectrograph and monochromator. Characteristic radiations from Ne VII, Ne VIII and Ne IX ions were observed in time-integrated spectra. Time histories of a few intense Ne VII and Ne VIII lines were measured. Near ultraviolet (NUV) emissions from Ne III and Ne VIII ions were recorded using two monochromators. Simultaneous measurements were made of the ultraviolet emission in the spectral region of the Ne VIII $1s^2 3s(^2S_{1/2})-1s^2 3p(^2P_{3/2})$ transition at 2820 Å in one monochromator and of the continuum emission in a nearby region in the other monochromator. A gated optical-multichannel-analyzer was mounted at the exit of one spectrometer to give spectral and spacial resolution. Emissions from Ne III and Ne VIII were recorded with this instrument. The arrangement of the spectroscopic instruments is indicated in Fig. 4.16.

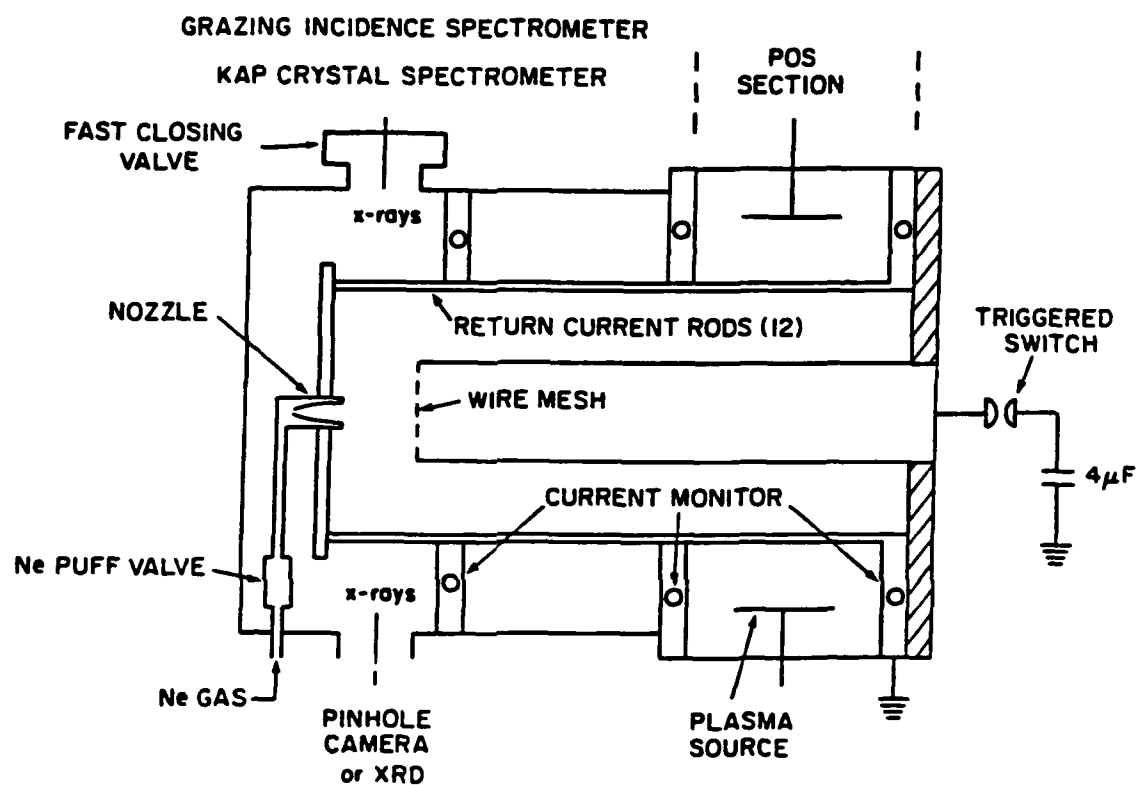


FIG. 4.16. Arrangement of spectroscopic instruments.

Chapter 5

SOFT X-RAY EMISSION

Spectral, spacial and temporal measurements of soft X-rays from the neon implosions were made to study the formation of the Ne IX and Ne X in the implosions and to determine the electron density and temperature of the plasma. An X-ray crystal spectrometer was used for spectral measurements; a filtered pinhole camera was used to image soft X-rays; and a filtered vacuum diode provided time-resolved measurements.

Similar measurements of soft X-rays from neon implosions have been made in two experiments that are directly relevant to the present investigation. Spectra from 0.9 to 1.4 keV (8.8 to 13.7 Å) were measured in the sodium/neon photopumping experiments on the Gamble II generator and in a study of neon gas-puff implosions on the Gamble I generator.^{4,12} For the Gamble I experiment, peak currents of 300 to 500 kA with a 100-ns risetime were used. The measurements indicated that Ne IX could be produced with a driving current as small as 300 kA but that the imploded neon was more highly ionized than desired for a lasant plasma. Spectra from these two experiments may be compared with spectra from the present experiments. The present investigation extends these measurements to peak currents less than 100 kA where soft X-ray emission is no longer observed. This study will identify

the optimum current to produce an appropriate neon lasing plasma.

5.1 Spectral Measurements

A convex curved-crystal spectrograph with a KAP crystal was used to measure the soft X-ray spectrum of the neon plasma in the region from 0.9 to 1.4 keV. A 1-mm wide slit, perpendicular to the Z-pinch axis, provided limited spatial resolution along the z-axis. A thin beryllium filter was used to remove ultraviolet and visible light. Spectral intensities were deduced from measured film densities by unfolding film response, filter absorption, and crystal efficiency. This same analysis was applied to spectra measured in the photopumping experiments on Gamble II, and therefore direct comparisons can be made.⁴ The spectrum recorded for a driving current of 250 kA and a gas-puff plenum pressure of 100 psi is given in Fig. 5.1(a). Transitions in Ne IX and Ne X are identified in this figure. The energy levels corresponding to these transitions with principal quantum numbers up to $n=4$ are given in Fig. 5.2 for the singlet levels and in Fig. 5.3 for the triplet levels. The energy levels were calculated by Martin using Rydberg-Ritz formulae.⁴⁹ Transitions for Ne IX from principal quantum numbers up to six are apparent in Fig. 5.1(a). Transitions up to $n=4$ are observed for Ne X. The ratio of the integrated intensities of the Ne X $1s-2p$ (Lyman- α) and Ne IX $1s^2-1s2p$ lines is 0.2. The spectrum recorded for 150-kA current and 100-psi plenum pressure is given in Fig. 5.1(b). Here, most of the spectral intensities are a factor of three smaller than in Fig. 5.1(a), and the ratio of the Lyman- α to the Ne IX $1s^2-1s2p$ line is 0.3.

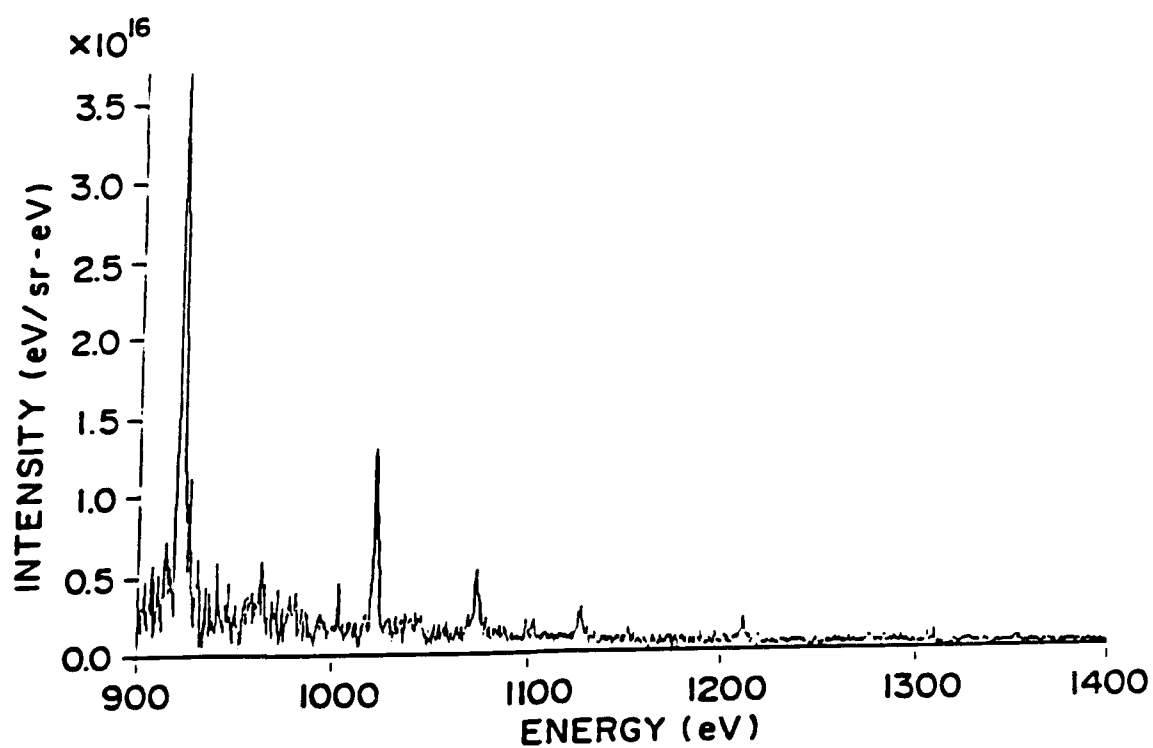
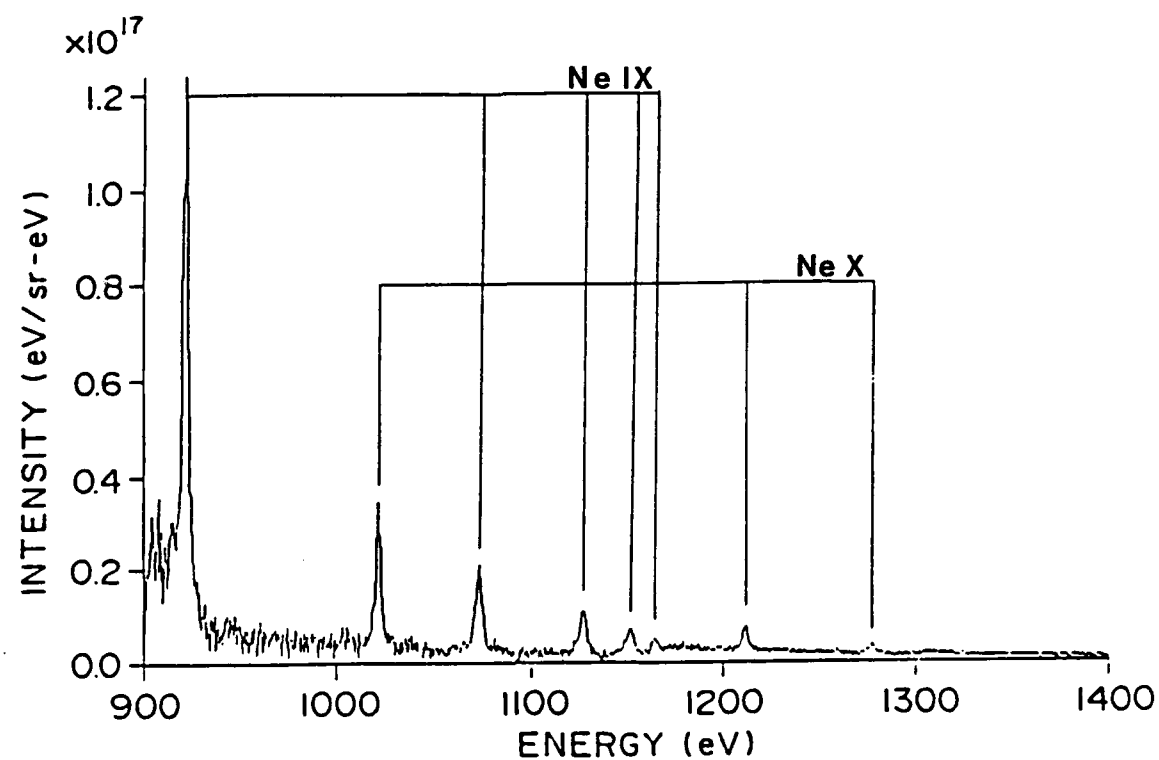


FIG. 5.1. Neon soft X-ray spectra (a) for 250-kA driving current (top) and (b) for 150-kA driving current (bottom).

9644840



n=4

9084100 9090700 9089200 9089240

n=3

8644769 8660410 8657091

n=2

7382563

7436433

¹S₀

¹P₁

¹D₂

¹F₃

FIG. 5.2. Energy-level diagram of Ne IX singlet levels in units of cm^{-1} .

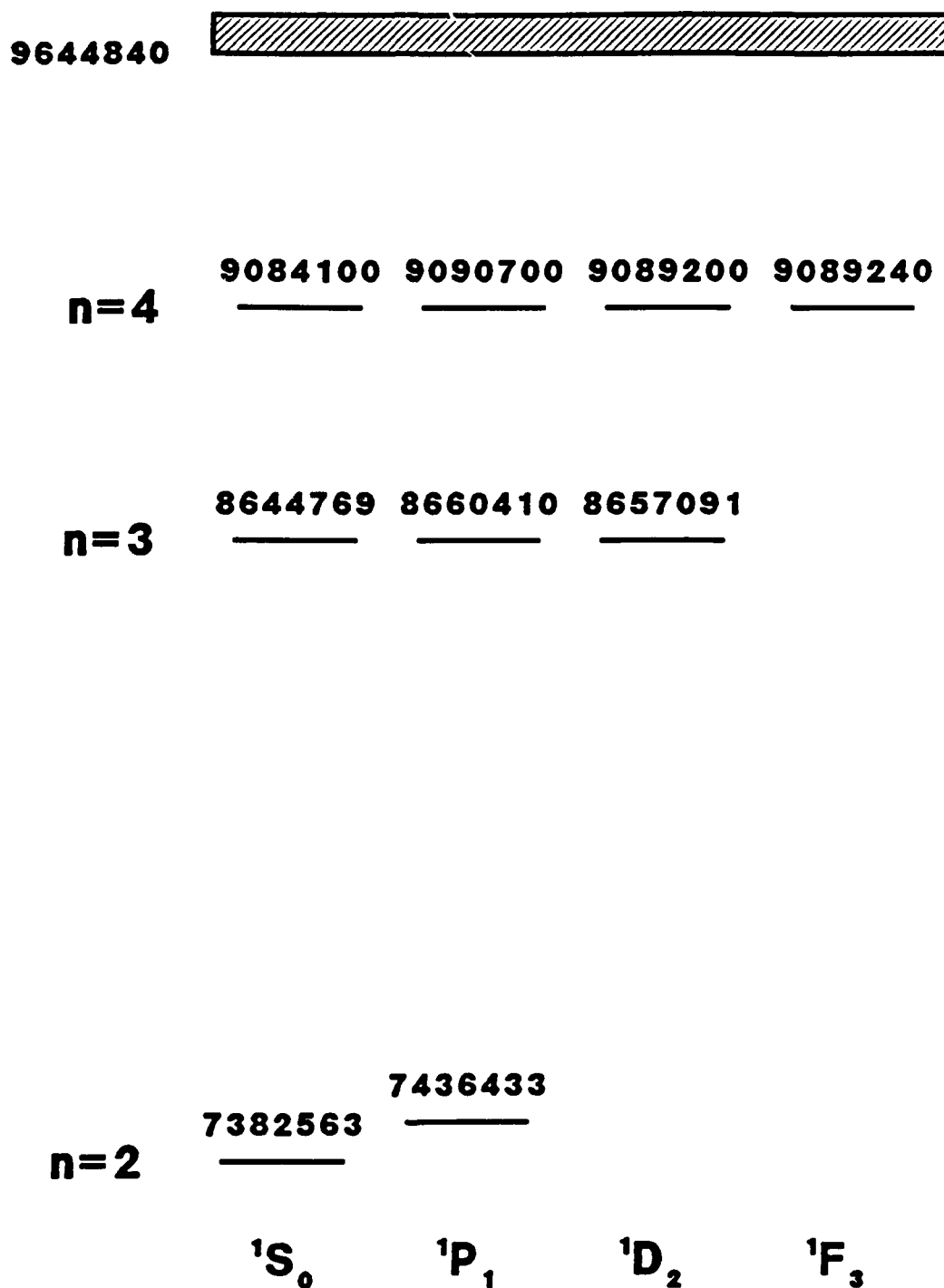


FIG. 5.3. Energy-level diagram of Ne IX triplet levels in units of cm^{-1} .

Attempts to record meaningful spectra from neon implosions using the plasma opening switch (POS) were unsuccessful. With the POS, only the Ne IX $1s-2p$ transition was observed for implosions with 100-psi plenum pressure and 250-kA current. With less plenum pressure considerable background fog was produced on the film. The reduced characteristic soft X-ray emission for implosions with the POS was also apparent in pinhole-camera images to be discussed in Sec. 5.2.

Spectra measured for neon implosions on Gamble II are given in Fig. 5.4. These spectra, obtained with a 1-cm diameter nozzle and 100-psi plenum pressure, may be compared directly with the spectra in Fig. 5.1. The 150-kA spectra appear very similar in intensity and spectral composition. The 250-kA spectra appear considerably different. The intensity of the Ne IX $1s^2-1s2p$ transition is a factor-of-two larger in the present experiment than in the Gamble II experiment, while the Lyman- α transitions have similar intensities. Time-resolved measurements provide a possible explanation for this difference and will be discussed in Sec. 5.3.

5.2 Pinhole-Camera Images

Time-integrated images of the soft X-ray emission were recorded with a pinhole camera and Kodak 2492 film. A 200- μm diameter pinhole and a magnification of 0.75 were used. The combination of a 6- μm thick aluminum filter and the 2492 film provided optimum sensitivity for the 0.9- to 1.5-keV photons from resonant transitions of Ne IX and Ne X. Details of the pinhole camera can be found in Appendix D.1. An example of a soft X-ray image for a neon implosion without the POS is shown in Fig. 5.5 (a). Six small regions of emission spaced at

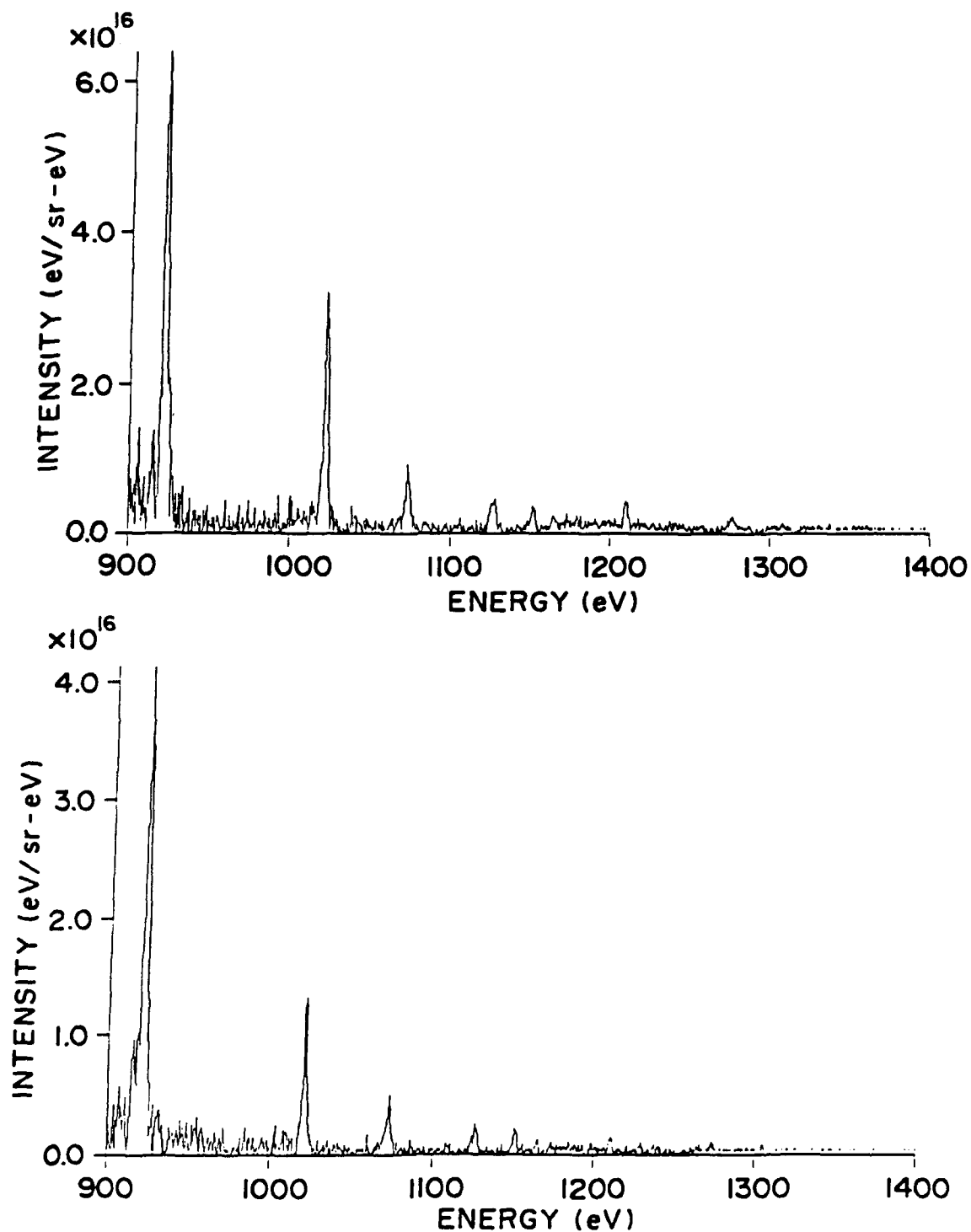


FIG. 5.4. Neon soft X-ray spectra on Gamble II (a) for 250-kA driving current (top) and (b) for 150-kA driving current (bottom).

WITHOUT POS



WITH POS

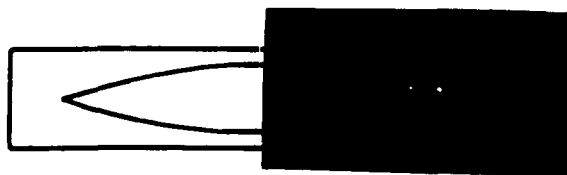


FIG. 5.5. Images of neon soft X-ray emission (a) without the plasma opening switch (POS) and (b) with the POS.

irregular intervals along the length of the plasma can be seen.

Densitometer traces of these images indicate that the size of the regions of emission are at or below a diameter of $470\text{ }\mu\text{m}$ (see Appendix D.1.1). An example of an X-ray image for an implosion with the POS is shown in Fig. 5.5 (b). Two small regions of emission are seen midway between the nozzle and the cathode, and one small region of emission is seen near the cathode. Densitometer traces indicate a considerable reduction in film density for the image in Fig. 5.5 (b) compared with that in Fig. 5.5 (a) (see Appendix D.1.1).

5.3 X-Ray Diode Measurements

A vacuum diode was used to record time histories of soft X-ray emission. A $0.5\text{-}\mu\text{m}$ thick aluminum filter plus a $2.0\text{-}\mu\text{m}$ thick polycarbonate (Kimfol) filter and a nickel cathode were used. This combination of filter and cathode provides a sharply peaked response for 0.83- to 1.56-keV photons (see Appendix D.1.2), which includes the resonant transitions of Ne IX and Ne X. Vacuum-diode signals are given in Figs. 5.6 and 5.7 for implosions corresponding to the spectra in Figs. 5.1 (a) and 5.1 (b), respectively. The peaks in the signal in Fig. 5.6 occur at times of 0.85 and 1.2 μs corresponding to when the gas-puff impedance significantly loads the generator, as previously discussed. The occurrence of two peaks in the signal could explain the difference in the time-integrated spectra of Figs. 5.1(a) and 5.4(a). Only one emission peak was observed for the implosion on the Gamble II generator.

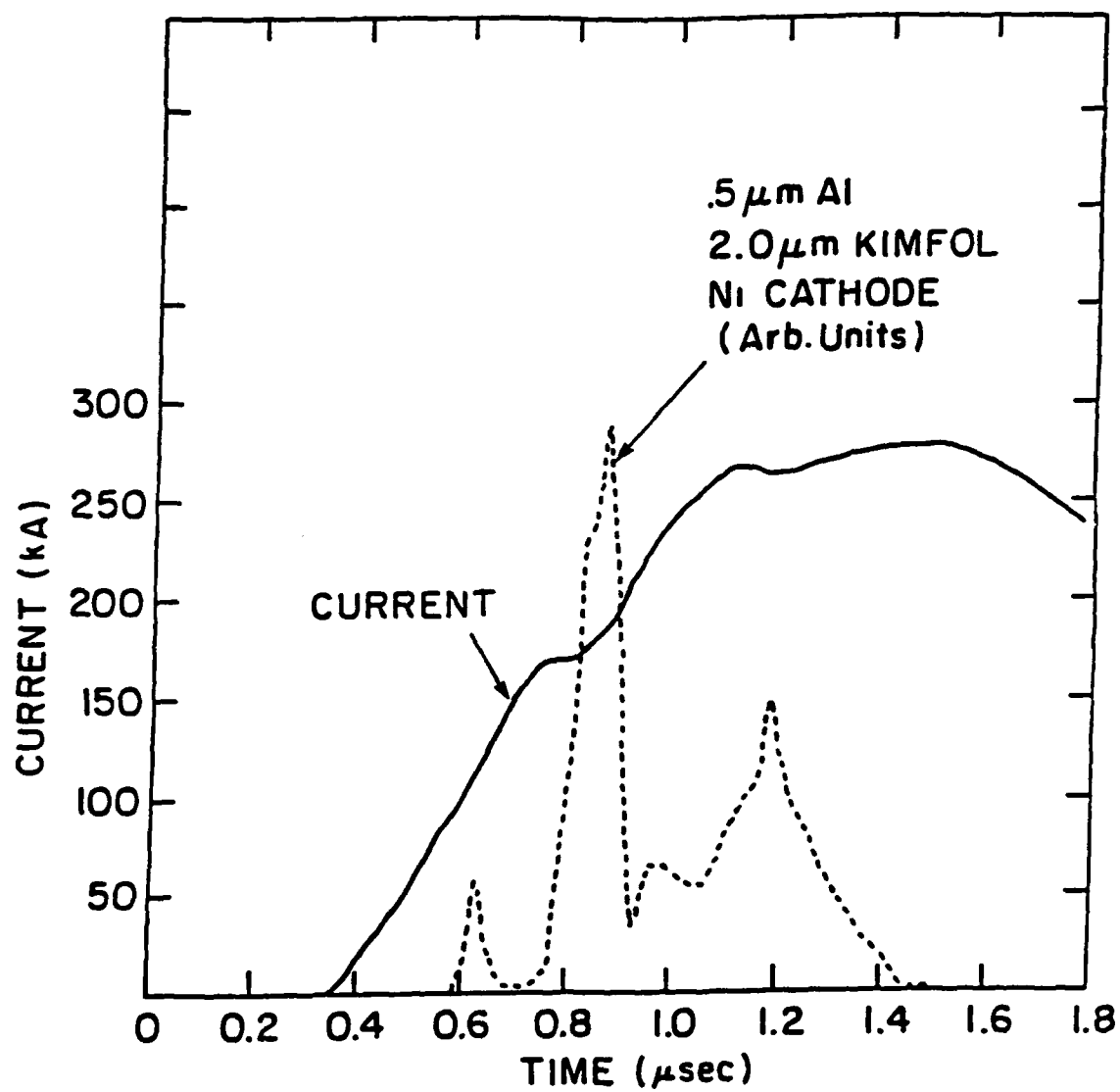


FIG. 5.6. Soft X-ray diode signals and current for a neon implosion driven with 250 kA.

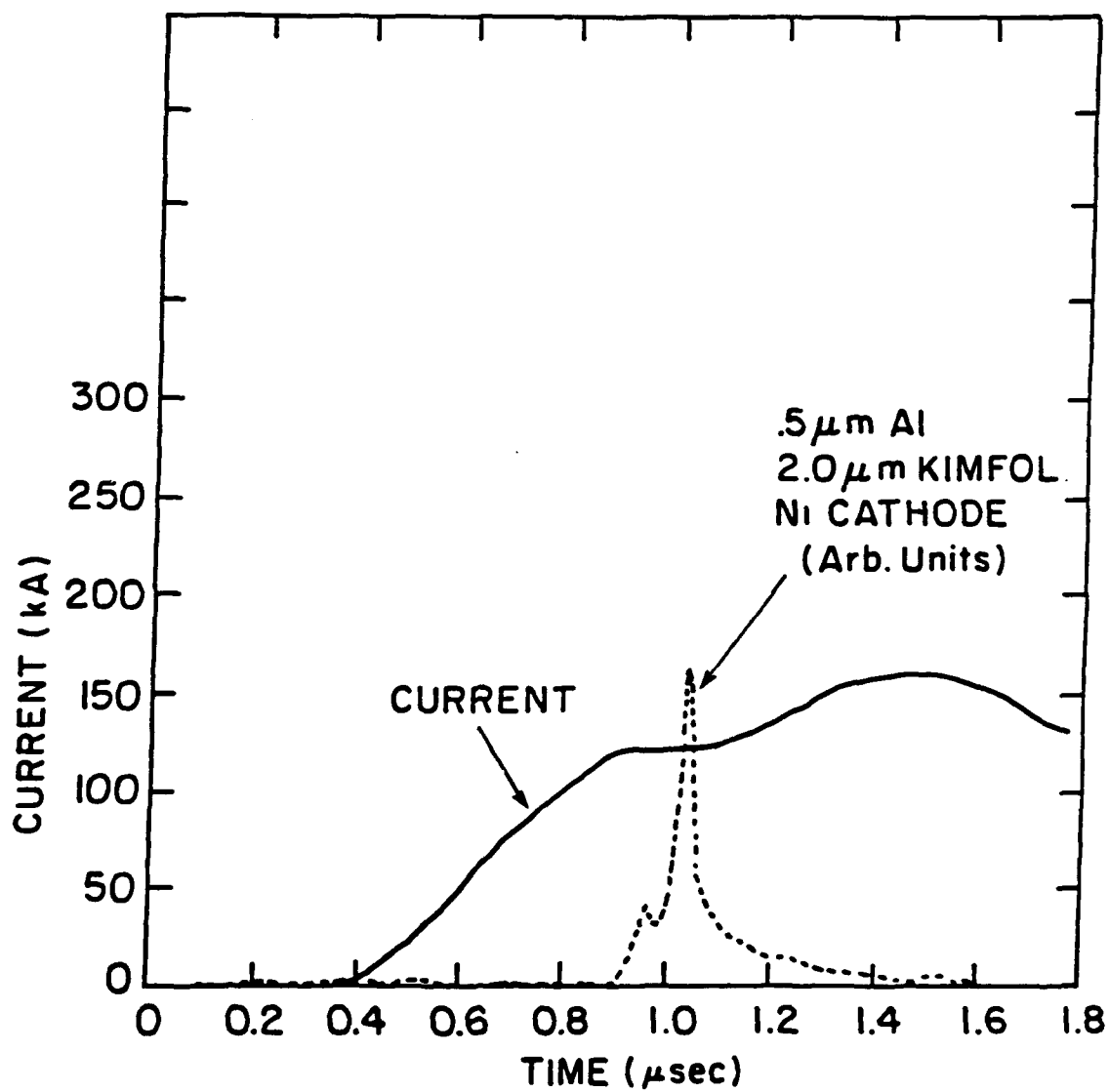


FIG. 5.7. Soft X-ray diode signals and current for a neon implosion driven with 150 kA.

5.4 Analysis

The soft X-ray measurements were used to estimate the conditions of the neon plasma. The soft X-ray images indicated several small regions with diameters less than 500 μm , and the vacuum-diode signals indicated multiple peaks in the soft X-ray output. The spectral measurements were used to estimate electron density and temperature.

5.4.1 Electron Density

The electron density was estimated from the advanced series limit of the Ne IX resonance series. For the spectrum in Fig. 5.1(a), transitions from above the $n=7$ level have merged to form the advanced series limit (Eq. A.21). The density dependence of the series limit is given in Fig. 5.8 for Ne VIII and Ne IX. A limit of seven for Ne IX indicates an electron density of $3 \times 10^{20} \text{ cm}^{-3}$. This limit was determined by comparing the Stark widths of the spectral lines with the separation of the energy levels, which converge at $n=7$.

The electron density was also estimated from the ratio of the intensities of the Ne IX $1s(^1S_0)-2p(^1P_1)$ resonance line and the Ne IX $1s(^1S_0)-2p(^3P_1)$ intercombination line. The density dependence of this ratio was inferred from the calculations of Boiko.¹¹⁴ This ratio is four for the spectrum in Fig. 5.1(a) implying an electron density of 10^{19} cm^{-3} . This estimate assumes that the plasma is optically thin and therefore is a lower limit if the plasma is optically thick to the Ne IX resonance line.

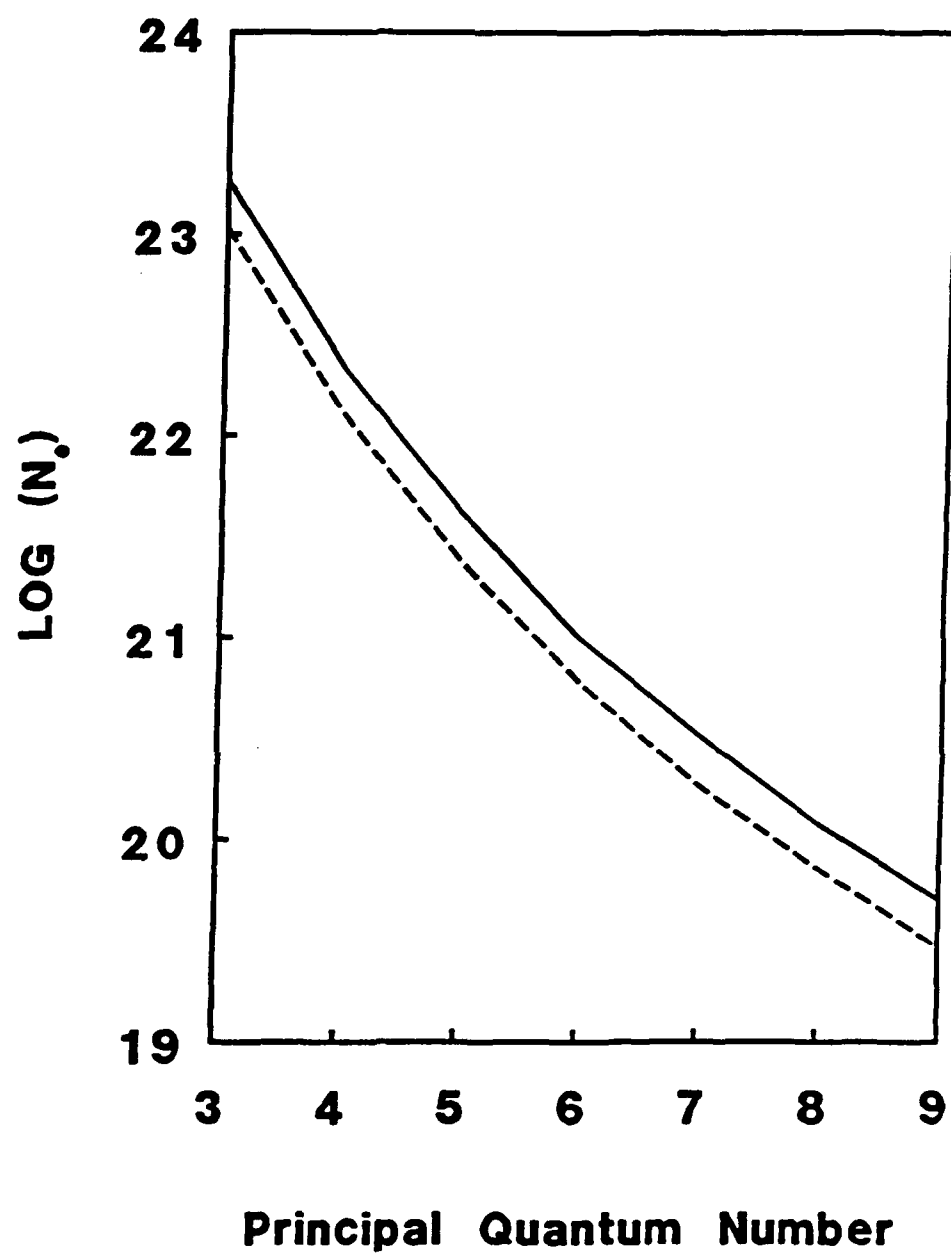


FIG. 5.8. Inglis-Teller limit for Ne IX (solid) and Ne VIII (dashed).

5.4.2 Electron Temperature

The electron temperature was estimated from the free-bound recombination continuum in the spectra. The slope of this recombination continuum provides a direct measure of the electron temperature according to Eq. A.25. The Ne IX recombination continuum in Fig. 5.1(a) indicates an electron temperature of 300 eV.

The relative populations of the excited states of different ions can also be used to determine the electron temperature. The relative intensities of line emissions from different ions can be used to measure the relative populations of the corresponding levels. Comparisons of these relative populations with atomic-physics-model predictions can be used to determine the electron temperature. When comparing relative intensities of spectral lines, care must be taken to select optically thin lines. Opacities were evaluated for the Ne IX lines observed in this experiment. An estimate of the physical depth for an optical depth of unity for the first three transitions of the Ne IX resonant series was presented in Fig. 2.5 for various temperatures and an electron density of 10^{19} cm^{-3} (assuming $z=8$ and Doppler broadening with $T_i=T_e$). For a 0.5-mm diameter neon plasma at an electron density of 10^{19} cm^{-3} , an optical depth of up to 50 is expected for the $1s^2-1s2p$ transition. Optical depths of five and one are expected for the $1s^2-1s3p$ and $1s^2-1s4p$ transitions, respectively. Therefore, measured intensities of the $1s^2-1s2p$ and $1s^2-1s3p$ transitions are not representative of the upper-level populations. The atomic-physics model appropriate to describe the populations depends on the electron density. The level populations above $n=4$ are expected to be in local thermodynamic equilibrium (LTE) with respect

to higher levels for electron densities above 10^{20} cm^{-3} . The ratio of the integrated intensities of the $1s^2-1s5p$ and the $1s^2-1s4p$ transitions suggests a temperature of 300 eV, based on Eqs. A.6 and A.17. For electron densities where these calculations are expected to be valid, the $1s^2-1s4p$ transition may be optically thick, and this 300 eV temperature therefore represents an upper limit.

For electron densities between 10^{19} and 10^{20} cm^{-3} , the levels are expected to be in collisional-radiative-equilibrium (CRE). A CRE model has been used to interpret neon spectra from Z-pinch plasmas produced by various pulsed power generators. The ratio of the Lyman- α line to the Ne IX resonance transition for spectra from three different generators, and the corresponding temperature estimated from those spectra, were given in Table 3.2. A comparison of the ratio of the Lyman- α line and the Ne IX resonance transition in Fig. 5.1(a) with the results in Table 3.2, indicates that the electron temperature is less than 150 eV.

Chapter 6

EXTREME VACUUM ULTRAVIOLET EMISSION

Extreme ultraviolet emission in the region of 120 to 280 eV has been studied to extend the investigation of neon implosions to conditions where the soft X-ray (900-1200 eV) emission discussed in the previous chapter is no longer observed. Those measurements were carried out for driving currents of 160 to 280 kA and with mass loadings and gas-puff geometry similar to the photopumping experiments on Gamble II. Analysis of the Ne IX and Ne X emissions in Chapter 5 indicated that higher temperatures and densities than desired could be achieved. The large energy separation between the ground state and the excited levels of Ne IX (> 920 eV) requires a high electron temperature to produce measureable radiation from these levels. The energy separation between the excited levels of Ne VIII and the ground state of Ne IX (< 100 eV) is considerably smaller, so that significant population of the Ne IX ground state by collisions occurs for an electron energy distribution of much lower temperature. Radiation from the excited levels of Ne VIII is therefore more appropriate for measuring conditions present in a plasma with a significant number of ions in the ground state of Ne IX and relatively few in the excited levels of Ne IX. These energy separations are apparent in the partial energy-level diagram of Ne IX and Ne VIII presented in Sec. 1.3 (Fig.

1.4). The present extreme ultraviolet (XUV) measurements of Ne VIII transitions, as well as of Ne VII, will be used to determine the implosion parameters required to produce the conditions desired for a neon laser plasma. The measurements in Chapter 5 indicated that soft X-ray radiation was emitted from regions less than 0.5 mm in diameter distributed at intervals of about 5 mm along the Z-pinch. The present XUV measurements will be used to determine the plasma conditions in regions where no soft X-ray emission is seen. Results of these measurements will be compared with an appropriate model to estimate plasma conditions.

When the soft X-ray spectra in Chapter 5 were recorded, an X-ray vacuum diode was used to monitor the time history of the soft X-ray power. A similar vacuum diode was used to monitor the soft X-ray power when the XUV measurements were carried out. Four different XUV techniques were used to measure properties of the plasma in four different sessions. First, a vacuum diode filtered for peak response in the region of 150 to 280 eV was used to record the time history of XUV radiation. Second, a pinhole camera filtered for peak response in the region of 160 to 280 eV was used to record the spatial distribution of XUV emission. Third, time-integrated spectra were recorded with a 1-meter grazing-incidence spectrograph to investigate the spectral content of the XUV emission in the region of 120 to 220 eV. Fourth, time-resolved Ne VIII line radiation was recorded with a grazing-incidence monochromator to determine the time history of emission from that ionization state. These measurements were combined with steady-state and time-dependent atomic-physics models to determine the neon plasma conditions.

6.1 X-ray Diode Measurements

A vacuum diode designed for peak sensitivity in the region of 150 to 280 eV was used to record the time history of XUV emission from the neon implosion (see Appendix D.1.2). The filter material was a 1.8- μm polycarbonate film (kimfol) with a 0.1- μm thick aluminum coating, and the cathode of the diode was aluminum. Simultaneous soft X-ray and XUV measurements were made to determine the relative power radiated in these two spectral regions. Also, soft X-ray diode measurements were taken simultaneously with XUV pinhole-camera images and grazing-incidence spectra in an effort to monitor the reproducibility of the implosions. These measurements were made for various driving currents and mass loadings, both with and without the plasma opening switch (POS).

Simultaneous time histories of soft X-ray and XUV emissions for neon implosions obtained with two different capacitor charging voltages are given in Fig. 6.1, along with the corresponding currents. The 45-kV discharge produced a peak current of 230 kA, and the 25-kV discharge produced a peak current of 160 kA. X-ray emissions occur at 0.45 μs and 1.1 μs in Fig. 6.1(a) and at 0.55 μs and 1.3 μs in Fig. 6.1(b). The peak soft X-ray signal in Fig. 6.1(a) at 0.45 μs corresponds to 12 MW radiated into 4π solid angle (see Appendix D.1.2), and the total integrated power is 0.75 J. The peak XUV signal in Fig. 6.1(a) at 0.45 μs corresponds to 17 MW radiated into 4π solid angle, and the total integrated power is 1.5 J.

Simultaneous time-histories of soft X-ray and XUV emissions for neon implosions driven by 45- and 25-kV capacitor discharges with the POS are given in Fig. 6.2, along with the corresponding currents

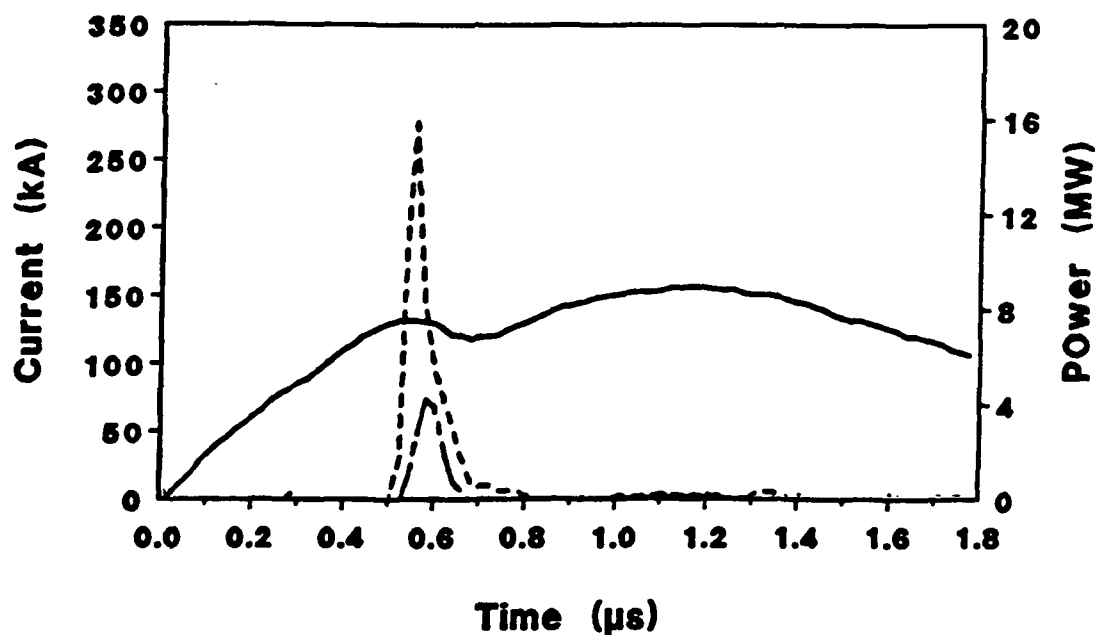
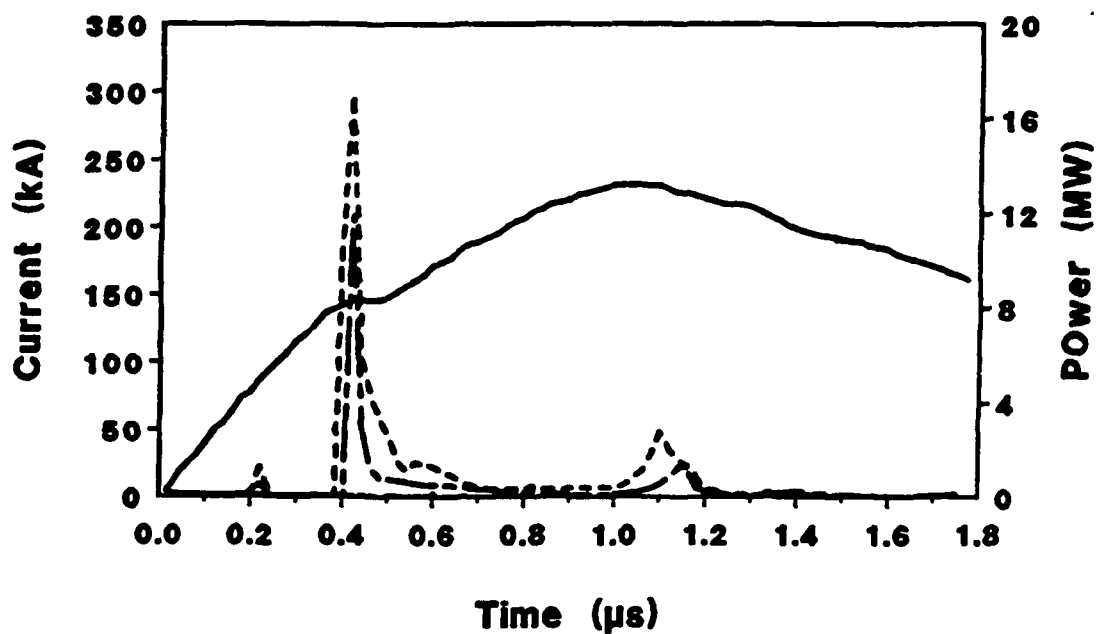


FIG. 6.1. Current (solid), XUV (dashed), and soft X-ray (dot-dash) signals from neon implosions driven by capacitor discharges of (a) 45 kV (top) and (b) 25 kV (bottom).

driving the implosions. The 45-kV discharge produced a peak current of 200 kA, and the 25-kV discharge produced a peak current of 150 kA. Peak emissions occurred near 0.10 μ s and 0.26 μ s after the beginning of the current signal in Fig. 6.2(a), and at 0.19 μ s after the start of the current signal in Fig. 6.2(b). The peak soft X-ray signal in Fig. 6.2(a) near 0.10 μ s corresponds to 7 MW radiated into 4π solid angle, and the total integrated power is 0.15 J. The peak XUV signal in Fig. 6.2(a) near 0.10 μ s corresponds to 9 MW radiated into 4π solid angle, and the total integrated power is 0.8 J. The measurements presented in Figs. 6.1 and 6.2 were obtained with a gas-puff plenum pressure of 50 psi.

6.1.1 Current Variations

Peak powers recorded with X-ray diodes for implosions driven by different currents with and without the POS are presented in Fig. 6.3. These soft X-ray powers were measured in three different sessions. In one session soft X-ray and XUV powers were measured simultaneously, similar to the data in Figs. 6.1 and 6.2. In addition, soft X-ray powers measured simultaneously with pinhole-camera images and grazing-incidence spectra are included in Figs. 6.3(a). These soft X-ray data provide a measure of the reproducibility of the implosions over the course of the experiment. The peak power was selected for this comparison, rather than the integrated energy, because the peak power usually corresponds to the first radiation pulse when more than one pulse is observed. If the integrated energy were selected for this comparison, it is ambiguous whether the integral should include multiple pulses or only one pulse.

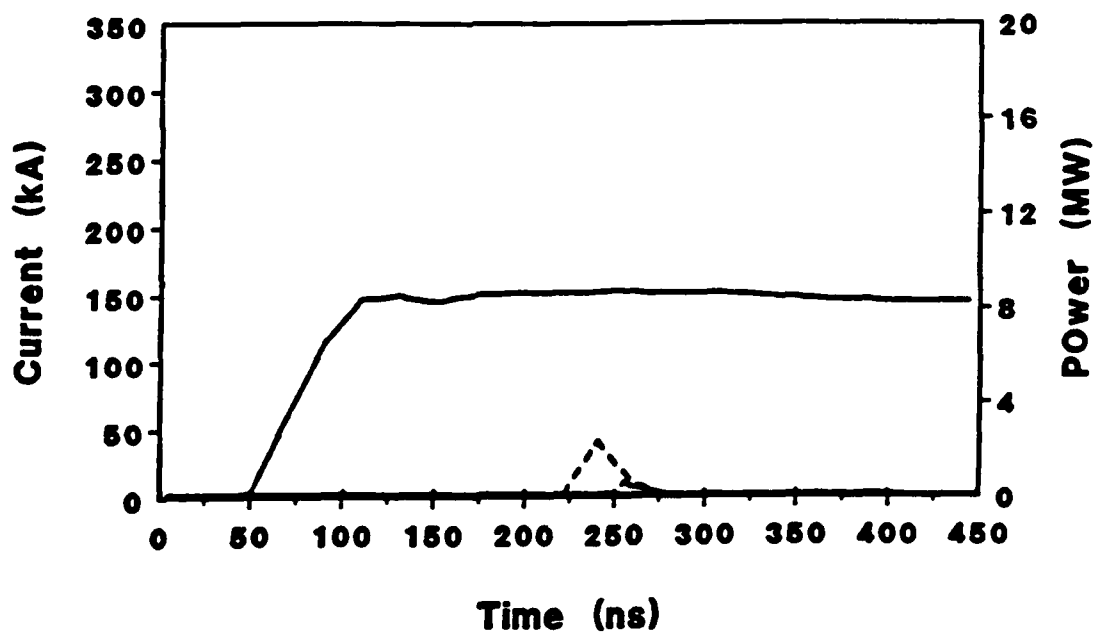
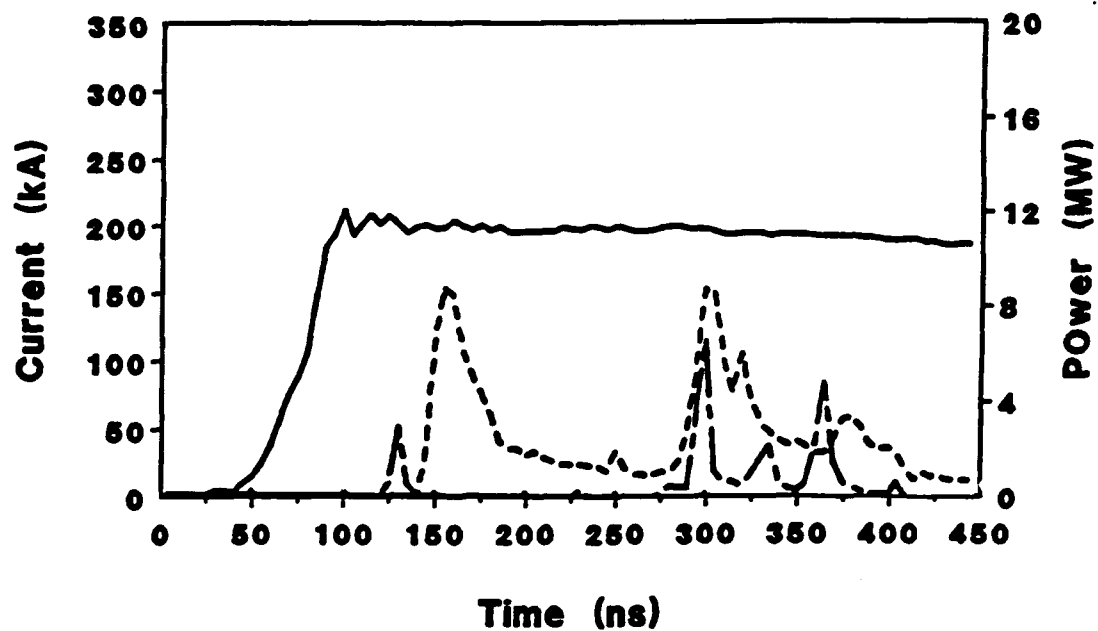


FIG. 6.2. Current (solid), XUV (dashed), and soft X-ray (dot-dash) signals from neon implosions driven by (a) 45-kV (top) and (b) 25-kV (bottom) capacitor discharge with the plasma opening switch.

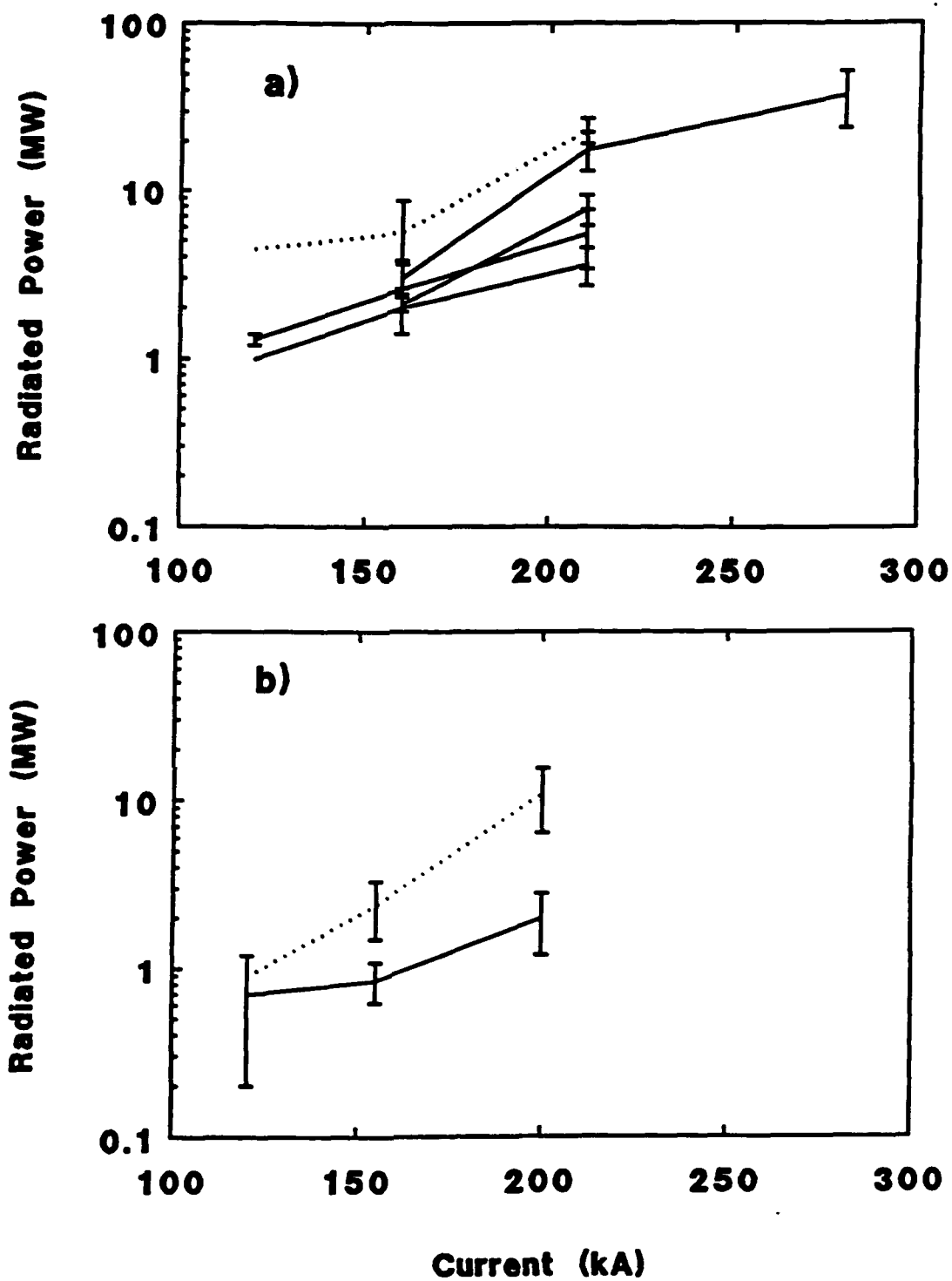


FIG. 6.3. Dependence of soft X-ray (solid) and XUV (dotted) peak powers on peak current for capacitor discharges (a) without the plasma opening switch (POS) and (b) with the POS.

The error bars in Fig. 6.3 represent a measure of the reproducibility of the signals during each session. The data in Fig. 6.3 are for implosions with 100-psi gas-puff plenum pressure.

The power radiated increases with current for both XUV and the soft x-ray emissions. Less power is radiated for implosions driven by the fast-risetime current than by the slow-risetime current for similar charging voltages and correspondingly similar peak currents.

6.1.2 Mass-Load Variations

Soft X-ray and XUV peak powers for implosions driven by similar peak currents but with different gas-puff plenum pressures are presented in Fig. 6.4. The power is only weakly dependent on the gas-puff plenum pressure and may either increase or decrease with pressure, depending on the current risetime. The emissions in Fig. 6.4 are for implosions driven by peak currents of 200 kA. For implosions driven by the slow-risetime current, the ratio of the XUV to soft X-ray intensity increases with increasing pressure. For implosions driven by the fast-risetime current, the radiated power decreases with increasing pressure, and the ratio of the XUV to soft X-ray intensity decreases with increasing plenum pressure.

6.2 Pinhole-Camera Measurements

A pinhole camera designed to image 150- to 280-eV radiation was used to record spacial distributions for various currents and mass loadings, both with and without the POS. The details of the pinhole-camera geometry, the filter material, and the recording film are

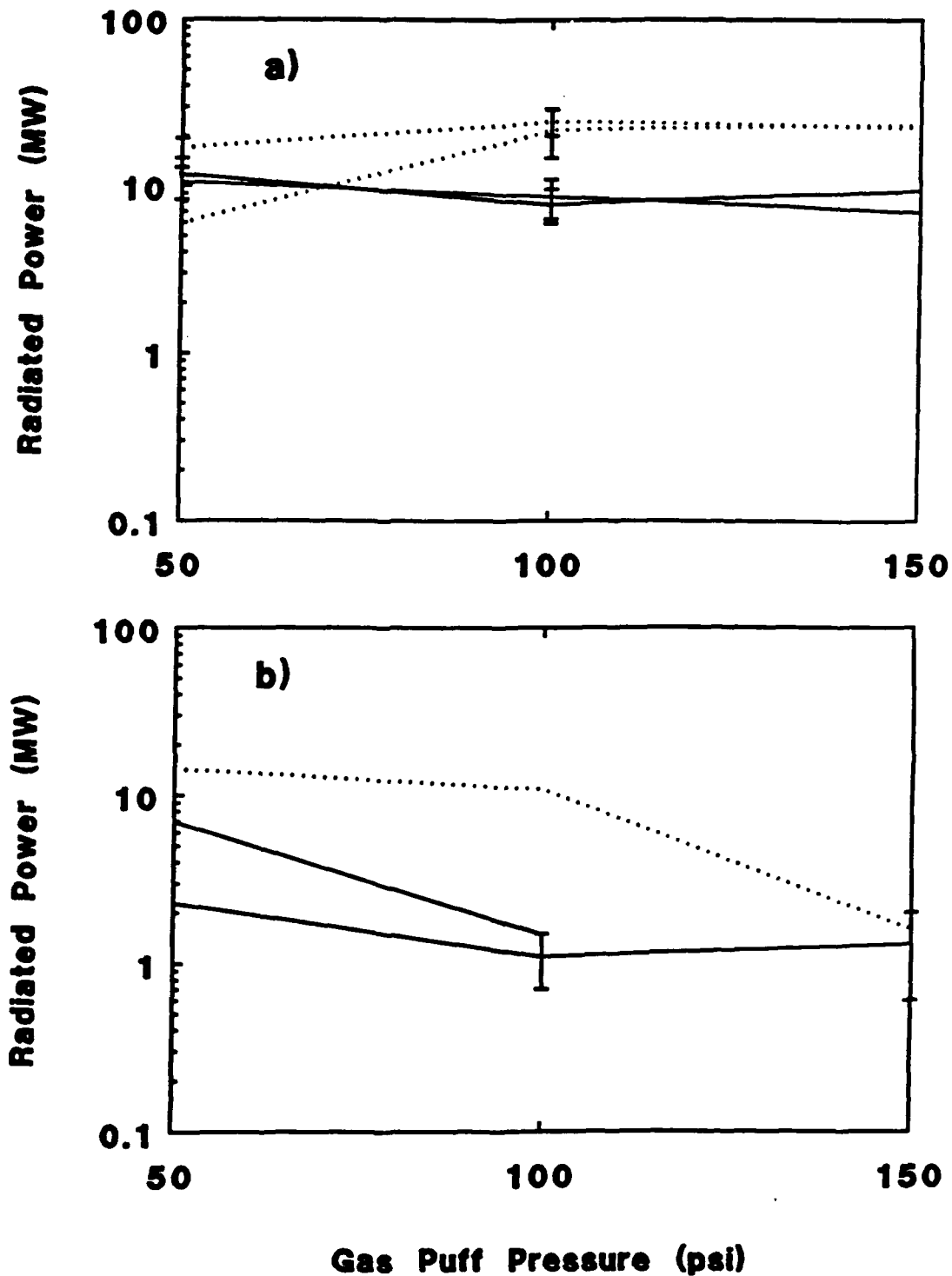


FIG. 6.4. Dependence of soft X-ray (solid) and XUV (dotted) peak powers on gas-puff pressure for capacitor discharges (a) without the plasma opening switch (POS) (b) with the POS.

described in Appendix D.1.1.

6.2.1 Current Variations

Images of XUV emission for implosions driven by different currents are presented in Fig. 6.5(a). The locations of the nozzle and the cathode are indicated at the top of the figure. Open-shutter photographs of visible-light emission for implosions with similar currents are presented in Fig. 6.5(b). For XUV emission, the length of the emitting region increases with current up to 180 kA; at which level the emission spans the cathode-to-nozzle gap. The appearance of localized regions of XUV emission in the image for 130 kA and the increase in the number and intensity of these localized regions with increasing current above 130 kA is correlated with the appearance of axially nonuniform regions in the open-shutter pictures. A detailed comparison of the features in the XUV and visible-light images in Fig. 6.5 is not possible because they were not taken on the same shot.

Radial dimensions of the plasma were determined from film density measurements by scanning the images with a densitometer transverse to the Z-pinch axis. The full-width at half-maximum of the XUV images ranged from 0.4 to 2.0 mm depending on the axial location. It is worth noting that for two of the visible-light images the maximum intensity was not on axis, but two peaks located symmetrically off axis were observed along a limited length of the pinch. These occurred for the 90- and 180-kA currents in Fig. 6.5. Possible explanations for these off-axis peaks could be either limb brightening of a cylindrical shell of light-emitting plasma or the occurrence of multiple events in a time-integrated picture.

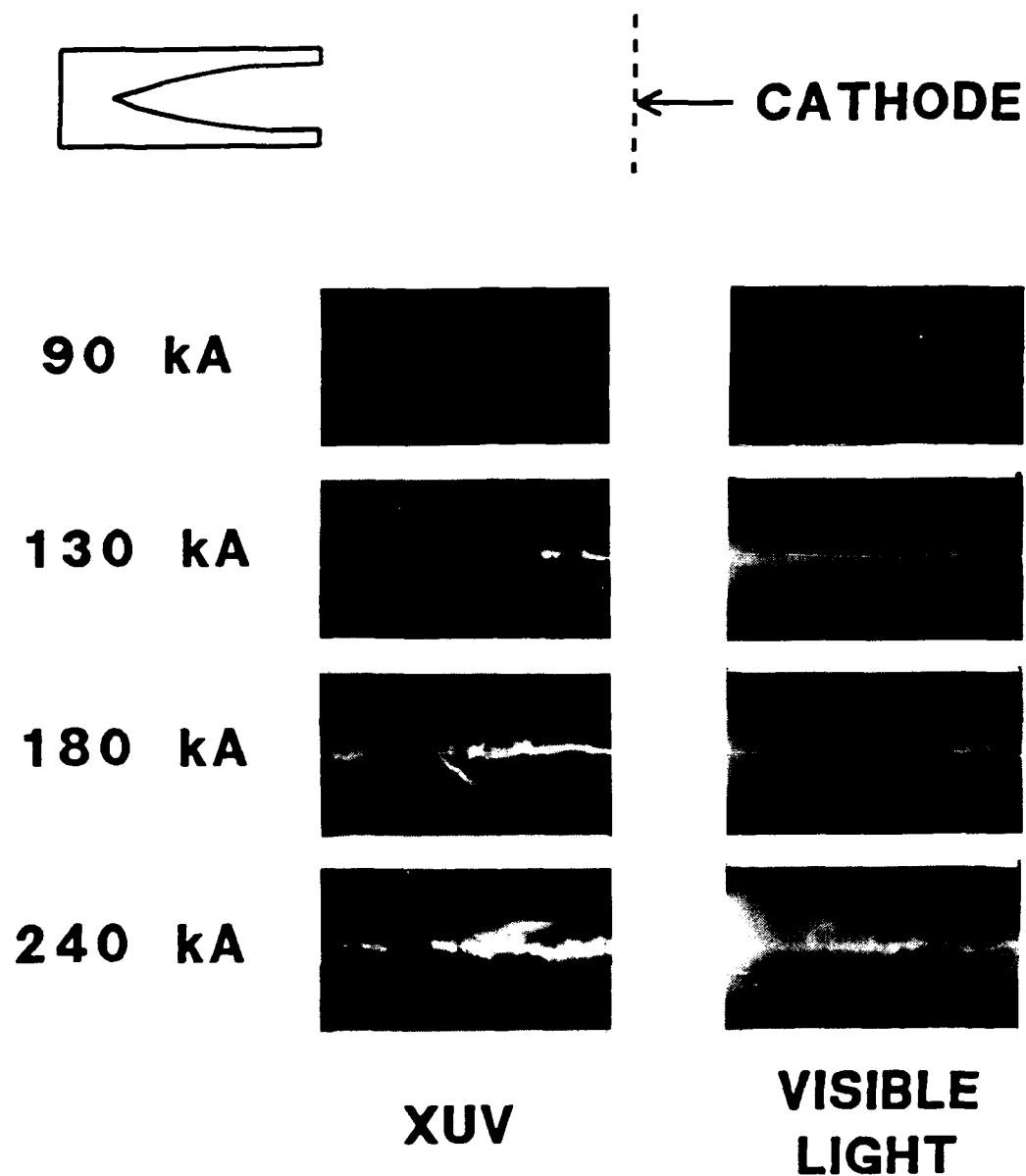


FIG. 6.5. (a) Pinhole-camera images of XUV radiation (LHS) and (b) visible-light open-shutter photographs (RHS) for different currents. The location of the nozzle and cathode are shown at the top of the XUV images. (All photos were taken on different shots.)

Pinhole-camera images of XUV emission for implosions driven by different peak currents with the POS are presented in Fig. 6.6(a). Open-shutter visible-light photographs for implosions with similar currents are presented in Fig. 6.6(b). A correlation between the appearance of localized regions of XUV emission and the appearance of axial nonuniformities in the visible-light emission with increasing current is observed, similar to that with the slow-risetime current. Two off-center peaks of emission are seen in the visible-light image in Fig. 6.6(b) for 160 kA. The implosions imaged in Figs. 6.5 and 6.6 were produced with 100-psi gas-puff plenum pressure.

6.2.2 Mass-Load Variations

Images of XUV radiation for implosions driven by similar currents but with different gas-puff plenum pressure are presented in Fig. 6.7. For the image with 50-psi plenum pressure in Fig. 6.7(a) two intensity peaks located symmetrically off axis are observed along a limited length of the pinch. Examples of radial densitometer scans of this image can be found in Appendix D.1. Increasing the pressure to 150 psi increased the emission beyond the dynamic range of the film so detailed structure cannot be resolved. In Fig. 6.7(b), images of XUV emission are presented for implosions with the POS. Increasing the plenum pressure to 100 psi increases the axial nonuniformity. The implosions in Fig. 6.7(a) were obtained with a peak current of 165 kA, and the implosions in Fig. 6.7(b) were obtained with a peak current of 190 kA.

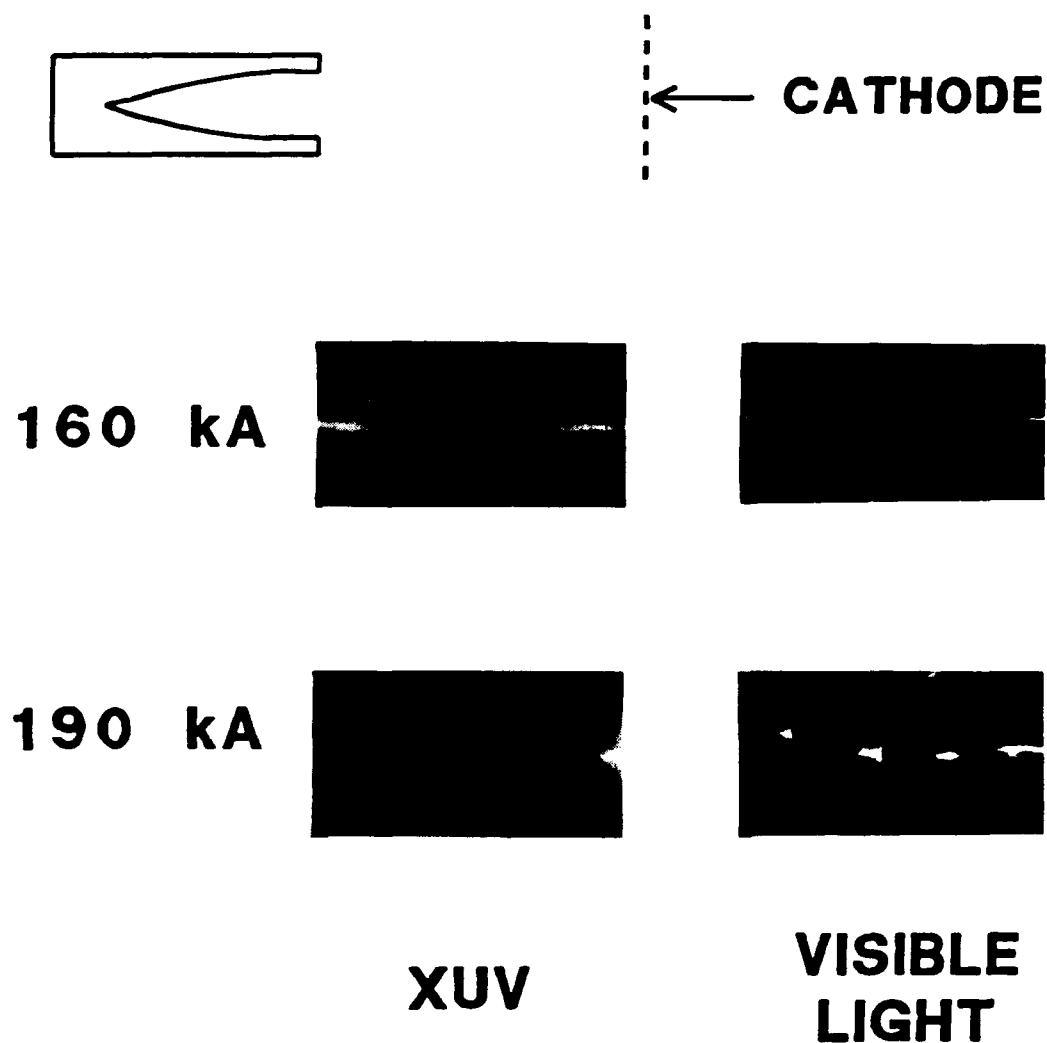


FIG. 6.6. (a) Pinhole-camera images of XUV radiation (LHS) and (b) visible-light open-shutter photographs (RHS) for different currents with the plasma opening switch. The location of the nozzle and cathode are shown at the top of the XUV images.



WITHOUT POS

50 psi

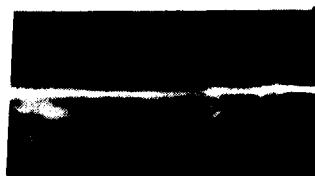


150 psi



WITH POS

50 psi



100 psi



FIG. 6.7. XUV images for different gas-puff plenum pressures (a) without the plasma opening switch (POS) and (b) with the POS. The location of the nozzle and the cathode as shown at the top.

6.3 Grazing Incidence spectra

Extreme ultraviolet spectra of neon implosions were measured with a 1-meter grazing-incidence spectrograph. Spectral lines were identified from tables of wavelengths and the dimensions of the spectrograph.^{115,116} Transitions from Ne VI through Ne IX ions were identified in time-integrated spectra. Spectra produced by implosions with various currents and gas-puff plenum pressures, both with and without the POS, were compared. These results, along with the time-resolved measurements discussed in Sec. 6.4, were compared with an appropriate plasma model to interpret the spectral variations.

The spectrograph is described in detail in Appendix D.2 and a brief description is given here. The spectrograph entrance slit was perpendicular to the Z-pinch axis and viewed the entire diameter of a 6-mm long section of the pinch. A 10- μ m entrance slit produced an instrumental line width of 0.25 Å for 100-Å radiation. The 1200-line/mm grating produced a linear dispersion along the Rowland circle of 1.3 Å/mm.

Measured spectra were scanned with a densitometer to record diffuse film density as a function of distance along the Rowland circle. An example of a neon spectrum between 120 and 220 eV (55 and 105 Å) is given in Fig. 6.8. This spectrum was produced by the implosion of a 100-psi neon gas puff with a 150-kA peak current. Various 2s-np and 2p-nd transitions of Ne VIII are identified for n=3 to n=6. Weaker transitions from Ne VII are also indicated.

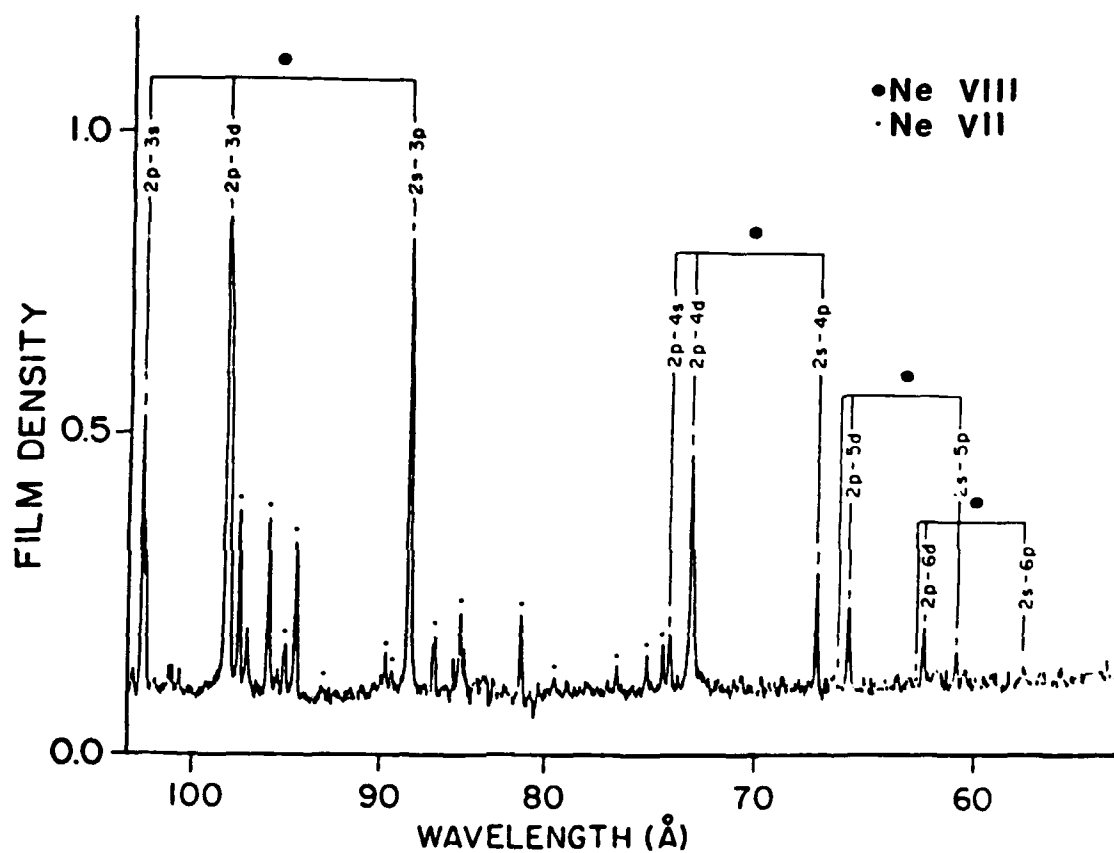


FIG. 6.8. XUV spectrum from the implosion of a neon gas-puff with 150-kA peak current and 100-psi plenum pressure. Lines from Ne VIII and Ne VII are identified.

6.3.1 Current Variations

Grazing-incidence spectra for neon implosions driven by 200-kA and 150-kA peak currents are compared in Fig. 6.9. As the current is increased, the Ne VIII lines increase in intensity relative to the Ne VII lines. This can be seen by comparing the Ne VII transitions at 94 to 97 Å to the Ne VIII transitions at 66 to 73 Å. These lines are chosen because they are of comparable density so non-linear film-density effects are minimized. Grazing-incidence spectra for neon implosions driven by 200-kA and 150-kA currents with the POS are compared in Fig. 6.10. The film density in Fig. 6.10(a) is similar to that of Figs. 6.9(a) and (b), but with the fast-risetime current the spectral intensity decreases considerably as the current is decreased. The ratio of the various Ne VIII and Ne VII lines in Fig. 6.10 is similar to that in Fig. 6.9. A Ne IX line, the 1s2p-1s3d transition at 78.3 Å is observed in the spectra of Fig. 6.9, whereas this line is not present in Fig. 6.10. The spectra in Figs. 6.9 and 6.10 were obtained with 100-psi plenum pressure.

6.3.2 Mass-Load Variations

Grazing-incidence spectra for neon implosions with different gas-puff plenum pressures are presented in Fig. 6.11. As the plenum pressure is decreased, the Ne IX line at 78.3 Å increases relative to the Ne VIII lines, and the Ne VII lines decrease relative to the Ne VIII lines. Grazing-incidence spectra for neon implosions with the POS are presented in Fig. 6.12. As the plenum pressure is decreased from 150 to 50 psi the Ne VIII lines at 66 to 73 Å increase

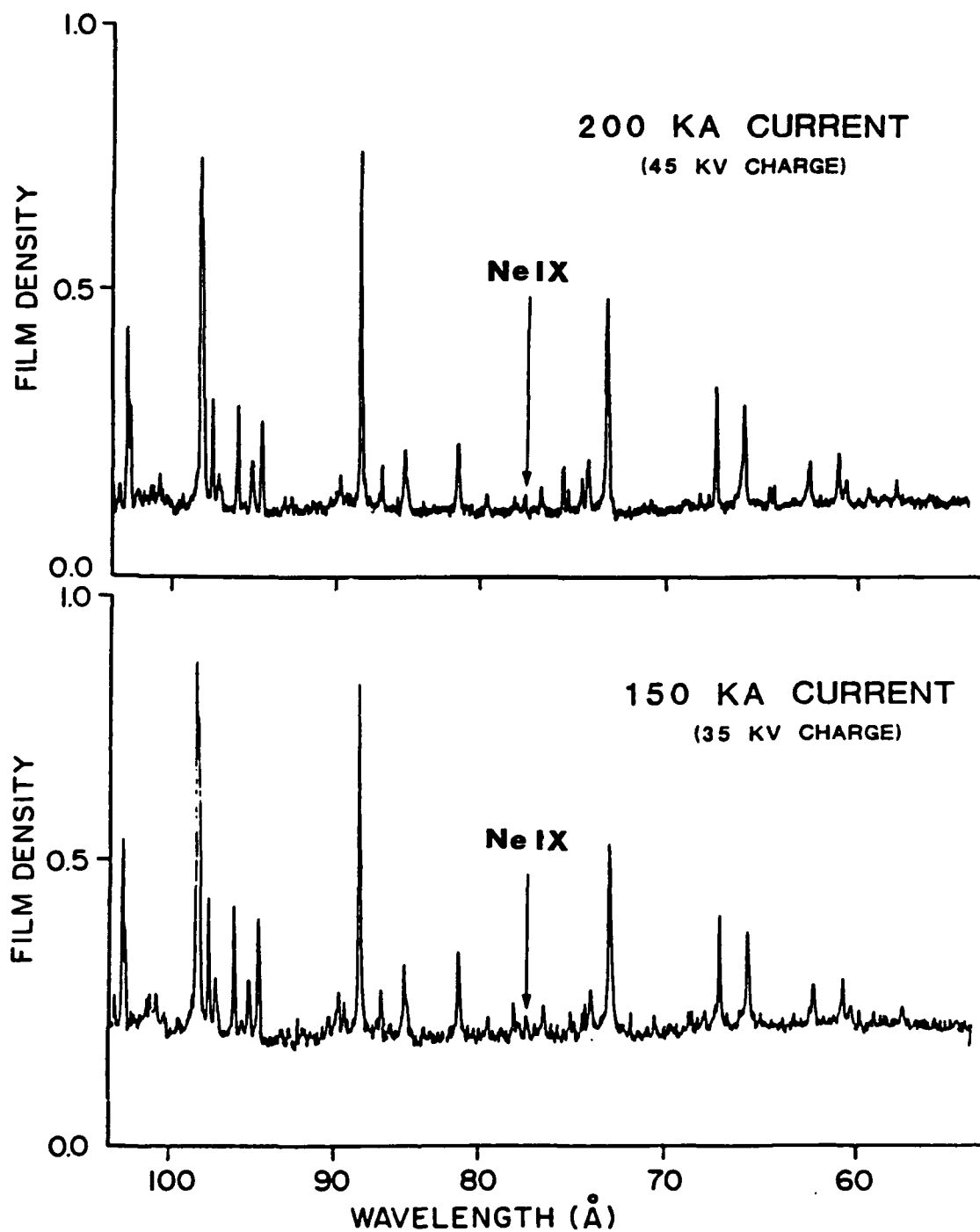


FIG. 6.9. Neon spectra without the plasma opening switch (a) for 200-kA peak current and (b) for 150-kA peak current.

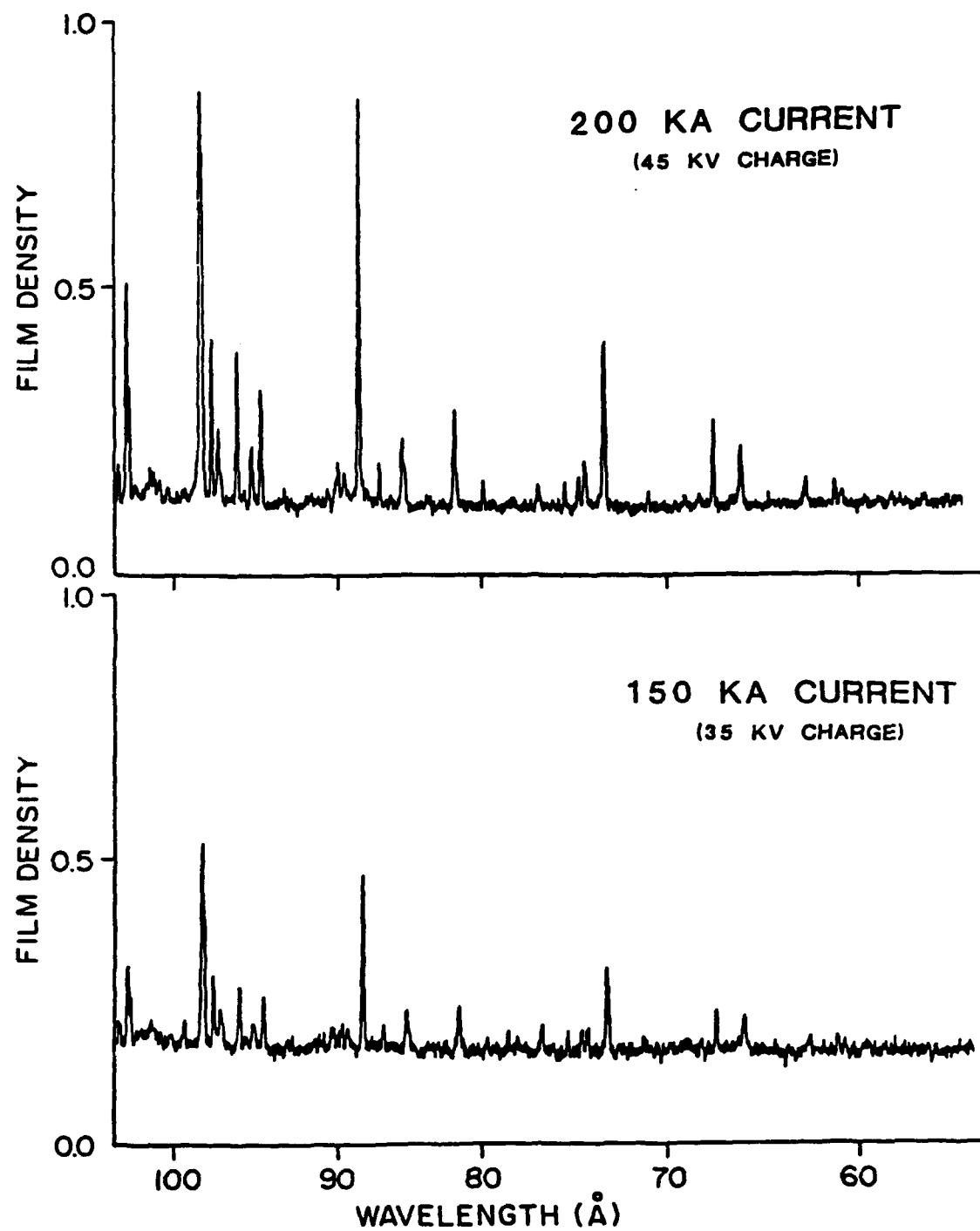


FIG. 6.10. Neon spectra with the plasma opening switch (a) for 200-kA peak current and (b) for 150-kA peak current.

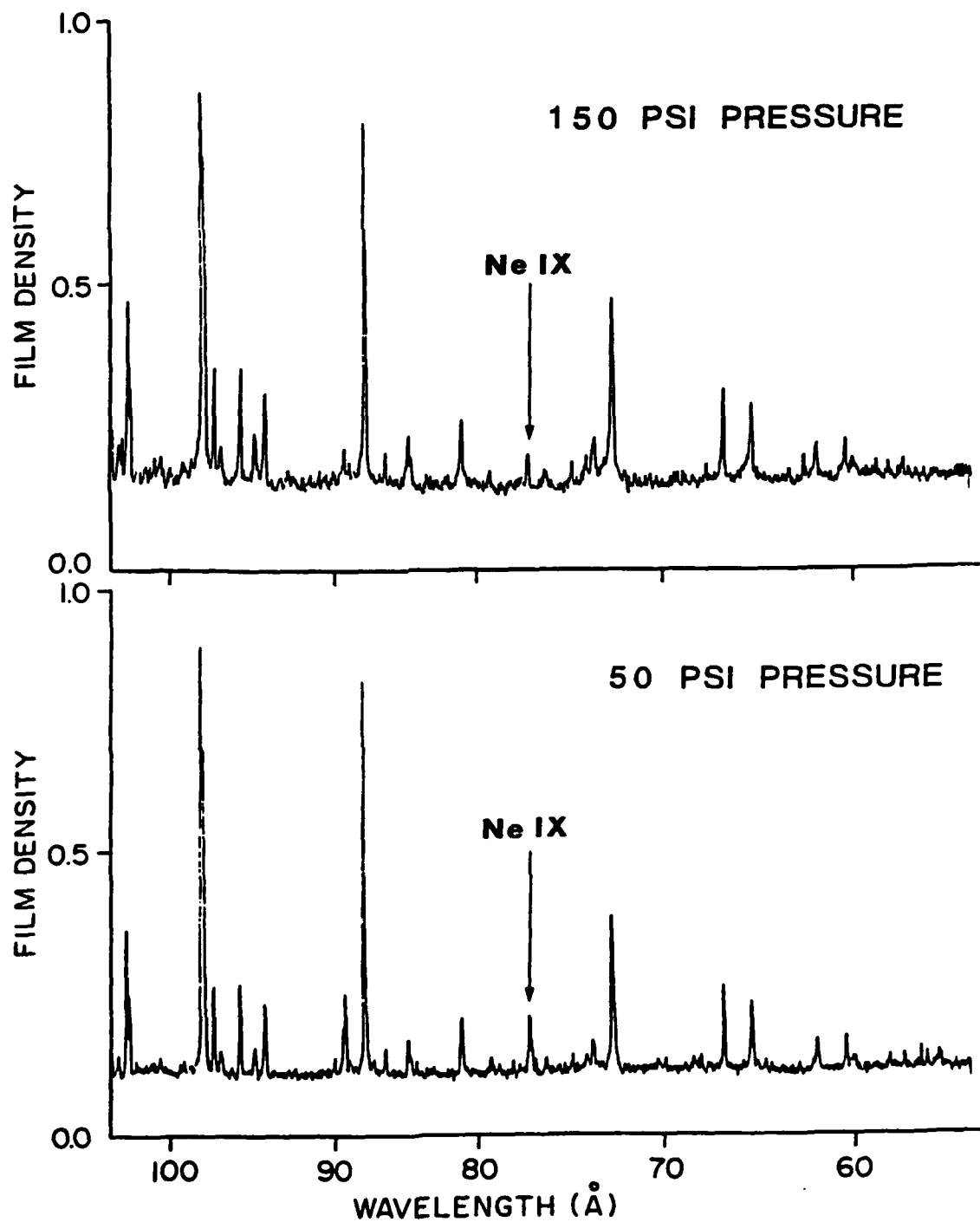


FIG. 6.11. Neon spectra without the plasma opening switch for (a) 150-psi plenum pressure and (b) 50-psi plenum pressure.

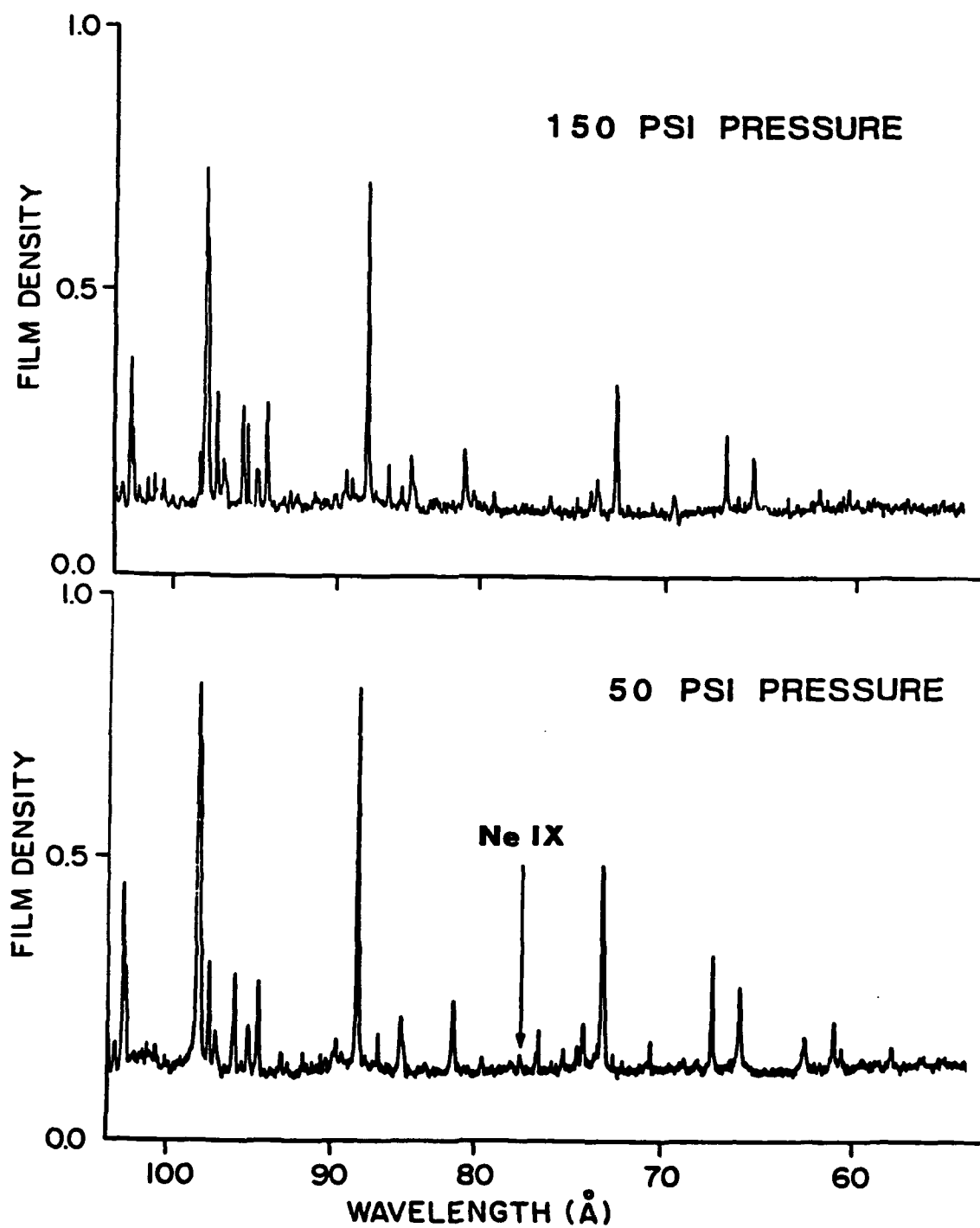


FIG. 6.12. Neon spectra with the plasma opening switch for (a) 150-psi plenum pressure and (b) 50-psi plenum pressure.

considerably relative to the Ne VII lines at 94 to 97 Å, and the Ne IX line at 78.3 Å appears. The spectra in Figs. 6.11 and 6.12 were obtained for implosions driven by peak currents of 200 kA.

6.4 Extreme Vacuum Ultraviolet Monochromator

Time-resolved XUV radiation from Ne VIII was measured with a grazing-incidence monochromator. A 35-μm wide exit slit mounted on the Rowland circle provided spectral resolution. Fluorescence of a thin layer of p-terphenyl mounted behind the exit slit was recorded with a photomultiplier tube mounted outside the vacuum system. Details of the grazing-incidence monochromator can be found in Appendix D.2.2. The Ne VIII $1s^2 2s-1s^2 3p$ ($^2S_{1/2}-^2P_{1/2,3/2}$) transitions at 88.09 and 88.13 Å (141 eV) were measured for various plenum pressures, driving currents, and current risetimes. The $1s^2 2s-1s^2 3p$ transition was chosen because a simultaneous measurement of the $1s^2 3s-1s^2 3p$ transition at 2820.7 Å can provide a relative calibration of the grazing-incidence and near ultraviolet (NUV) spectrographs by the branching-ratio technique, as will be discussed in Chapter 7. Time histories of the Ne VIII 88-Å emission are compared with simultaneous soft X-ray measurements in Fig. 6.13(a). Without the POS, two peaks are seen in both the 88-Å and soft X-ray signals near 0.6 μs and 1.2 μs after the current starts. The Ne VIII signal precedes the soft X-ray signal by 40 ns for both peaks. The relative intensity of the 88-Å and soft X-ray signals changes drastically, being nearly equal for the first peak to greater than nine for the second peak. These observations will be discussed further in Secs. 6.4.3 and 6.5.2. A similar comparison of 88-Å and soft X-ray time-histories for an

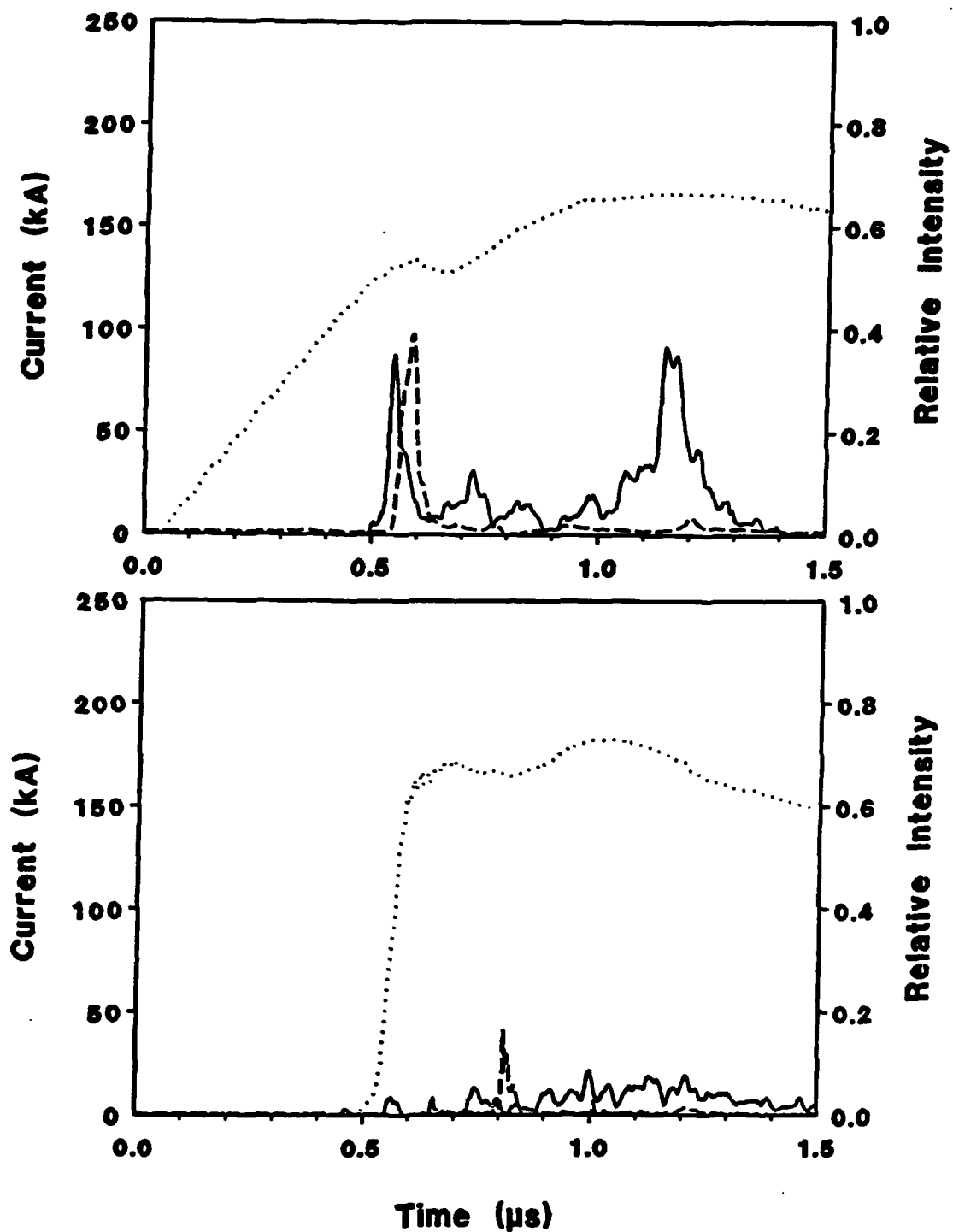


FIG. 6.13. Time histories of 88-Å (solid) and soft X-ray (dashed) emissions for neon implosions (a) without the POS (top) and (b) with the POS (bottom). The current (dotted) driving each implosion is also shown.

implosion with the POS is given in Fig. 6.13(b). Again, two peaks are seen in the soft X-ray signal, the first 300 ns after the current starts and then 700 ns. The 88-Å emission is considerably reduced compared with that in Fig. 6.13(a), and the emission occurs over a longer time interval, including the times of soft X-ray emission. The gas-puff plenum pressure was 100 psi for both implosions in Fig. 6.13.

6.4.1 Current Variations

Comparisons of the Ne VIII 88-Å emission for different capacitor charging voltages are presented in Figs. 6.14 and 6.15. Time histories of 88-Å emission for two different charging voltages and the corresponding current traces are given in Fig. 6.14. Peak currents of 140 and 200 kA were measured for the 35- and 45-kV charging voltages, respectively. Multiple peaks in the Ne VIII emission are observed. As the charging voltage is increased, the intensity of emission increases and the time of peak signal decreases relative to the start of the current. The first peak occurs prior to peak current in both cases. The second peak occurs near peak current for 35-kV charge. Ne VIII 88-Å time histories and current traces are given in Fig. 6.15 for implosions with the POS. Peak currents of 115 and 190 kA were measured for charging voltages of 35 and 45 kV, respectively. Differences in the opening switch plasma resulted in different current risetimes: 100 ns in Fig. 6.15(a) and 50 ns in Fig. 6.15(b). In all cases the implosions occur earlier in time for larger current as expected. Also, the 88-Å emission is larger for the slower risetime current.

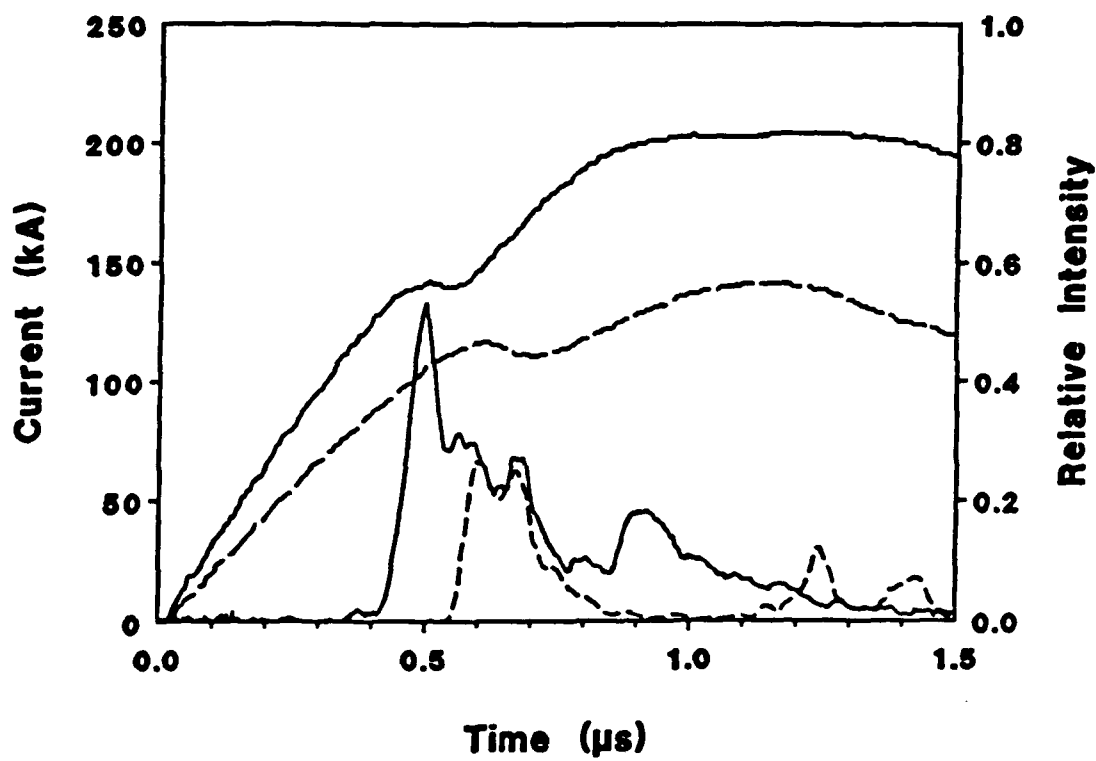


FIG. 6.14. Ne VIII 88-Å emissions and currents for charging voltages of 35 kV (dashed) and 45 kV (solid).

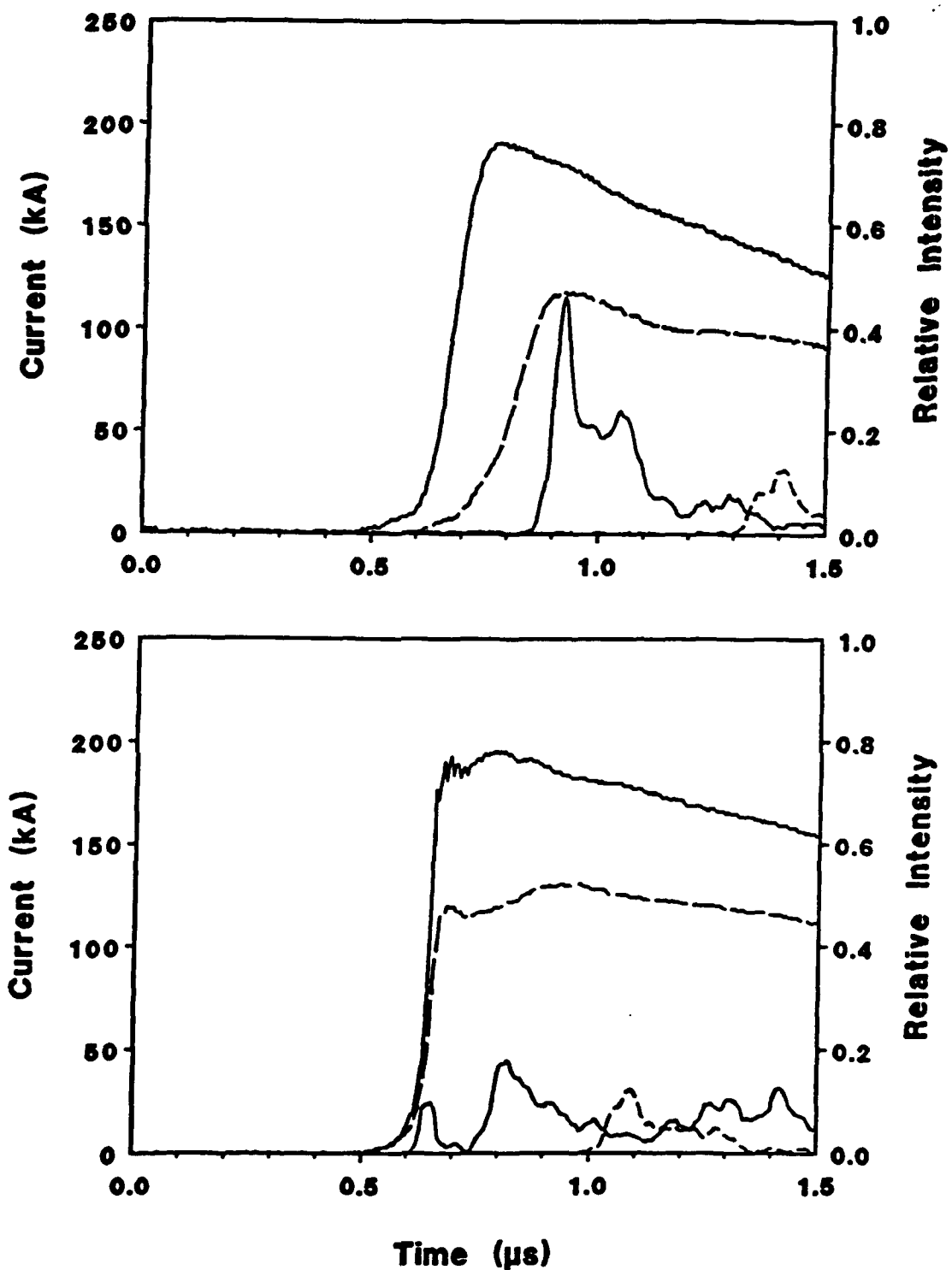


FIG. 6.15. Ne VIII 88-Å emission and currents for charging voltages of 35 kV (dashed) and 45 kV (solid) with the plasma opening switch for current risetimes of (a) 100 ns (top) and (b) 50 ns. (bottom).

6.4.2 Mass-Load Variations

Comparisons of Ne VIII 88-Å emission for different mass loadings are presented in Fig. 6.16. Measurements for plenum pressures of 50 and 150 psi without the plasma opening switch are given in Fig. 6.16 (a). The first XUV peak occurs slightly later (600 ns versus 550 ns) for larger plenum pressure, and the second XUV peak occurs considerably later (1.25 μ s versus 1.1 μ s) for larger plenum pressure. The relative intensity of the 88-Å signal at the first peak to that at the second peak decreases from 2 to 0.5 as the plenum pressure is increased from 50 to 150 psi. This behavior will be discussed in Secs. 6.4.3 and 6.5.2. The dip in the current trace at the time of the first implosion is larger for larger plenum pressure. The corresponding dip at the second implosion is larger for lower plenum pressure. These dips in the current indicate increased loading of the electrical circuit as the neon implodes. Time histories of the 88-Å line emission and the current with the POS are given in Fig. 6.16 (b) for plenum pressures of 50 and 150 psi. Here, the implosions occur later in time for higher plenum pressure and with reduced intensity.

6.4.3 Various Ionization States

Time histories of emissions from Ne VII, Ne VIII, and Ne IX were measured for various mass loadings and currents to study the time dependence of the ionization balance during the implosions. For Ne VII, the $1s^2 2s 2p - 1s^2 2s 3d$ transition at 106 Å was used, and for Ne VIII the $1s^2 2s - 1s^2 3p$ transition at 88 Å was used. The soft X-ray vacuum diode was used to measure Ne IX time histories. The sensitivity of

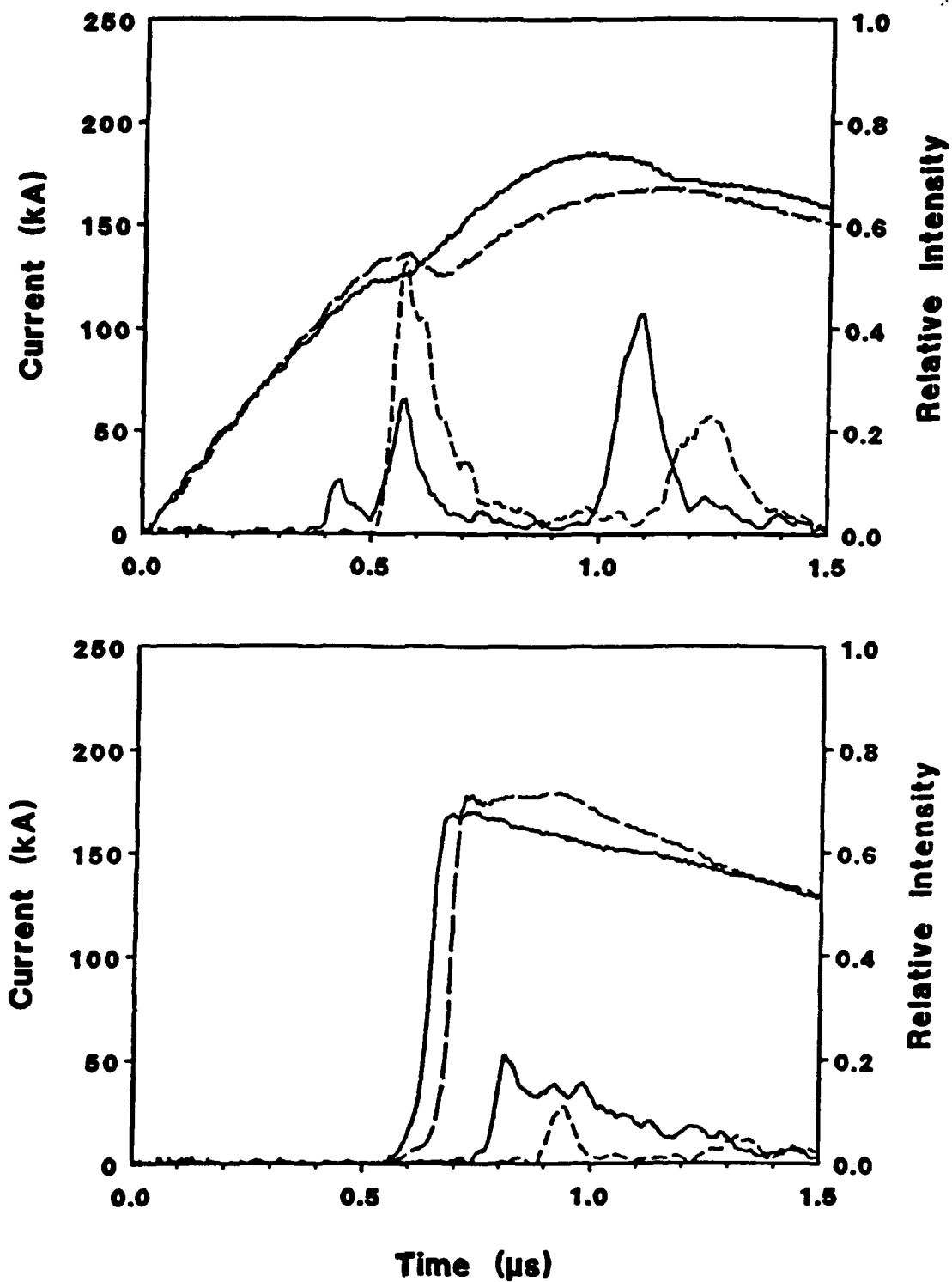


FIG. 6.16. Ne VIII 88-Å emission and currents for plenum pressures of 50 psi (solid) and 150 psi (dashed) (a) without the POS (top) and (b) with the POS (bottom).

the soft X-ray diode allows discrimination of the high energy resonance transitions of Ne IX and Ne X (> 900 eV) from the lower energy transitions of lower ionization states. It should be pointed out, however, that the soft x-ray vacuum diode measures radiation from the entire 4-cm plasma length, whereas the Ne VII and Ne VIII emissions are from a 6-mm central portion of this plasma.

Simultaneous measurements of Ne VIII and Ne IX are given in Fig. 6.17 for gas-puff plenum pressures of 50, 100, and 150 psi. These measurements are for 40-kV charging voltages without the plasma opening switch. As noted previously, the intensity of the second peak decreases considerably relative to the first peak as the plenum pressure is increased. This behavior is observed for both Ne VIII and Ne IX emissions. Also, for the 100-psi plenum pressure the relative intensity of Ne VIII to Ne IX increases considerably for the second peak as noted previously (see Fig. 6.13(a)). This behavior is not observed for the other pressures. The second peak is absent for 150-psi pressure, and the relative intensity of Ne VIII to Ne IX remains constant for 50-psi pressure. Time histories of Ne VII emission are given in Fig. 6.18 for conditions similar to those of Fig. 6.17. Two peaks are observed for all plenum pressures with the intensity of the first peak increasing with pressure and the intensity of the second peak decreasing with pressure. The intensity ratio of the first peak to the second peak decreases with increasing plenum pressure, as was observed for the Ne VIII and Ne IX emissions. These Ne VII, Ne VIII, and Ne IX emissions were also measured for 48-kV charging voltage and are compared with 40-kV measurements in Figs. 6.19 and 6.20.

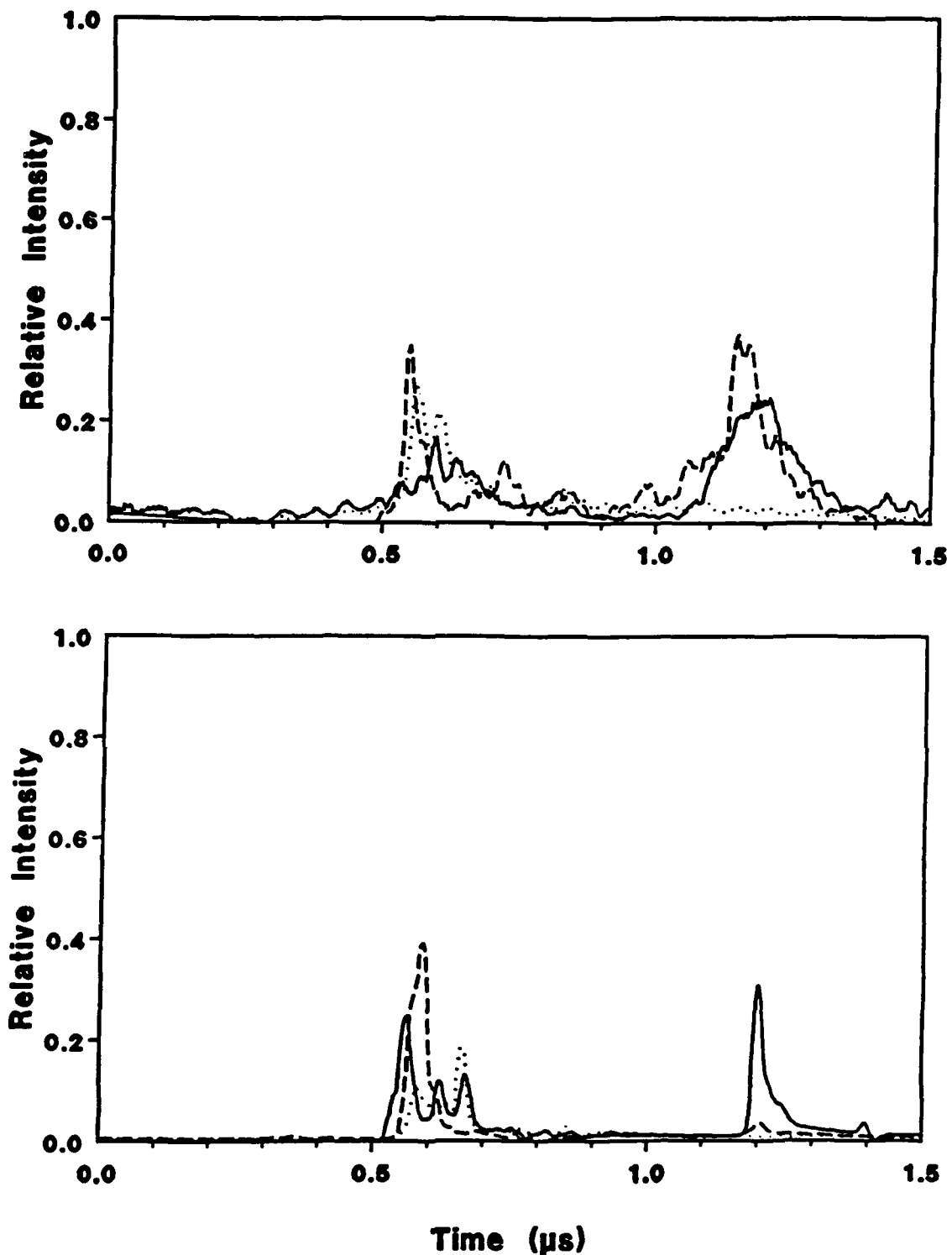


FIG. 6.17. Time histories measured simultaneously for emissions from (a) Ne VIII (top) and (b) Ne IX (bottom) for different plenum pressures: 50 psi (solid), 100 psi (dashed) and 150 psi (dotted).

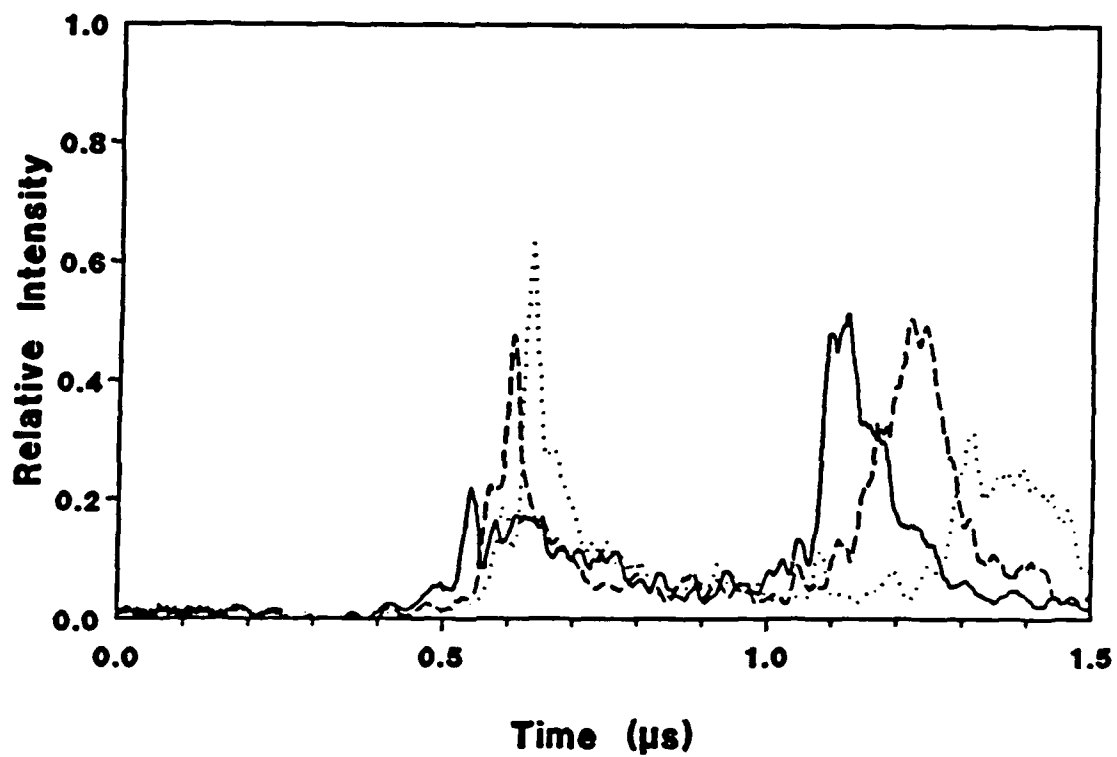


FIG. 6.18. Time histories of Ne VII emission for different plenum pressures: 50 psi (solid), 100 psi (dashed) and 150 psi (dot).

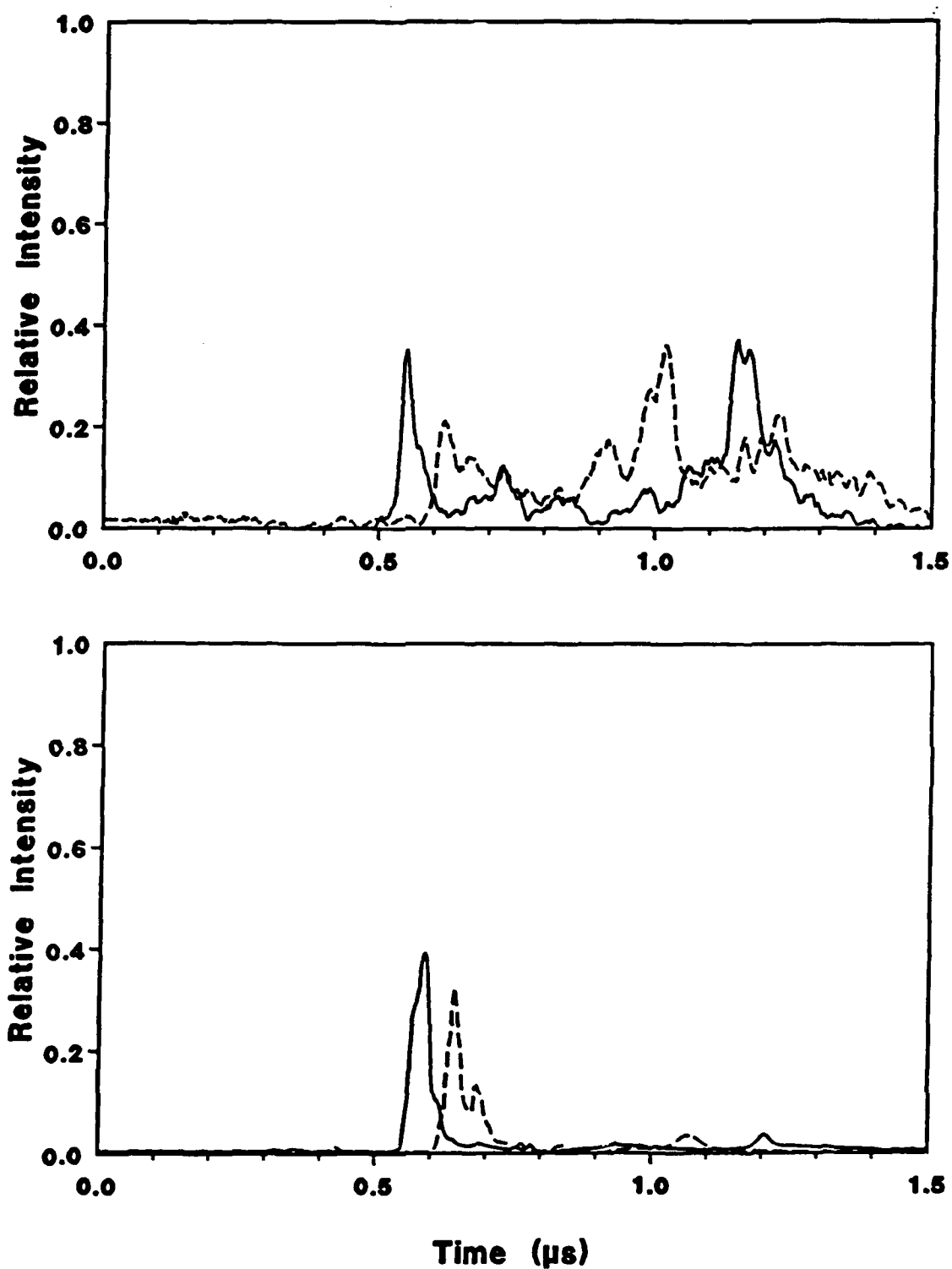


FIG. 6.19. Time histories measured simultaneously for emissions from (a) Ne VIII (top) and (b) Ne IX (bottom) for charging voltages of 40 kV (dashed) and 48 kV (solid).

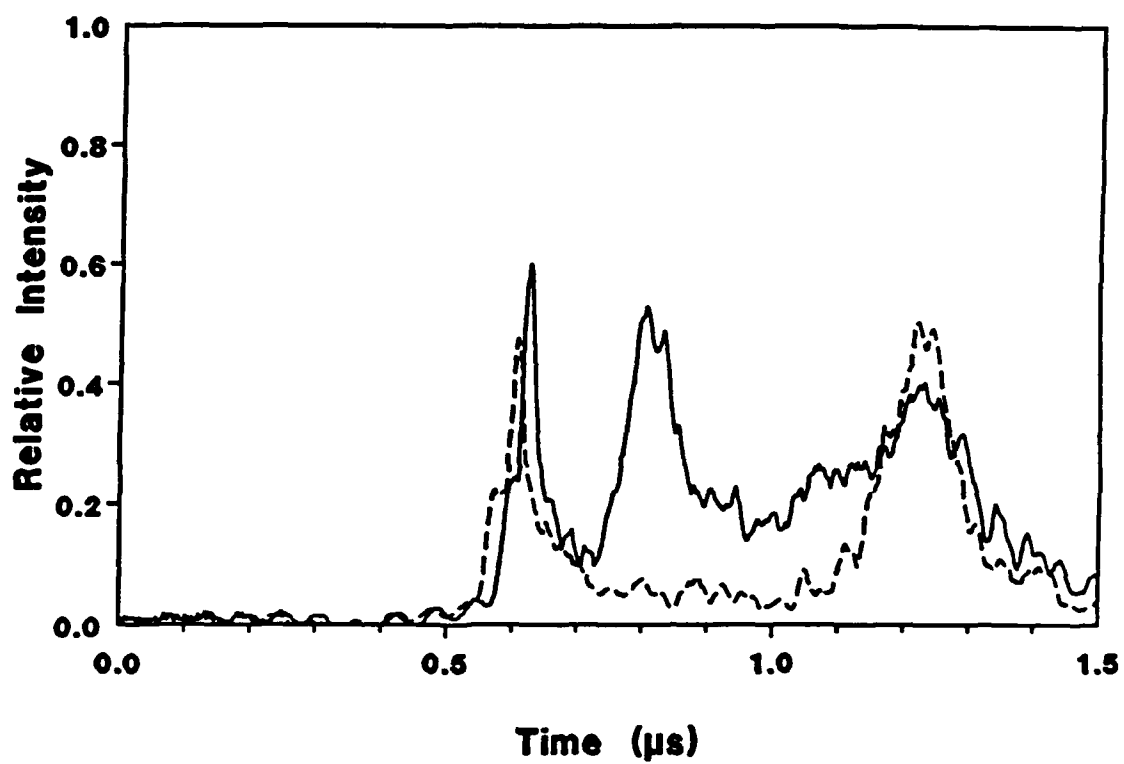


FIG. 6.20. Time histories of Ne VII emission for charging voltages of 40 kV (dashed) and 48 kV (solid).

6.5 Analysis

These spatially, temporally, and spectrally resolved measurements were analysed with steady-state and time-dependent atomic-physics models to determine the neon plasma conditions. The advance of the Ne VIII series limit (Inglis-Teller Limit) was used to estimate an upper limit on the density. Steady-state coronal-equilibrium and local-thermodynamic-equilibrium (LTE) calculations were made to interpret selected line-intensity ratios for Ne VII, Ne VIII, and Ne IX. The temperature dependence of the ionization balance was determined by comparing time-dependent calculations with measured time histories of Ne VII, Ne VIII, and Ne IX transitions.

6.5.1 Electron Density

An upper limit on the electron density can be estimated from the advance of the Ne VIII $1s^2 2p-1s^2 n d$ series limit. The Ne VIII spectrum in Fig. 6.21 shows transitions originating from levels up to $n=9$ for this series. The density dependence of the Inglis-Teller limit for Ne VIII was presented in Fig. 5.10. The analysis in Fig. 5.10 indicates that the $n=9$ level would not appear distinct from the recombination continuum at an electron density above $5 \times 10^{19} \text{ cm}^{-3}$. This implies that the electron density was at or below this value at the time the Ne VIII radiation was emitted.

6.5.2 Electron Temperature

Intensity ratios of XUV spectral lines were used to determine the

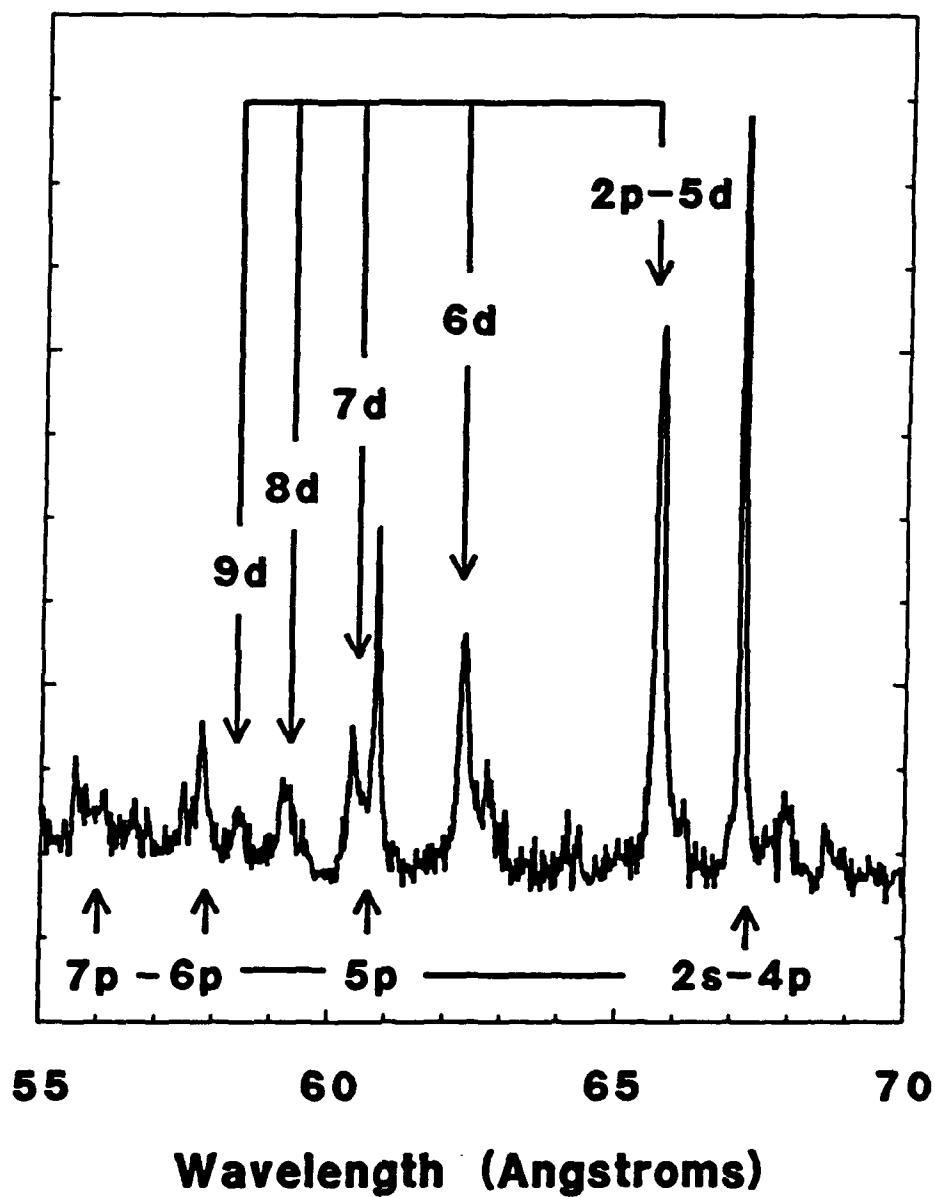


FIG. 6.21. Spectrum of Ne VIII emission from 55 to 70 eV showing the 2p-nd series limit. Also spectral lines from the 2s-np series for Ne VIII are identified.

relative populations of the upper levels of the transitions. Measured ratios were compared with coronal-equilibrium and local-thermodynamic-equilibrium (LTE) calculations to estimate the electron temperature. A time-dependent coronal model based on collisional excitation rates was used to determine the time dependence of the ionization balance. Results of these calculations were compared with measured time histories of transitions from various ionization states to estimate the time dependence of the electron temperature. Details of these calculations can be found in Appendix C.

The ratio of the intensity of the Ne IX $1s2l-1s3l'$ ($l=s,p$ and $l'=p,d$) transitions at 78.26 Å and 78.30 Å to the Ne VIII $1s^22s-1s^23p$ transitions at 88 Å was calculated using coronal and LTE models. The results of these calculations are presented in Fig. 6.22. The coronal model uses the ionization balance presented in Fig. 2.2 and assumes that collisional excitation is balanced by radiative decay. In this model, the Ne IX to Ne VIII ratio is independent of the electron density and should be appropriate for electron densities below the collision limit for the upper levels of interest (10^{20} cm^{-3}). For the LTE model, which uses the Saha and Boltzmann relations to determine the relative populations of the various levels, this ratio was calculated for an electron density of 10^{21} cm^{-3} , a density above which LTE should hold for the upper levels of these transitions.

The ratios of the Ne VIII $1s^22s-1s^23p$ transitions at 88 Å to the Ne VII $1s^22s2p-1s^22s3d$ transitions at 106 Å and to the Ne VII $1s^22s^2-1s^22s3p$ transition at 97.5 Å were also calculated. The coronal model and the model based on LTE were used. An example of the ratios from these calculations is presented in Fig. 6.23. For this example, an electron density of 10^{21} cm^{-3} was used in the LTE calculation.

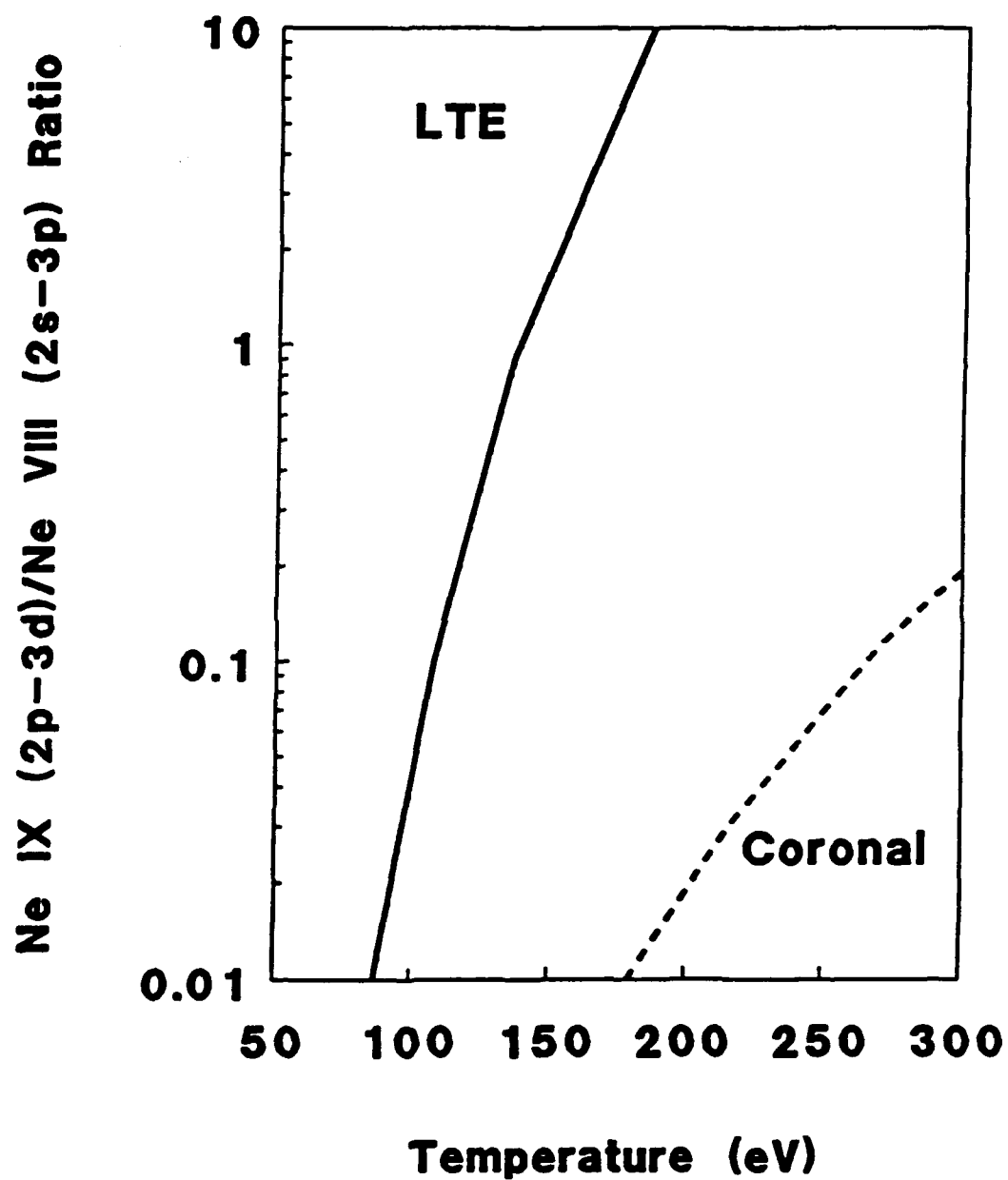


FIG. 6.22. Temperature dependence of Ne IX to Ne VIII line ratio from two atomic-physics models for electron densities described in the text (LTE-solid and Coronal-dashed).

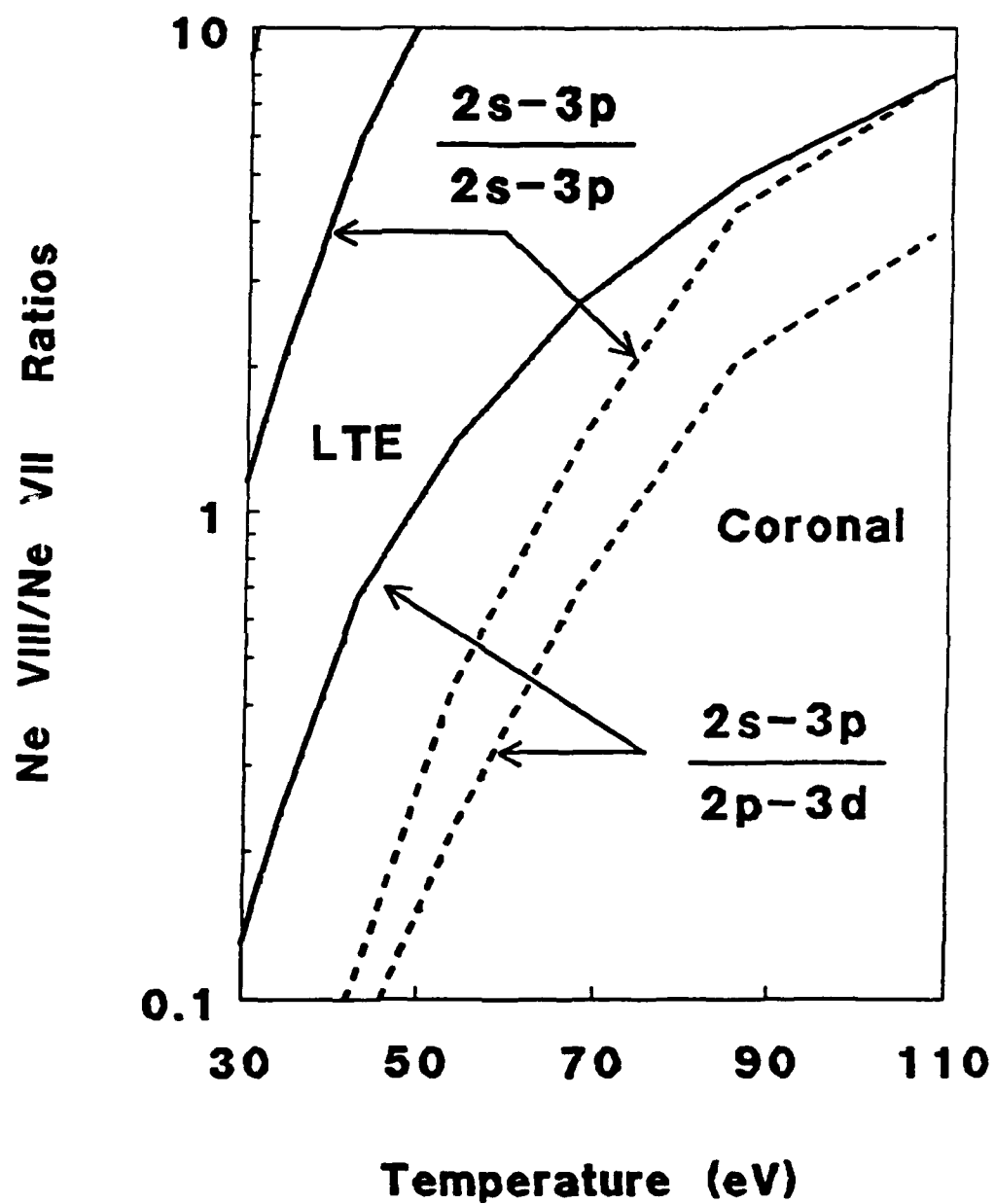


FIG. 6.23. Temperature dependence of Ne VIII to Ne VII line ratios for two atomic-physics models (LTE-solid and Coronal-dashed).

The electron temperature was determined by comparing measured line ratios with the calculations presented in Figs. 6-22 and 6-23. A portion of an XUV spectrum (Fig. 6.11(a)) with the appropriate Ne IX, Ne VIII, and Ne VII transitions identified is given in Fig. 6.24. The measured density was corrected for the nonlinearity of density verses exposure using an analytic fit to the measured relations.¹¹⁷

Integrated intensities of the lines of interest were determined and compared with the calculations. The measured Ne IX to Ne VIII ratio of 0.11 indicates a temperature of 110 eV (LTE) to 270 eV (coronal) depending on the model. The electron density is less than $5 \times 10^{19} \text{ cm}^{-3}$ from the Inglis-Teller limit (Sec 6.5.1). At this density LTE should not be valid and a temperature larger than that indicated by LTE is expected. This estimate assumes that the Ne VIII and Ne IX lines are emitted from the same spacial region. Soft X-ray and XUV pinhole photographs (see Figs. 5-7 and 6-6) indicate that the Ne IX emission originates from a much smaller region than the Ne VIII emission. This suggests that the Ne IX to Ne VIII ratio is larger for the region of Ne IX emission than that measured in the XUV spectra. If no more than two regions of Ne IX emission in the 6-mm length of plasma are viewed by the spectrograph, each with a 0.4-mm length, a line ratio of 0.8 is estimated for the region of Ne IX emission. For this ratio an electron temperature of 140 eV (LTE) to greater than 300 eV (coronal) is estimated. In the region where no soft x-ray emission was seen, the Ne IX to Ne VIII intensity ratio is expected to be smaller than that measured in the XUV spectra and the temperature is correspondingly smaller.

The ratio of Ne VIII to Ne VII emission was used to estimate the temperature in the region where no Ne IX emission was observed. The

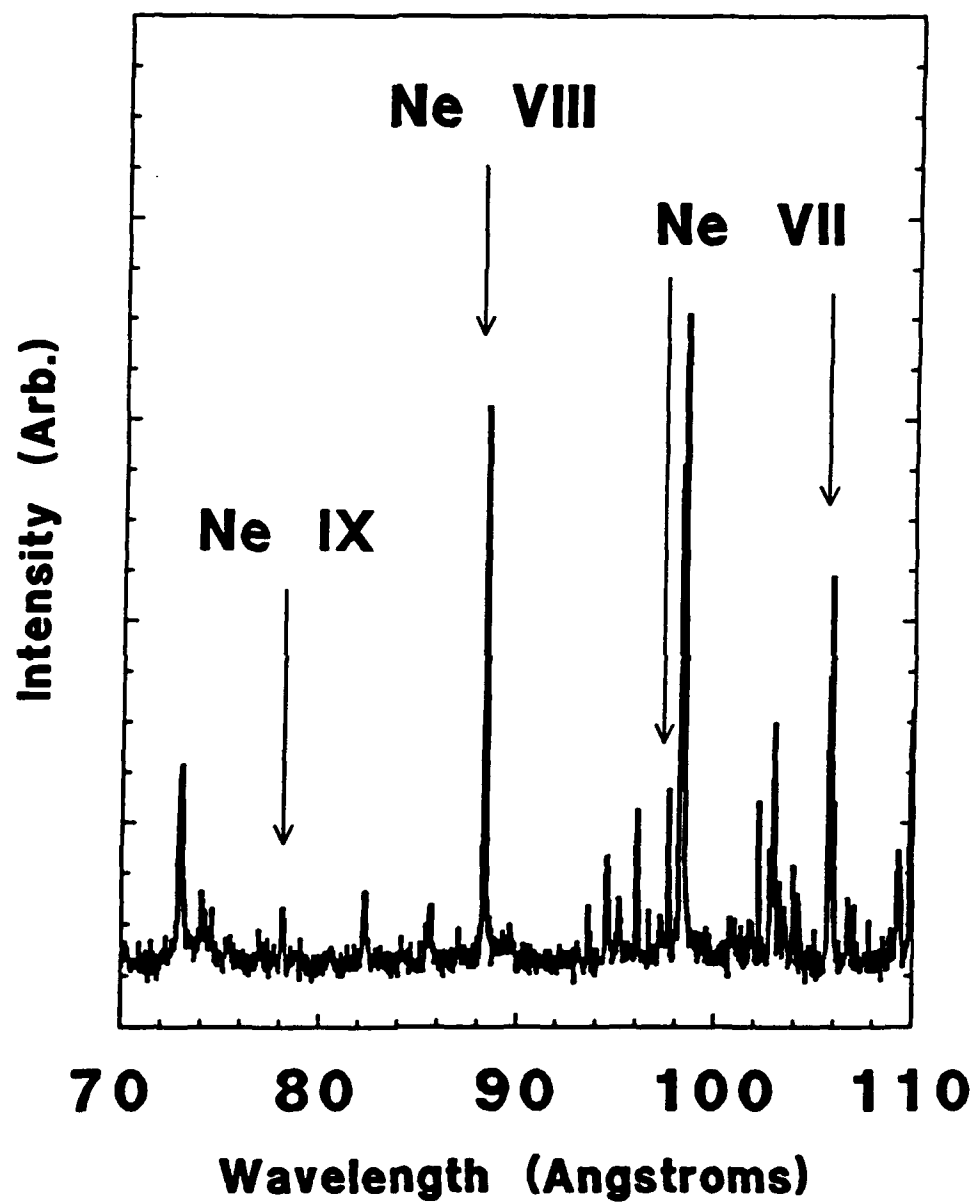


FIG. 6.24. Neon XUV spectrum in which Ne VII, Ne VIII, and Ne IX transitions used in the line-ratio analysis are identified.

measured ratio of the Ne VIII $1s^2 2s-1s^2 3p$ transition at 88 Å to the Ne VII $1s^2 2s 2p-1s^2 2s 3d$ transition at 106 Å is 1.3 for the spectrum in Fig. 6.24. For this ratio, the electron temperature is 55 eV (LTE) or 80 eV (coronal), depending on the model used. The measured ratio of the Ne VIII $1s^2 2s-1s^2 3p$ transition at 88 Å to the Ne VII $1s^2 2s^2-1s^2 2s 3p$ transition at 97.5 Å was 5.6 for the spectrum of Fig. 6.24. For this ratio, the electron temperature is 40 eV (LTE) or 100 eV (coronal). These coronal and LTE temperatures are averaged over the time duration that the radiation was emitted.

Time histories of emissions from Ne VII, Ne VIII, and Ne IX were measured to provide information on the time dependence of the line ratios. These measurements are compared with time-dependent CRE model calculations to estimate the time dependence of the electron temperature. The time histories of these emissions in Figs. 6.17 and 6.18 were used to estimate peak electron temperatures for implosions with different gas-puff plenum pressures. Ne VII emission is observed at both peaks for all pressures (Fig. 6.18). Ne VIII emission is observed at the first peak for all pressures; however this emission is observed at the second peak for only 50 and 100 psi (Fig. 6.17(a)). Ne IX emission is observed at the first peak for all pressures; however at the second peak no emission is observed for 150 psi; a small signal is observed for 100 psi; and a large signal is observed for 50 psi. These observations indicate that ionization states up to Ne IX are produced at the first peak for all three pressures. At the second peak, ionization states up to Ne VII are observed for 150 psi, up to Ne VIII for 100 psi, and up to Ne IX for 50 psi. Comparisons with time-dependent rate-equation CRE calculations indicate a peak temperature greater than 200 eV was achieved during the first

implosion. For the second peak, these calculations indicate that the peak temperature is less than 60 eV or 100 eV for plenum pressures of 150 psi and 100 psi, respectively. For a plenum pressure of 50 psi, the peak temperature at the second peak is similar to that of the first peak. Examples of calculated time-dependent ionization states can be found in Appendix C.2. The time dependence of the ionization states will be discussed further in Chapter 7, after the relative timing of the Ne VII and Ne VIII emissions is presented.

Chapter 7

NEAR ULTRAVIOLET RADIATION

To investigate the imploding neon plasma beyond the limits of the XUV instruments, near ultraviolet (NUV) emission in the region of 4.3 to 4.6 eV (2700–2900 Å) was studied. The focusing properties of NUV optics allows spacial resolution of the plasma emissions and the spectral resolution in the NUV allows line-width measurements. Comparison of the intensity of emission with that of a source of known intensity in the NUV region provides absolute intensities. Comparison of these temporal, spectral, and absolute intensity measurements with results of atomic-physics models provides quantitative information about the state of the plasma.

The Ne VIII $1s^23s-1s^23p$ transitions at 2820.7 and 2860.1 Å were chosen for this investigation because measurements of absolute intensities and line widths for these transitions can provide both the Ne VIII $1s^23p$ level population and the electron density. Furthermore, a simultaneous measurement of these transitions and the Ne VIII $1s^22s-1s^23p$ transition can provide a relative-intensity calibration of the NUV spectrometer at 2820.7 or 2860.1 Å and the XUV spectrometer at 88 Å, by the branching ratio technique.¹¹⁸⁻¹²⁰ A partial energy-level diagram of the $n=2$ and $n=3$ levels of Ne VIII is given in Fig. 7.1 showing these NUV transitions along with the Ne VIII $1s^221'-1s^231$

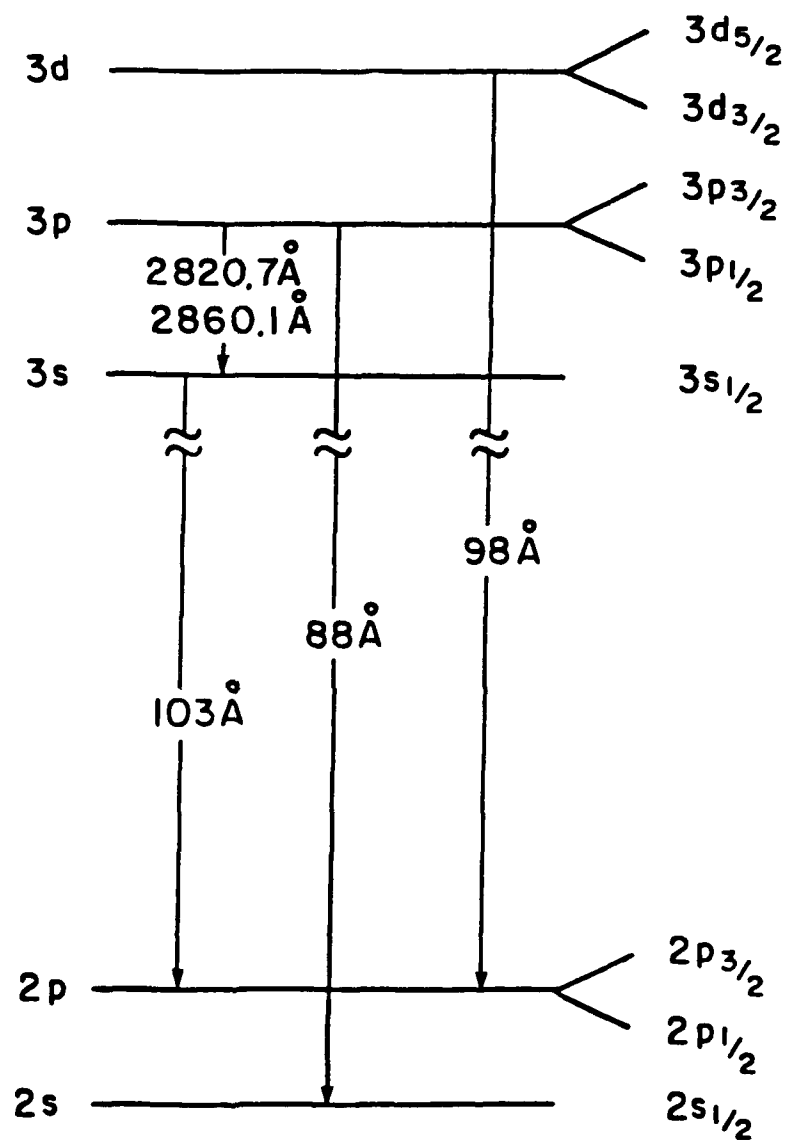


FIG. 7.1. Partial energy-level diagram of Ne VIII $n=2$ and $n=3$ levels.

transitions at 88, 98, and 103 Å. Simultaneous time-histories of Ne VII and Ne VIII emissions were measured by using the NUV spectrometer to monitor Ne VIII emission (2820.7 Å) while the XUV spectrometer was used to record Ne VII emission (106 Å). The Ne VII and Ne VIII time histories, along with the Ne VIII and Ne IX time histories (previously discussed in Sec 6.4.3), can be compared with time-dependent ionization-state model calculations to estimate the electron temperature. The time dependence of the continuum intensity in this spectral region can also be used to estimate temporal variations in the electron density.

Two different NUV spectrometers with photomultiplier tubes mounted behind the exit slits were used to record the Ne VIII line emission and the nearby continuum emission simultaneously. These spectrometers were located at 180° to the grazing-incidence monochromator but viewed the same region of plasma. A two-dimensional time-gated optical multichannel analyzer (OMA) was mounted at the exit of one spectrometer to record neon emission in the region of 2750 to 2900 Å. Imaging the neon NUV emission at the entrance of the spectrometer provided spacial resolution across the diameter of the pinch for a spectral range of about 180 Å. Details of the optical system can be found in Appendix D.3.

7.1 Near Ultraviolet Monochromator Measurements

Time histories of continuum emission near 2810 Å and Ne VIII $1s^23s-1s^23p$ line emission at 2820.7 Å were measured using the NUV monochromators. The continuum intensity was measured for various mass loadings and peak driving currents at the same time as XUV

measurements of the Ne VIII $1s^2 2s-1s^2 3p$ transition (see Secs. 6.4.1 and 6.4.2). The Ne VIII $1s^2 3s-1s^2 3p$ line emission was measured for various mass loadings at the same time as XUV measurements of the Ne VII $1s^2 2s2p-1s^2 2s3d$ transition (see Sec. 6.4.3).

7.1.1 Continuum Intensity Measurements

The time history of the NUV radiation in a 4-Å spectral region near 2810 Å was measured at the same time that the time history of the XUV radiation presented in Figs. 6.15 - 6.17 was measured. The spectral region near 2810 Å was chosen because it is free of spectral lines and gives the time history of continuum radiation nearby to the 2820.7- and 2860.1-Å lines of Ne VIII. The measured continuum intensity was compared with calculations of free-free and free-bound continuum intensities to estimate variations in the electron density. This analysis will be used to estimate the electron density at times other than when the electron density is determined from line-width measurements. The continuum emission near 2810 Å and driving currents are given in Fig. 7.2 for implosions with two different charging voltages. The time of peak signal decreases as the charging voltage is increased. Peak emission occurs prior to peak current with similar continuum intensities for both currents. This behavior differs from the Ne VIII signals of Fig. 6.15, where the intensity increases by a factor of two when the current is increased.

Time histories of continuum emission and the corresponding currents are given in Fig. 7.3 for implosions using the plasma opening switch (POS) with different charging voltages. Differences in the opening-switch plasma result in the 100-ns current risetimes of Fig.

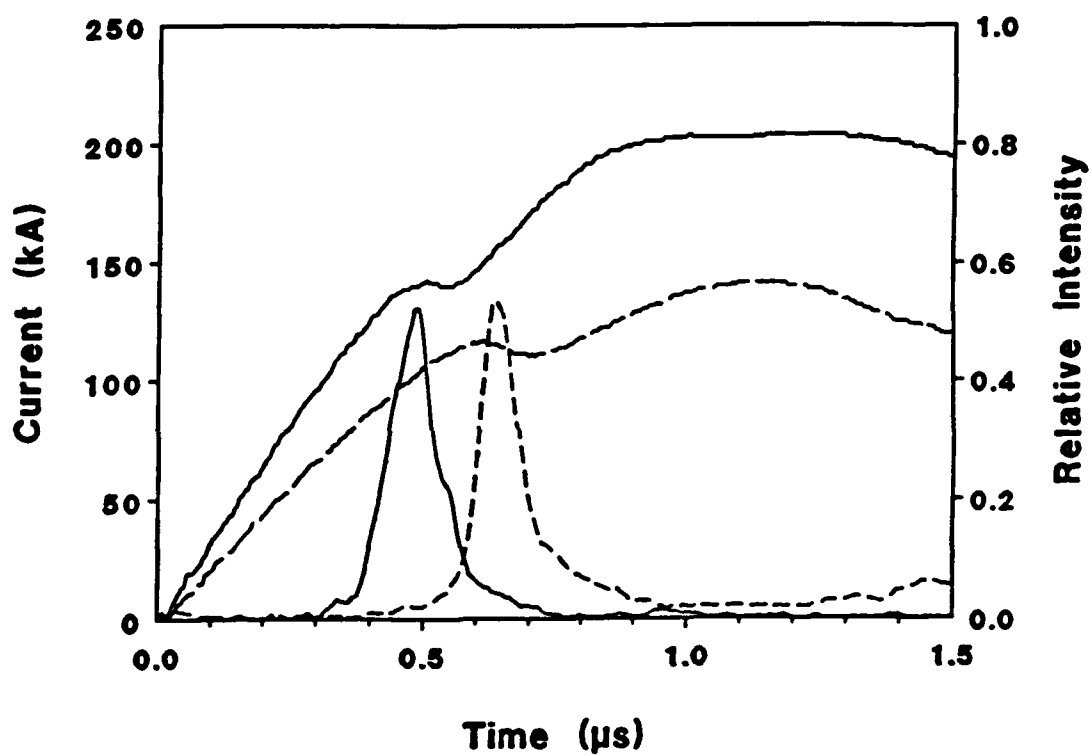


FIG. 7.2. Continuum emission near 2810 Å and currents for charging voltages of 45 kV (solid) and 35 kV (dashed).

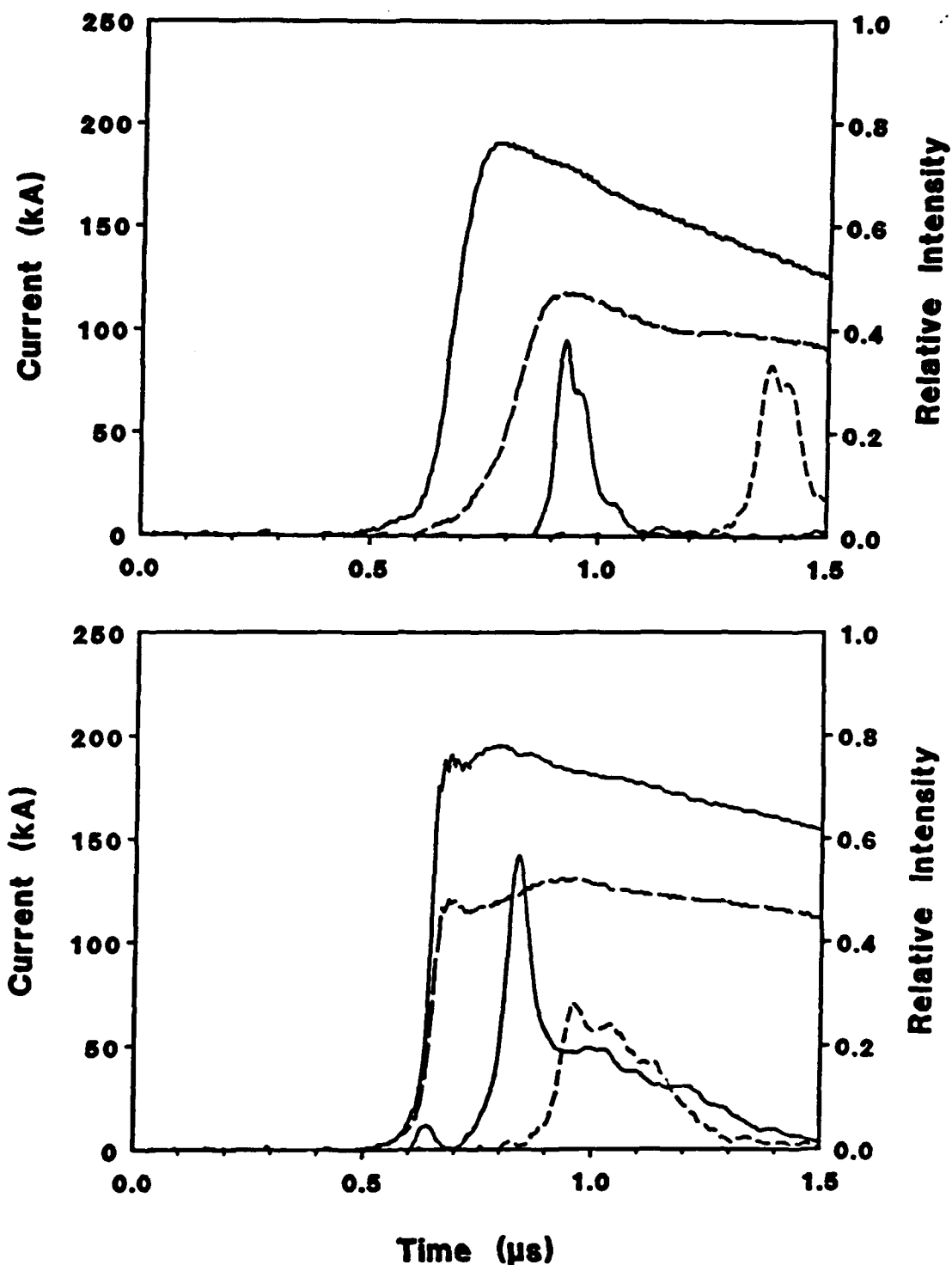


FIG. 7.3. Continuum emission near 2810 Å and currents with the plasma opening switch for charging voltages of 45 kV (solid) and 35 kV (dashed). Current risetimes are (a) 100 ns (top) and (b) 50 ns (bottom).

7.3(a) or the 50-ns current risetimes of Fig. 7.3(b). The implosions occur earlier for larger current as expected. Again the continuum intensities in Fig. 7.3(a) are similar for both currents in contrast to the Ne VIII emission in Fig. 6.16(a). For the faster risetime current in Fig. 7.3(b), the peak continuum intensity decreases by a factor of two, in contrast to the nearly constant intensity of Ne VIII emission for different currents in Fig. 6.16(b).

The variation of the continuum emission with the initial neon mass loading is presented in Fig. 7.4. Continuum emission and current traces are given in Fig. 7.4(a) for two different plenum pressures without the POS. The continuum intensity at the first peak increases by a factor of four as the gas-puff plenum pressure is increased from 50 to 150 psi in contrast to the Ne VIII intensity which increased by only a factor of two. Also, the intensity of the continuum at the first peak relative to the second peak increases from 1.5 to 5.5 as the plenum pressure is increased from 50 to 150 psi. A similar behavior was observed for Ne VIII emission in Fig. 6.17 although the magnitude of the change was less. Continuum emission and current traces with the POS are given in Fig. 7.4(b) for plenum pressures of 50 and 150 psi. The continuum intensities are similar for both plenum pressures. This differs from the Ne VIII emission which decreases considerably as the plenum pressure is increased.

7.1.2 Line-Emission Measurements

The time history of the Ne VIII 3s-3p line emission at 2820.7 Å was determined by using the two monochromators to measure the continuum emission at 2810 Å and the total emission at 2820.7 Å.

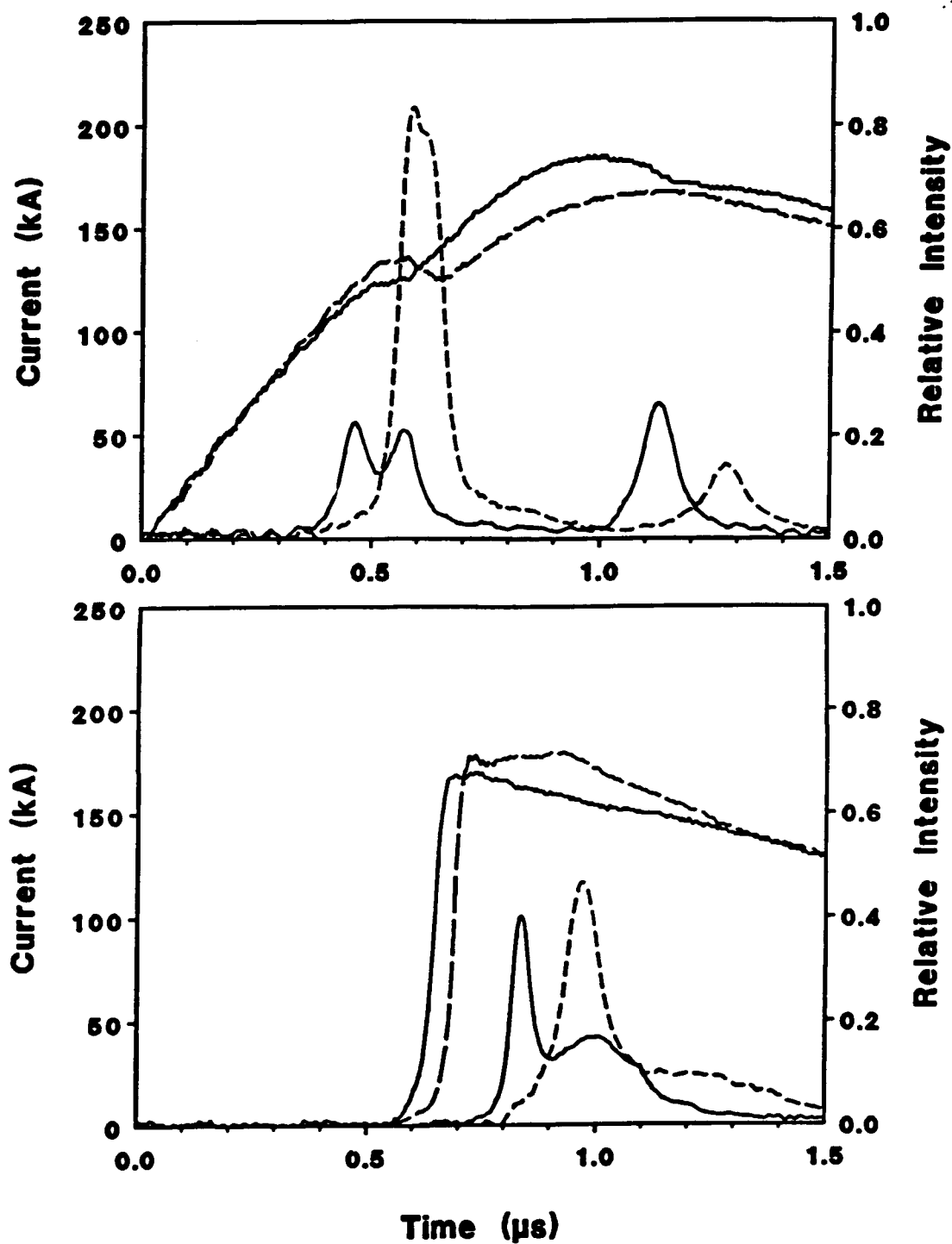


FIG. 7.4. Continuum emission at 2810 Å and currents for plenum pressures of 50 psi (solid) and 150 psi (dotted) (a) without the POS (top) and (b) with the POS (bottom).

Details of the monochromators can be found in Appendix D.3.1. Time histories on (2820.7 Å) and off (2810 Å) the 3s-3p line are compared in Fig. 7.5(a). At the first implosion, the emission is nearly all continuum, while at the second implosion, significant 2820.7 Å emission is observed. The difference between these signals corresponds to the Ne VIII 3s-3p line. This difference is compared with the Ne VIII 2s-3p line (88-Å) emission in Fig. 7.5(b). Emissions at both 2820.7 Å and 88 Å are observed at the second implosion. The reproducible correlation from shot-to-shot of these two emissions at the second implosion indicates the presence of the Ne VIII $1s^2 3p$ excited state. A similar comparison of these Ne VIII emissions is given in Fig. 7.6 for an implosion driven with the POS. Time histories on (2820.7 Å) and off (2810 Å) the 3s-3p line are given in Fig. 7.6(a). The difference between these time histories is given in Fig. 7.6(b), along with the Ne VIII emission at 88 Å. Emission from the Ne VIII $1s^2 3p$ level is observed after an initial peak in the continuum.

Simultaneous measurements of Ne VII and Ne VIII line emissions were also made. The two NUV monochromators were used to monitor the Ne VIII 3s-3p transition (2820.7 Å) while Ne VII line emission was measured with the XUV monochromator. These measurements will be presented in Sec. 7.3.1 and used to estimate the electron temperature. The numbers 1, 2, and 3 in Figs. 7.5(a) and 7.6(a) indicate the times when the NUV spectra presented in Sec. 7.2 were obtained.

7.2 NUV Optical- Multichannel-Analyzer Measurements

One of the NUV spectrometers was fitted with an optical

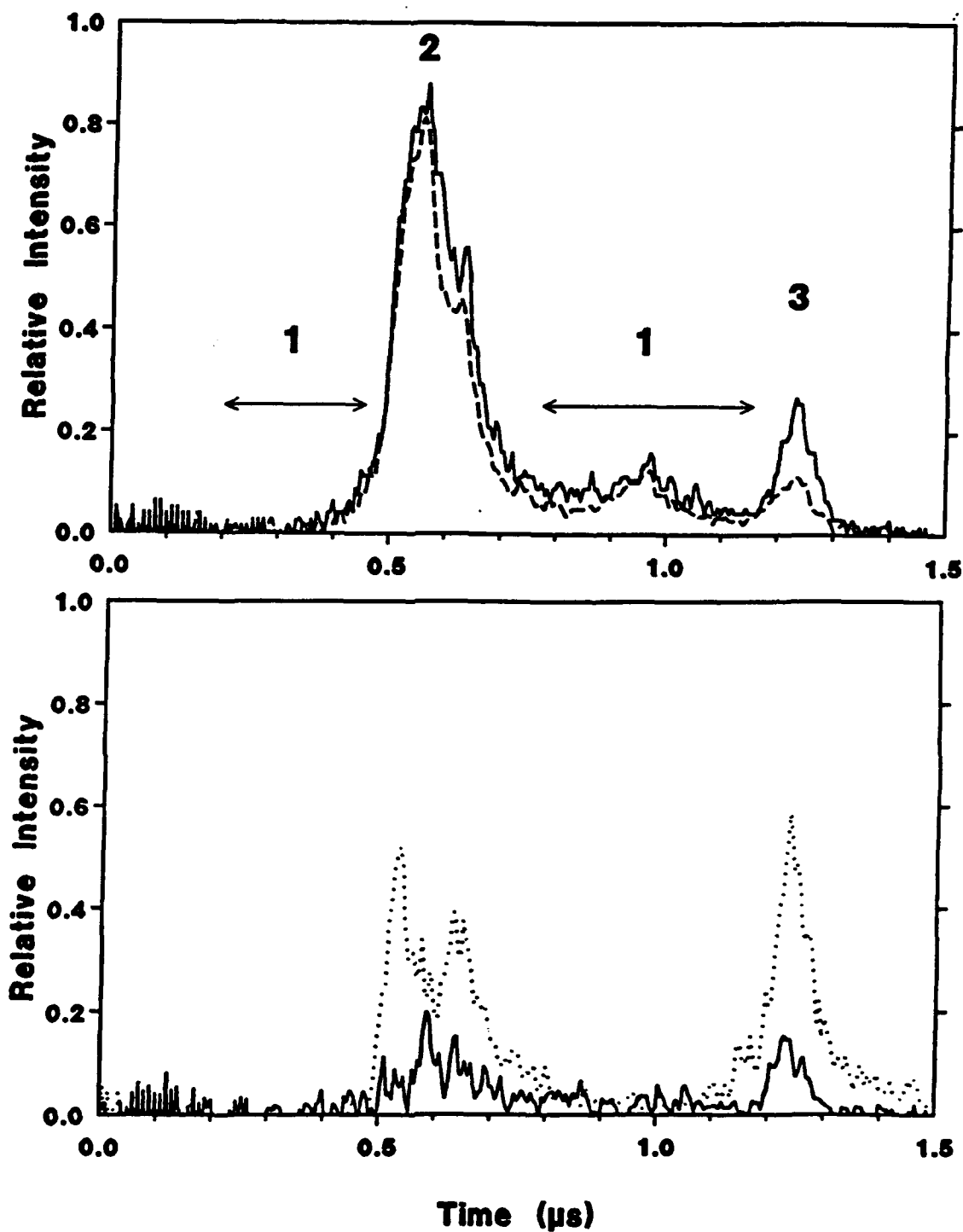


FIG. 7.5. (a) Total NUV emission at 2820.7 \AA (solid) and at 2810 \AA (dashed) for a neon implosion (top). (b) Ne VIII 3s-3p line emission at 2820.7 \AA (solid) and at 88 \AA (dotted) from the same neon implosion (bottom). The numbers in (a) denote different temporal regions.

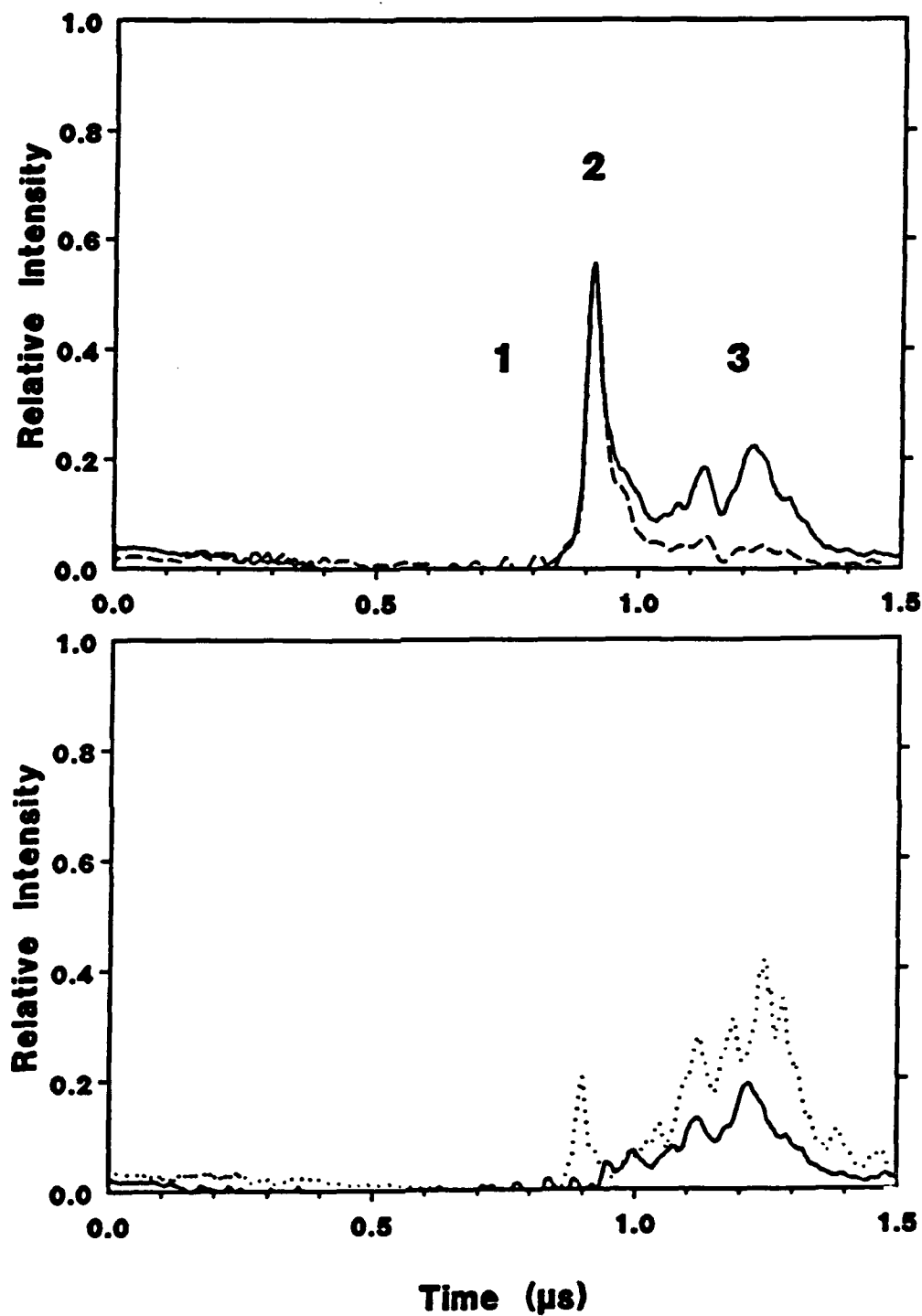


FIG. 7.6. (a) Total NUV emission at 2820.7 \AA (solid) and at 2810 \AA (dashed) for a neon implosion with the POS. (b) Ne VIII $3s-3p$ line emission at 2820.7 \AA (solid) and at 88 \AA (dotted) from the same neon implosion. The numbers in (a) denote different temporal regions.

multichannel analyzer (OMA) to spatially resolve the NUV emission in the region from 2730 to 2910 Å. Comparison of the OMA response with the other NUV monochromator response indicated that the OMA signal was linear over the intensities encountered in these measurements. The OMA was calibrated by comparison with a deuterium lamp of known intensity. Details of the OMA detector and its calibration may be found in Appendix D.3.2. The OMA was gated on for 100 ns at various times during the discharge, and spectra near 2820.7 Å were measured. Spectra of the Ne VIII 3s-3p transitions were obtained at times suggested by the monochromator results.

Spacially-resolved spectra corresponding to the times indicated in Figs. 7.5 and 7.6 are shown in Figs. 7.7, 7.8, and 7.9. At time 1 (Fig. 7.7), the spectra are characterized by strong lines identified with Ne III 3s-3p transitions, and the diameter of the plasma is 3.5 mm.¹²¹⁻¹²³ At time 2 (Fig. 7.8), no spectral lines are observed; the emission consists of an intense continuum, and the plasma diameter is 1 mm. At time 3 (Fig. 7.9), the 2820.7 and 2860.1 Å lines from Ne VIII are observed, and the plasma diameter is 3.5 mm. The size of this plasma and the absolute intensity of this emission can be used to estimate the Ne VIII population fraction. The width of the Ne VIII spectral lines can be used to estimate the electron density.

7.3 Analysis

The XUV and NUV radiation measurements are used to determine the plasma conditions. Time histories of Ne VII, Ne VIII, and Ne IX emissions are compared with a time-dependent ionization model to estimate the plasma temperature. The measured width of the Ne VIII

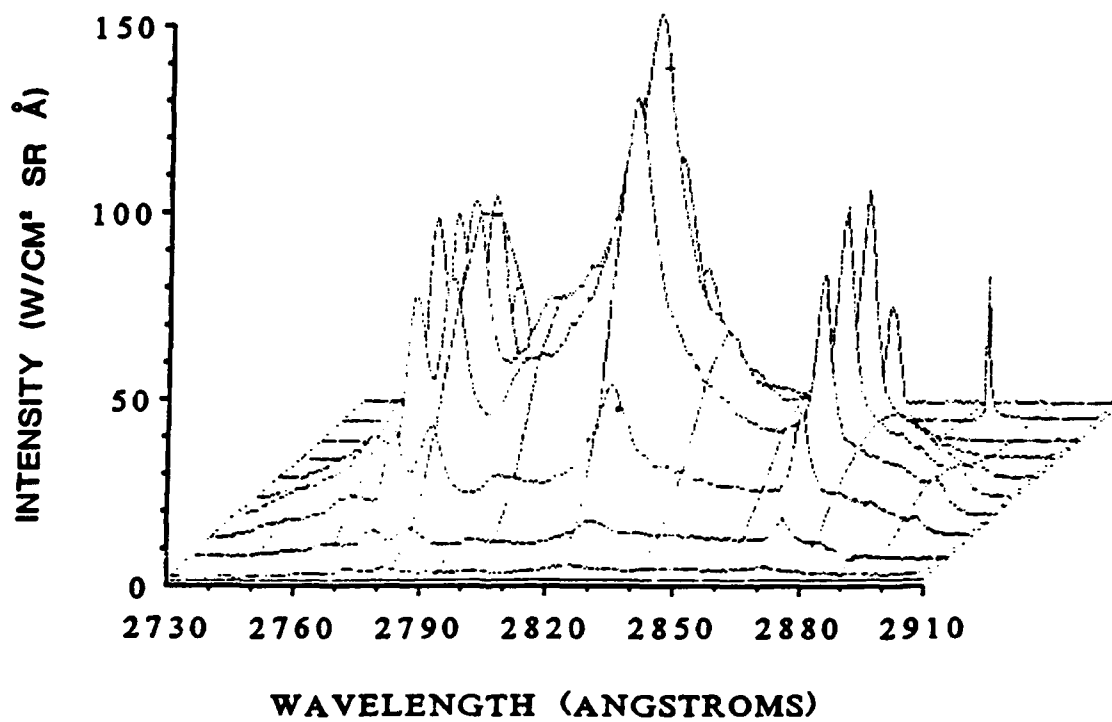


FIG. 7.7. Spatially-resolved NUV emission for time 1 in Figs. 7.5 and 7.6. The lines are Ne III 3s-3p transitions.

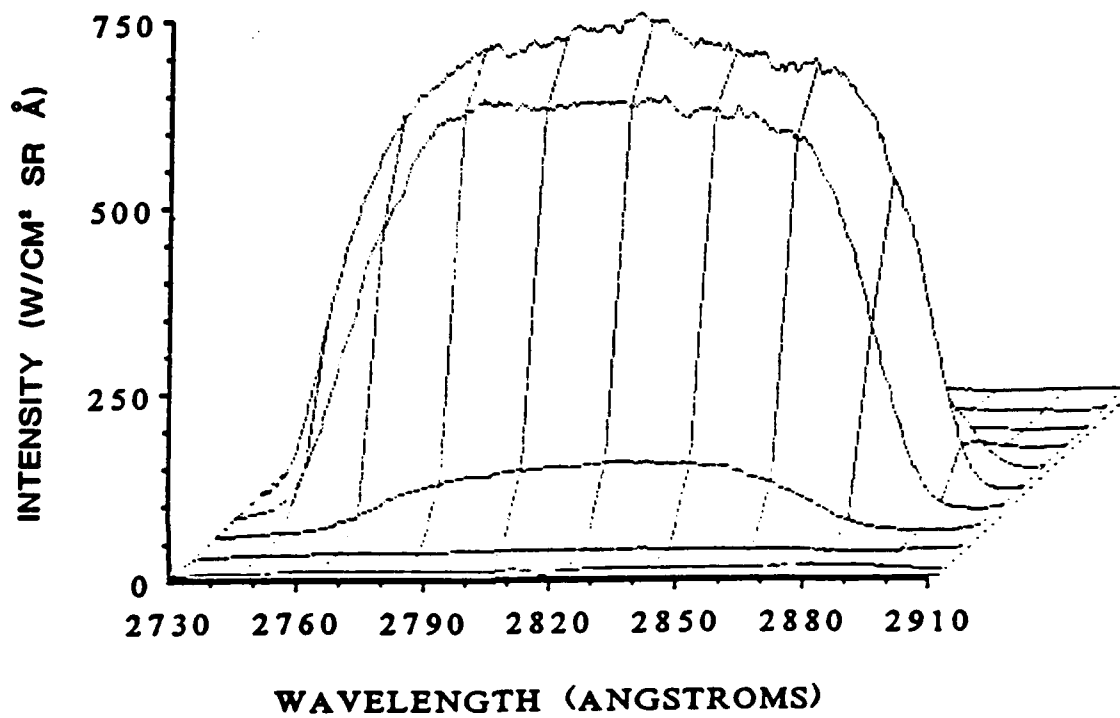


FIG. 7.8. Spatially-resolved NUV emission for time 2 in Figs. 7.5 and 7.6.

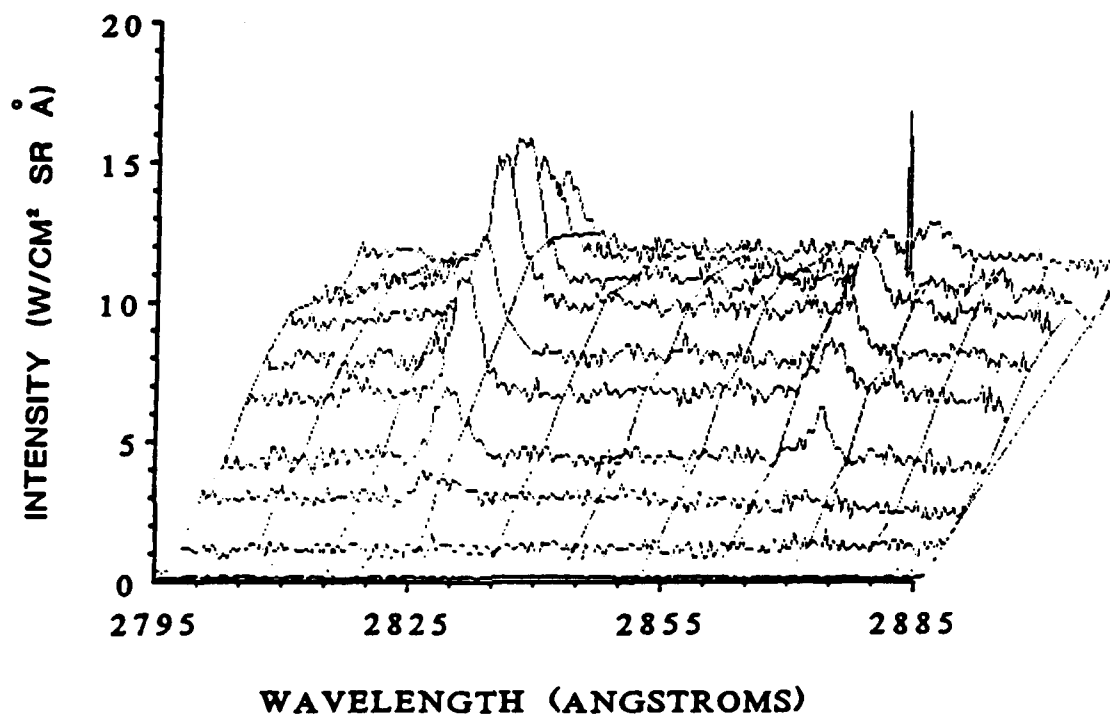


FIG. 7.9. Spatially-resolved NUV emission for time 3 in Figs. 7.5 and 7.6. The lines are Ne VIII emissions at 2820.7 and 2860.1 Å.

$1s^23s-1s^23p$ transition is compared with Stark broadening estimates to determine the electron density. The absolute intensity of the Ne VIII $1s^23s-1s^23p$ transition is used to estimate the Ne VIII $1s^23p$ level population. Then, the Ne IX ground-state population can be evaluated using an atomic-physics model for the plasma.

7.3.1 Electron Temperature

Time histories of Ne VII, Ne VIII, and Ne IX emissions were measured simultaneously in pairs. Ne VIII and Ne IX emissions were recorded simultaneously using the XUV monochromator and a soft X-ray diode. Examples were given in Fig. 6.17 for various gas-puff plenum pressures. Ne VII and Ne VIII emissions were recorded simultaneously using the XUV and NUV monochromators, and examples of Ne VII emission were given in Fig. 6.18 for various plenum pressures. Simultaneous with these Ne VII measurements, the two NUV monochromators were used to measure Ne VIII time histories (as discussed in Sec. 7.1). An example of these Ne VII and Ne VIII time histories, measured on the same shot, is given in Fig. 7.10. For Ne VII, the $2s2p-2s3d$ (106 Å) transition was used. This emission is the same as that in Fig. 6.19 for 50-psi plenum pressure. For Ne VIII, the $3s-3p$ (2820.7 Å) radiation with continuum subtraction was used. Two peaks are evident in Fig. 7.10 and emissions from Ne VII and Ne VIII are observed from both peaks.

Emissions from Ne VII, Ne VIII, and Ne IX produced under similar conditions are compared with the ionization-balance calculations to determine the electron temperature. Examples of these emissions over a 500-ns time period are given in Fig. 7.11 for implosions with 50-

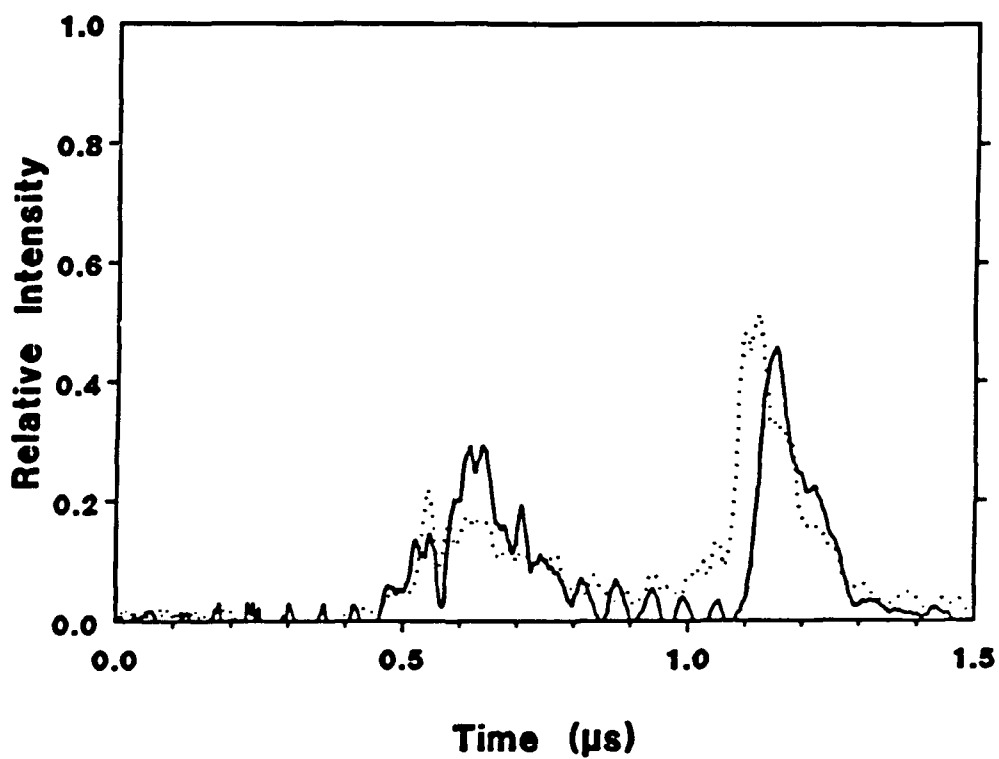


FIG. 7.10. Emissions from Ne VII at 106 Å (dotted) and from Ne VIII at 2820.7 Å (solid) for an implosion with 40-kV charging voltage and 50-psi plenum pressure.

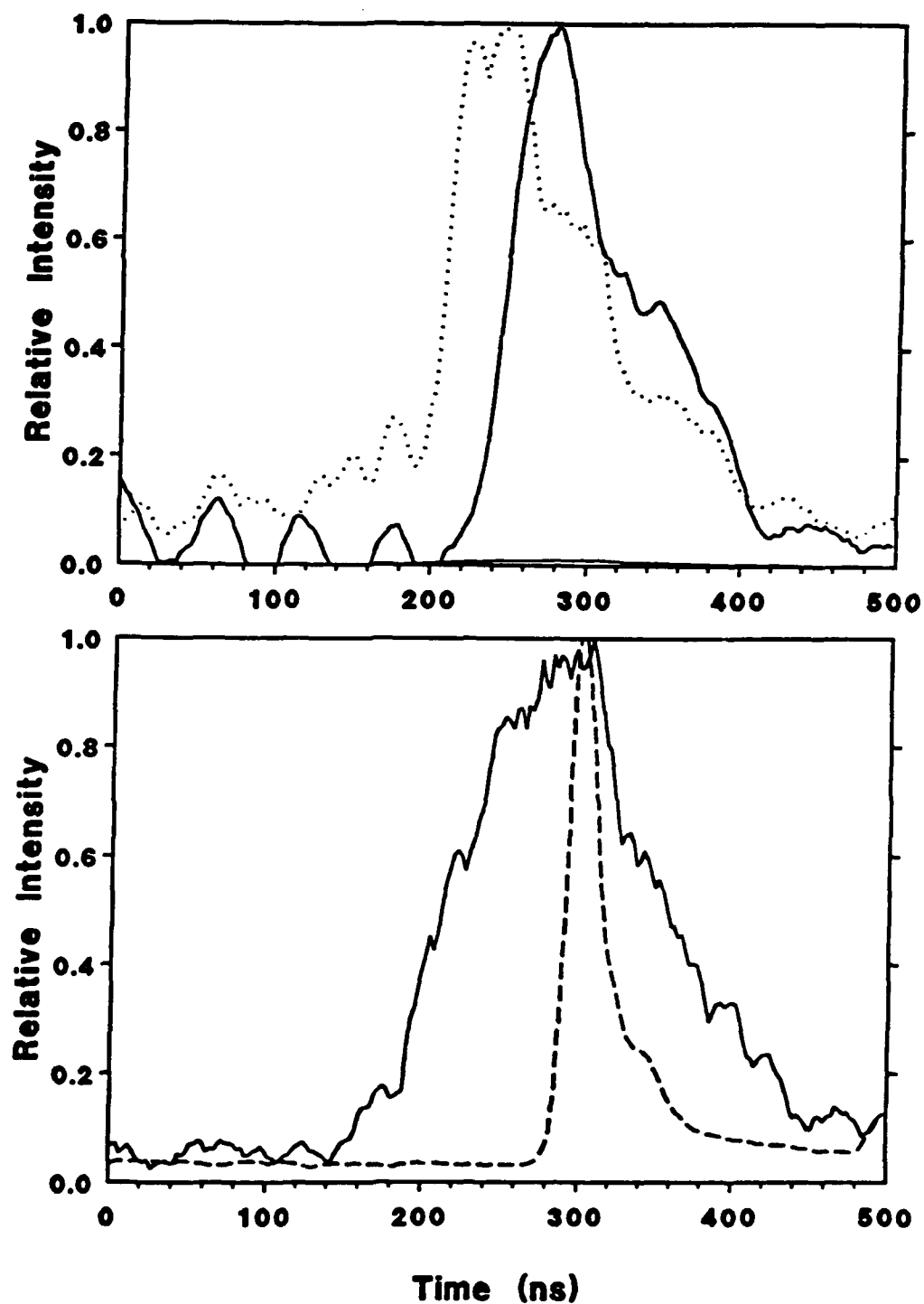


FIG. 7.11. Simultaneous time-resolved measurements of (a) Ne VII (dotted) and Ne VIII (solid) emissions (top) and (b) Ne VIII (solid) and Ne IX (dashed) emissions (bottom) from the second implosion for a 40-kV charging voltage.

psi plenum pressure and 200-kA peak current. This 500-ns interval includes the second implosion when emission from the second peak occurs. The Ne VII and Ne VIII emissions in Fig. 7.11(a) are the same as in Fig. 7.10. The time of the second peak was chosen because the Ne VIII (3s-3p) measurement is more reliable at this time. The Ne VIII and Ne IX emissions of Fig. 7.11(b) are the same as in Fig. 6.17. Time-dependent ionization-state calculations (see Appendix C) were compared with the measurements in Fig. 7.11 to determine the electron temperature. An example of the results of the calculations is given in Fig. 7.12 for a peak electron temperature of 200 eV and a peak electron density of $5 \times 10^{18} \text{ cm}^{-3}$. The temperature was adjusted in the calculation to fit the duration of emission and the time of peak emission for the Ne VII, Ne VIII, and Ne IX time histories in Fig. 7.11. A peak temperature of 200 eV is inferred for a plenum pressure of 50 psi. For larger mass loading (i.e. plenum pressure) these time histories change (see Figs. 6.17 and 6.18) so that lower temperatures are required to fit the measurements. For 100 and 150 psi, the peak electron temperatures of 100 and 60 eV, respectively are required to fit the measurements. These temperatures are for the second implosion for all three plenum pressures. At the first implosion, the presence of Ne IX emission and the reduction in the pulse width of Ne VII and Ne VIII emissions for all three plenum pressures suggest peak temperatures of at least 200 eV. An uncertainty of $\pm 20\%$ can be expected in these temperature measurements based on comparison of the measured time history with various calculated time histories.

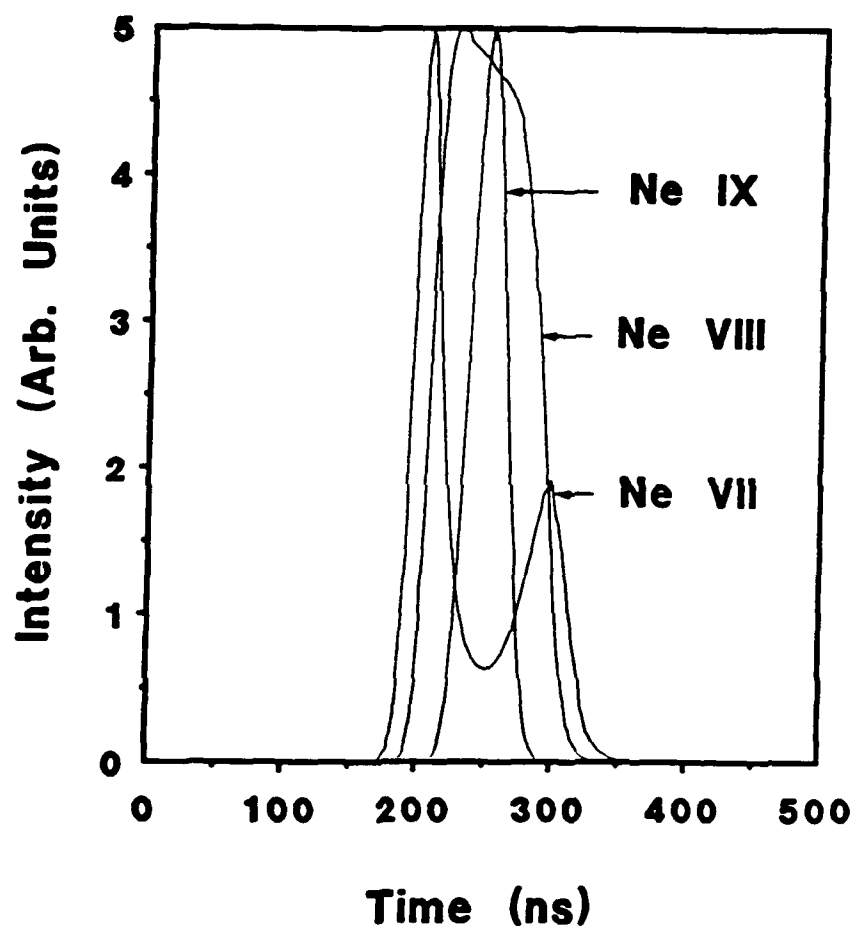


FIG. 7.12. Time dependence of Ne VII, Ne VIII, and Ne IX emissions from a time-dependent coronal-model calculation.

7.3.2 Stark Broadening

The measured line width of the Ne VIII $1s^2 3s(^2S) - 1s^2 3p(^2P^o)$ transition is used to estimate the electron density of the plasma. A spectrum taken at time 3 in Fig. 7.5 is shown in Fig. 7.13. This spectrum is spacially integrated to improve the signal-to-noise ratio. The two spectral lines correspond to Ne VIII 3s-3p transitions. The ratio of these lines is 2:1 as expected for an optically-thin plasma. A full-width at half-maximum (FWHM) of 4.1 Å is determined for the 2820.7 Å line. This line profile is a combination of instrumental broadening and the emitted-line profile. The emitted-line profile is a result of broadening primarily due to the Doppler and Stark effects. The measured line profile is a convolution of these effects. The magnitude of the various broadening mechanisms must be determined in order to unfold the Stark broadening from the measured FWHM. An instrumental width of 1.5 Å was determined by measuring the width of a Hg I line from a low-pressure mercury lamp in this spectral region. Doppler broadening due to ion thermal motion at a temperature of 75 eV results in a Gaussian line shape with a FWHM of 0.4 Å. Doppler broadening due to macroscopic motion of the plasma at a velocity of 10 cm/μs produces a Gaussian line shape with a FWHM of 0.8 Å. Convolution of Gaussian profiles with full-widths at half-intensity of 1.5, 0.4, and 0.8 Å gives a Gaussian profile with a FWHM of 1.75 Å.¹²⁴ This Gaussian profile is convoluted with Lorentzian profiles of various width to produce Voigt profiles which are compared with the measured width.¹²⁵ The Lorentzian FWHM that results in a Voigt profile with a FWHM that best fits the measured FWHM is used as a measure of the Stark broadening. The convolution of a 1.75-Å FWHM

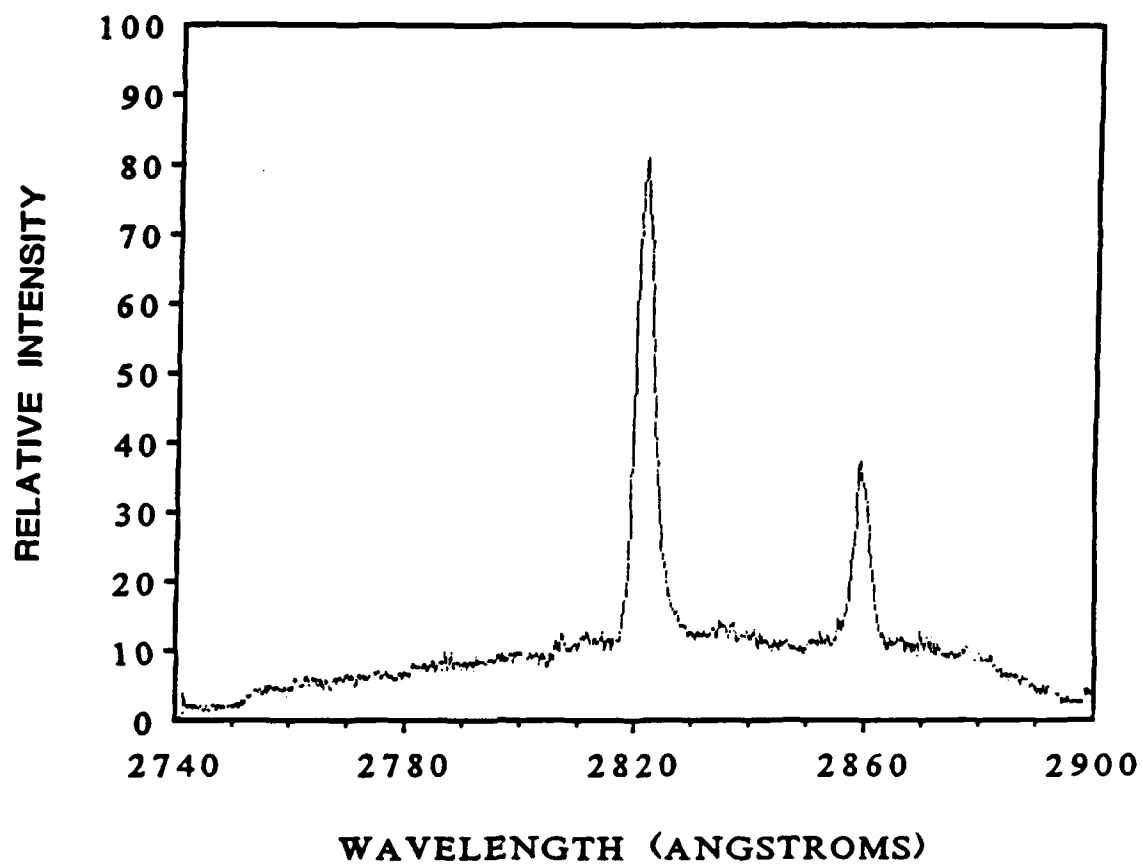


FIG. 7.13. Spatially-integrated spectrum for time 3 in Figs. 7.5 and 7.6. The lines are Ne VIII emissions at 2820.7 Å and 2860.1 Å.

Gaussian line shape with a 2.9-Å FWHM Lorentzian line shape results in a Voigt profile of 4.1-Å width. Therefore, the Stark broadening is 2.9 Å. An uncertainty of $\pm 15\%$ is based on comparison of the measured line shape with various Voigt profiles.

Stark broadening measurements for carbon, nitrogen, and oxygen ions were used to determine the electron density required to produce the Stark broadening measured for this Ne VIII line. Simultaneous measurements of electron density and the corresponding Stark broadening have been reported for this same $1s^2 3s-1s^2 3p$ transition in C IV, N V and O VI.^{126,127} Extrapolating these results to neon, assuming a $\Delta\lambda/\lambda^2 \propto Z^{-1}$ scaling, gives a Stark width of 0.9 Å for an electron density of $1.8 \times 10^{18} \text{ cm}^{-3}$. Therefore, the measured Stark broadening of 2.9 Å corresponds to an electron density of $5.8 \times 10^{18} \text{ cm}^{-3}$, assuming the electron density scales linearly with Stark width. The uncertainty in Stark broadening data results in a $\pm 30\%$ error in the electron density.

7.3.3 Continuum Intensity

Calculations of the continuum intensity were carried out for temperatures and densities relevant to this experiment. The continuum intensity was evaluated using a coronal-equilibrium model to determine the ionization balance. The temperature dependence of the fractional population of various ionization states given in Fig. 2.2 was used to determine the ionization-state populations. The temperature dependence of the bremsstrahlung radiation for each ionization state was calculated from Eq. A.25 and the temperature dependence of the recombination continuum was calculated for each ionization state from

Eq. A.26. The recombination continuum was summed over levels within the photon energy of the reduced ionization limit. Correction for transitions into merged levels above the advanced series limit is included in Eq. A.25. Recombination into levels with $n \leq 3$ would produce photons of 4.3 eV (2810 Å) for only Ne I, and was not included in the calculation. The Gaunt factors were assumed to be unity. The neon continuum intensity is given in Fig. 7.14 for an ion density of $6.25 \times 10^{17} \text{ cm}^{-3}$ along with the bremsstrahlung and recombination components. The continuum is primarily bremsstrahlung in this spectral region. The total continuum intensity varies by less than a factor-of-two over the temperature range from 50 to 200 eV. On the other hand, the continuum intensity has a strong dependence on the electron density (N_e^2), and therefore is a good indicator of the temporal variation of the electron density. The absolute intensity of the continuum emission in Fig. 7.8 is $1.2 \text{ kW/cm}^2 \cdot \text{sr} \cdot \text{Å}$. For a 1-mm diameter plasma this corresponds to an electron density of $9 \times 10^{19} \text{ cm}^{-3}$, assuming an electron temperature of 200 eV. Uncertainties in the absolute calibration and plasma-size measurement results in an uncertainty of $\pm 30\%$ in the density.

7.3.4 Ne VIII $1s^2 3p$ Level Population

The measured absolute intensity of the Ne VIII $1s^2 3s-1s^2 3p$ transition is used to determine the Ne VIII $1s^2 3p$ level population. An intensity of $175 \text{ W/cm}^2 \cdot \text{sr}$, integrated over the linewidth, was determined from a comparison with a calibrated deuterium lamp. For a photon energy of 4.3 eV, a transition probability of $7 \times 10^7 \text{ sec}^{-1}$, and a plasma size of 3.5 mm; a Ne VIII $1s^2 3p$ level population of $1.3 \times$

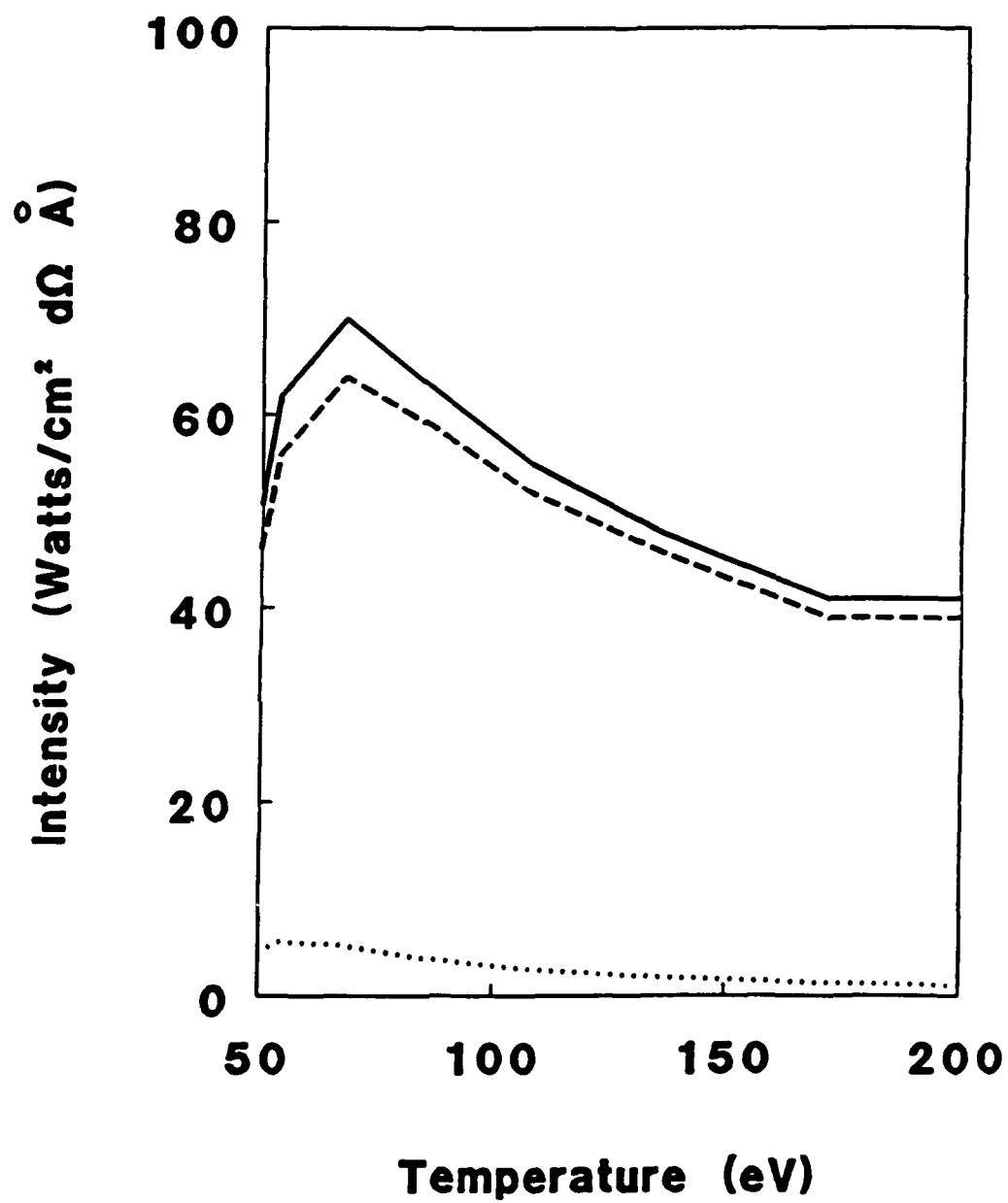


FIG. 7.14. Temperature dependence of bremsstrahlung (dashed), recombination (dotted), and total (solid) continuum emission for an ion density of $6.25 \times 10^{17} \text{ cm}^{-3}$.

10^{14} cm^{-3} was determined from Eq. A.17. This assumes that the transition probability is not influenced by the properties of the plasma, which has been shown to be valid for the electron density measured in this experiment.¹²⁸ Uncertainty in the absolute calibration results in an uncertainty of $\pm 30\%$ in this population.

The electron density and temperature are combined with the Ne VIII $1s^2 3p$ level population to determine the Ne IX ground-state population. An electron density of $5.8 \times 10^{18} \text{ cm}^{-3}$, an electron temperature of 75 eV, and a Ne VIII $1s^2 3p$ level population density of $1.3 \times 10^{14} \text{ cm}^{-3}$ were determined at the time of the second implosion in the neon Z-pinch discharge for 100-psi plenum pressure and 40-kV charging voltage. The ratio of the Ne IX ground-state population to the Ne VIII $1s^2 3p$ level population was calculated using three atomic-physics models. If LTE is appropriate for the Ne VIII $1s^2 3p$ level, the Saha relation can be used to relate that level to the ground-state population of the next higher ionization state. Partial LTE for the $n=3$ level is expected for an electron density greater than 10^{20} cm^{-3} . The temperature dependence of the ratio of the Ne IX ground-state population to the Ne VIII $1s^2 3p$ level population calculated from the Saha relation is given in Fig. 7.15. Also shown are results of calculations based on coronal equilibrium and collisional radiative equilibrium (CRE).¹²⁹ The coronal calculation of the level populations is based on the ionization balance given in Fig. 2.1, and then balances collisional excitation against radiative decay. The CRE model uses collisional and radiative rates, along with radiative transport, to determine the level populations. For the CRE calculation, an electron density of $5 \times 10^{18} \text{ cm}^{-3}$ was used. A ratio of 4.0×10^4 is seen for a temperature of 75 eV for the CRE model.

This implies a Ne IX ground-state population of $5 \times 10^{17} \text{ cm}^{-3}$. An uncertainty of $\pm 20\%$ in the temperature measurement results in an uncertainty of $\pm 45\%$ in the Ne IX ground-state population.

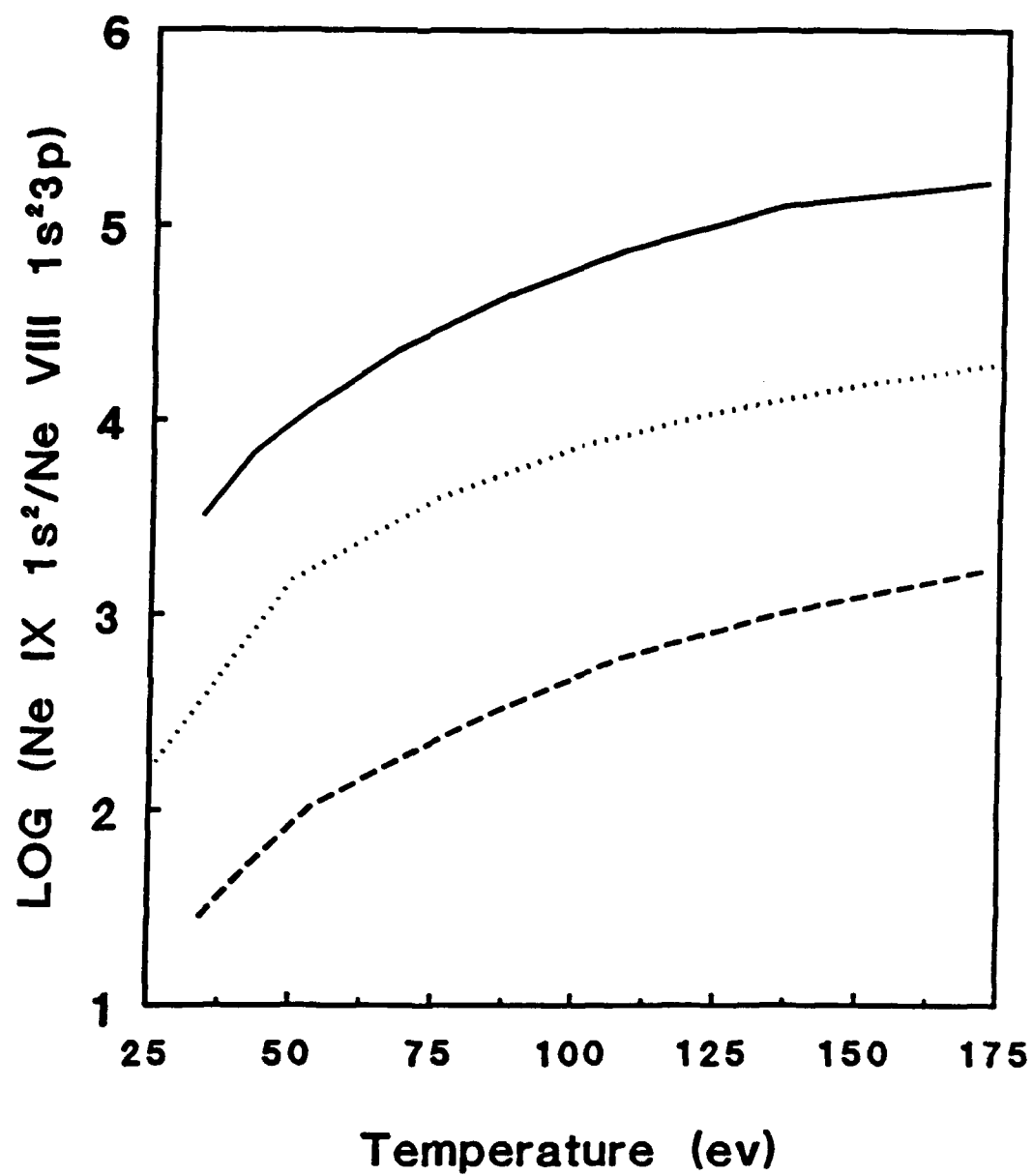


FIG. 7.15. Temperature dependence of Ne IX ($1s^2$ ground state)/Ne VIII ($1s^23p$) ratio for LTE (solid), CRE (dot), and Coronal models.

Chapter 8

CONCLUSIONS

Neon gas-puff Z-pinch implosions, driven by currents of up to 300 kA, were investigated using various spectroscopic diagnostics. The motivation was to produce a neon lasant plasma appropriate for resonant photopumping experiments. Soft x-ray, extreme ultraviolet, and near ultraviolet emissions were recorded and compared with plasma models to determine the electron temperature and density of the neon plasma. A measurement of the Ne VIII $1s^2 3p$ level population was used to estimate the Ne IX ground-state population. The dependence of the plasma emissions on experimental parameters was also investigated. Various gas-puff plenum pressures were used to produce different linear mass loadings. Different capacitor charging voltages were used to drive the implosion with different peak currents. Also, the risetime of the current was reduced with a plasma opening switch (POS).

8.1 Neon IX Ground-State Density

The possibility of using a neon gas-puff Z-pinch as the lasant in a sodium/neon photopumping experiment has been investigated. The photopumping scheme uses 11-Å radiation from Na X to excite the

$1s^2$ - $1s4p$ transition in Ne IX. A significant population of the Ne IX ground state is necessary to absorb the photopump line. Therefore, an estimate of the Ne IX $1s^2$ level population was made from measurements of the plasma electron temperature, electron density and the Ne VIII $1s^23p$ level population. The results indicate that 70% of the neon ions are in the Ne IX ground state.

Temporally, spatially, and spectrally resolved measurements of the $1s^23s$ - $1s^23p$ transitions in Ne VIII at 2820.7 and 2860.1 Å were used to determine the plasma density. The absolute intensity of the line emission was used to determine the Ne VIII $1s^23p$ level population. A measured intensity of $175 \text{ W/cm}^2\text{sr}$ for both lines indicated a population of $1.3 \times 10^{14} \text{ cm}^{-3}$ for the Ne VIII $1s^23p$ level. The line width of these two $3s$ - $3p$ transitions was used to determine the electron density. A full-width at half-maximum of 2.9 Å due to Stark broadening indicates an electron density of $5.8 \times 10^{18} \text{ cm}^{-3}$. Time-resolved measurements of Ne VII, Ne VIII, and Ne IX emissions were used to determine the plasma temperature. Comparison of measured time histories with a time-dependent ionization-state model indicates a peak temperature of 100 eV, and a 75-eV temperature at the time of Ne VIII line-width measurement. A collisional-radiative-equilibrium code was used to predict the ratio of the Ne IX ground-state population to the Ne VIII $1s^23p$ level population for this electron temperature and density. The code gives a ratio of 4.0×10^4 corresponding to a Ne IX ground-state population of $5 \times 10^{17} \text{ cm}^{-3}$. For an effective charge of $z=8$, the measured electron density and the estimated Ne IX ground-state population indicate that 70% of the neon ions are in the Ne IX ground state. This estimate was made from radiation emitted at the time of the second peak for the implosion

driven by a slow rising (1 μ s) current pulse. To relate this estimate to the plasma produced by a fast rising (100 ns) current pulse as used in previous photopumping experiments, an investigation was carried out into the effects of the initial neon mass loading, peak current, and current rise-time on the implosion dynamics.

8.2 Neon Plasmas Produced by Slow-Risetime Currents

Neon Z-pinch implosions driven with a capacitor discharge produced peak currents of 150 to 300 kA with a 1.1- μ s quarter period. Two "dips" in the current waveshape were observed corresponding to inductive loading of the electrical circuit by the imploding plasma. The first "dip" occurred 500 to 600 ns after the beginning of the current. At that time the current was 75% of peak current. The second "dip" occurred near peak current, i.e., 1.0 to 1.2 μ s after the beginning of the current. Peaks in the X-ray emission from the plasma were observed at the times of these current "dips". The current "dips" and the X-ray peaks correspond to implosions of the neon gas puff. The conditions of the neon plasma at these two times differ considerably, as discussed below.

8.2.1 Time Histories of Electron Temperature and Density

Soft X-ray spectra of the neon implosions were recorded, and spectral lines from Ne IX and Ne X transitions were identified. The ratio of the Ne IX $1s^2-1s2p$ transition to the Ne X $1s-2p$ transition indicates an electron temperature of 200 to 250 eV, while the slope of the Ne IX recombination continuum suggests an electron temperature of

300 eV. These temperatures are different because the measurements are time-integrated and represent an average temperature over the duration of the corresponding soft X-ray emissions. The advance of the Ne IX series limit implies an electron density of $3 \times 10^{20} \text{ cm}^{-3}$. The ratio of the intensities of the Ne IX resonance to intercombination lines indicate an electron density of 10^{19} cm^{-3} . This is an under estimate because the resonance line is optically thick for plasmas larger than 100 μm . Soft X-ray images indicate that the emission is from small regions less than 500 μm in diameter, spaced at irregular intervals along the length of the pinch. Up to eight small regions are seen along the 4-cm length of the plasma. The electron density determined from the advanced series limit and the plasma size determined from the soft X-ray images imply a linear mass loading of 1.2 $\mu\text{g/cm}$ or a linear ion density of $3.6 \times 10^{16} \text{ cm}^{-1}$ for $Z=8$.

Extreme ultraviolet (XUV) spectra of the neon implosion were recorded, and spectral lines from Ne VII, Ne VIII, and Ne IX were identified. The advance of the Ne VIII $1s^2 2p-1s^2$ series limit implies an electron density of $5 \times 10^{19} \text{ cm}^{-3}$. Extreme ultraviolet images indicate that the plasma is radiating along the entire 4-cm length with a diameter of about 1 mm. This electron density and diameter imply a linear mass loading of 1.6 $\mu\text{g/cm}$ or a linear ion density of $4.8 \times 10^{16} \text{ cm}^{-1}$ for $Z=8$. This result compares well with the result determined from the soft X-ray measurements. The Ne VIII $1s^2 2s-1s^2 3p$ to Ne IX $1s 2p-1s 3d$ intensity ratio indicates an electron temperature of 125 eV. This interpretation assumes that the Ne VIII and Ne IX emissions are radiating from the same region over the same time period. Pinhole-camera images indicate that the extreme

ultraviolet emission (e.g., Ne VIII) is from the entire length of the pinch, whereas the soft X-ray emission (e.g., Ne IX) is restricted to small spacial regions. Consequently, for these small regions, the ratio of Ne VIII to Ne IX emission is much smaller. In addition, the longer pulse width of the Ne VIII emission (150 ns) compared with the Ne IX emission (50 ns) indicates that the ratio of Ne VIII to Ne IX emission is even smaller during the time that the Ne IX is emitting. Correcting for the source-size and pulse-duration differences increases the temperature estimate to 250 to 300 eV for the plasma that is spatially and temporally restricted to Ne IX emission. This temperature is consistent with the estimates from the soft X-ray spectra. The electron temperature was also determined for regions of the plasma where no soft X-ray emission was seen, but XUV emission was observed. Intensity ratios of Ne VII and Ne VIII transitions combined with a steady-state coronal model give electron temperatures of 80 to 100 eV.

Time-resolved measurements of Ne VII, Ne VIII, and Ne IX emissions were compared with a time-dependent ionization model to determine electron temperatures. At the time of the first implosion, a peak temperature of 200 eV was estimated, and at the second implosion, the peak temperature was 100 eV.

Near ultraviolet spectra of the neon implosions were recorded, and spectral lines from Ne III and Ne VIII transitions were identified. Spectra were recorded for 100-ns duration at various times during the discharge. Radiation from Ne III was emitted early in the discharge, prior to the first implosion, from a 3.5-mm diameter plasma. At the first implosion no NUV line radiation was observed but intense continuum emission was observed from a 1-mm diameter plasma.

The continuum results from compression of the plasma to high density. A spatially resolved measure of the continuum absolute intensity gave a peak value of $1.2 \text{ kW/cm}^2 \cdot \text{sr} \cdot \text{\AA}$ at the first implosion. For a 1-mm diameter plasma, this intensity corresponds to an electron density of $9 \times 10^{19} \text{ cm}^{-3}$, assuming an electron temperature of 200 eV. At the second implosion, Ne VIII emission was observed from a 3.5-mm diameter plasma. Also, time-resolved measurements of NUV emission in the region of 2810 Å and 2820.7 Å indicated an intense continuum (2810 Å) at the first implosion and Ne VIII emission (2820.7 Å) at the second implosion. Between the two implosions, Ne III emission was observed. The presence of Ne III indicates a much lower electron temperature than indicated by emission from higher ionization states (e.g., Ne VIII). For the coronal-equilibrium model discussed in Appendix A, Ne III is the dominant ion species for temperatures of 5 to 10 eV. The time-dependent ionization model suggests a similar temperature range for Ne III.

A representation of the electron temperature and density determined at various times during the discharge is given in Fig. 8.1. The electron temperature in Fig. 8.1(a) was determined from the presence of various ionization states and the duration of their presence. The cross in Fig. 8.1(a) represents the temperature of the "hot spot". The electron density in Fig. 8.1(b), between implosions when Ne III is present, was estimated by scaling the electron density from Ne VIII to Ne III (assuming charge neutrality) and using the measured radius (which is the same for Ne III and Ne VIII emission).

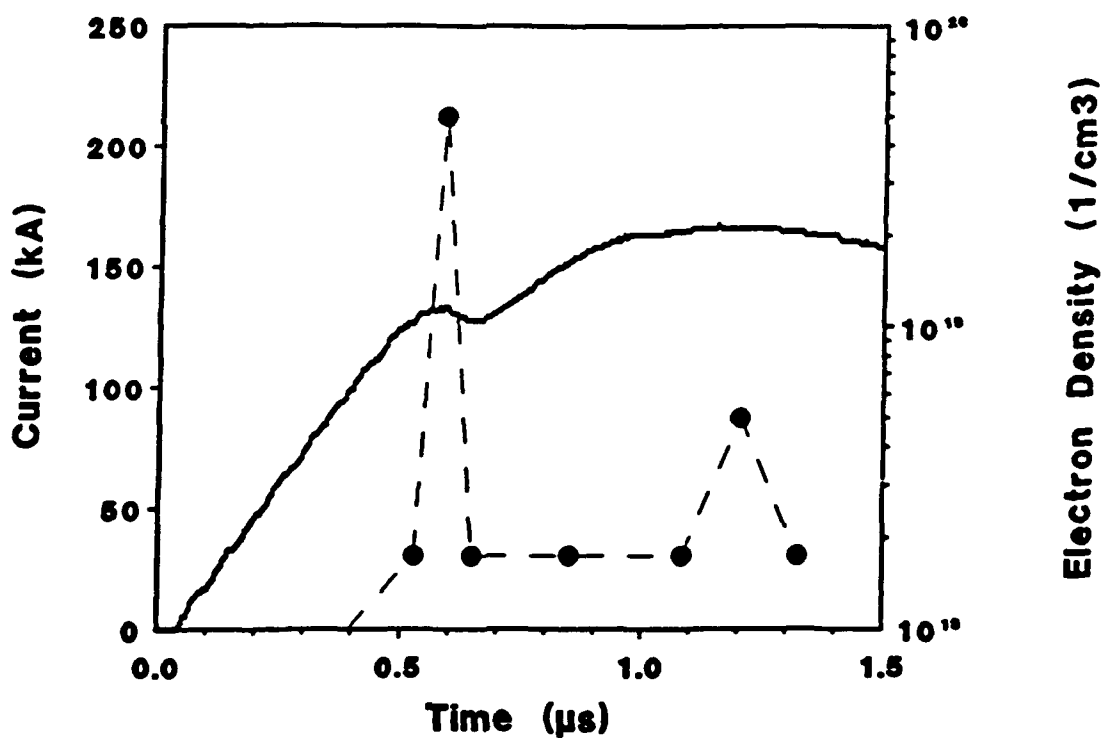
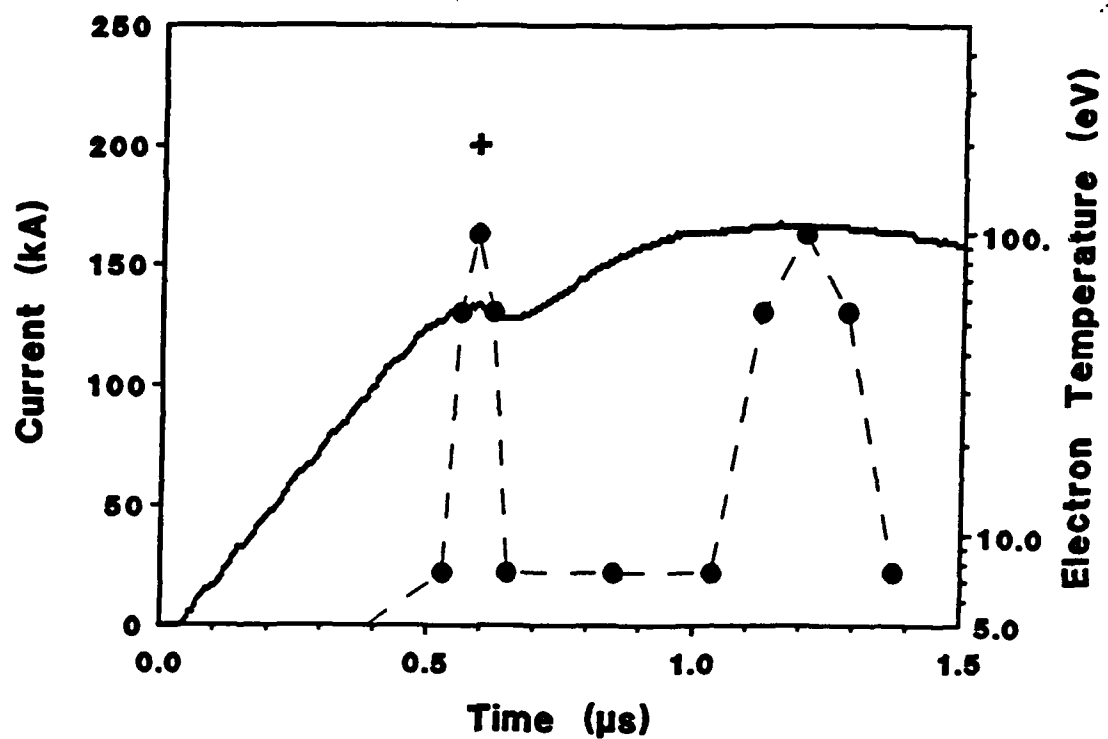


FIG. 8.1. Time dependence of (a) electron temperature and (b) electron density for a neon implosion. The time history of the current is also given for reference.

8.2.2 Current Variations

Changes in the various neon plasma emissions with driving current indicate that the amount of neon gas heated by the implosion increases with current, rather than the increase in current causing the plasma temperature or density to increase. Visible-light images indicate that the radial extent of the emission region increases as the current is increased. For higher currents these images exhibit axial nonuniformities which increase in number with current. The XUV images increase in length as the current is increased and develop axial nonuniformities which increased in number. These nonuniformities are associated with small regions of soft X-ray emission. An increase in the amount of neon plasma heated with increasing current is consistent with the soft X-ray and XUV measurements. The time-integrated spectra vary little in ionization-state composition or in the relative intensity of various ionization states as the current is increased. The XUV spectra show Ne IX emission only for implosions driven by the largest currents. This observation is understood in terms of more small regions of soft X-ray emission being produced in the field of view of the spectrograph, and not because the bulk plasma temperature increases. Although the time-resolved Ne VIII line emission increased with current, there is little variation in the ionization-state composition. The lack of variation in the spectra or in the relative line emissions indicates similar peak temperatures for the various currents. Also, the NUV continuum intensity did not change with current which indicates that the peak electron density is nearly constant. In summary, increasing the current driving the implosion increases the amount of neon gas that is heated, rather than

increasing the electron temperature or density.

8.2.3 Mass-Load Variations

The mass load varies by changing the plenum pressure on the gas puff; the mass load scales linearly with pressure for the puff valve used in these experiments. Increasing the mass load decreases the peak electron temperature, particularly at the second implosion. Time resolved Ne VII, Ne VIII, and Ne IX line emissions at the second implosion were used to estimate electron temperatures of 250, 100, and 60 eV for pressures of 50, 100, and 150 psi, respectively. At the first implosion, the line intensity from all three ionization states, as well as the NUV continuum, increases when the pressure is increased from 50 to 100 psi. These increases scale linearly with pressure. When the pressure is further increased to 150 psi, only the Ne VII intensity continues to increase linearly with pressure. These changes in temperature are less apparent in the time-integrated spectra, and this behavior is consistent with the time-integral of the time-resolved signals. There is little change in the soft X-ray signals and images as the mass is increased.

8.3 Neon Plasmas Produced by Fast-Risetime Currents

A plasma opening switch was used in parallel with the neon gas puff to reduce the risetime of the current driving the Z-pinch. Currents of up to 200 kA were conducted through the opening switch for up to 800 ns before the switch opened and delivered current to the load. Peak currents of 100 to 200 kA with risetimes of 50 to 100 ns

were measured between the opening switch and the load. Again, two implosions were observed. Peaks in the emitted radiation correlated with "dips" in the current, as seen with the slow-risetime current, however, the "dips" are less apparent. For a given charging voltage, peak currents are similar for the fast- and slow-risetime current pulses, however the implosions occur at higher current levels when driven by the plasma opening switch. The first implosion occurs 350 ns after the beginning of the current, near peak current, while the second implosion occurs 700 ns after the beginning of the current, when the current has decreased to 75% of peak value. Trends in intensity and spectral content of the XUV emission indicate that less mass and more current is needed to produce a spectrum similar to that obtained with the slow-risetime current. For example, similar XUV spectra were measured for a 45-kV charge, 50-psi pressure with the plasma opening switch and a 35-kV charge, 100-psi pressure without the switch.

8.3.1 Time Histories of Electron Temperature and Density

Time histories of the electron temperature and density were determined for the fast-risetime current using the same initial mass load and driving-current magnitude as for the previous slow-risetime-current discussion. The soft X-ray emission was minimal so that spectra could not be used for density and temperature determinations. Soft X-ray diode signals were observed only at the first implosion, and an electron temperature of 200 eV was inferred. At the second implosion simultaneous measurements of Ne VII and Ne VIII line emissions were used to determine an electron temperature of 60 eV.

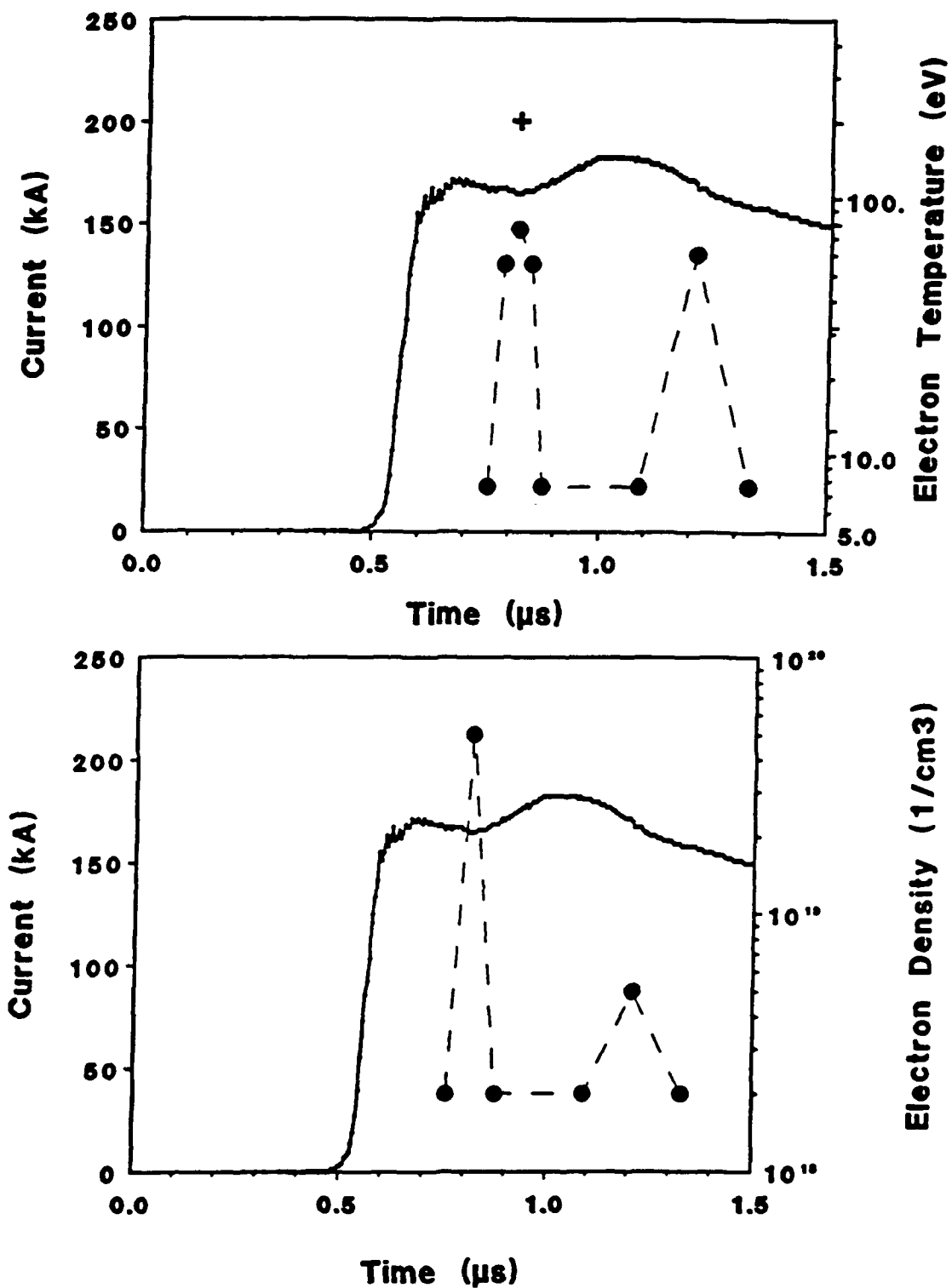


FIG. 8.2. Time dependence of (a) electron temperature and (b) electron density for a neon implosion using a plasma opening switch. The time history of the current is also given for reference,

Between the implosions only Ne III was observed corresponding to electron temperatures of 5 to 10 eV. The NUV continuum intensities were similar to the intensities observed with the slow-risetime current. A representation of the time histories for electron temperature and density is given in Fig. 8.2.

8.3.2 Current Variations

Increasing the current driving the implosion increases the amount of neon gas that is heated with little increase in electron temperature or density. This behavior is similar to the slow-risetime current variation. Visible-light images indicate an increase in the radial extent of the emission region, as well as an increase in the axial nonuniformities, as the current is increased. Axial nonuniformities are also evident in XUV images and increase in number and extent as the current is increased. The soft X-ray and XUV emission increases as more neon plasma is heated. Time-resolved Ne VIII line emission also increases in intensity with increasing current, indicative of more neon plasma being heated. Time-integrated spectra vary little in ionization-state composition or in the relative intensity of various ionization states as the current is increased. This lack of spectral variation indicates similar peak temperatures for the various currents. The NUV continuum intensity showed little variation with current implying nearly constant peak electron density. Implosions driven by the faster-risetime currents (50 ns) produced significantly less Ne VIII emission, and a reduction in the NUV continuum emission was seen for the lower current levels. These measurements suggest that a lower temperature and density plasma is

produced with the fast-risetime current.

8.3.3 Mass-Load Variations

Increasing the mass load decreased the peak electron temperature for implosions using the plasma opening switch. This temperature change was deduced from the time-integrated XUV spectra, where the ratio of the Ne VIII to the Ne VII line intensity decreased as the gas-puff plenum pressure was increased. The soft X-ray emission and the time-resolved Ne VIII line emission decreased in intensity with increasing pressure, and the XUV images indicated that the spatial extent of the emission region decreased. These observations indicate that the plasma is insufficiently heated to produce significant soft X-ray and XUV radiation.

8.4 Imploded Neon Plasma as the Lasant for Photopumping

The suitability of the imploded neon Z-pinch as the lasant in a photopumped XUV laser is discussed. Spectroscopic measurements indicate two time intervals when the plasma temperature is such that a significant Ne IX ground-state population is expected (see Figs. 8.1 and 8.2). At the first implosion, Ne VIII is observed for 50 ns from a 1-mm diameter plasma with an electron density of $5 \times 10^{19} \text{ cm}^{-3}$. At the second implosion Ne VIII is observed for 150 ns from a 3.5-mm diameter plasma with an electron density of $5 \times 10^{18} \text{ cm}^{-3}$. Peak optical depths in the Ne IX $1s^2-1s4p$ line of 20 and 7 are expected at the first and second implosions, respectively. This indicates that 99% of the photopumping radiation at the energy of the Ne IX $1s^2-1s4p$

transition is absorbed by the plasma. For the higher density, collision rates from the $n=4$ level to higher levels are comparable to the Ne IX $1s^2-1s4p$ transition probability. Also the optical depth for transitions from the lower laser levels is larger at the higher density. For the lower density, collision rates between the $4l$ ($l=s,p,d,f$) levels are comparable to the Ne IX $1s^2-1s4p$ transition probability.

8.4.1 Mass-Load Control of the Temperature

The peak temperature of the neon plasma could be changed by adjusting the initial mass load or plenum pressure of the gas puff. This was determined from the ionization states present at various times. With the slow-risetime current, a pressure of 100 psi gave a temperature of 100 eV at the second implosion and appeared optimal for maximizing Ne VIII emission while minimizing Ne IX emission. As the pressure was decreased from 100 to 50 psi the Ne VIII emission did not increase although the Ne IX emission increased considerably. As the pressure was increased from 100 to 150 psi the Ne VIII emission decreased considerably. As the pressure was decreased from 100 to 50 psi the emission from Ne VIII decreased at the time of the first implosion, by an amount consistent with the decreased mass. As the pressure was increased from 100 to 150 psi, no increase in the Ne VIII emission was seen. With the fast-risetime current a pressure of 50 psi appeared optimal. For example, time-integrated XUV spectra at this pressure are similar to those taken with 100-psi pressure using the slow-risetime current.

8.4.2 Current Control of the Lasant Uniformity

The axial uniformity of the plasma decreased as the current driving the implosion increased. For example, soft X-ray images indicate regions less than 500 μm in size with temperatures greater than 200 eV. The number of these "hot spots" increased with current. For lower currents, radial nonuniformities were observed in XUV and visible-light images. A 500- μm thick plasma shell, located at an average diameter of 2 mm, is evident in these images. These radial nonuniformities were apparent at lower current levels than the axial nonuniformities.

Electron temperatures and densities with and without the plasma opening switch are similar, although the fast-risetime current requires larger current and smaller mass. For similar currents and mass loads, the plasmas produced with the fast-risetime current appear to be more uniform axially than the plasmas driven by the slow-risetime current. However, when the current is increased and the mass-load decreased to produce a plasma with similar characteristics, axial nonuniformities become apparent.

8.4.3 Comparison with Photopumping Experiments

The plasma produced at the first implosion is similar to the neon plasma produced in previous photopumping experiments on the Gamble II generator. The neon soft X-ray spectra measured in the photopumping experiments are indicative of a plasma with small regions of soft X-ray emission. The electron temperature in these small regions exceeds 100 eV and is larger than desired for optimum Ne IX ground-state

population. The Ne IX ground-state population is expected to be optimum for a brief period prior to maximum compression. The occurrence of a second implosion was not determined in the photopumping experiment. Even though the current risetime and magnitude were comparable in the photopumping experiments and in the present experiment, the implosion occurred 100 ns after the beginning of the current in the photopumping experiment compared with 350 ns in the present experiment. The reason for this difference is not revealed by the present investigation.

8.5 Suggestions for Future Work

A neon Z-pinch plasma, produced by the implosion of a neon gas puff, achieved a density and temperature conducive for photopumping with 11-Å sodium radiation. The plasma appeared axially nonuniform as indicated by the occurrence of small regions of soft X-ray emission or "hot spots". The uniformity may be improved by imbedding the plasma in a magnetic field. Experiments with a plasma focus indicated that a background axial magnetic field inhibited "hot spot" formation in a similar neon plasma.¹³⁰ A sodium/neon photopumping experiment with parallel Z-pinches could incorporate this technique. A background magnetic field could improve the axial uniformity as well as reduce the perturbation of the neon plasma by the azimuthal magnetic field associated with the sodium implosion.

An alternative technique to make the lasant plasma is to heat a solid neon fiber. Z-pinch experiments using a frozen neon fiber have formed a plasma containing Ne IX and Ne X, although soft X-ray spectra indicate higher temperatures than desired for photopumping.¹³¹ The

use of a frozen neon fiber provides a way to create the neon plasma in a favorable lasing geometry. Heating of neon gas or frozen neon with visible and infrared lasers has also been reported.^{60,132}

Intense soft X-ray radiation produced by imploding a sodium wire array on a 10-MA pulsed-power generator is used to heat a neon gas by direct photoionization and to provide the 11-Å pump power.^{101,106} The neon is contained in a gas cell in this experiment. Enhancement of the Ne IX $1s^2-1s4p$ radiation at 11 Å is observed in soft X-ray spectra; however, XUV spectra are needed to confirm population inversion and lasing.

Recent experiments using high-current generators to implode sodium wire arrays or NaF capillary-discharge plasmas have made advances in increasing the power in the 11-Å Na X $1s^2-1s2p$ transition.^{101,106} An initial pump power of 25 GW at 1 MA has been increased to 150 GW at 3 MA and 200 GW at 10 MA. Soft X-ray spectra from the high-power experiments indicate that the majority of the line radiation is produced by Lyman series transitions of Na XI. High pump powers are achieved by increasing the mass load and reducing the initial radius to achieve the implosion time appropriate for optimum coupling of energy from the generator to the load. As the density and/or final diameter of the imploded sodium plasma increases, the optical depth of the 11-Å Na X line will increase and opacity broadening can disperse the pump-line power into energies other than the energy of peak absorption of the neon plasma. The increased inductance of an increased-mass and decreased-radius wire-array load and the increased optical depth of the resulting plasma represent unfavorable scalings of the pump power with mass.

A possible geometry that overcomes many of the above mentioned

problems is to use an array of sodium wires surrounding a neon lasant on axis. Although a greater solid angle of the sodium emission is subtended by the neon plasma in a geometry where the sodium pump is surrounded by the neon lasant, a larger flux per volume of neon plasma is seen with the sodium pump surrounding the neon lasant. If an array of wires can be made to explode (as in a single-wire experiment) without an on-axis implosion, a neon lasant on axis may remain undisturbed. By dividing the generator current into numerous current channels, a lower-inductance load is possible. The number of sodium wires and their diameter can be adjusted to control the sodium-plasma temperature. The smaller current in each sodium wire results in the plasma not being overheated, and the lower mass of each wire avoids the opacity-broadening problem on the pump line. Although the required lasant can be produced by a neon gas-puff implosion on axis, it suffers from axial nonuniformity. Photoionization of the neon gas by sufficient sodium radiation from a high-current generator can heat the neon gas uniformly in a cylindrical geometry. This geometry avoids the attenuation of pump radiation along the length of the lasant and the attenuation of the lasing radiation at the end of the lasant associated with the use of a gas cell.^{72,101,106}

Alternatively, a frozen neon fiber heated by radiation from the sodium pump or by a modest visible or infrared laser could be used to produce the lasant. Experiments could be performed to determine if a neon fiber can be heated to the appropriate temperature by radiation from a sodium Z-pinch, or if auxiliary laser heating is required. Neon expansion velocities associated with laser heating will produce a blue Doppler shift that could help offset the modest wavelength mismatch and increase the pump power in the region of neon absorption. A

geometry where the current pulse of the Gamble II generator is divided to produce multiple sodium Z-pinch implosions has been proposed, however no experiments have been performed.¹³³ Although technically more difficult than the original parallel Z-pinch plasmas driven by the same current pulse, this geometry overcomes many of the potential problems.

Appendix A

ATOMIC PHYSICS

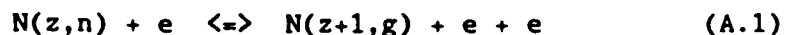
The transition energies and pump powers required for XUV lasers are typical of high-temperature, high-density plasmas created by high-power lasers and pulsed-power devices. Considerable theoretical and experimental efforts have been made to understand the atomic processes in these plasmas. A brief discussion of the basic atomic physics relevant to hot dense plasmas that is necessary for theoretical modeling and experimental analysis is presented. This discussion is by no means complete and standard references may be consulted for further details.^{134,135}

Since spectroscopic measurements are the primary diagnostic used to study hot dense plasmas, this discussion focuses on radiation from highly ionized atoms and its dependence on the bulk properties of the plasma. First, the effects of plasma properties on the relative populations of various ionization states and the subdivision of these states into various excitation levels is discussed. This information is required to relate radiation from a particular level to the bulk plasma properties. Second, how plasma properties effect the detailed spectral features of the emission is discussed. This division is artificial in that the two are related. Since the emission and absorption of radiation is due to the transition of an electron from

one energy level to another, it obviously effects the population of the corresponding levels, and the conditions where this is important are discussed.

A.1 Equilibrium Relations

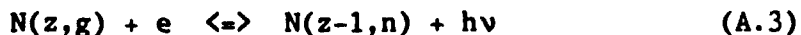
In general, the relative abundances of the various ionization states in a plasma, as well as the populations of the excited levels of the ionization states, are determined by electron-collisionally-induced transitions and the emission and absorption of radiation. A detailed model including the rates of all these various transitions is necessary to determine the populations. As an illustration of some of the processes involved, they may be represented by:



where $N(z,n)$ represents an ion of charge z in state n (or g for the ground state) and e represents an electron. The forward process is referred to as electron collisional ionization and the reverse process is known as three-body recombination. Electron collisional excitation and de-excitation can be represented in a similar manner:



where excitation may take place from any level (n,m) , not just the ground state. Similar processes involving the emission and absorption of radiation are referred to as radiative recombination and photoionization:



where $h\nu$ represents the energy of the photon. Included with radiative recombination should be dielectronic recombination followed by a stabilizing transition. In this situation a doubly-excited intermediate state $N(z-1, n, m)$ exists, which leads back to the left-hand side of Eq. A.3 if an autoionizing transition occurs, and to the right-hand side of Eq. A.3 if a radiative transition occurs. Spontaneous emission and absorption of photons are responsible for transitions between levels of an ion:

$$N(z, n) \rightleftharpoons N(z, m) + h\nu. \quad (A.4)$$

These processes do not necessarily involve the ground state. The rates of these processes have different dependences on electron density; consequently, the process which dominates is quite different at low and high electron densities. In many plasmas, particular processes totally dominate atomic physics, and considerable simplification can be made. For low-density plasmas this simplification results in a coronal model. For high-density plasmas, a model based on local thermodynamic equilibrium (LTE) can be used. At intermediate densities these simplifications cannot be made and a complete collisional-radiative-equilibrium (CRE) model must be used.

Since electron-collisional-transition rates depend on the electron density and radiative transition rates do not, plasmas with electron densities above a certain value are dominated by electron collisional processes. In this situation the plasma is said to be in local thermodynamic equilibrium (LTE) and the populations of the various energy levels can be described by a temperature which corresponds to the Maxwellian velocity distribution of the electrons. A generally accepted criterion for the density above which LTE holds,

is that the collisional population rate be an order-of-magnitude larger than the radiative population rate.¹³⁶ When this condition exists for all states of an ion, then complete LTE exists. The condition for complete LTE can be estimated by:

$$N_e \geq 9 \times 10^{17} \left(\frac{E_2^{z-1}}{E_H} \right)^3 \left(\frac{kT}{E_H} \right)^{1/2} \text{ (cm}^{-3}\text{)} \quad (\text{A.5})$$

where N_e is the electron density, k is the Boltzmann constant, T is the electron temperature, E_H is the ionization energy of hydrogen, and E_2^{z-1} is the excitation energy of the resonance transition. When this condition is fulfilled, the relative populations of the various levels of a particular ionization state can be determined from the corresponding Boltzmann factor and the partition function:

$$\frac{N_n^{z-1}}{N^{z-1}} = \frac{g_n \exp(-E_n / kT)}{Z(T)} \quad (\text{A.6})$$

where N^{z-1} is the total population of the ion with charge $z-1$, N_n^{z-1} is the excited-state population of a particular level n , g_n is the degeneracy of level n , E_n is the energy of the level, and $Z(T)$ is the partition function. The partition function is a measure of the number of states available in an ion at a particular temperature. It can be evaluated from:

$$Z(T) = \sum_n g_n \exp(-E_n / kT) \quad (\text{A.7})$$

where the symbols have been defined previously. To evaluate the partition function, various approximations have been used to overcome the divergence of the summation.¹³⁷ The Boltzmann relationship can be extended to relate the population of a particular ionization state to

the next higher ionization state and to the electron density.¹⁴³ This relationship is given by the Saha equation:

$$\frac{N_e N^z}{N^{z-1}} = \frac{2Z^z(T)}{Z^{z-1}(T)} \left(\frac{2\pi m k T}{h^2} \right)^{3/2} \exp \left(- \frac{E_\infty^{z-1} - \Delta E_\infty^{z-1}}{kT} \right) \quad (\text{A.8})$$

where m is the electron mass, h is Planck's constant, E_∞^{z-1} is the ionization energy, and ΔE_∞^{z-1} is the lowering of the ionization energy, which is defined below. All other symbols have been defined previously. The reduction of the ionization energy ΔE_∞^{z-1} of a particular ionization state accounts for the energy released when an electron-ion pair is immersed in a plasma. It is given by:

$$\Delta E_\infty^{z-1} = \frac{ze^2}{4\pi\epsilon_0\rho_D} \quad (\text{A.9})$$

where z is the charge seen by the electron for which the ionization energy is reduced (e.g., $z=8$ for Ne VIII), e is the charge of the electron, ϵ_0 is the permittivity of free space, and ρ_D is the Debye radius. The Debye radius represents a distance beyond which the potential of the individual charged particles in a plasma are exponentially reduced below the Coulomb potential. It is given by:

$$\rho_D = \left(\frac{\epsilon_0 k T}{e^2 (N_e + \sum_z z^2 N^z)} \right)^{1/2} \quad (\text{A.10})$$

for a single species plasma. The summation is over all charge states in the plasma and should be extended to include all atomic species for a multicomponent plasma.

The condition for LTE requires extremely large electron densities and is difficult to achieve in laboratory plasmas. The electron-

collisional-transition rates and the radiative-transition rates have different dependences on the energy of the levels involved in the transition. The density at which a particular energy level, described by its principal quantum number n , is in equilibrium with all higher levels depends on the energy of that level. A level described by principal quantum number n is said to be in partial LTE with all levels of higher principal quantum number when the electron-collisional-population rate from all higher energy levels exceeds the total-radiative-decay rate by an order of magnitude.¹⁴¹ The condition for partial LTE is given by:

$$N_e \geq 7 \times 10^{18} \frac{z^7}{n^{17/2}} \left(\frac{kT}{z^2 E_H} \right)^{1/2} \text{ (cm}^{-3}\text{)} \quad (\text{A.11})$$

where n is the principal quantum number of the transition of interest, and the remaining symbols have the same meanings as described above. For levels that satisfy this density requirement, the population is collisionally coupled to higher levels and to the ground state of the next higher ionization stage. For these levels, another form of the Saha equation can be used, which relates the population of a particular excited level of a particular charge state N_n^{z-1} to the population of the ground state of the next higher ionization state N_1^z .¹³⁸ It is given by:

$$\frac{N_e N_1^z}{N_n^{z-1}} = \frac{2g_1^z}{g_n^{z-1}} \left(\frac{2\pi m k T}{h^2} \right)^{3/2} \exp \left(- \frac{E_n'}{kT} \right) \quad (\text{A.12})$$

where E_n' is the binding energy of the electron in this level.

Another situation in which the atomic physics of the level populations can be greatly simplified is in a plasma of low electron

density in which a coronal equilibrium exists. Here, the electron density is too low for LTE to exist, and radiative decay is important compared to electron collisional excitation for some levels. A comparison can be made between the total electron-collisional-excitation rate from a particular level to all higher levels and the total radiative-decay rate from a particular level to all lower levels. This comparison is similar to the condition for partial LTE except that the rates are equal rather than different by an order of magnitude. Equating these rates provides an estimate of the principal quantum number n' above which collisional ionization is more likely and below which radiative decay is more likely. This value of n' is referred to as the "collision limit", and may be approximated by:

$$n' \approx 1.26 \times 10^2 \left(\frac{z^7}{N_e} \right)^{2/17} \left(\frac{kT}{z^2 E_H} \right)^{1/17} \exp \left(\frac{4z^2 E_H}{17n'^3 kT} \right) \quad (\text{A.13})$$

where the symbols have their standard meanings.¹³⁹ The value of n' in the exponential in Eq. A.13 usually can be approximated so that the equation can be solved by iteration. Ionization balance is determined by equating the effective ionization rate and the effective recombination rate. The effective ionization rate is determined by direct ionization and electron collisional excitation from levels below n' to levels above n' . The effective recombination rate is determined from actual recombination rates and from radiative and collisional rates from levels above n' to levels below n' . This ionization balance is expressed by:

$$\frac{N^2}{N^2-1} = \frac{S}{\alpha} \quad (\text{A.14})$$

where S is the collisional-radiative ionization coefficient and α is the collisional-radiative recombination coefficient.¹⁴⁰ An important point to note is the lack of dependence on electron density. The rate coefficients depend on the energy levels involved and on the electron temperature, but not on the electron density. Other models based on the coronal relation may vary in the detailed ionization and recombination rates used, however the lack of dependence on electron density is common to all coronal models.^{48,140-142} The excited-state populations of levels below the collision limit of a particular ionization state are determined by a balance between the collisional excitation rate from the ground state and the total rate of spontaneous decay.¹⁴³ This can be expressed as:

$$N_g^{z-1} C_{ng}^{z-1} = N_n^{z-1} \sum_{m < n} A_{nm} \quad (\text{A.15})$$

where C_{ng}^{z-1} is the collisional transition rate per atom as described below, and A_{nm} is the transition probability from state n to state m . The summation is taken over all levels less than n . An expression for the collisional excitation rate is given by:

$$C_{ng}^{z-1} = \frac{9 \times 10^{-8}}{z^3} f_{ng} N_e \left(\frac{z^2 E_H}{\Delta E} \right) \left(\frac{z^2 E_H}{kT} \right)^{1/2} \exp \left(- \frac{\Delta E}{kT} \right) \quad (\text{A.16})$$

where f_{ng} is the oscillator strength, and ΔE is the energy of the transition.¹⁴⁴

Techniques for determining level populations and ionization balance have been discussed for two situations where simplifications in the atomic physics can be made. For low-density plasmas, levels below the collision limit can be modeled using the conditions for

coronal equilibrium. Ionization balance is determined by collisional ionization and radiative recombination, and the population of a particular level is determined by the excitation rate from the ground state and by the sum of transition probabilities to all lower levels. For high-density plasmas in total LTE, level populations are determined by their Boltzmann factors, and ionization balance is determined from the Saha equation. For energy levels in partial LTE, the population relative to the ground state of the next higher ionization state can be determined from the Saha equation. For intermediate densities a collisional-radiative model must be used which includes the rates of the various processes which determine ionization balance and level population.

A.2 Spectral Emission

Detailed spectral features of the radiation emitted from a plasma can provide information about the conditions in the plasma. Relative intensities of radiation at different energies can be used to determine relative populations of the levels from which this radiation originated. Absolute intensity measurement provide an absolute measure of populations of the corresponding levels. When compared with a model of the populations of various levels based on an electron temperature and electron density, an estimate of these plasma parameters can be made. The profile of characteristic radiation emitted by transitions between energy levels can also be used to determine properties of the plasma at the location where the radiation was emitted. Motion of emitting ions relative to the observer produces Doppler shifts in the energy of the radiation. Electric

fields associated with charged particles in the plasma cause perturbations in the energy levels of the ions and in the corresponding energy of the radiation produced by transitions between these levels. These effects cause a broadening of the characteristic line radiation, and this broadening depends on the temperature and density of the plasma.

A.2.1 Line Intensity

The total intensity of a spectral line emitted from a plasma, integrated over the entire line shape, is given by:

$$\int I_{mn} d\lambda = \frac{2\pi h c^2 r_0}{\lambda_{mn}^3} f_{mn} \frac{g_n}{g_m} \int N_m dx = \frac{E_{nm} A_{nm}}{4\pi} \int N_m dx \quad (A.17)$$

where λ_{mn} is the wavelength of the transition, E_{nm} is the energy, f_{mn} is the oscillator strength, A_{nm} is the transition probability, c is the speed of light, r_0 is the classical electron radius, and N_m is the population of the upper level.¹⁴⁵ The integral over the population of the upper level is taken along the line of sight. If this population is constant along the line of sight or a line-average value is sufficient, then the integral may be replaced by the product of the density and the spatial dimension of the source. If not, then a spatially-resolved emission profile must be inverted to determine the spatial distribution of the upper-state density.^{146,147} The integral over the wavelength must include the entire spectral line, or errors in the intensity may occur.¹⁴⁸ Therefore, knowledge of the line width is necessary to ensure that the entire line is included. This assumes that the line of interest is optically thin. The optical depth of the

line should be estimated to determine if this assumption is valid.

The optical depth τ of the resonant line of a particular ionization state that is Doppler broadened is given by:

$$\tau(\omega_0) \approx 3 \times 10^{-9} \left(\frac{A E_H}{kT} \right)^{1/2} \lambda_{mn} f_{mn} N_n^{Z-1} d \quad (\text{A.18})$$

where A is the atomic weight, N_n^{Z-1} is the lower-level density, and d is the optical path length.¹⁴⁹ If the line broadening is larger than that caused by Doppler broadening, then the optical depth in Eq. A.18 must be multiplied by the ratio of the Doppler broadening to the actual broadening. Techniques to estimate these broadening mechanisms are discussed below.

A.2.2 Line Broadening

The measured profile of the characteristic radiation from a plasma is determined by a combination of three factors: (1) the conditions present in the plasma where the radiation is emitted, (2) the path traveled by the radiation to the detector, and (3) the response of the detector. If these factors can be unfolded, the profile can be used to estimate conditions in the plasma by comparing the profile with various line-broadening theories. In situations where the profile is determined primarily by one factor, the unfolding can be simplified considerably. The primary broadening mechanisms in high-temperature high-density plasmas are Doppler broadening due to ion temperature and Stark broadening due to density. Reabsorption of radiation in the plasma modifies the line profile and can lead to opacity broadening. The theory of these broadening mechanisms will be

discussed, and techniques to estimate the conditions under which they are important will be presented.

The frequency of radiation emitted by a system moving relative to the observer is Doppler shifted by an amount proportional to the relative velocity. Because of this, the profile of radiation emitted by particles in a plasma is determined by the velocity distribution of the particles. If the profile of a spectral line emitted by ions with a thermal velocity distribution is determined solely by Doppler broadening, then the resulting profile is Gaussian, and the width can be determined from:

$$w_{\lambda} = \left(\frac{2 k T_i \ln 2}{M c^2} \right)^{1/2} \lambda_o \quad (\text{A.19})$$

where w_{λ} is the half-width at half-maximum, M is the ion mass, T_i is the ion temperature, and λ_o is the central wavelength of the transition.¹⁵⁰ A measure of this width can be used to determine the plasma ion temperature. If unresolved macroscopic motion is present, Doppler broadening may also result in a Gaussian line shape with a width determined by:

$$w_{\lambda} = \left[\left\{ \left(\frac{v_r}{c} \right)^2 \right\}_{av} \ln 2 \right]^{1/2} \lambda_o \quad (\text{A.20})$$

where v_r is the mean velocity of relative motion along the line of sight. This width does not reflect the ion temperature and care must be taken not to interpret this type of broadening as such.

Atoms and ions in a plasma are influenced by the electric field produced by the other ions and electrons. The energy levels of atoms or ions are perturbed by this electric field. This causes energy-

level shifts and a corresponding change in the energy of radiative transitions. The energy-level shift due to an electric field is known as the Stark effect. The nature of this change depends on the strength of the field and the structure of the atom or ion. A discussion of the effects of these electric fields is usually divided into two parts because the nature of the effects is different for electrons and ions. For ions, the quasistatic approximation is generally used. The ions are assumed to be static, and effects on the radiating system by the static field of the ions are considered. For electrons, the impact approximation is generally used. In this approximation, the effects of collisions between electrons and the radiating system are considered. The general calculation involves a combination of these two approximations. The impact approximation is used to calculate the effect of a collision between an electron and a radiating system. The radiating system is under the influence of the static field of the ions (in the quasistatic approximation). Then the line profile is determined by averaging over various impact parameters and velocities for the collisions (under the impact approximation) and various static field strengths (under the quasistatic approximation). A qualitative discussion of the contributions of these two approximations follows. The static field of the ions produces a shift or splitting of the energy levels due to the Stark effect. The separation of these various "Stark levels" depends on the electric-field strength. For hydrogenic radiators, this dependence is linear with field strength and is referred to as the "linear Stark effect". For non-hydrogenic radiators, the shift depends, to lowest order, on the square of the field strength and is referred to as the "quadratic Stark effect". Collisions between the radiating system and electrons

effectively reduce the lifetime of excited levels. This reduction produces an increase in the uncertainty in energy of the excited level due to the uncertainty principle. This energy uncertainty is manifested in a "collisional broadening" of the line radiation. In many situations the resulting line profile can be represented by a Lorentzian line shape. The result of splitting one level into several levels and the subsequent broadening of these levels produces a line shape that depends upon both electron and ion densities. If the dependence of the line shape on electron and ion density is known, a line-shape measurement can be used to determine the density. This density dependence is not simple and has been the topic of considerable research.¹⁵¹ Because line-broadening calculations depend on the particular energy levels involved, no general theory for all transitions is available.¹⁵² Specific calculations pertaining to transitions of interest will be discussed where appropriate.

A general theory of Stark broadening has been developed to describe the merging of a spectral-line series as the ionization limit is approached. As the principal quantum number of transitions in a particular series increases, the separation in energy between the transitions decreases. Also, as the principal quantum number increases, line broadening due to the Stark effect increases. Therefore, for a given density there is a principal quantum number above which the separation between spectral lines is equal to or less than the width of the lines. For transitions above this limit, the lines become merged and appear as continuum. This results in an apparent advance of the series limit, known as the Inglis-Teller limit. For hydrogenic ions the advanced series limit, in terms of the last discernible line of a series n_s^{z-1} , is given by:

$$n_s^{z-1} \approx \frac{1}{2} \left(\frac{z^9}{a_0^6 N_e^2} \right)^{1/15} \quad (\text{A.21})$$

where a_0 is the Bohr radius (0.53 Å).¹⁵³ This relation can also be expressed in terms of the ionization energy of the level described by the principal quantum number n_s^{z-1} :

$$\Delta E_s^{z-1} = 4 z^{4/5} (a_0^3 N_e)^{4/15} E_H \quad (\text{A.22})$$

In general, the profile of a particular line will be influenced by both Doppler and Stark broadening. The contributions of both broadening mechanisms must be determined before quantitative comparisons with theory can be made. Contributions from both broadening processes must be folded together by means of a convolution integral. In the situation where Doppler and Stark broadening can be represented by Gaussian and Lorentzian line shapes, respectively, the convolution integral results in a Voigt profile.^{125,126}

The response of the spectrograph must also be considered before interpreting a measured profile. This is typically done by measuring the apparent width of a line from a low-pressure lamp or laser because these sources produce lines with widths below the resolution of most instruments. This apparent width or the corresponding instrument function is folded with the other broadening mechanisms. To obtain meaningful measurements the instrument function should be narrow compared with the other broadening mechanisms. In this case, assuming a Gaussian line shape for the instrument function does not result in significant errors. For a Gaussian instrument function and a Doppler profile, the folding is straightforward because the convolution of two Gaussian functions is a Gaussian function with a width determined by

the root of the sum of the squares of the individual widths. The total width is used to determine the final profile.

If the optical depth of the plasma is less than unity for a particular transition, then the plasma is optically thin for that transition, and the intensity and shape of the line can be interpreted in terms of the upper-level population and line-broadening processes. If the optical depth is greater than unity, the plasma is optically thick and the emitted intensity is not representative of the line-integrated upper-level density. Also the line shape will be distorted due to re-absorption at and near the wavelength of peak intensity. For large optical depth this will produce an apparent broadening of the line which can be estimated by:

$$\Delta\lambda_{\tau} = 2 \Delta\lambda (\tau)^{1/2} \quad (\text{A.23})$$

where $\Delta\lambda_{\tau}$ is the half-intensity width of the opacity-broadened line, and $\Delta\lambda$ is the optically-thin half-intensity width of a Lorentzian profile.³

A.2.3 Continuum Intensity

The radiation emitted from a plasma consists not only of line radiation, but also of continuum radiation arising from free-electron transitions. If the continuum radiation is due a transition between two free states, it is referred to as bremsstrahlung radiation. If the continuum radiation is due to a transition between a free state and a bound state, it is referred to as recombination continuum. In both cases, the transitions involve ions (or atoms) in the plasma, and

the total emission is determined by summing contributions from the various ionization states. The continuum emission ϵ_{ff}^z (energy per unit volume, time, solid angle, and frequency interval) for a particular ionization state due to free-free transitions is given by:

$$\epsilon_{ff}^z = \frac{16 (\alpha a_0)^3 z^2 E_H^{3/2} g_f}{(9\pi kT)^{1/2}} N_e N^z \exp\left(\frac{z^2 E_H / n_1^2}{kT}\right) \times \exp\left(\frac{-\Delta E_{\infty}^{z-1} - h\nu}{kT}\right) \quad (A.24)$$

where α is the fine structure constant, g_f is a correction due to non-classical behavior (Gaunt factor), $h\nu$ is the energy of the radiation, and n_1 is the principal quantum number of the series limit (Eq. A.21).¹⁵⁴ The continuum emission ϵ_{fb}^z for a particular ionization state due to free-bound transitions is given by:

$$\epsilon_{fb}^z = \frac{32\pi (\alpha a_0)^3 z^4 E_H^{5/2}}{(3\pi kT)^{3/2}} N_e N^z \exp\left(\frac{-\Delta E_{\infty}^{z-1} - h\nu}{kT}\right) \times \left[\sum_n \frac{N_1^z}{N^z} \frac{g_{n1}^z}{n^3} \exp\left(\frac{E_{\infty}^{z-1} - E_{n1}^{z-1}}{kT}\right) + \sum_n' \frac{g_n^z}{n^3} \exp\left(\frac{z^2 E_H}{n^2 kT}\right) \right] \quad (A.25)$$

where the factors g_{n1}^z and g_n^z are Gaunt factors and depend on the energy of the emitted radiation. The factors E_{∞}^{z-1} and E_{n1}^{z-1} are the ionization energy and excitation energy, respectively. The limits on the sums depend on the energy of the radiation for which the emission is being calculated. The only levels included in these sums are levels with excitation energies larger than the difference between the effective ionization energy and the energy of the photon of interest. This can be expressed as:

$$E_{nl}^{z-1} \geq (E_{\infty}^{z-1} - \Delta E_s^{z-1}) - h\nu \quad (\text{A.26})$$

where the effective ionization energy has been defined as the ionization energy minus the advance of the series limit (Eq. A.22). For non-hydrogenic ions, the g_{nl} in the first sum also correct for non-hydrogenic behavior, and the sum is then over states with $n < 4$ that fulfill the above requirement. If there are no such states, this sum is omitted. The lower limit of the second sum is $n=4$ unless that state does not fulfill the above requirement. In that case the lower limit is the first level that does fulfill the requirement. The upper limit of the second sum is determined by the advanced series limit (Eq. A.21). Both quantities ϵ_{ff}^z and ϵ_{fb} are in units of angular frequency interval. To transform to wavelength interval, they must be multiplied by $2\pi c/\lambda^2$. Then the dimensions become energy per unit volume, time, solid angle, and wavelength interval.

Appendix B

MODELING OF DYNAMIC IMPLOSIONS

An investigation was made to determine the driving current and mass load required to implode a neon gas puff and produce a 50 to 100 eV plasma with an ion density of 10^{18} to 10^{19} cm⁻³. The motivation is to produce an optimum neon plasma for photopumping with radiation from a nearby sodium plasma. A 0-D implosion code, used previously to simulate neon and argon implosions on the Gamble II generator, was modified for this study. Resistive effects, which were added to the code, produced a hotter initial plasma and a smaller peak density for the imploded plasma. The optimum parameters to obtain the desired plasma conditions were driving currents of 120 to 240 kA and mass loads of 3 to 9 μ g/cm for an initial gas-puff radius of 6 mm. For a 3-mm initial radius, either more mass or less current was required to achieve the same plasma conditions. For a 9-mm initial radius, less mass or more current was required to achieve these plasma conditions.

B.1 Applicability of the Original Code

A 0-D implosion code was developed and used to simulate neon Z-pinch implosions on the Gamble II generator and to predict X-ray outputs of these plasma radiation sources.⁸⁰ Megampere level currents

were used to implode annular gas puffs with linear mass densities of 30 to 50 $\mu\text{g}/\text{cm}$. Imploded plasma temperatures of 300 to 800 eV and ion densities of 10^{20} cm^{-3} were predicted. An example of time histories of temperature and ion density for a 42- $\mu\text{g}/\text{cm}$ neon implosion driven by Gamble II with a peak voltage of 3.0 MV is given in Fig. B.1(a). Time histories of K-shell and L-shell radiation outputs are given in Fig. B.1(b). The results of similar calculations for mass loads of 35 $\mu\text{g}/\text{cm}$ and 50 $\mu\text{g}/\text{cm}$ are given in Table B.1. These results will be compared with calculations which include resistive heating in Sec. B.2.

It was desired to use this code to study the implosions of a solid cylinder of neon with smaller driving current and mass loads. Since the original code was used to simulate implosions of annular gas puffs, the effect of increasing the width of the annular region to model a solid puff was investigated. The relevant parameters for the annular geometry are illustrated in Fig. B.2, where A is the outer radius of the puff, W is the width of the annulus, and R is the radius of thermalization. The radius of thermalization is an artificial distance introduced into the calculation to establish the point at which the kinetic energy of the imploding ions is converted into internal energy. When the inner radius of the annulus becomes equal to the radius of thermalization ($A - W = R$), the ion kinetic energy in the imploding annulus is converted into internal energy of the plasma and the plasma temperature increases. An initial radius of 1.0 cm and a width of 0.3 cm were used for the calculations presented in Figs. B.1(a) and B.1(b). Attempts were made to investigate the effect of increasing this width. For a 0.45-cm width the implosion produced a plasma of unrealistically high density. Increasing the

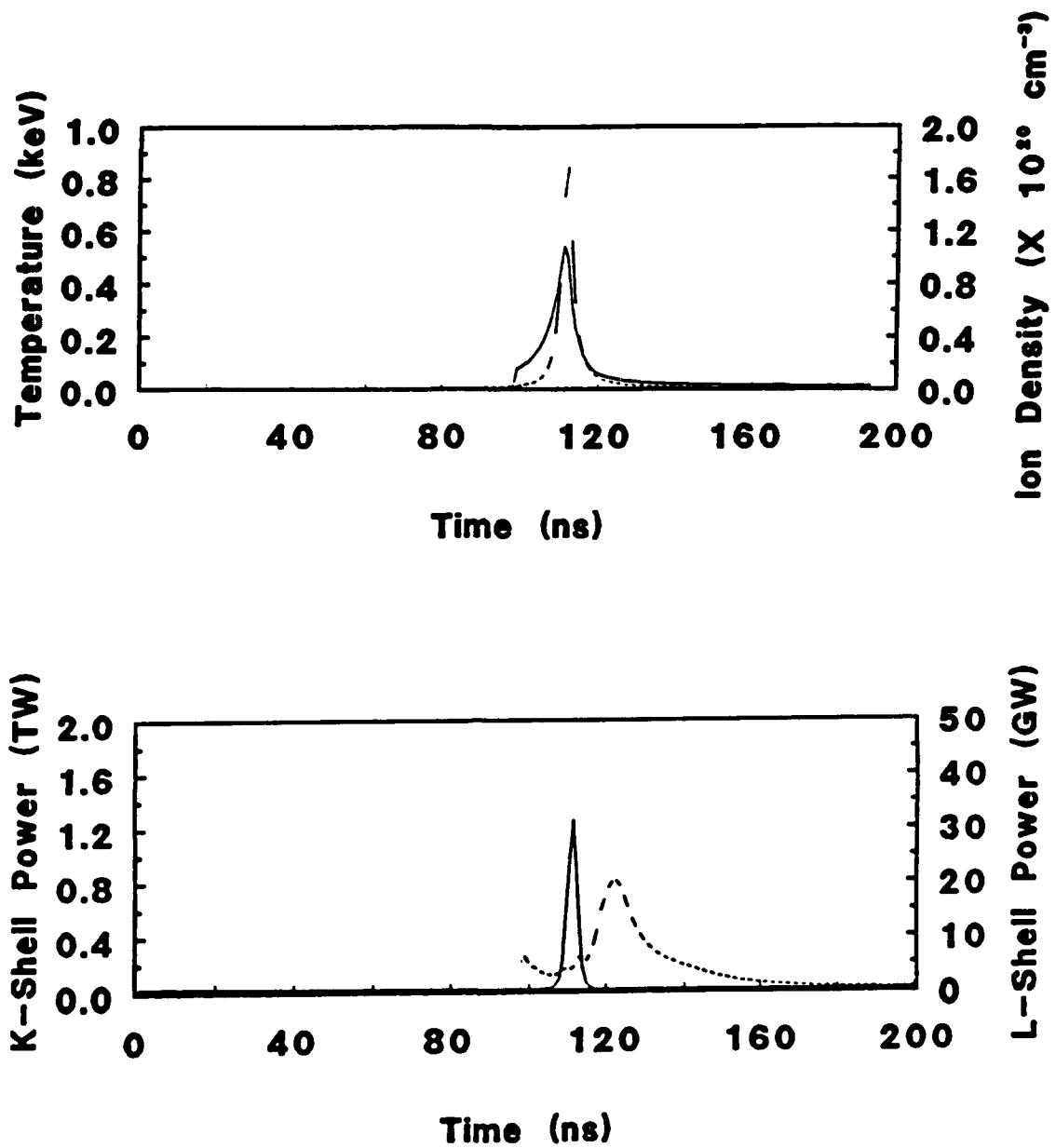


FIG. B.1. (a) Calculated time histories of temperature (solid) and density (dashed) and (b) K-shell (solid) and L-shell (dashed) radiation for an implosion on Gamble II with 3-MV peak voltage.

Mass Load (ug/cm)	Temp. (ev)	Ion Density (1/cm ³)	K Shell (KJ)	(GW)
35	858	1.2e20	1.9	422
42	532	1.6e20	4.2	1250
50	357	1.9e20	4.4	1270

Table B.1. Comparison of temperature, density, and radiation for various mass loads without resistance (I=1.25 MA, A=1.0 cm, W=0.3 cm).

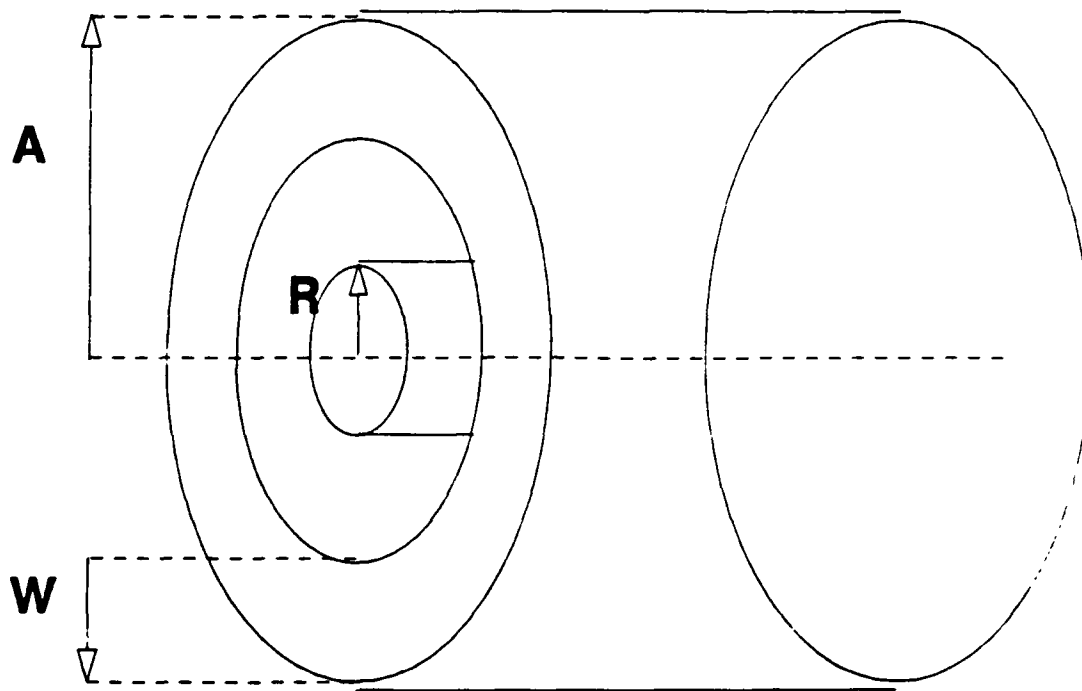


FIG. B.2. Annular gas-puff geometry with outer radius A , width W , and radius of thermalization R .

width to 0.6 cm caused the calculation to terminate when the outer radius of the implosion decreased to less than a preset (unphysical) value of 0.001 cm.

Code calculations were carried out successfully for different annular widths by reducing the peak voltage associated with the Gamble II waveshape to 0.75 MV. The width W was varied from 0.1 to 0.4 cm while the outer radius A and radius of thermalization R remained fixed at 0.6 cm and 0.05 cm, respectively. The peak temperatures and ion densities for this calculation for a 20 $\mu\text{g}/\text{cm}$ mass load and 300 kA peak current are shown in Fig. B.3(a). As the width increases from 0.1 to 0.4 cm, the temperature increases a factor of two and the density increases a factor of 17. When the radius of thermalization was varied the peak temperature and ion density changed less, as shown in Fig. B.3(b) for a mass load of 30 $\mu\text{g}/\text{cm}$. This larger mass load was used to prevent the calculation from terminating as the radius of thermalization R was varied. As R increased from 0.02 to 0.10 cm, the peak temperature increases only 17% and the density increases a factor of 7.

B.2 Modification of the Code

Resistive effects were not included in the original code because most of the heating in megampere-driven implosions is from thermalization of kinetic energy of the implosion. For calculations at lower current levels, which would be more appropriate for preparing a neon laser for photopumping, the run-in kinetic energy produced a small core temperature, and the implosion resulted in an unrealistic small-radius, high-density plasma. In order to account for resistive

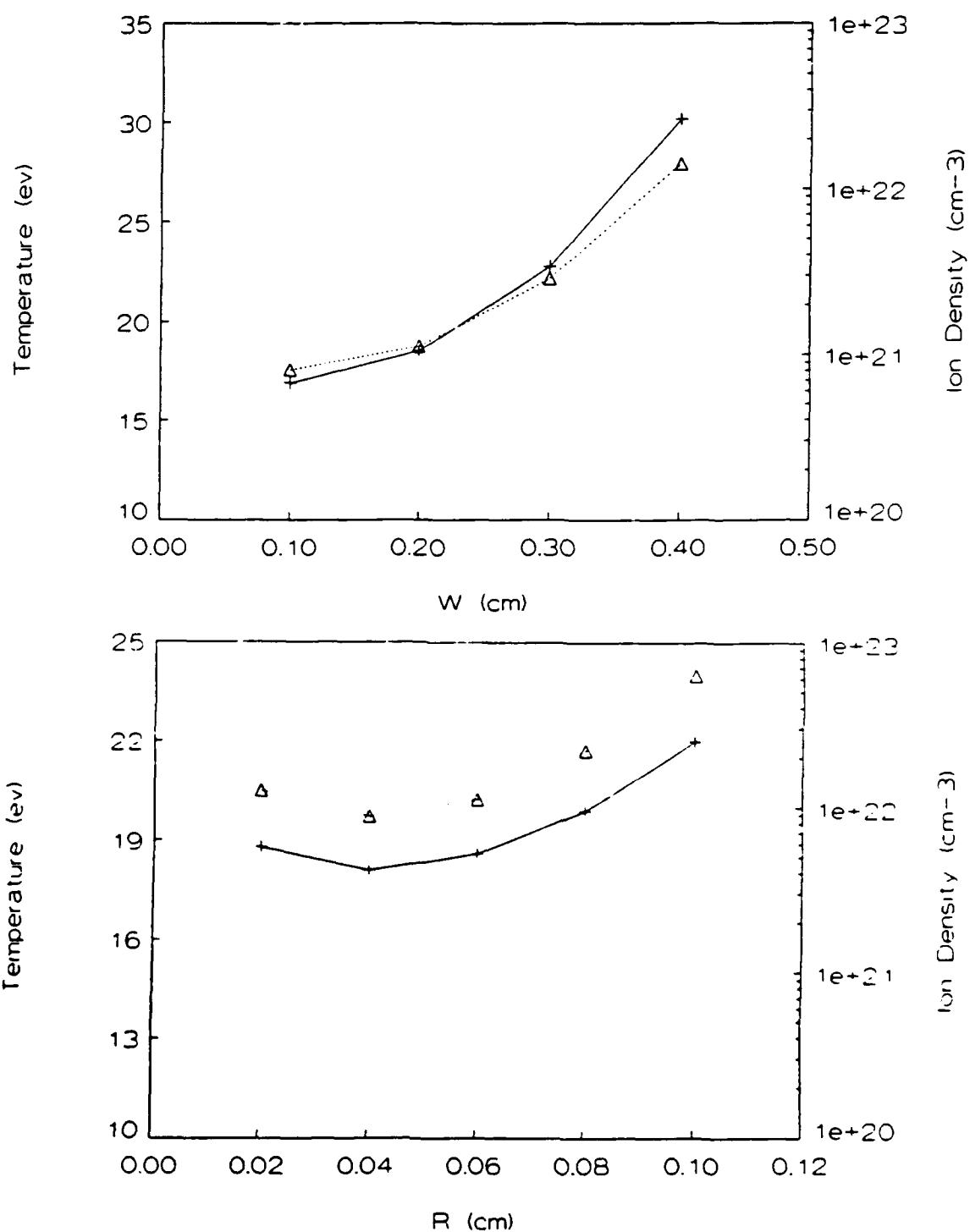


FIG. B.3. Peak temperatures (solid) and ion densities (dashed) for various (a) widths W ($I=300$ kA, $M=20$ $\mu\text{g}/\text{cm}$, $R=0.5$ cm, $A=0.6$ cm) and (b) thermalization radii R ($I=300$ kA, $M=30$ $\mu\text{g}/\text{cm}$, $W=0.5$ cm, $A=0.6$ cm).

heating of the plasma, Spitzer resistivity was added to the power-balance equation according to:

$$dE/dt = P_w + P_\eta - P_R, \quad (B.1)$$

where dE/dt is the change in total internal energy of the core per unit time, P_w is the compressional work done per unit time, P_η is the power added from resistive effects, and P_R is the power lost due to radiation. The resistive power is given by:

$$P_\eta = I^2 R = I^2 \frac{\eta L}{A}, \quad (B.2)$$

where $\eta = 1.03 \times 10^{-2} Z \ln \Lambda / T_e^{3/2}$ is the resistivity¹⁵⁵ with $\ln \Lambda$ being the Coulomb logarithm (see Eq. 3.4). With resistive heating, the total energy of the plasma is increased early in time and the temperature prior to implosion is correspondingly higher. This results in a smaller, more realistic peak density and a correspondingly larger final radius at implosion. Examples of time histories of the temperature and ion density for an implosion driven by the Gamble II waveshape with a peak voltage of 3.0 MV are given in Fig. B.4(a) for a mass load of 42 $\mu\text{g}/\text{cm}$. Time histories of the L-shell and K-shell radiation are given in Fig. B.4(b). These results can be compared with similar results in Figs B.1(a) and B.1(b) to see the effect of including resistive heating. The same results for mass loads of 35 $\mu\text{g}/\text{cm}$ and 50 $\mu\text{g}/\text{cm}$ are given in Table B.2 and can be compared with those of Table B.1.

The effect of the width of the annulus on the peak temperature and ion density was investigated with resistive heating included in the analysis. The results, presented in Fig. B.5(a), show that the peak temperature increased by more than a factor of two and the ion

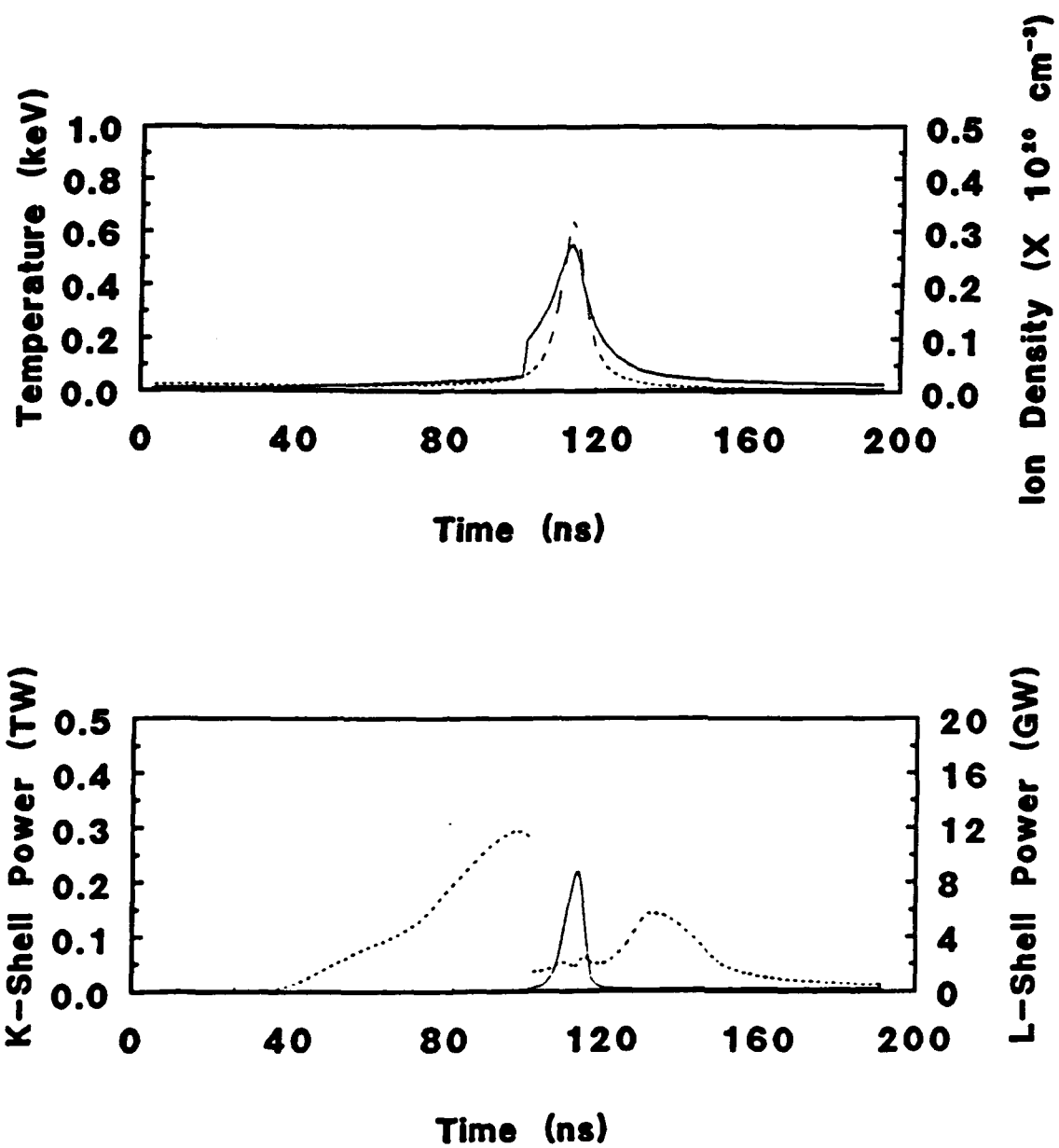


FIG. B.4. Calculated time histories of (a) temperature (solid) and density (dashed) and (b) K-shell (solid) and L-shell (dashed) radiation for an implosion on Gamble II with 3-MV peak voltage.

Mass Load (ug/cm)	Temp. (ev)	Ion Density (1/cm ³)	K Shell (KJ)	Shell (GW)
35	766	2.8e19	1.1	109
42	536	3.1e19	1.8	220
50	374	3.1e19	2.0	263

Table B.2. Temperatures, densities, and radiation for various masses with resistance. (I=1.25 MA, A=1.0 cm, W=0.3 cm)

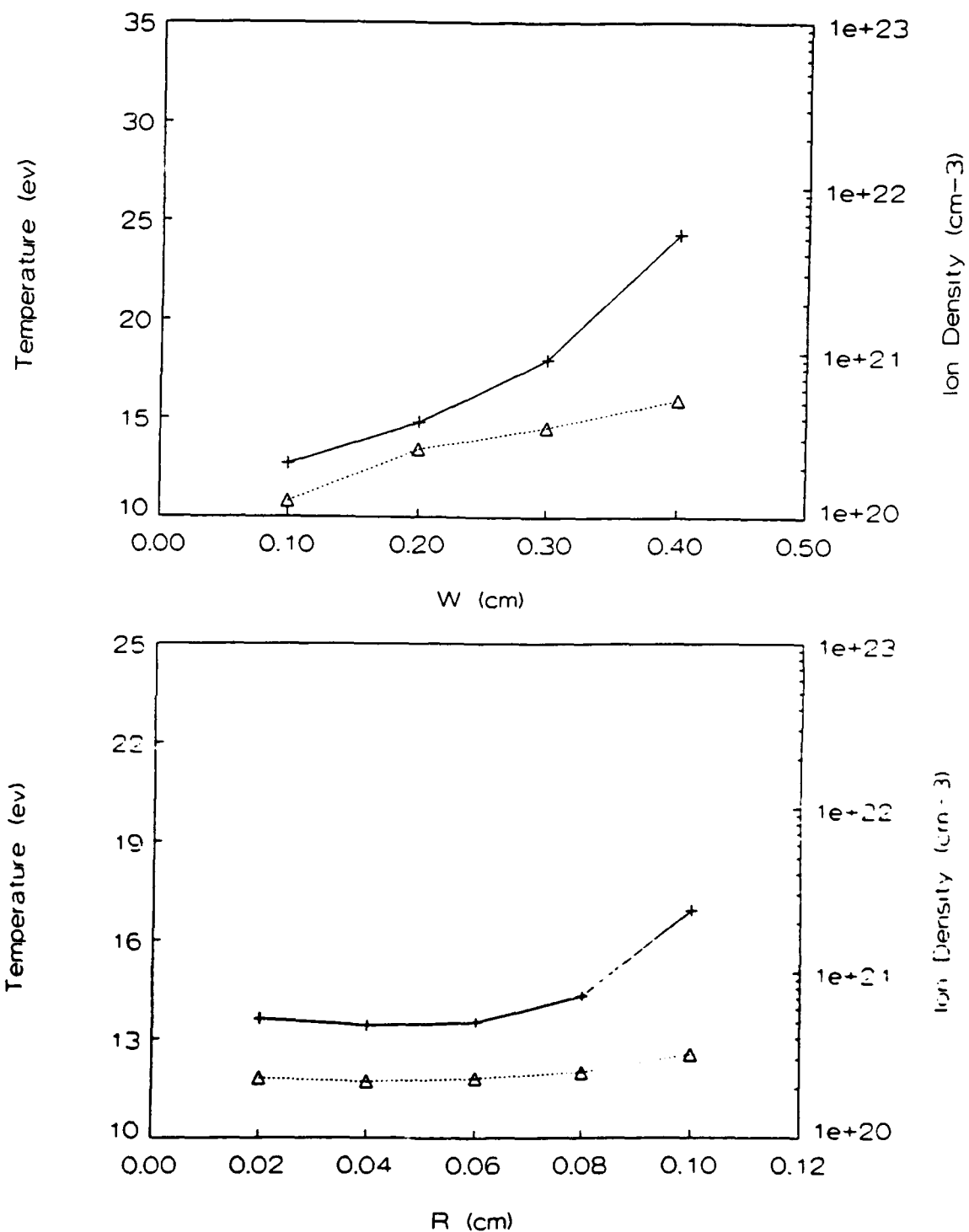


FIG. B.5. Peak temperature (solid) and ion density (dotted) for various (a) widths W ($I=300$ kA, $M=20$ $\mu\text{g}/\text{cm}$, $R=0.05$ cm, $A=0.6$ cm) and (b) thermalization radii R ($I=300$ kA, $M=30$ $\mu\text{g}/\text{cm}$, $W=0.5$ cm, $A=0.6$ cm).

density increased by a factor of 7 as the width was varied from 0.1 to 0.4 cm. Over this range of widths, the final density is reduced by a factor of 5 to 30 compared with results without resistive heating. This indicates that resistive heating early in time produces a plasma which does not implode to as small a radius due to increased internal pressure throughout the implosion.

The effect of changing the radius of thermalization on the peak temperature and density is shown in Fig. B.5(b). The peak temperature varied by 24% and the peak density varied by a factor of 1.5 as the radius of thermalization was changed from 0.06 to 0.1 cm. When the radius of thermalization was decreased below 0.06 cm, there was little change in the temperature or ion density.

B.3 Optimization

To achieve conditions of optimum gain for the $n=3$ to $n=4$ singlet lines of heliumlike neon in a plasma photopumped by 11-Å radiation from a sodium plasma, temperatures of 50 to 100 eV and ion densities of 10^{18} to 10^{19} cm^{-3} have been predicted to be required for the neon plasma.⁶ To achieve these conditions in an imploding neon Z-pinch, an investigation into the appropriate driving current and mass load was made. Also, effects of variations of the risetime of the driving current, the width of the annulus, and the initial radius of the neon plasma were investigated.

The current driving the implosion was varied indirectly by changing the charging voltage of the capacitor bank. This approach models the experimental conditions because the current in the plasma depends on the changing inductance and resistance of the plasma during

the current pulse. The waveshape used is a fit to the normal Gamble II generator waveshape which rises to a peak in 70 ns. The mass load and charging voltage are input parameters to the code. Mass loads of 1 to 14 $\mu\text{g}/\text{cm}$ and charging voltages corresponding to peak currents ranging from 95 to 275 kA were used. The current risetime was varied indirectly by changing the timescale of the input voltage waveshape. For all of these calculations the ion density and the temperature of the plasma were maximum at the time of implosion.

Calculations were made to establish limits on the mass load and peak driving currents to achieve the desired plasma conditions. Results for an initial radius of 6 mm are presented in Figs. B.6 to B.8. The peak temperature versus the mass load is given in Fig. B.6(a) for seven different driving currents. For each driving current there is a range of mass loads which correspond to peak temperatures of 50 to 100 eV. This relationship between current and mass loading for a 75 ± 25 -eV neon plasma is presented in Fig. B.6(b). To maintain this temperature, the mass load increases with the driving current. In Fig. B.7(a), the ion density at implosion versus the mass load is shown. For larger currents, larger ion densities were produced at implosion. For each current, there is a mass load required to produce a 50 to 100 eV plasma. This mass load produces the peak ion densities given in Fig. B.7(b). This relationship between the driving current and peak density indicates that currents of 120 to 240 kA are required to produce ion densities at implosion of 10^{18} to 10^{19} cm^{-3} . This range of currents restricts the mass load to 3 to 9 $\mu\text{g}/\text{cm}$ (see Fig. B.6(b)).

The voltage waveshape was varied to determine the effect of the current risetime on the relation between the current and mass load at

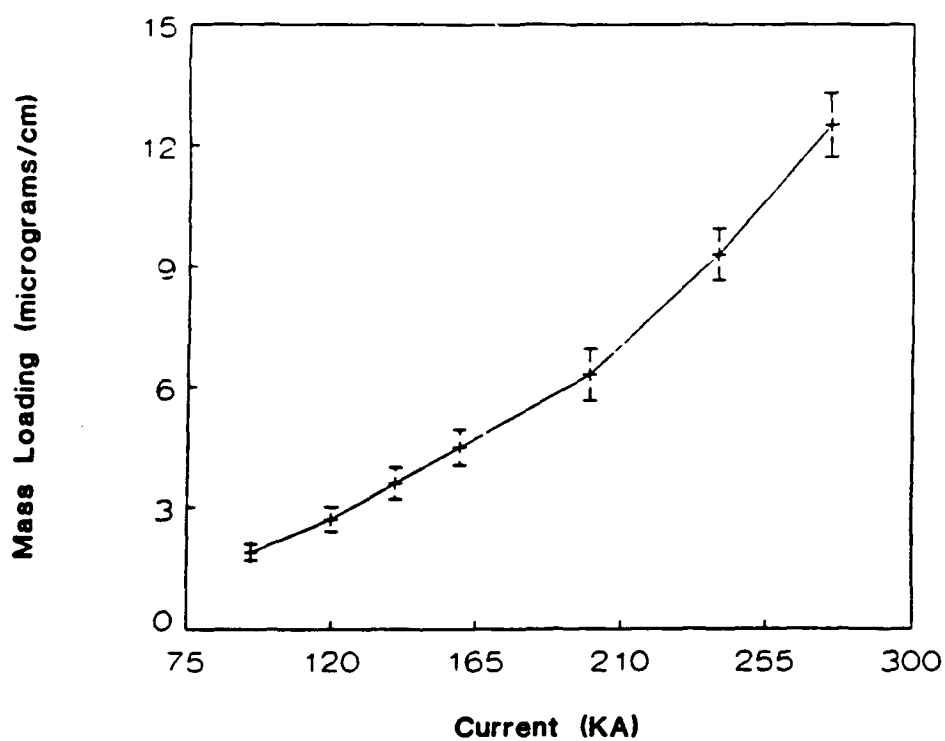
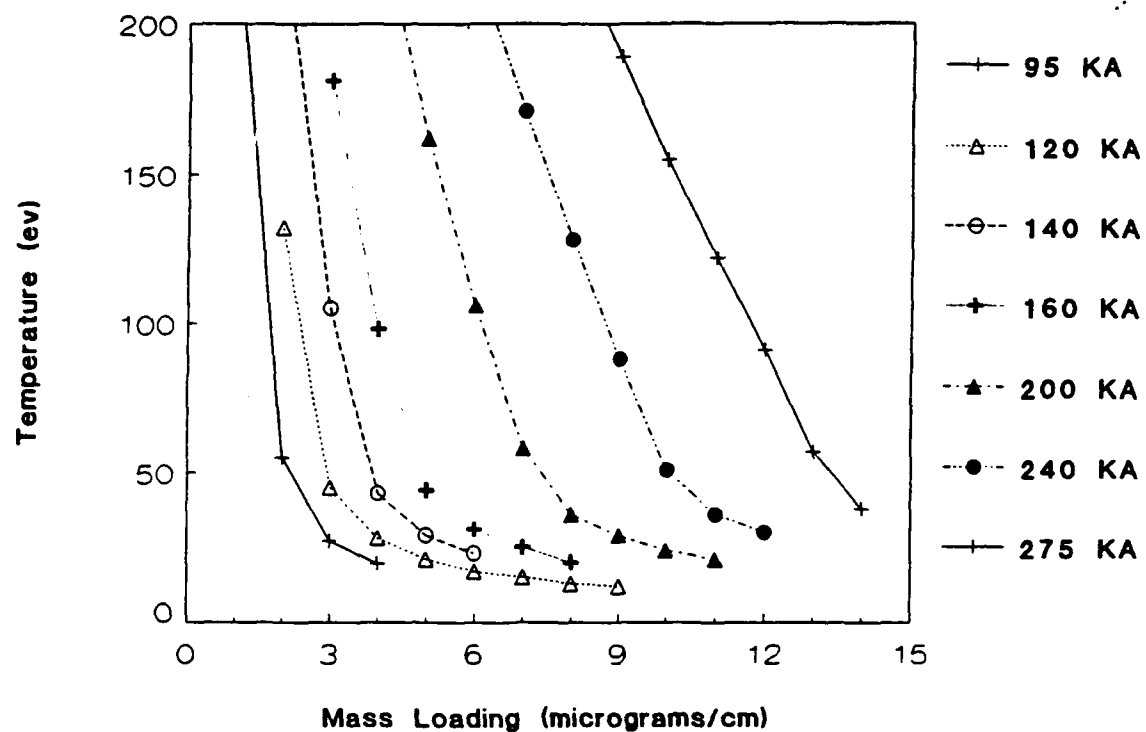


FIG. B.6. (a) Peak temperature versus mass load for various currents and (b) mass load versus current for 50 to 100 eV neon plasma. ($A=0.6$, $W=0.5$, $R=0.07$)

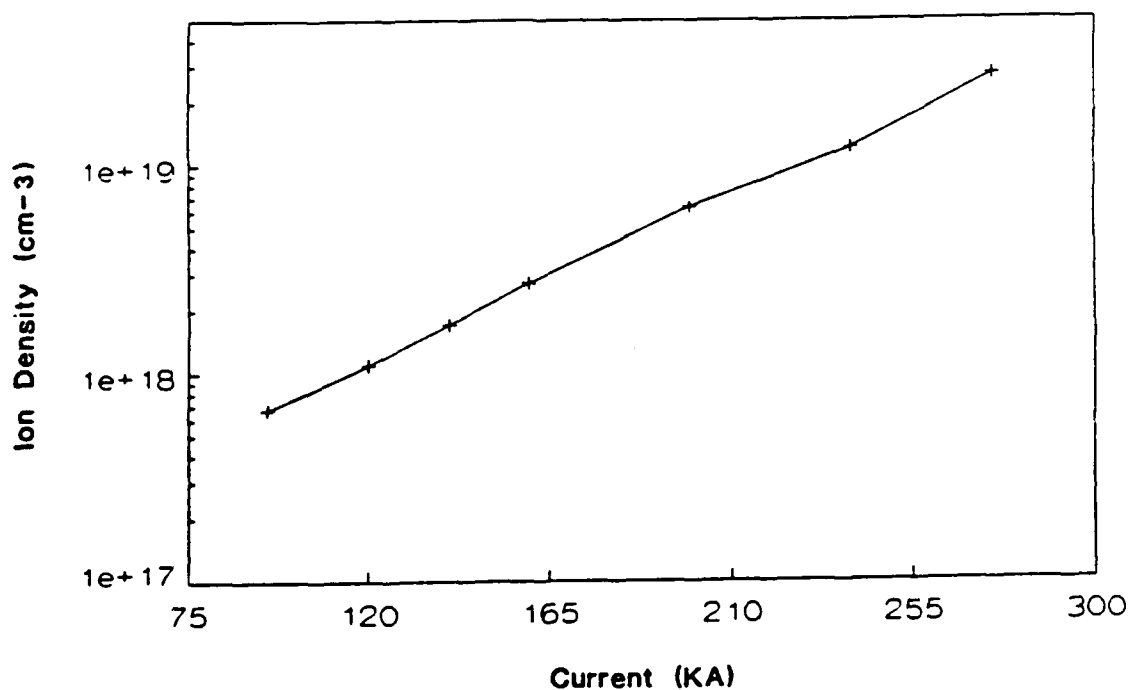
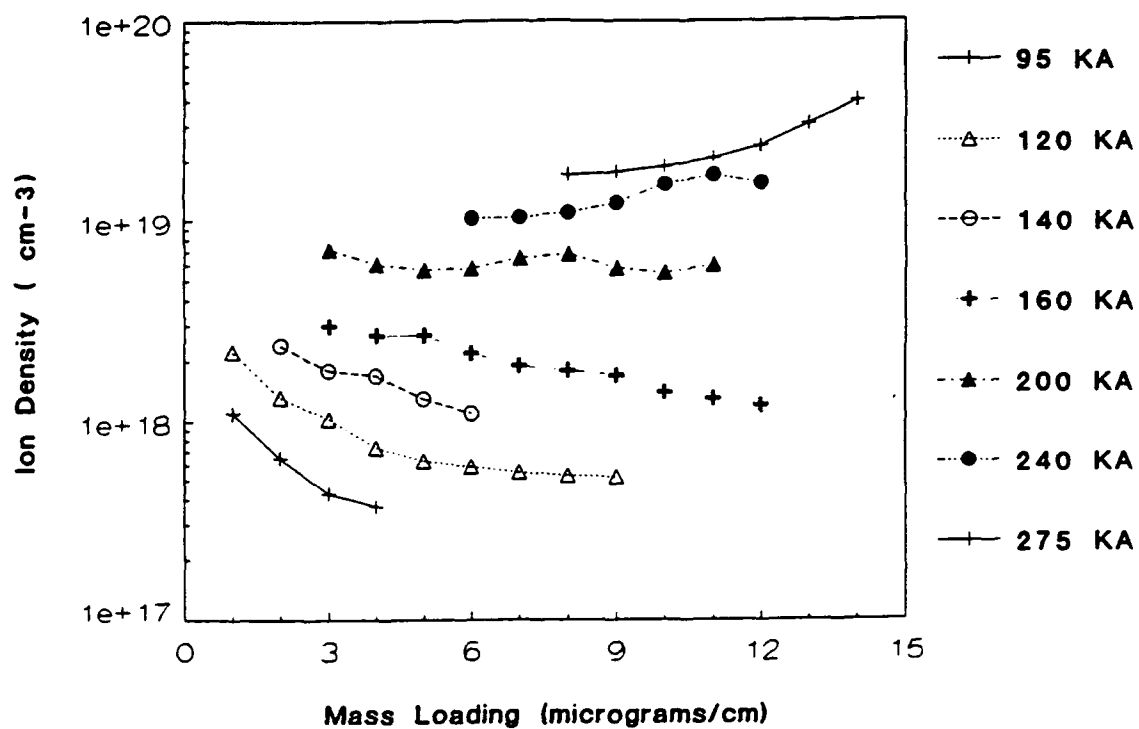


FIG. B.7. (a) Ion density at implosion versus mass load for various currents and (b) peak ion density (for 50 to 100 eV neon plasma) for various currents. ($A=0.6 \text{ cm}$, $W=0.5 \text{ cm}$, $R=0.07 \text{ cm}$)

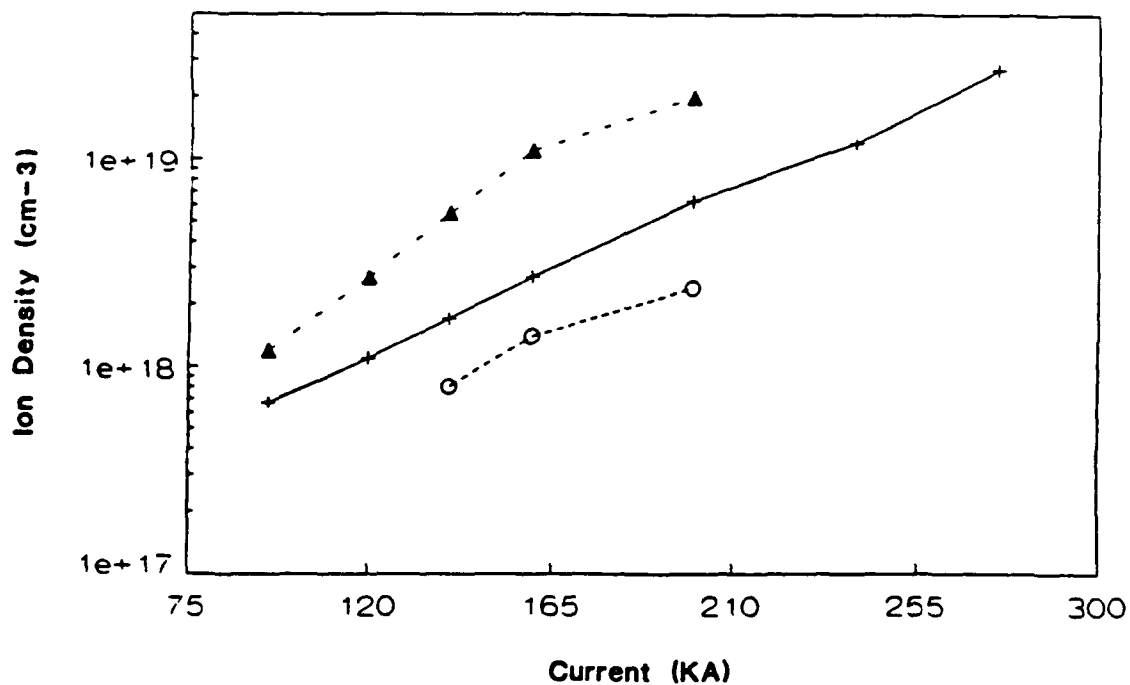
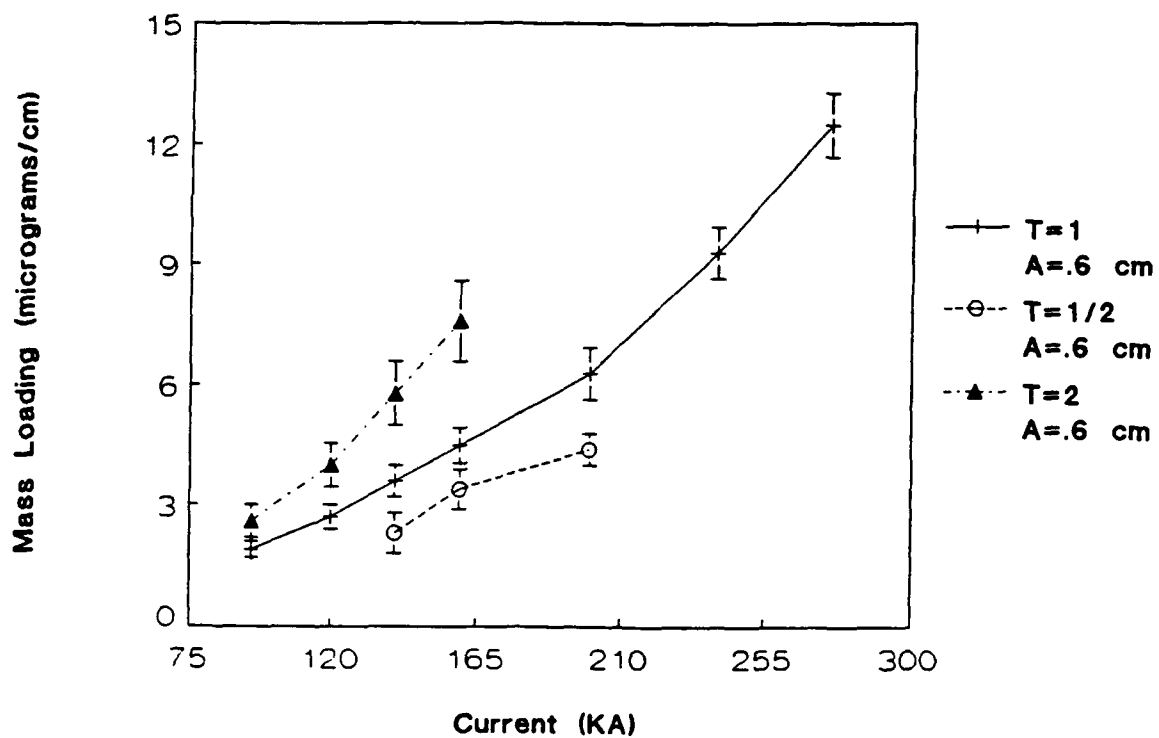


FIG. B.8. (a) Current versus mass load for 50 to 100 eV plasma and (b) peak ion density (for 50 to 100 eV plasma) versus current for various timescales. (T:solid, T/2:dash, 2T:dot-dash)

75-eV temperature. Figure B.8(a) gives this result for the normal Gamble II waveshape (T), for the Gamble II waveshape compressed in time by a factor of two (T/2), and for the normal Gamble II waveshape expanded in time by a factor of two (2T). For a given mass load, the shorter duration waveshape required a larger magnitude current to achieve a 75-eV temperature. The scaling of peak ion density with driving current for these different waveshapes is presented in Fig. B.8(b). Ion densities of 10^{18} to 10^{19} cm⁻³ were produced with all three waveshapes, but larger magnitude currents were required for shorter duration waveshapes.

This same analysis was carried out for plasmas with initial radii of 3 and 9 mm. The relationship between current and mass load for a 75-eV temperature is given in Fig. B.9(a) for initial radii of 3, 6, and 9 mm. These results show the relationship between the current and the mass load as the initial radius is changed. The relationship between current and peak ion density for a 75-eV plasma is given in Fig. B.9(b) for the different initial radii. Ion densities of 10^{18} to 10^{19} cm⁻³ were achieved with all three initial radii for driving currents of 120 to 170 kA.

The results in Section B.1 for a 0.75-MA driving current indicated that lower peak temperatures and ion densities were produced when the width of the annulus was decreased. This effect also occurs for smaller driving currents as shown in Fig. B.10(a) where the relationship between the current and the mass load with 0.2-cm and 0.5-cm annular widths to produce a 75-eV plasma are compared. The relation between the current and peak ion density for these two widths is given in Fig. B.10(b). To achieve this temperature with a fixed driving current, the smaller width required a smaller mass load and

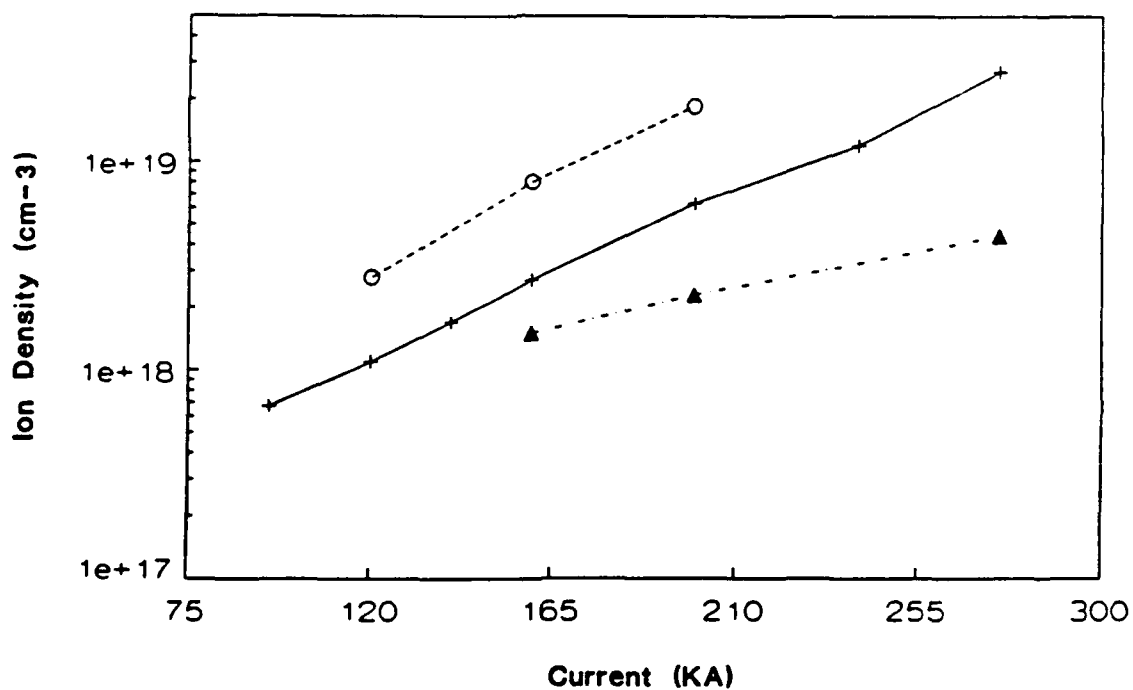
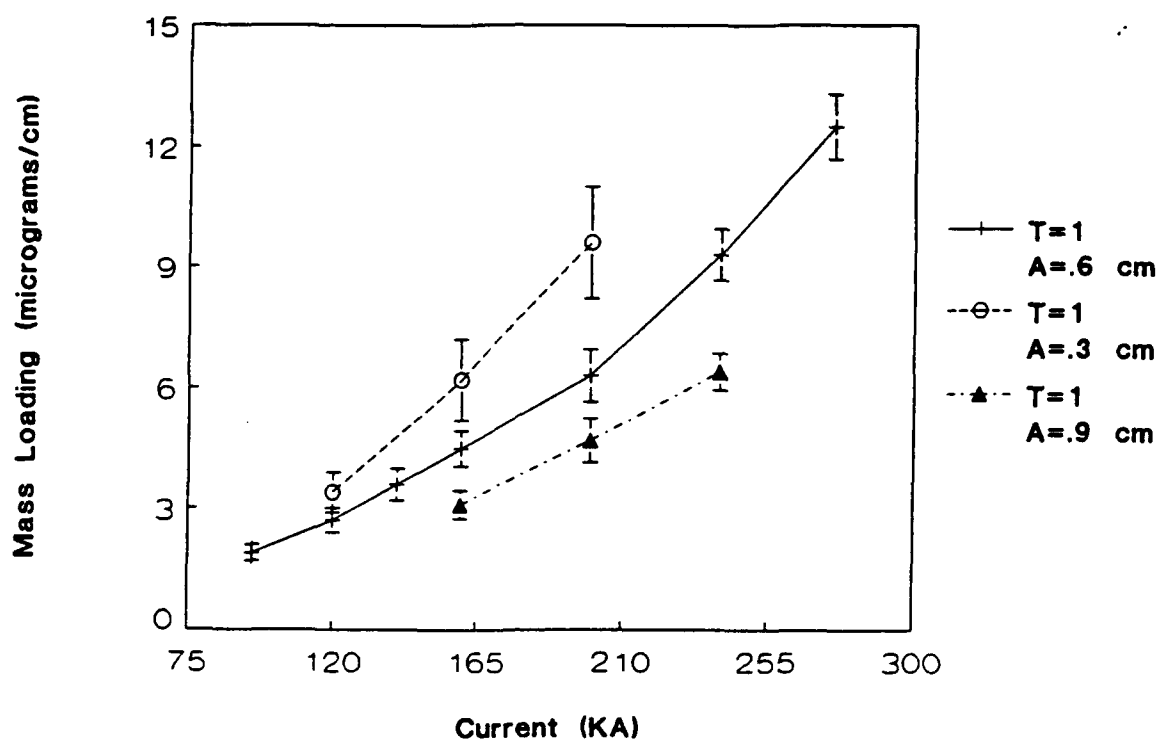


FIG. B.9 (a) Current versus mass load for 50 to 100 eV plasma and (b) peak ion density (for 50 to 100 eV plasma) versus current for various initial radii. ($A=0.6$ cm:solid, $A=0.3$ cm:dash, $A=0.9$ cm:dot-dash)

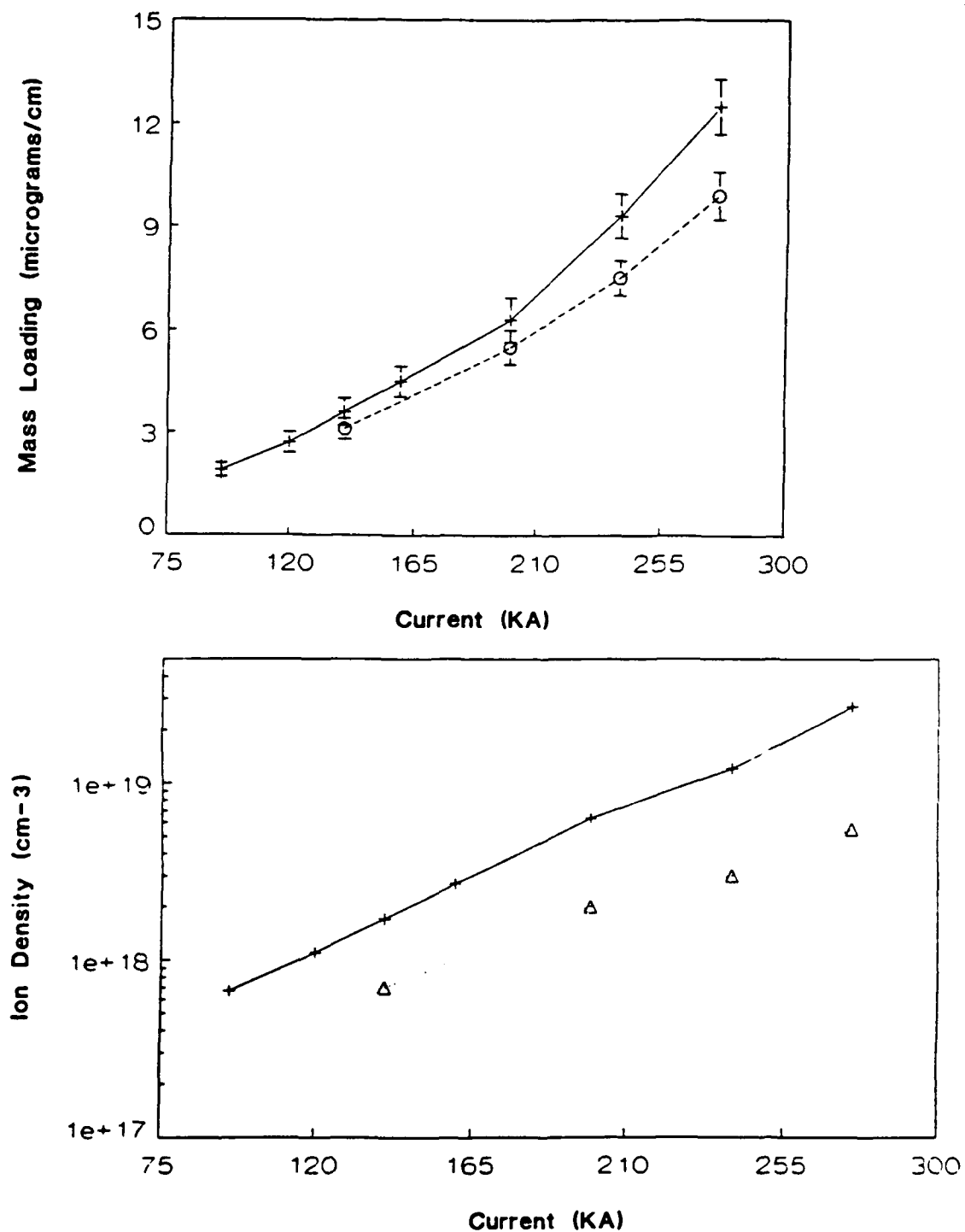


FIG. B.10. (a) Current versus mass load for 50 to 100 eV plasma and (b) peak ion density (for 50 to 100 eV plasma) versus current for various widths. (W=0.5 cm:solid, W=0.2 cm:dash)

produced a smaller ion density at implosion.

B.4 Conclusions

Resistive effects were added to a 0-D implosion code which had been used to predict radiation outputs from neon implosions on Gamble II. This modification reduced the peak ion density and the K-shell X-ray output power by a factor of 5, while maintaining similar temperatures and total K-shell radiated energies.

The code was used to study the relation between the mass load and driving current required to produce a 50 to 100 eV, 10^{18} to 10^{19} cm⁻³ neon plasma. Peak driving currents of 120 to 240 kA and mass loads of 3 to 9 μ g/cm were required to produce these plasma conditions using the Gamble II waveshape and a uniform cylindrical 6-mm radius plasma.

For calculations where the duration of the voltage pulse was increased or decreased by a factor of two, but the peak voltage was unchanged, the driving current and mass load scaled as expected. The energy coupled to the imploding neon plasma was proportional to the duration of the voltage pulse; consequently, a longer voltage pulse required more mass or less current to achieve the lasing conditions. Driving currents of 100 to 160 kA were sufficient to achieve imploded ion densities of at least 10^{18} cm⁻³ at temperatures of 50 to 100 eV.

Variation of the ion density with the driving current for the two different annular widths can be understood in terms of how the kinetic and internal energy are coupled to the implosion in the calculations. As the implosion progresses, the velocity of the outer radius increases until the internal pressure balances the magnetic pressure. The magnetic pressure is determined by the current, and the internal

pressure is determined by the temperature of the plasma and the average ionization state. At thermalization (i.e., when the inner radius of the annulus equals the radius of thermalization), less energy is coupled to the larger annulus because it is thermalized earlier in time when the velocity is smaller. After thermalization, both calculations proceed by compressing the existing plasma in a cylindrical geometry. The implosion continues until the internal pressure exceeds the magnetic pressure by an amount sufficient to halt the implosion. The maximum ion density occurs when the outer radius is a minimum; this condition exists when the velocity of the outer radius goes to zero. For the larger annulus, the implosion continues to a smaller final radius because the lower temperature produces a smaller internal pressure. Therefore the larger annulus leads to larger ion densities as shown in Fig. B.10(b).

The dynamics of the implosion process can be understood in terms of the radial velocity equation (Eq. 17 in Ref. 80) used in the calculation. For the following discussion, the magnitude of the radially-inward implosion velocity is positive. Setting the derivative of the velocity equation to zero ($dv/dt=0$), which corresponds to no acceleration of the outer radius, results in the "Bennett Pinch" relation for a Z-pinch. This relation corresponds to balancing the magnetic pressure and the internal pressure. At the time of this condition, the implosion speed has reached its maximum and thereafter begins to decrease. The temperature continues to increase as the plasma is compressed until the velocity reaches zero. At this time, the outer radius is a minimum, and the temperature and ion density are maxima. Since resistive heating depends on the area, a larger annulus is heated less, which results in a larger velocity

because there is less internal pressure acting against the magnetic pressure. The larger implosion velocity leads to a smaller final radius for two reasons: (1) because the implosion occurs earlier in time when the current is larger, and (2) because a larger internal pressure is needed to stop the implosion.

In general, an implosion with a smaller initial radius resulted in a larger final temperature and ion density which caused it to require less mass for a fixed driving current in order to achieve temperatures of 50 to 100 eV. Since implosions with a larger initial radius took longer, the temperature prior to implosion was larger due to the resistive heating over a longer time interval. This caused the implosions to be softer, and therefore less mass was needed to reach temperatures of 50 to 100 eV.

Appendix C

PLASMA MODELING

Three atomic-physics codes were used to interpret spectral measurements of the neon implosions. Temperature dependences of selected transitions of Ne VII, Ne VIII, and Ne IX were calculated with these codes in order to determine electron temperatures. The transitions selected for the calculations are based on the experimental measurements. Line ratios from local-thermodynamic-equilibrium (LTE) and coronal-equilibrium calculations are presented for comparison with time integrated spectra. A time-dependent coronal model was used to estimate temperatures from time-resolved Ne VII, Ne VIII, and Ne IX line emissions. In this appendix, the calculations with these models are described and the temperature dependences of the line emissions are presented.

C.1 Line Ratios from LTE Model

Line-intensity ratios for Ne VII, Ne VIII, and Ne IX transitions were calculated assuming local thermodynamic equilibrium (LTE). The ionization-state fractions were determined by the Saha relation and the excited-state populations were determined by their Boltzmann factors as discussed in Sec. A.1. Oscillator strengths (f_{mn}),

transition energies (E_{mn}), and statistical weights (g_n, g_m) are given in Table C-1 for the transitions selected for these calculations. The temperature dependence of the ratio of the Ne IX $1s2l-1s3l'$ ($l=s, p$ and $l'=p, d$) transitions at 78.26 and 78.3 Å to the Ne VIII $1s^2 2s-1s^2 3p$ transition at 88 Å is given in Fig. C.1 for an electron density of 10^{21} cm^{-3} . The electron density of 10^{21} cm^{-3} was chosen because the upper levels of the transitions are expected to be in LTE at this electron density. The temperature dependences of the ratios of the Ne VIII $1s^2 2s-1s^2 3p$ transitions at 88 Å to two different Ne VII transitions are given in Fig. C.2 for an electron density of 10^{21} cm^{-3} . The Ne VII lines selected for these calculations are the $1s^2 2s2p-1s^2 2s3d$ transitions at 106 Å and the $1s^2 2s^2-1s^2 2s3p$ transition at 97.5 Å.

C.2 Line Ratios from Coronal Model

Line-intensity ratios for Ne VII, Ne VIII, and Ne IX transitions were calculated assuming coronal equilibrium. The temperature dependence of the relative populations of the ionization states was determined from the results presented in Fig. 2.2. Excited-state populations were determined by balancing the collisional-excitation rate with the radiative-decay rate (see Eqs. A.15 and A.16). Transition probabilities (A_{ng}), upper-level excitation energies (E_{gn}), and ground-state to upper-level absorption oscillator strengths (f_{gn}) are given in Table C.2 for the transitions selected for these calculations. For transitions with no allowed ground-state to upper-level transition, oscillator strengths of allowed transitions from the ground-state to an upper-level with the same principal quantum number

Table C.1

Transition	f_{mn}	g_n	g_m	E_{mn} (eV)	Ref
Ne VII					
$1s^2 2s^2 - 1s^2 2s3p$	0.48	1	3	127.1	156,157
$1s^2 2s2p - 1s^2 2s3d$	0.68	9	15	116.8	156,157
Ne VIII					
$1s^2 2s - 1s^2 3p$	0.298	2	6	140.7	157
$1s^2 3s - 1s^2 3p$	0.256	2	6	4.33	157
Ne IX					
$1s2s - 1s3p$	0.386	1	3	158.2	157
$1s2p - 1s3d$	0.627	9	15	158.2	157

Table C.1 Oscillator strengths (f_{mn}), transition energies (E_{mn}), and statistical weights (g_n, g_m) for selected transitions of Ne VII, Ne VIII, and Ne IX.

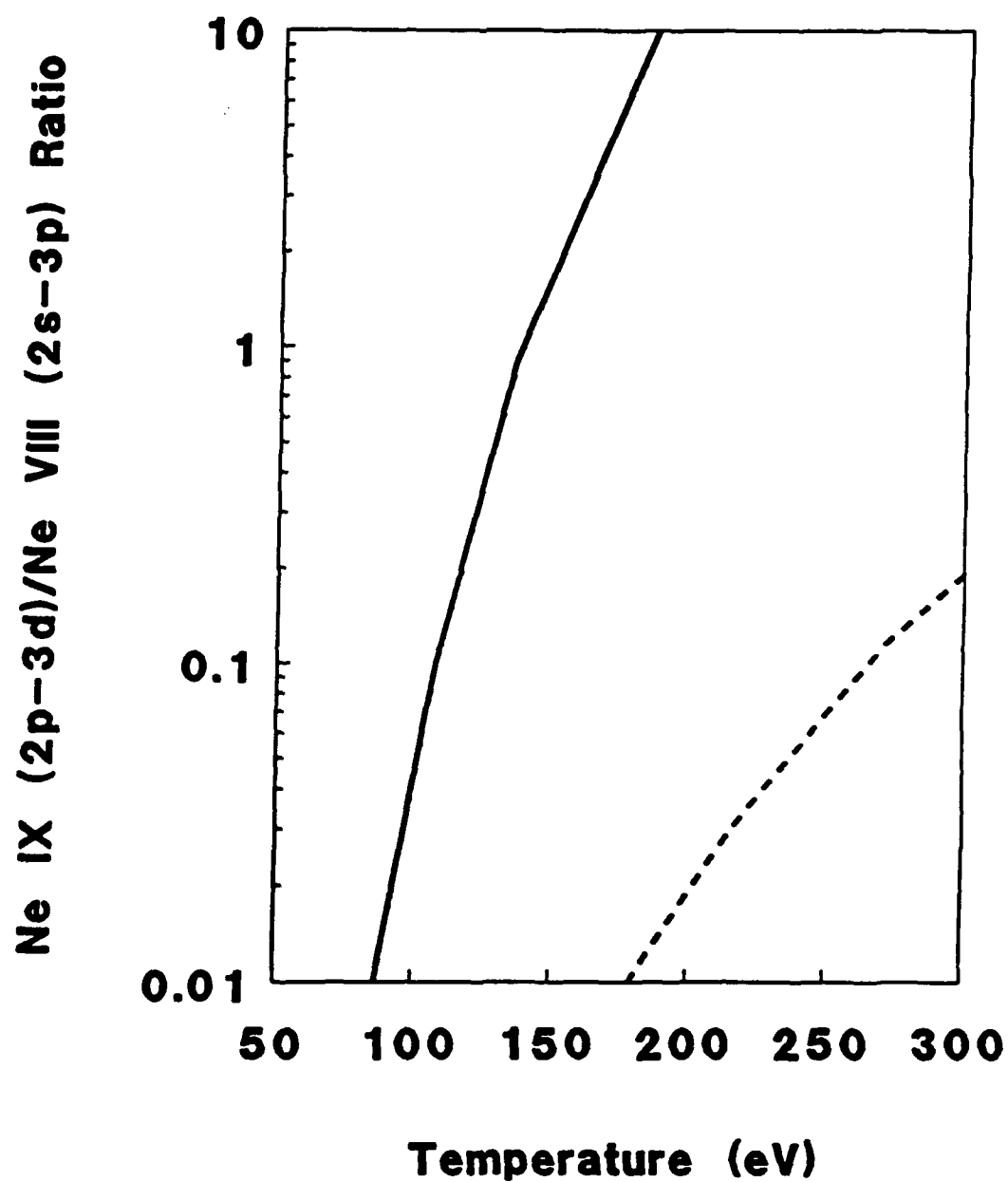


FIG. C.1. Temperature dependence of the ratio of Ne IX to Ne VIII transitions for LTE (solid) and coronal (dashed) calculations.

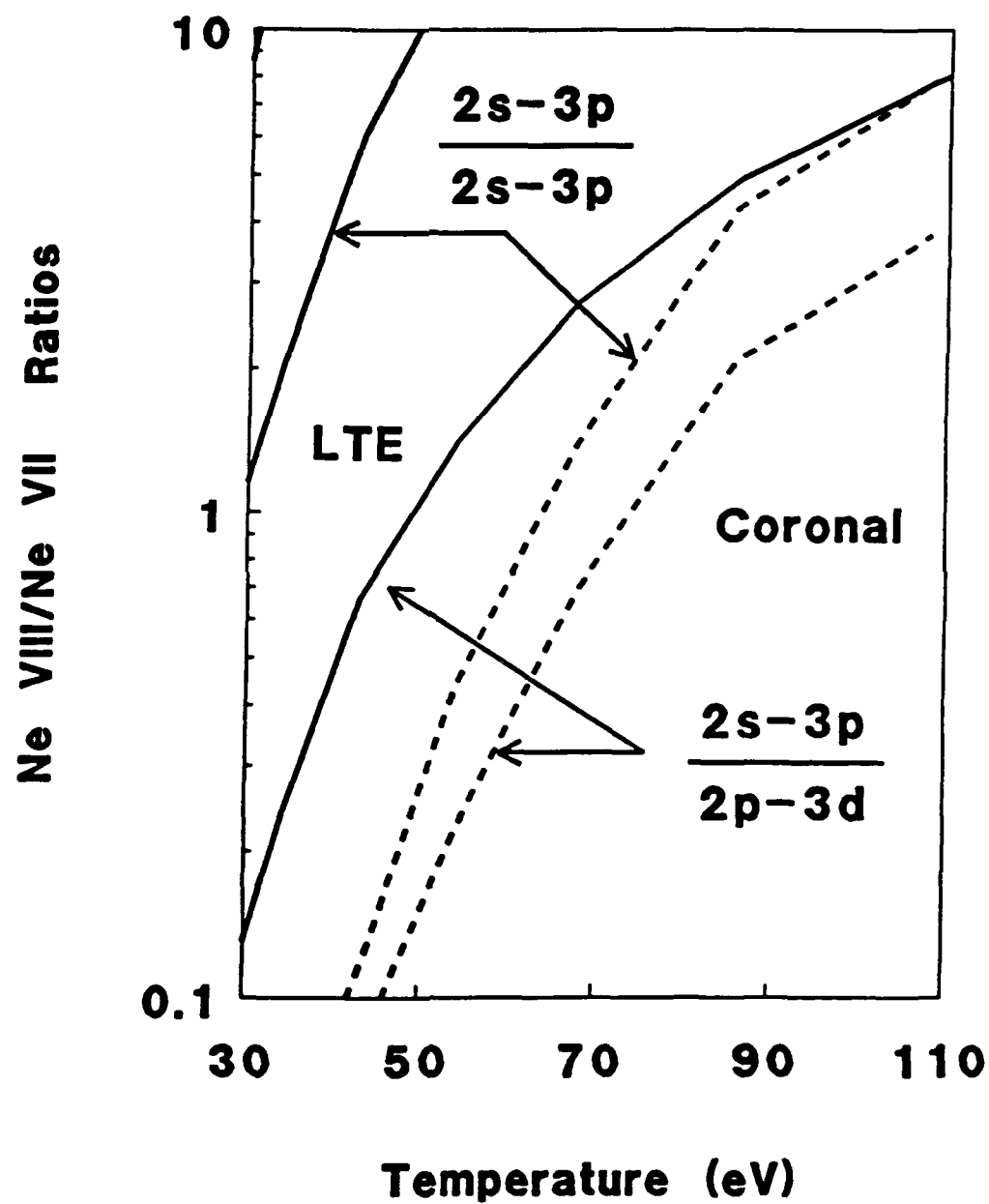


FIG. C.2. Temperature dependence of the ratio of Ne VIII and Ne VII transitions for LTE (solid) and Coronal (dashed) calculations.

Table C.2

Transition	A_{gm} (10^{-8} 1/s)	E_{gm} (eV)	f_{gm}	Ref
Ne VII				
$1s^2 2s^2 - 1s^2 2s3p$	1100	127.2	0.48	115,156
$1s^2 2s2p - 1s^2 2s3d$	2400	130.7	0.68	115,157
Ne VIII				
$1s^2 2s - 1s^2 3p$	853	140.6	0.30	157
$1s^2 3s - 1s^2 3p$	0.69	140.6	0.30	157
Ne IX				
$1s2s - 1s3p$	26200	1072	0.15	157
$1s2p - 1s3d$	26200	1072	0.15	157

Table C.2 Transition probabilities (A), upper-level excitation energies (E), and ground-state to upper-level absorption oscillator strengths (f) for selected transitions of Ne VII, Ne VIII, and Ne IX.

were used. The temperature dependence of the ratio of the Ne IX $1s2l-1s3l'$ ($l=s,p$ and $l'=p,d$) transitions at 78.26 and 78.3 Å to the Ne VIII $1s^22s-1s^23p$ transition at 88 Å is given in Fig. C.1. The temperature dependence of the ratios of the Ne VIII $1s^22s-1s^23p$ transition at 88 Å to the Ne VII $1s^22s2p-1s^22s3d$ transition at 106 Å and to the Ne VII $1s^22s^2-1s^22s3p$ transition at 97.5 Å are given in Fig. C.2. These ratios are independent of electron density because both upper levels have the same electron-density dependence. For a given temperature, these ratios are smaller than the corresponding LTE ratios.

C.3 Rate-Dependent Model

A time-dependent atomic-physics code, developed at the University of Maryland, was used to calculate the time histories of ionization balance.¹⁵⁹ The code uses a semiempirical formula of Kunze et al. to determine ionization rates.¹⁶⁰ Time histories of electron temperature and density are entered into the code, and relative populations of ionization states are calculated as a function of time. The timestep is variable and depends on the ionization rates. An example of the electron temperature time history is given in Fig. C.3. The same profile was used for electron density. This profile has a full-width at half-intensity of 85 ns. This width could be adjusted to fit experimental results. The initial and peak temperatures and densities could be varied while maintaining the same time profile. To analyze the measurements in this experiment the peak electron temperature was varied and the calculated time dependence of the fractional abundances of the ionization states was compared with the experimental results.

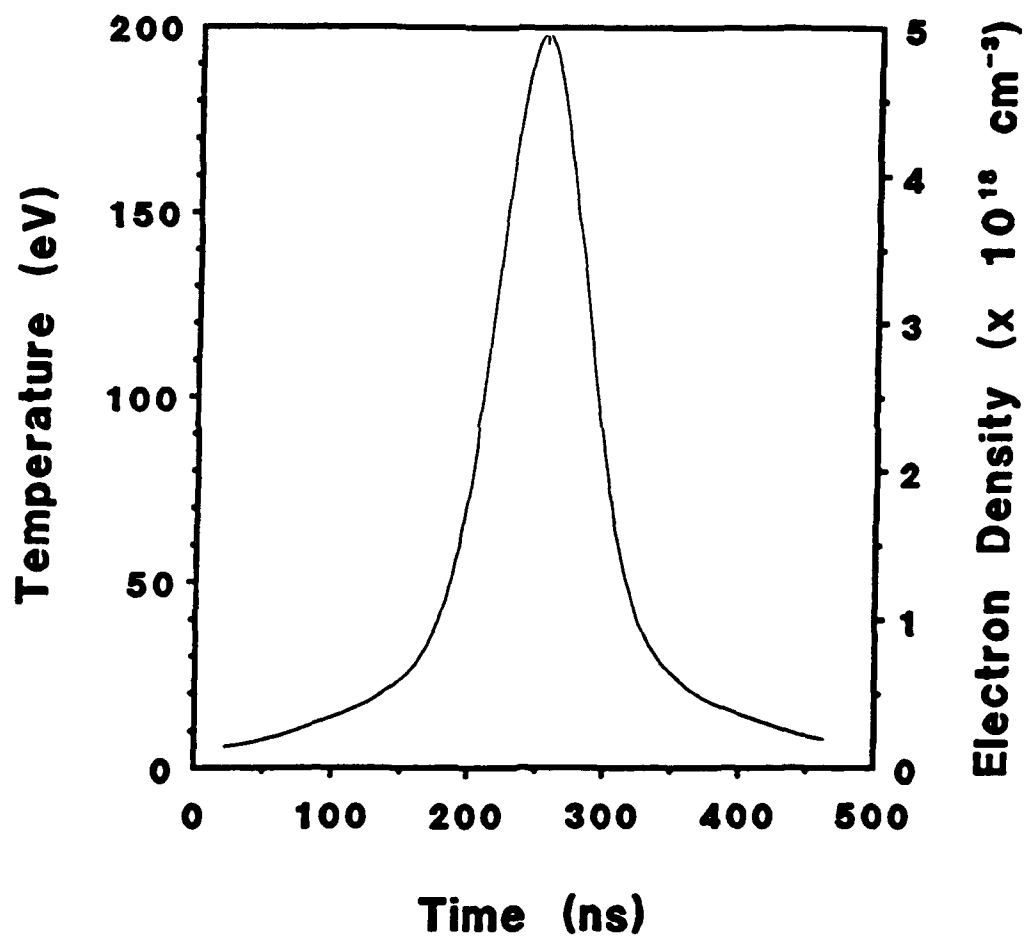


FIG. C.3. Example of the time history of electron temperature and electron density for the rate-dependent model.

Time histories of Ne VII, Ne VIII, and Ne IX populations are given in Fig. C.4 for a peak electron temperature of 60 eV. For this temperature, the population is primarily Ne VII. Similar results are presented in Figs C.5 and C.6 for peak temperatures of 100 and 200 eV, respectively. The predominant ionization state is Ne VIII at 100 eV and Ne IX at 200 eV. Time histories of line radiation from excited levels of these ionization states were also calculated. Comparisons of pulse durations and relative times of emission with experimental results were used to determine electron temperatures. Examples of time histories of emission from $n=3$ levels of Ne VII, Ne VIII, and Ne IX are given in Figs. C.7, C.8 and C.9 for peak temperatures of 60, 100, and 200 eV, respectively. An electron density of $5 \times 10^{18} \text{ cm}^{-3}$ was used for these calculations. The peak intensities are normalized to unity for all of the transitions.

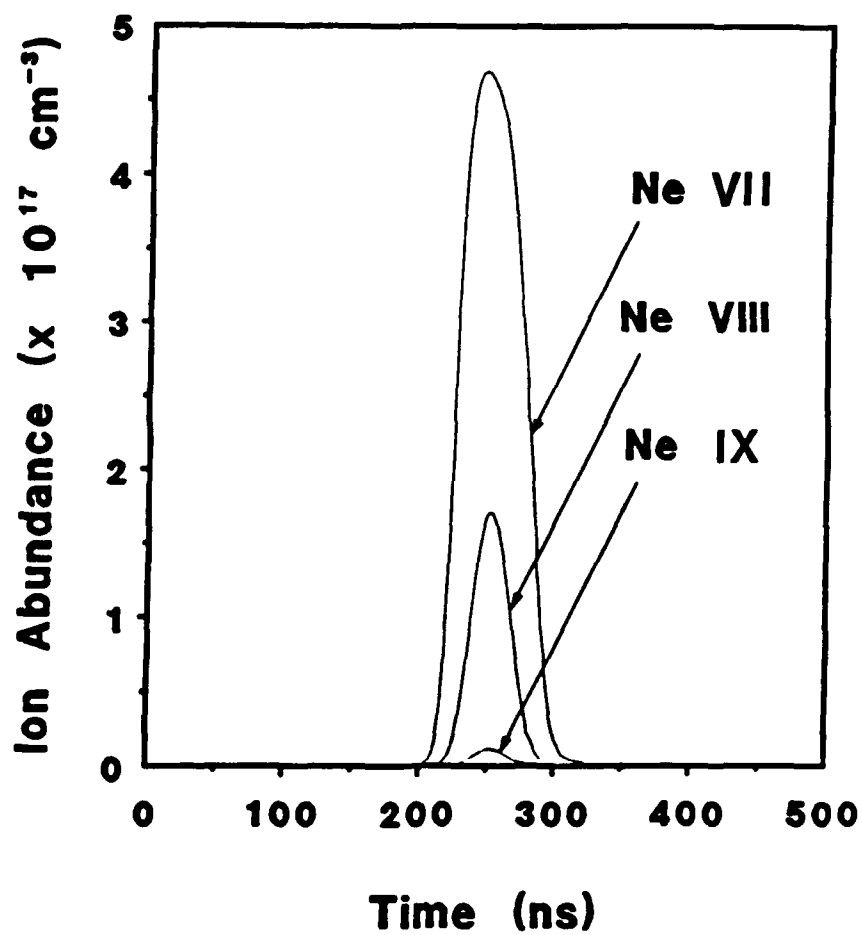


FIG. C.4. Time histories of Ne VII, Ne VIII, and Ne IX ionization states for a peak electron temperature of 60 eV.

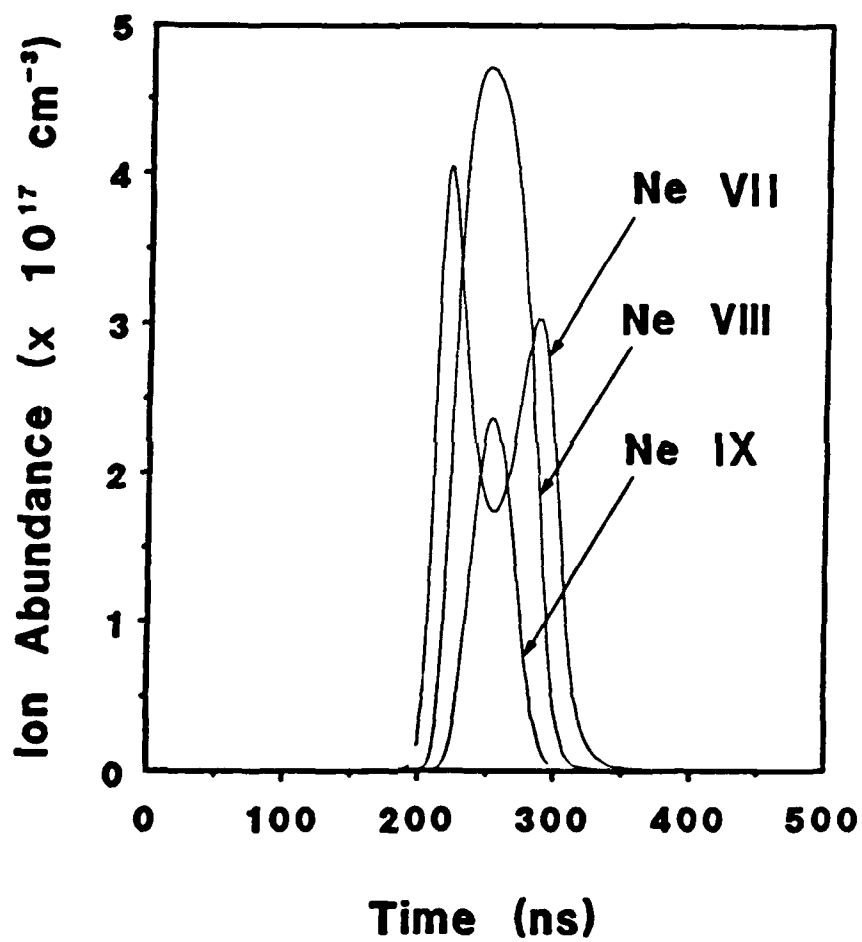


FIG. C.5. Time histories of Ne VII, Ne VIII, and Ne IX ionization states for a peak electron temperature of 100 eV.

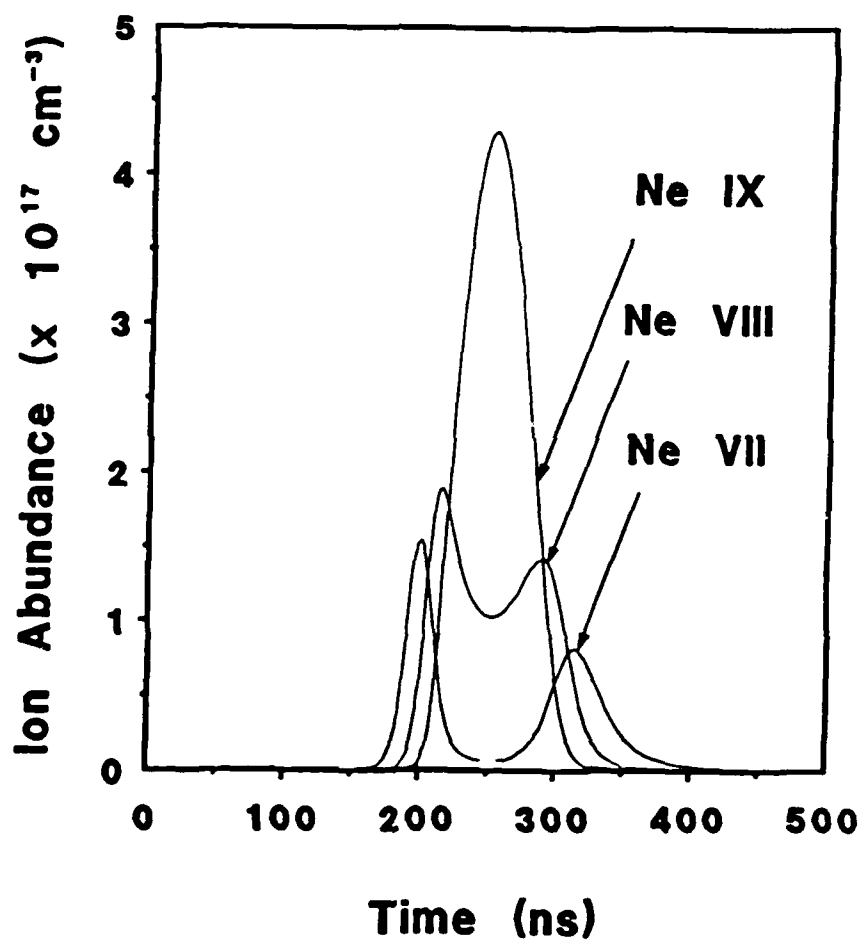


FIG. C.6. Time histories of Ne VII, Ne VIII, and Ne IX ionization states for a peak electron temperature of 200 eV.

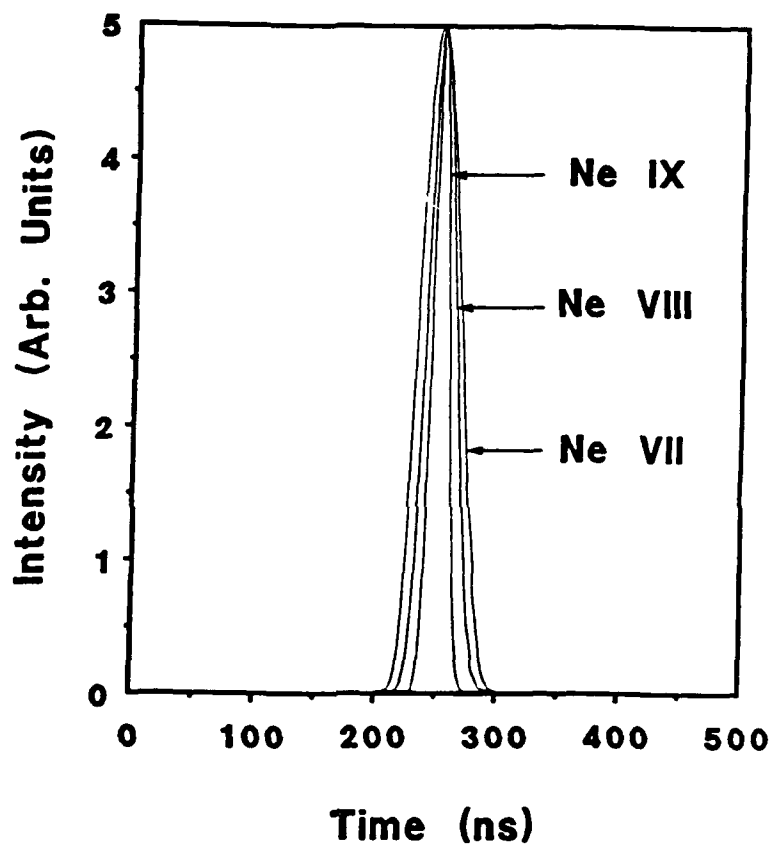


FIG. C.7. Time histories of Ne VII, Ne VIII, and Ne IX line emissions for a peak electron temperature of 60 eV.

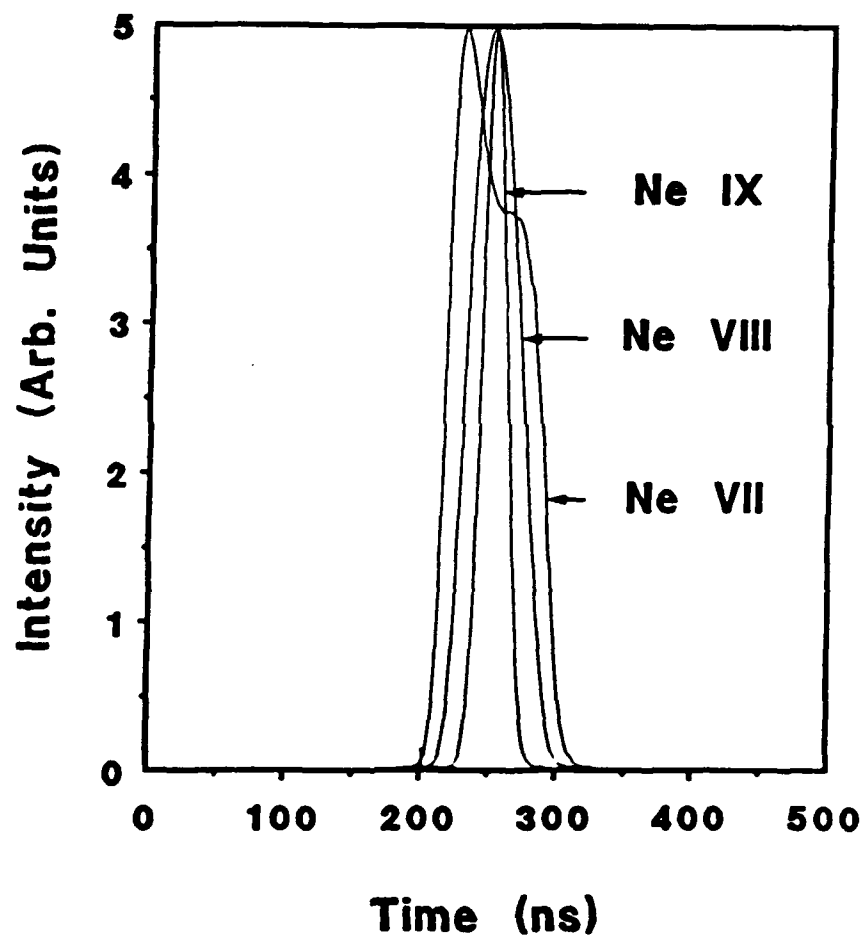


FIG. C.8. Time histories of Ne VII, Ne VIII, and Ne IX line emissions for a peak electron temperature of 100 eV.

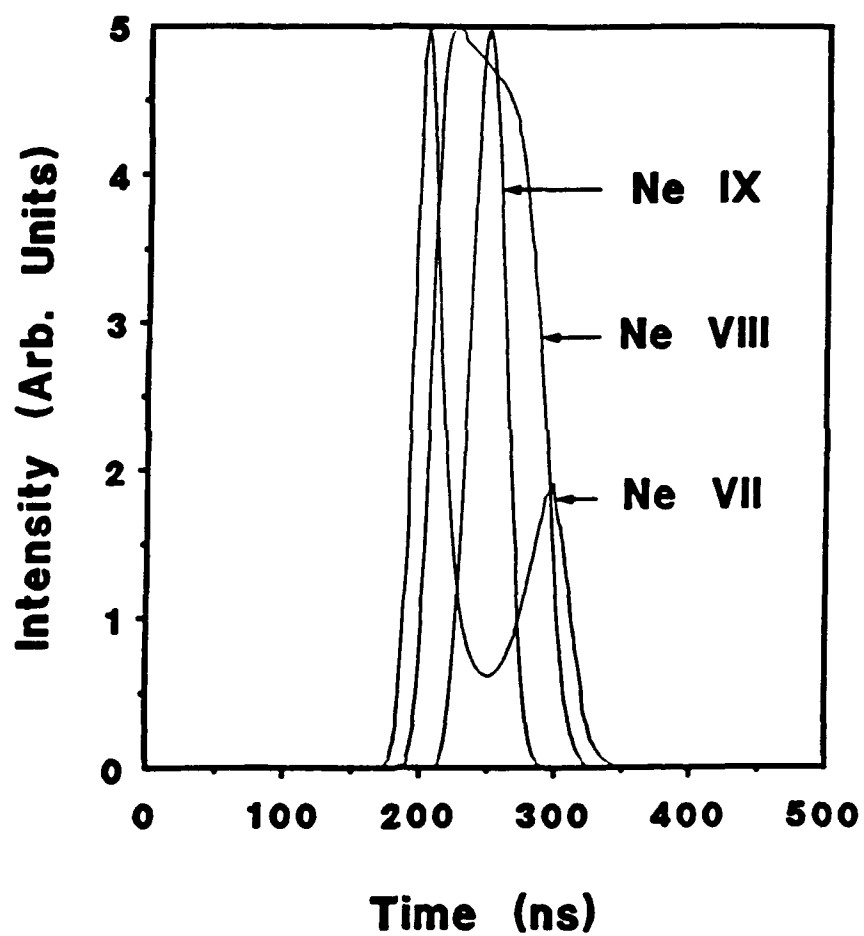


FIG. C.9. Time histories of Ne VII, Ne VIII, and Ne IX line emissions for a peak electron temperature of 200 eV.

Appendix D

RADIATION DETECTORS

D.1 Detectors for Soft X-ray and XUV Emissions

Pinhole cameras and vacuum diodes were used to record soft X-ray and extreme ultraviolet (XUV) emissions from the neon implosions. The pinhole camera provided spacial resolution, and the vacuum diode provided a time history of the radiated power. Different filter materials, films, and cathode materials were used to tailor the detector responses to either soft X-ray or XUV emissions. These detectors are described in detail in this Appendix.

D.1.1 Pinhole Camera

Two different pinhole cameras were used to record the spacial distribution of the emissions from the neon implosions. For soft X-rays in the 0.5- to 6-keV region, a 6- μm thick aluminum filter and Kodak 2492 film were used. The high-energy cutoff is determined by the absorption edge of aluminum (1.6 keV) and the low-energy cutoff is determined by absorption in the emulsion of the 2492 film. For XUV emission in the 100- to 280-eV region, a 2- μm thick polycarbonate filter (Kimfol) coated with a 0.1- μm layer of aluminum and Kodak

101-07 film were used. Here, the high-energy cutoff is determined by the absorption edge of carbon (280 eV) in the Kimfol. The thin aluminum layer eliminates visible and ultraviolet radiation which otherwise would be transmitted by the Kimfol. Due to the thickness of this aluminum layer, radiation above the aluminum K-edge is attenuated very little so that this radiation is also recorded by the XUV pinhole camera.

The magnification of the pinhole camera image was determined by the location of the pinhole relative to the film. For soft X-rays, the pinhole was located 18 cm from the axis of the pinch and the film was located 13 cm from the pinhole giving a magnification of 0.72. For XUV emission, the pinhole was located 27 cm from the pinch axis, and the film was located 20 cm from the pinhole, giving a magnification of 0.74. A 0.2-mm diameter pinhole was used for both cameras. Emission from a point source would project this diameter to a size of 0.34 mm at the film location for both cameras. For an extended source, 0.34 mm would represent the resolution of the camera. For a source smaller than 0.34 mm, the size of the image would be limited to 0.34 mm (i.e., pinhole limited).

Densitometer scans of the images for various pinhole pictures were taken to determine the size of the emitting region. Examples are given in Figs. D.1(a) and (b) for the soft X-ray images of Figs. 5.7(a) and (b). The full-width at half-maximum of the scan in Fig. D.1(a) is 0.47 mm. The scan in Fig. D.1(b) has a similar size, but is considerably reduced in intensity. The photograph in Fig. 5.7(a) includes four small regions with intensities similar to those of Fig. D.1(a) and two regions with intensities similar to those of Fig. D.1(b). The photograph in Fig. 5.7(b) includes one region with an

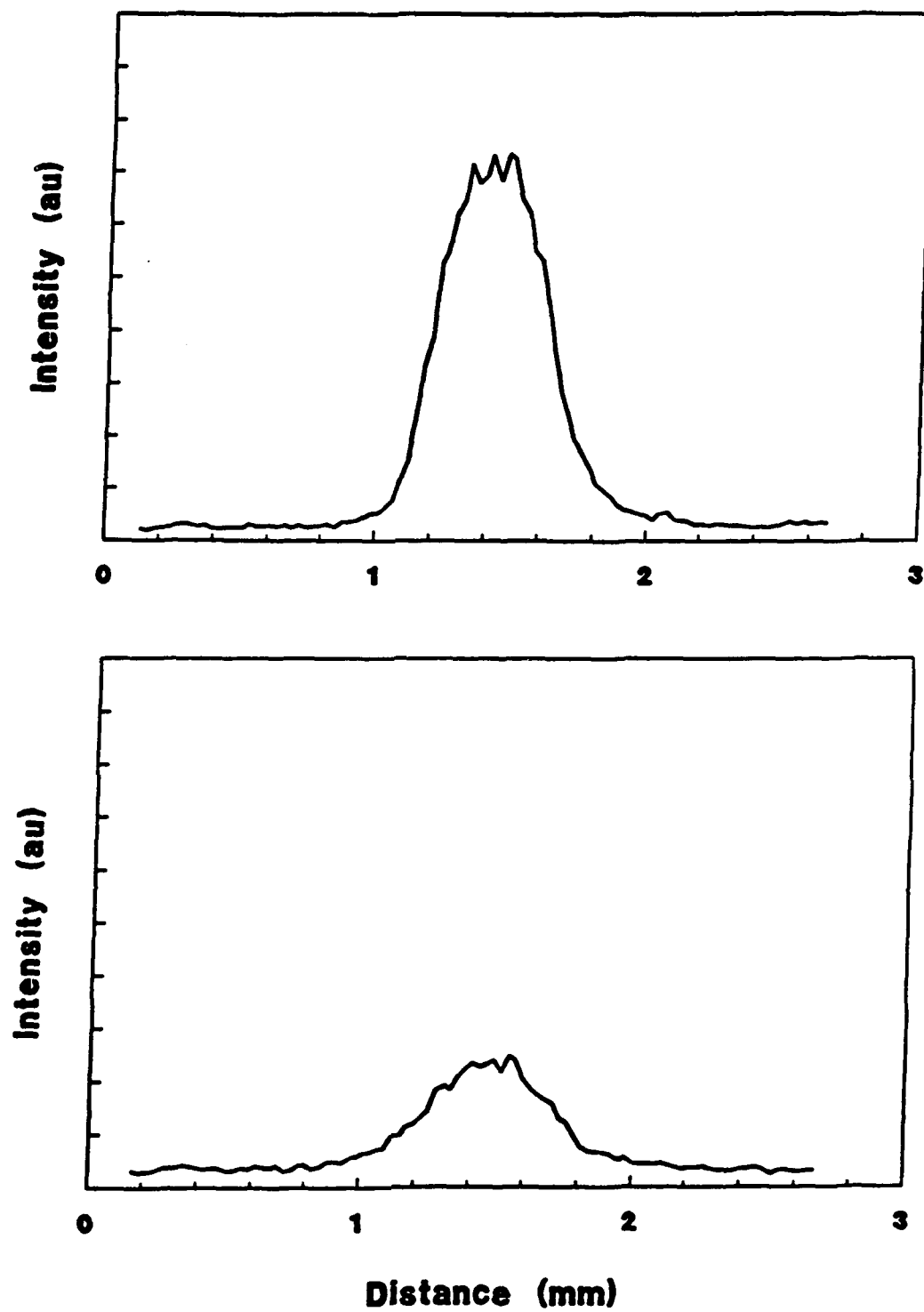


FIG. D.1. Radial densitometer scans of small regions in Fig. 5.7 of (a) high intensity (top) and (b) low intensity soft X-ray emission (bottom).

intensity similar to Fig. D.1(a) and one region with intensities similar to Fig. D.1(b).

Radial scans of the XUV image in Fig. 6-7(a) produced with 50-psi pressure are presented in Fig. D.2. The dashed curve in Fig. D.2(a) is a scan at the exit of the nozzle. There is one on-axis peak with a full-width at half-intensity of 0.32 mm. The solid curve in Fig. D.2(a) is a scan in the center of the nozzle-cathode gap. This scan has less intensity, and there are two peaks located symmetrically 0.3-mm off axis. The scans in Fig. D.2(b) were taken in the center of the nozzle-cathode gap, similar to the solid curve in Fig. D.2(a), but they are plotted on a different intensity scale. These scans also show symmetrical off-axis peaks.

D.1.2 Vacuum Diodes

Vacuum diodes were used to record time histories of X-ray power emitted from the neon implosion. For soft X-rays in the 0.8- to 1.6-keV region, a 0.5- μ m aluminum and an aluminum-coated 2- μ m polycarbonate (Kimfol) filter were used with a nickel cathode. For XUV emission in the 100-to 280-eV region, a 2- μ m aluminum-coated Kimfol filter was used with an aluminum cathode. Absolute responses of the vacuum diodes were determined by combining the filter attenuation with the photoionization efficiency of the cathode.⁸⁷ Soft X-ray and XUV responses as a function of the photon energy are given in Figs. D.3 and D.4, respectively. The responses are in units of MW of X-ray power incident on the cathode per Ampere of output current. The 2.5-cm diameter cathode was located 34 cm or 46 cm from the Z-pinch for the soft X-ray and XUV diodes, respectively.

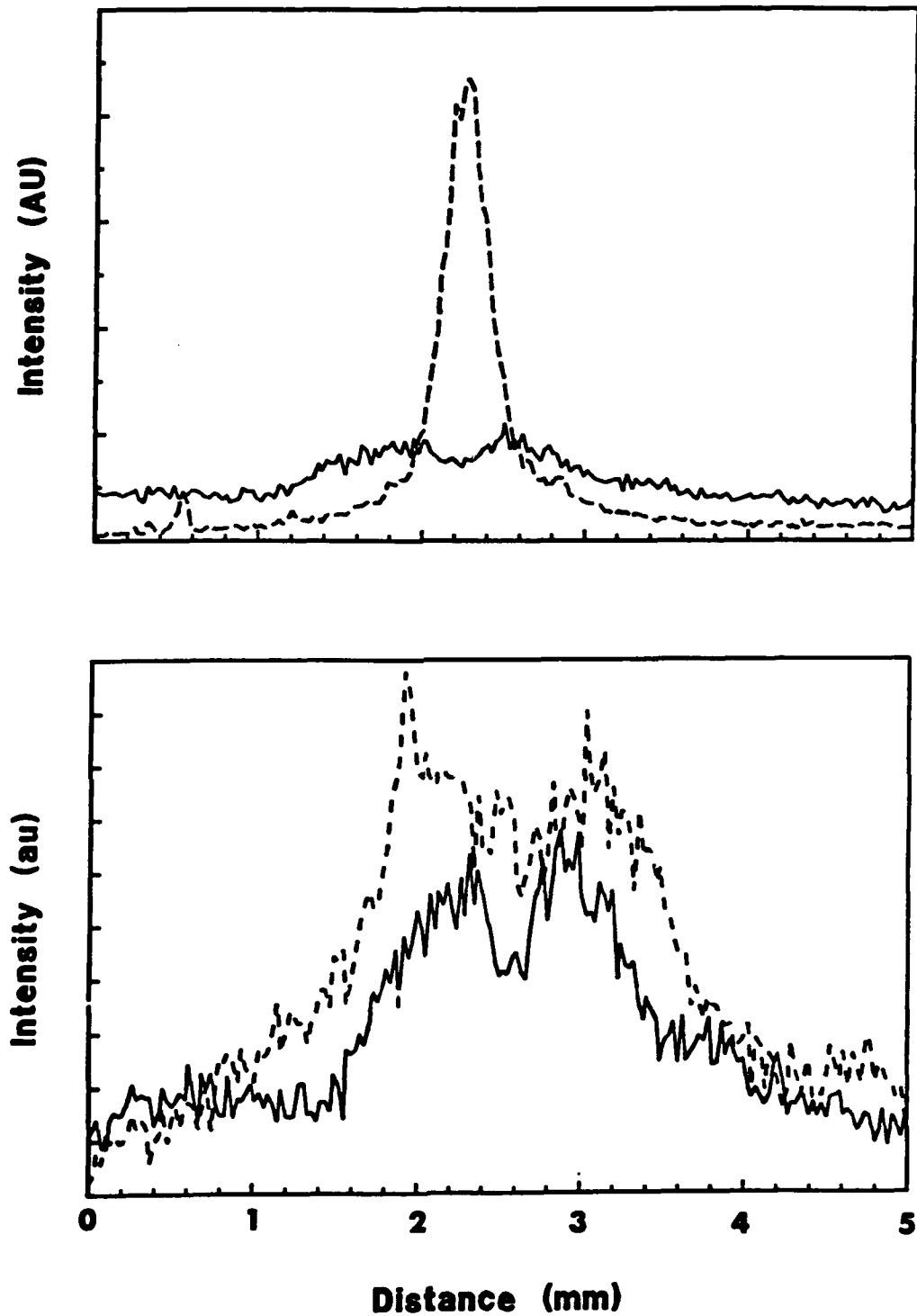


FIG. D.2. Radial densitometer scans of the XUV image in Fig. 6.7(a)
 (a) (top) near the nozzle (dashed) and the center of the image (solid)
 and (b) (bottom) near the center of the image (solid and dashed).

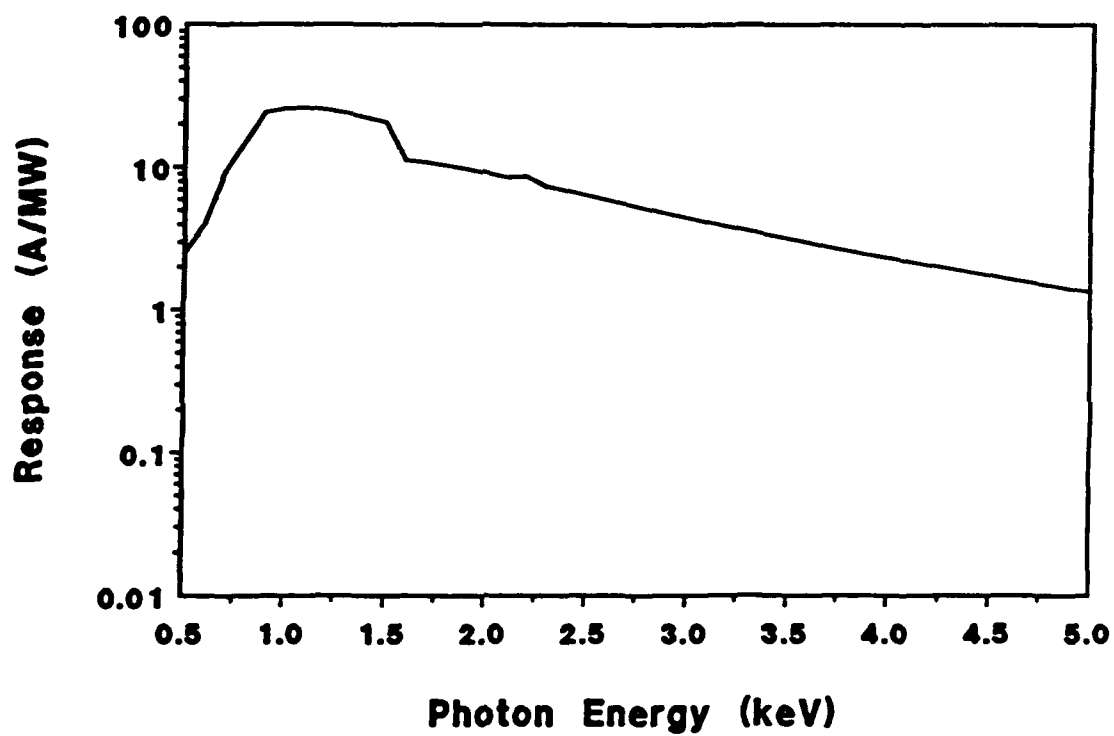


FIG. D.3. Response of the vacuum diode filtered for soft X-rays.

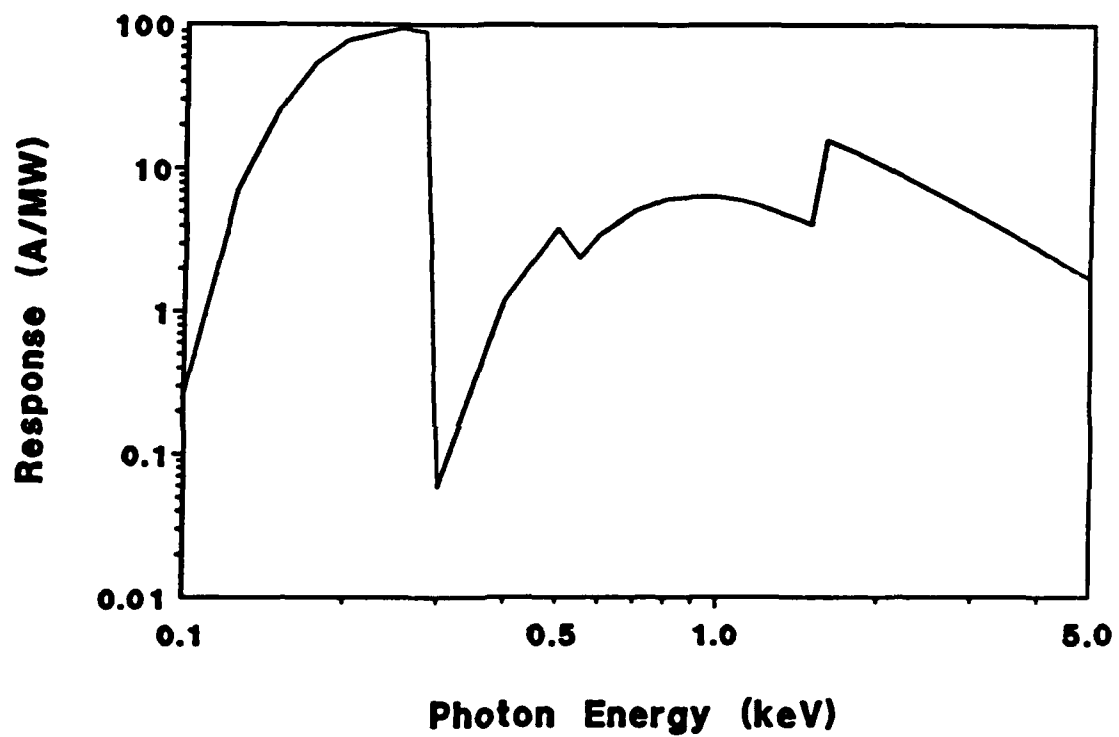


FIG. D.4. Response of the vacuum diode filtered for XUV radiation.

This gives solid angle fractions ($\Delta\Omega/4\pi$) of 3.4×10^{-4} or 1.8×10^{-4} .

D.2 Grazing Incidence Spectrometer

A 1-meter grazing-incidence spectrometer was used to record XUV radiation from the neon Z-pinch. The angle of incidence of the spectrograph was 87° and a 1200-line/mm grating was used. The blaze angle of the grating was 1° which produced a peak response at 290 Å for normal incidence or a peak response at 20 Å for grazing incidence.¹⁶¹ Photographic film (Kodak 101-07) sensitive to XUV radiation was mounted along the Rowland circle to record time-integrated spectra. Alternatively, a scintillator-photomultiplier mounted behind an exit slit on the Rowland circle was used to record time-resolved measurements of specific spectral regions.

D.2.1 Time-Integrated Spectra

The 10- μm entrance slit of the spectrograph was oriented perpendicular to the axis of the Z-pinch at a distance of 50 cm. A 400- μm slit was placed 3.5 cm behind this entrance slit to restrict the area of the grating that was illuminated. This second slit also limited the axial extent of the Z-pinch viewed by the spectrograph to 6 mm. The entire diameter of the Z-pinch could be viewed through the 1-cm long entrance slit and the 2-cm long fast-closing-valve aperture located 20 cm from the plasma. For this 1-meter 1200-line/mm instrument, a linear dispersion along the Rowland circle of 1.3 Å/mm is produced at 100 Å.¹⁶² The width of the entrance slit is magnified by the spectrograph depending on the distance from the grating to the

Rowland circle. The slit width is magnified by a factor of three at a wavelength of 100 Å. This magnification and linear dispersion produce an instrumental width of 0.25 Å when projected onto the Rowland circle at the 100-Å location.

D.2.2 Time-Resolving Monochromator

The grazing-incidence spectrometer was configured as a monochromator for time-resolved measurements. An exit slit was mounted on the Rowland circle in place of the film holder and a 35-μm exit slit was used to provide optimum throughput of both components of the Ne VIII $1s^2 2s-1s^2 3p$ ($^2S_{1/2}-^2P_{1/2,3/2}$) transition (40-mÅ separation). This slit produced an instrument function of 300 mÅ width. A thin layer of p-terphenyl deposited on the vacuum side of a glass vacuum window converted the XUV radiation to visible radiation that was detected outside the vacuum system with a photomultiplier tube. The response time of the p-terphenyl is 2 ns, which is the resolution of the oscilloscope used to record the photomultiplier signal.¹⁶³ A photomultiplier time-delay of 40 ns was measured by comparison with a photodiode using a nitrogen-laser source. Measured photomultiplier signals were corrected accordingly for comparison with X-ray diode signals and current traces.

The neon Z-pinch plasma is an intense source of visible light which could be scattered through the monochromator and contribute to the photomultiplier signal. To attenuate this light, a 0.33 μm thick boron foil was mounted behind the exit slit. This boron filter attenuated the XUV radiation less than the visible light and therefore improved the signal-to-noise ratio. The XUV monochromator was scanned

over the wavelength region of the Ne VIII 2s-3p transition (88 Å) to locate this transition. The continuum intensity in this spectral region was found to be a factor of five smaller than the Ne VIII 2s-3p emission at the time of the first signal, and no continuum was observed at the time of the second signal. Similar continuum intensities were found in the spectral region near 106 Å.

D.3 Near Ultraviolet Spectrometers

Two different near ultraviolet (NUV) spectrometers were used in three different arrangements to record NUV emission from the neon plasma. In the first arrangement the two instruments were used as monochromators with photomultiplier-tube detectors for time resolution. In the second arrangement, the photomultiplier on one instrument was replaced with an optical multichannel analyzer (OMA). For both arrangements, the relative response of the two instruments was determined. In the third arrangement, comparison with a source of known intensity provided a measure of the absolute sensitivity of the instruments. These three arrangements are discussed below.

D.3.1 Monochromators

The two instruments were used as monochromators to record simultaneously selected NUV time histories from a neon implosion. The arrangement of the monochromators is shown in Fig. D.5. Comparison of the photomultiplier signals when the two monochromators were set on the same spectral region provided a measure of their relative sensitivity. Comparison of signals when the monochromators were set

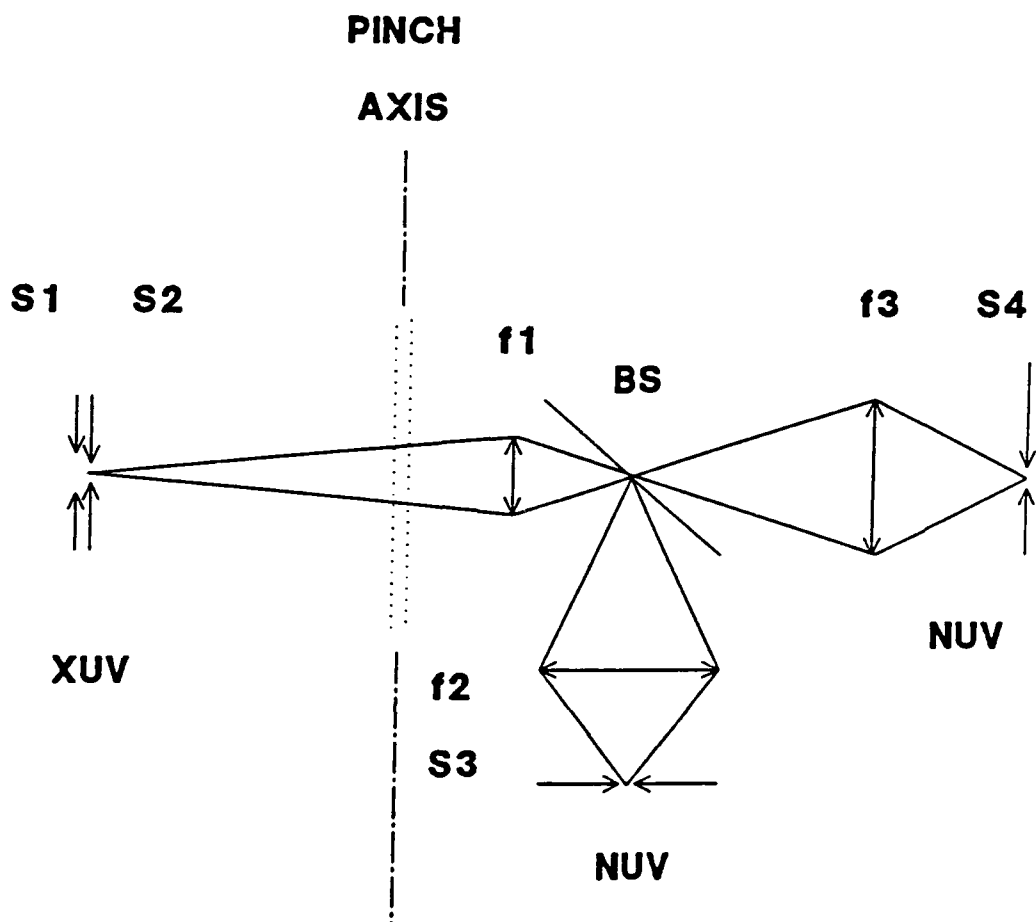


FIG. D.5. Arrangement of the NUV monochromators, the XUV monochromator and the associated optics. S2, S3, and S4 are spectrometer entrance slits. F1, F2, and F3 are lenses. BS is a beam splitter.

on different spectral regions provided a measure of the difference in the emission between the two spectral regions. This technique was used to separate the time history of line radiation from continuum radiation in a nearby but broader spectral region.

The two NUV instruments were used in conjunction with the XUV monochromator (see Fig. D.5) to provide a measure of the relative sensitivity of the NUV and XUV monochromators by the branching-ratio technique. The Ne VIII 3s-3p signal in the NUV monochromator was measured simultaneously with the Ne VIII 2s-3p transition in the XUV monochromator. When the NUV and XUV spectrometers were set up to view the same region of the imploding plasma, good correlations between the time histories were recorded by the three instruments, as expected in this setup.

With the monochromator arrangement in Fig. D.5, time histories of Ne VII, Ne VIII, and continuum emission were measured. One spectrometer, S3 in Fig. D.5, (Bausch and Lomb, 0.5 meter) was mounted with an exit slit and photomultiplier to monitor continuum emission at 2810 Å. The photomultiplier was operated at current levels that were determined to be linear. Two lenses, f1 and f2, with focal lengths of 100 mm and 125 mm imaged the entrance slit of XUV monochromator S2 at the entrance slit of NUV monochromator S3. A 6-mm diameter aperture on lens f1 restricted the area and solid angle of the plasma viewed by the NUV monochromators to that viewed by the XUV monochromator (see Sec. D.2). The other NUV spectrometer, S4 in Fig. D.5, (Spex, 0.5 meter) was also mounted with an exit slit and photomultiplier. A beam splitter BS was used to direct light from the plasma to NUV monochromators S3 and S4. Lens f3 with a 125-mm focal length was used to image the entrance slit of the XUV monochromator S2 at the entrance

slit of NUV monochromator S4. Lens f3 and monochromator S4 were adjusted to view the same region of plasma as NUV monochromator S3.

Time histories of NUV emission from a neon implosion measured with the two NUV monochromators are given in Fig. D.6 along with a time history of the XUV monochromator. Similar time histories of continuum emission are observed for the two NUV monochromators. The good agreement between the two NUV instruments is a measure of the precision of their relative sensitivity. All three instruments record peak emissions at a single implosion, however the XUV emission has a different time history because this instrument is recording the Ne VIII 2s-3p line emission. The NUV monochromators were also used to record emissions in two different spectral regions simultaneously. One monochromator positioned at 2820.7 Å recorded the Ne VIII 3s-3p emission as well as the continuum, whereas the other monochromator positioned at 2810 Å recorded only the continuum (for Ne VIII 3s-3p line-widths less than 20 Å). The difference in these two signals provided a measure of the time history of the Ne VIII 3s-3p emission. This time history is compared with the Ne VIII 2s-3p emission, recorded simultaneously with the XUV monochromator, to determine the relative sensitivity of the XUV and NUV monochromators by the branching-ratio technique. The time histories of neon emission at 2810 and 2820.7 Å taken with the two NUV monochromators are given in Fig. D.7(a). The difference in these signals (Ne VIII 3s-3p transition) is given in Fig. D.7(b) along with the XUV signal at 88 Å (Ne VIII 2s-3p transition). The time histories in Fig. D.7(b) show good correlation particularly in the interval from 0.8 to 1.2 μs when the continuum emission is small. Similar time histories of 2810 and 2820.7 Å emissions for an implosion driven with the plasma opening

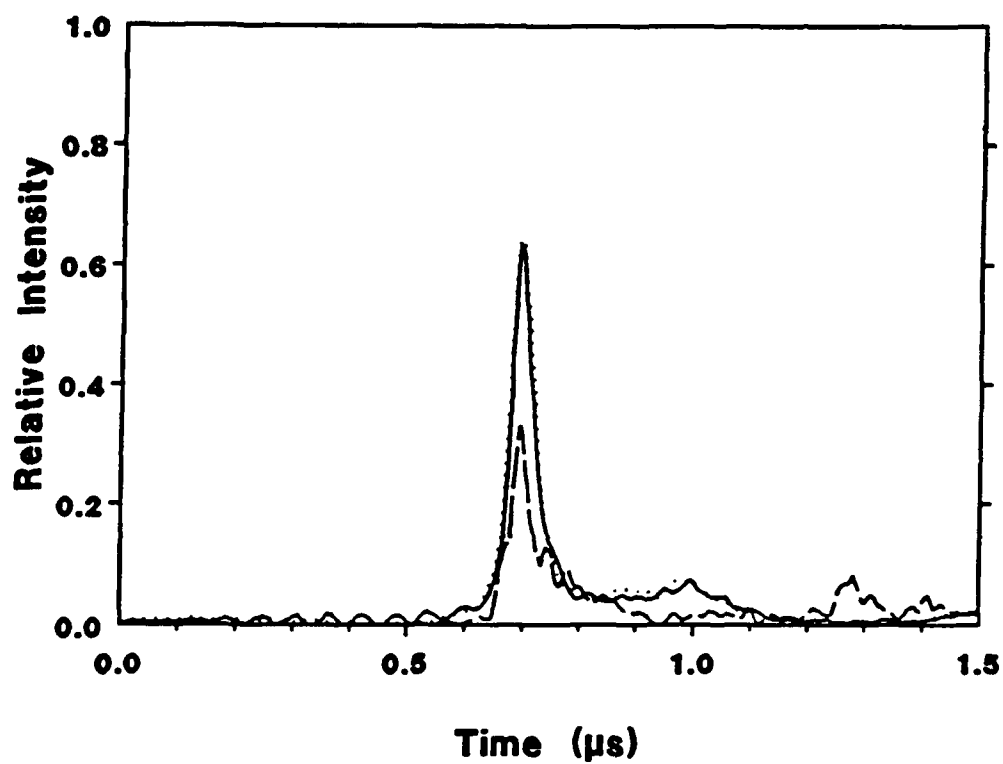


FIG. D.6 Neon emission at 2810 Å from both NUV monochromators (solid and dotted) and neon emission at 88 Å from the XUV monochromator (dashed).

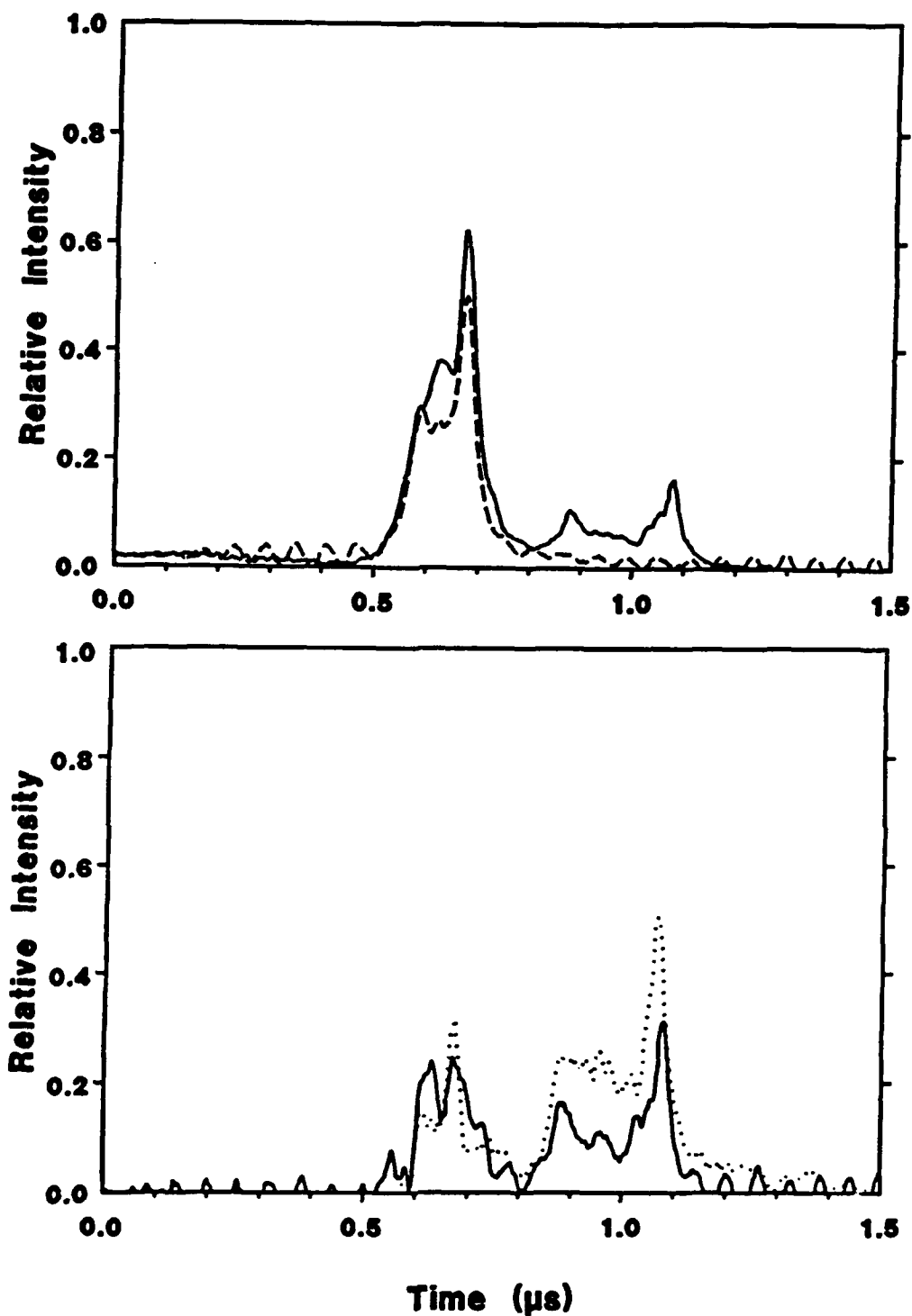


FIG. D.7. (a) Neon NUV emissions at 2810 \AA (dashed) and 2820.7 \AA (solid). (b) Ne VIII emissions at 88 \AA (dotted) and at 2820.7 \AA (solid). The solid curve is the difference between two NUV time histories in Fig. D.7(a).

switch are given in Fig. D.8(a). The difference in these signals is given in Fig. D.8(b) along with the XUV signal at 88 Å. The time histories in Fig. D.8(b) show good correlation in the interval from 1.0 to 1.4 μs. When the continuum emission is large, 0.65 μs in Fig. D.7 and 0.9 μs in Fig. D.8, the difference signals are less reliable, and the correlations are not as good. Also, the correlations may be impaired by continuum emission at 88 Å or by variations in the Ne VIII 3s-3p line width. Continuum emission at 88 Å could account for up to 20% of the XUV signal at the time of the first peak, and considerably less at other times. The instrument function of the monochromator used to monitor the Ne VIII 3s-3p transition was fixed by the entrance- and exit-slit widths and the dimensions of the spectrograph and grating. The instrumental width was measured by scanning the monochromator in wavelength through the Hg I 2753-Å line from a mercury lamp. A full-width at half-intensity of 1.5 Å was measured. The Ne VIII 3s-3p transition was broadened to several Angstroms by plasma effects (see Sec. 7.3.2). Therefore, the NUV monochromator sampled only a portion of the line profile. The slit widths of the NUV monochromator were chosen to maximize the Ne VIII 3s-3p signal relative to the continuum.

The difference between the two NUV monochromators was also used to monitor the emission from Ne VIII while a simultaneous measurement was made of the emission from Ne VII with the XUV monochromator. The difference between the emission at 2810 Å and 2820.7 Å, as previously discussed, gave a reliable measure of the time history of emission from the 3p level of Ne VIII. The XUV monochromator was scanned in wavelength to locate the Ne VII 2p-3d transition at 106 Å. Then, the three monochromators provided simultaneous measurements of time

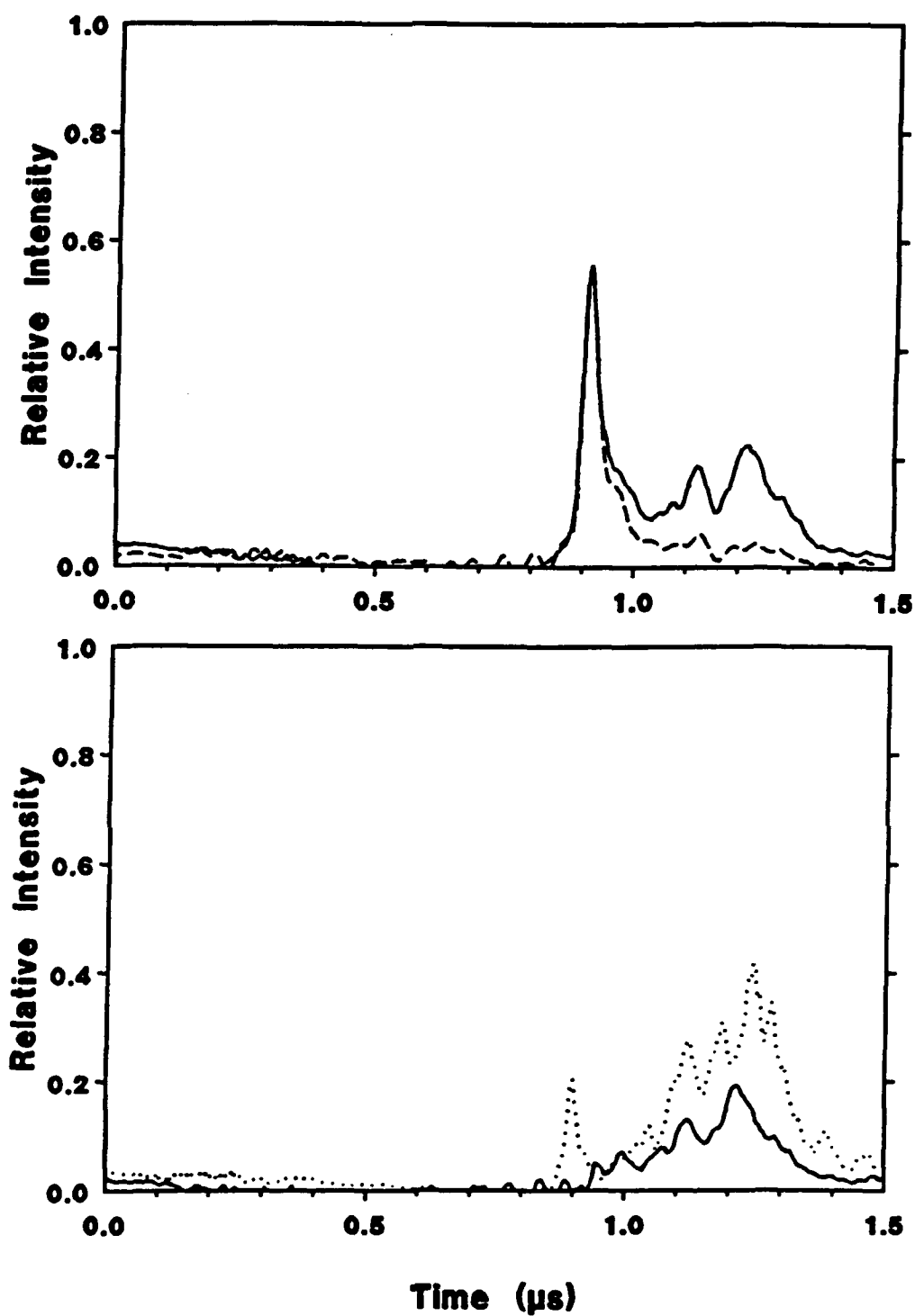


FIG. D.8. (a) Neon NUV emissions at 2810 Å (dashed) and 2820.7 Å (solid) for an implosion with the POS. (b) Ne VIII emissions at 88 Å (dotted) and at 2820.7 Å (solid) for the same implosion. The solid curve is the difference between two NUV time histories in Fig. D.8(a).

histories of Ne VII and Ne VIII emissions. As an example, neon emission at 2810 Å and 2820.7 Å, taken with the two NUV monochromators, is given in Fig. D.9(a), while the difference in these signals (Ne VIII 3s-3p transition) is given in Fig. D.9(b) along with the XUV signal at 106 Å (Ne VII 2p-3d transition). Differences in the Ne VII and Ne VIII time histories are evident in Fig. D.9(b). The Ne VIII emission is delayed relative to Ne VII emission, particularly for the second peak, and maximum Ne VIII emission occurs after maximum Ne VII emission. Ne VII and Ne VIII time histories for an implosion with the plasma opening switch are given in Fig. D.10. Emissions at 2810 and 2820.7 Å are given in Fig. D.10(a) while the difference in these signals is given in Fig. D.10(b) along with the XUV signal at 106 Å. The time histories in Fig. D.10(b) indicate that the Ne VIII and Ne VII emissions occur at similar times, and that the duration of the Ne VII emission is longer.

D.3.2 Optical Multichannel Analyzer

A gated optical multichannel analyzer (OMA) was mounted to the exit of NUV spectrograph S4 (see Fig. D.5). Initially measurements were taken with both NUV spectrographs viewing the same region of plasma to determine the relative response of the OMA detector and the photomultiplier tube. The OMA was found to be linear over the range of intensities encountered in these measurements. Then the optics were changed to provide spacial resolution in the direction transverse to the Z-pinch axis at the location of the OMA. The OMA was calibrated by comparison with a deuterium lamp of known intensity. The OMA was gated to provide a spacial and spectral measure of the

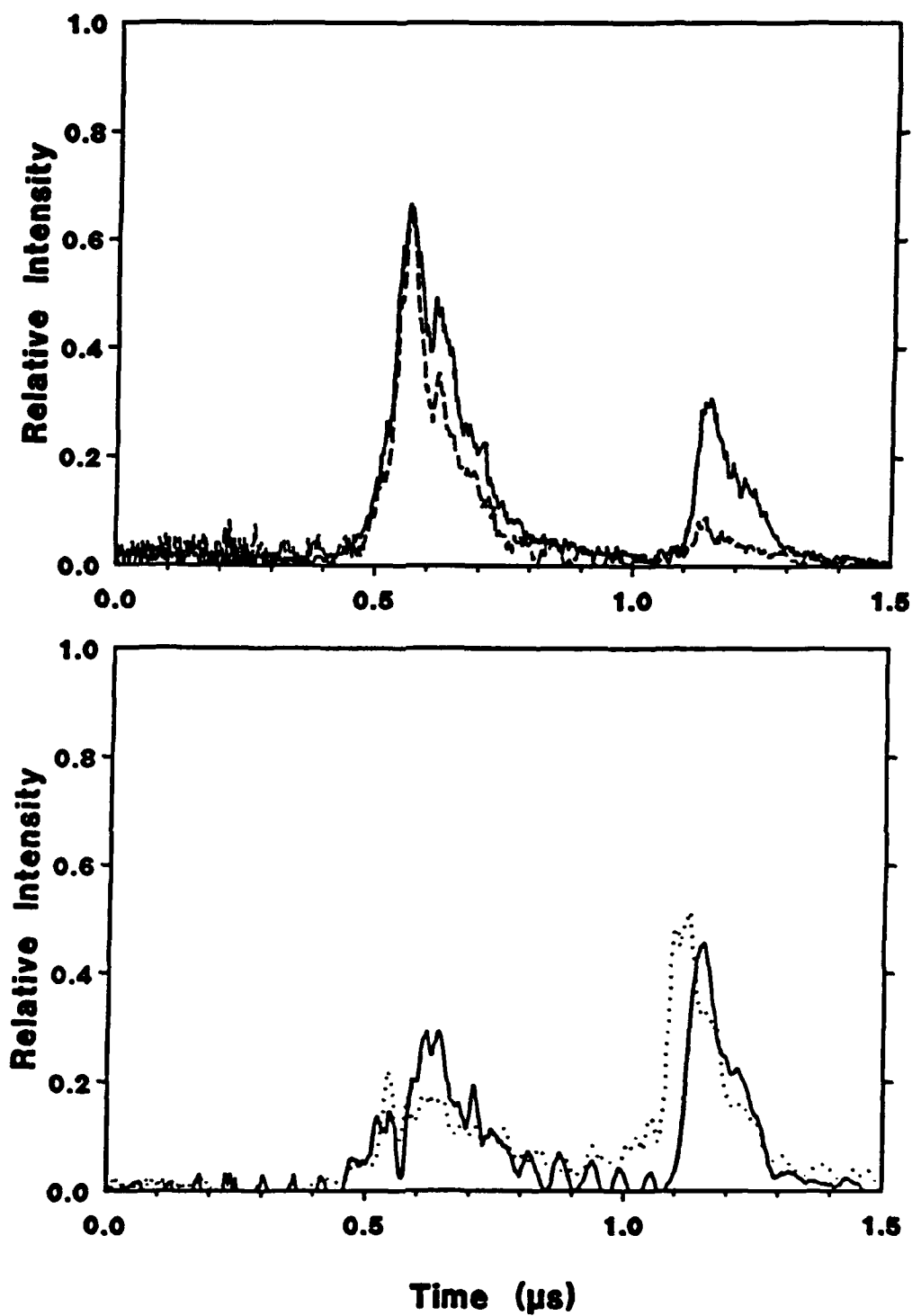


FIG. D.9. (a) Neon emissions at 2810 \AA (dashed) and 2820.7 \AA (solid) for an implosion without the POS. (b) Ne VII emission at 106 \AA (dotted) and Ne VIII emission (solid). The solid curve is the difference between the two NUV time histories in Fig. D.9(a).

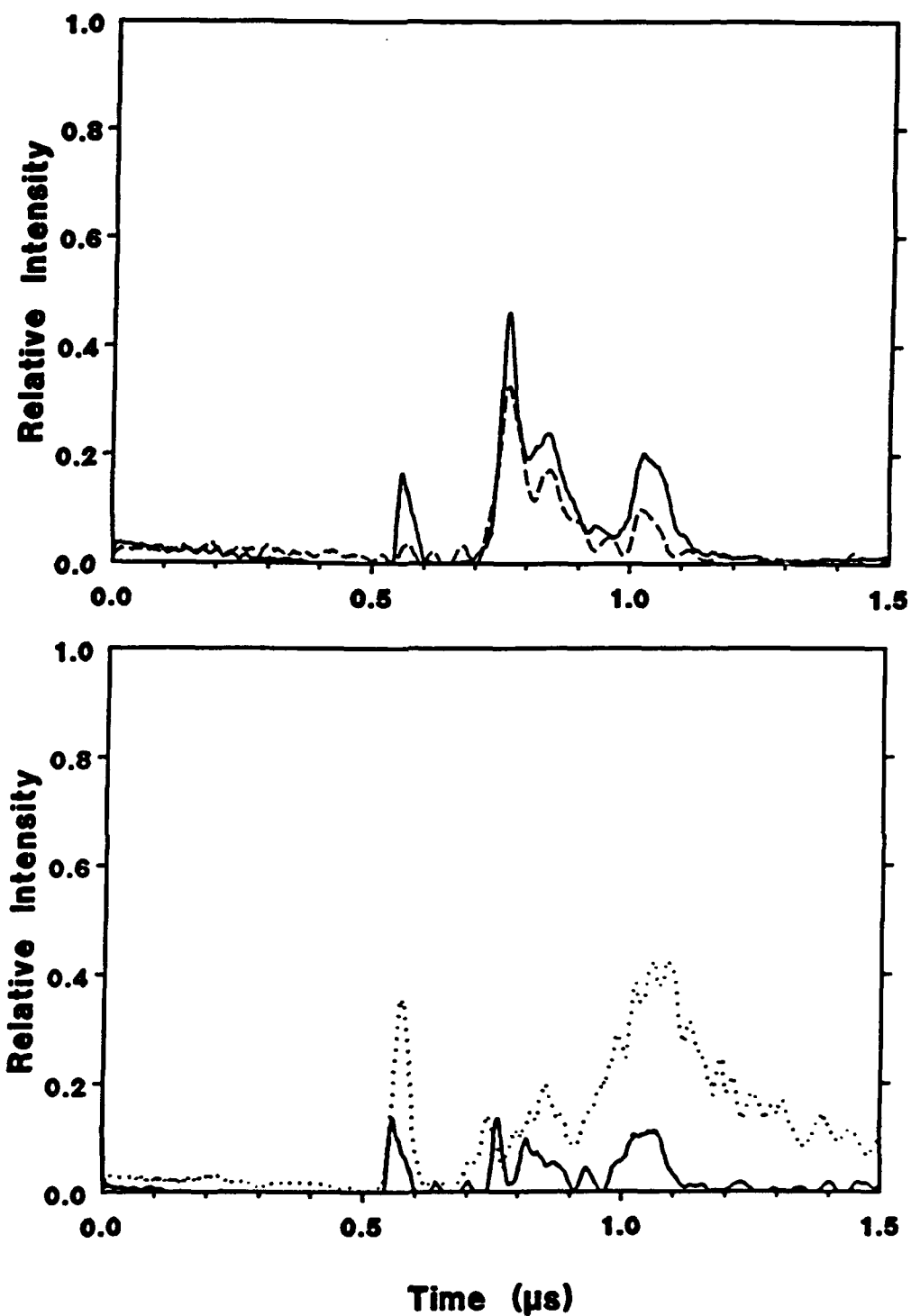


FIG. D.10. (a) Neon emissions at 2810 Å (dashed) and 2820.7 Å (solid) for an implosion with the POS. (b) Ne VII emission at 106 Å (dotted) and Ne VIII emission at 2820.7 Å (solid). The solid curve is the difference between the NUV time histories in Fig. D.10(a).

intensity of the radiation integrated over the 100-ns gate pulse. A 512 by 512 array of silicon detectors located in a 1-inch by 1-inch area gave 50- μm spacial separation between tracks along the entrance slit and 0.4- \AA spectral separation along the dispersion axis. The signal was summed over ten tracks giving a 500- μm spacial resolution along the entrance slit. The spectral resolution of the OMA was determined by measuring the Hg I 2753- \AA transition from a mercury lamp. The width of this line is expected to be smaller than the instrumental broadening of the spectrometer. A full-width at half-intensity of 1.5 \AA was measured.

The initial arrangement of the spectrometers was the same as shown in Fig. D.5, with the OMA mounted on S4. This insured that the spectrometer with the OMA was viewing the same area of plasma as NUV monochromator S3 and XUV monochromator S2. The OMA and photomultiplier responses were used to determine the relative sensitivity of these two NUV instruments. The OMA was gated with a 100-ns voltage pulse adjusted to occur at various times during the discharge to provide a spectrum integrated over the duration of the gate. The intensity of radiation at 2810 \AA measured with the OMA was summed over the diameter of the plasma and compared with the intensity of the radiation at 2810 \AA measured with the photomultiplier tube after summing over the time period of the gate pulse. Various intensities were recorded depending on the timing of the gate pulse. A comparison of spacially-integrated OMA signals and time-integrated photomultiplier signals is given in Fig. D.11. The deviation from linearity at 5 mV is a result of electrical noise present during the Z-pinch discharge contributing to the photomultiplier signal. A comparison of the response of these detectors to a lower-intensity

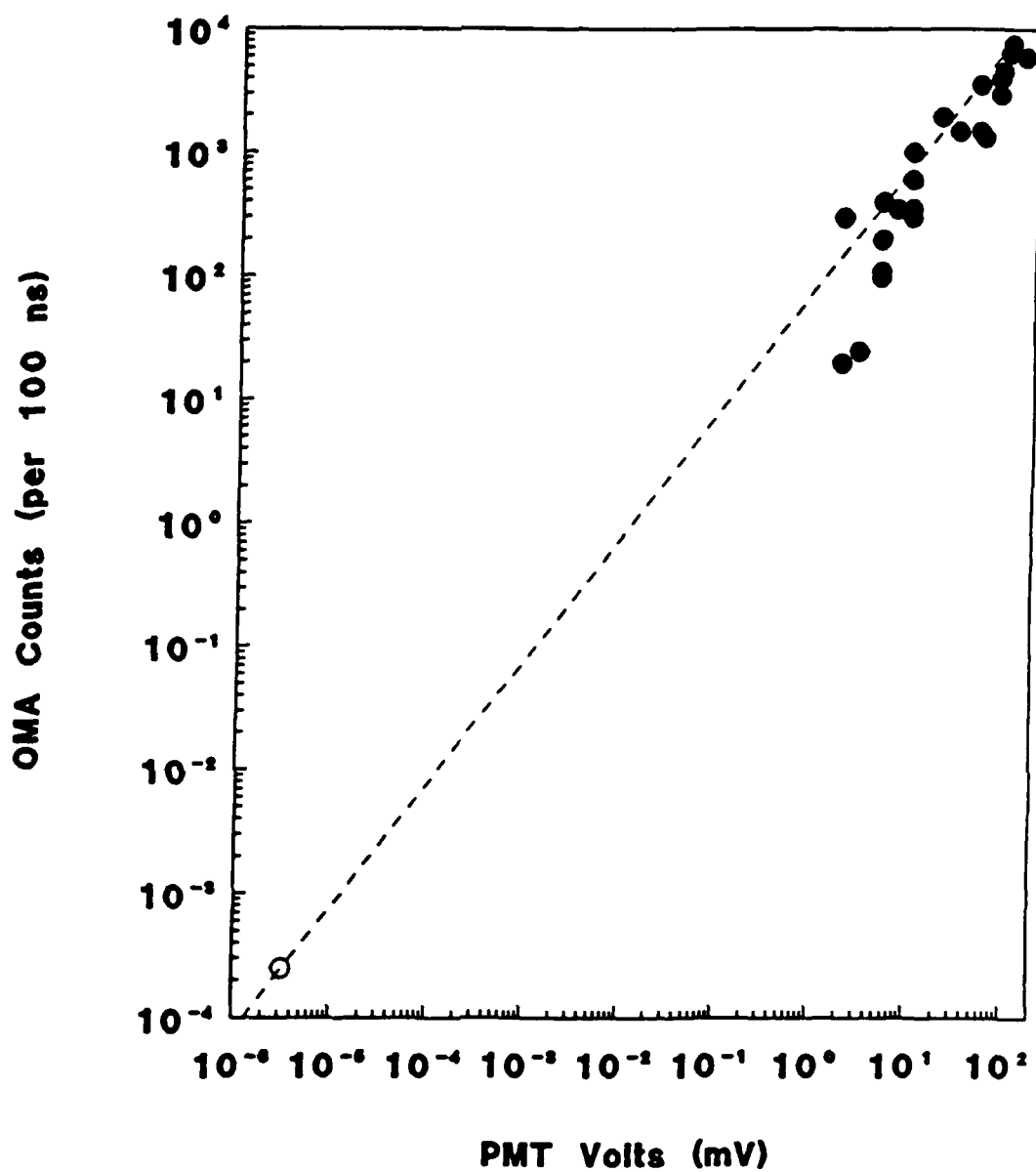


FIG. D.11. Comparison of the OMA and photomultiplier (PMT) responses at 2810 Å. The solid circles are for the neon Z-pinch while the open circle is for the deuterium lamp.

source was made with a deuterium lamp. The dynamic range of the OMA detector was extended for this measurement by increasing the time period over which the intensity was recorded. A time period of 92 ms was used. The results in Fig. D.11 demonstrate a linear relationship between the OMA and the photomultiplier detectors over more than seven orders of magnitude.

After the linear response of the OMA was established, the optical path between the plasma and the spectrometer with the OMA was changed to provide spacial resolution of the plasma at the entrance slit of the spectrograph. This optical arrangement is shown in Fig. D.12. A lens with a focal length of 100 mm (f4) was used to image emission from the Z-pinch at the entrance slit of the spectrometer. The appropriate location for this lens was determined when the instruments were initially aligned so that interference with the alignment of the other instruments was minimal with this change. The spacially resolving property of this optical arrangement is illustrated by the side view in Fig. D.13. The spacial resolution of the OMA was determined by placing a small Hg lamp with a 3-mm aperture at the location of the Z-pinch. A spacial resolution of 0.5 mm was determined. This is consistent with the OMA instrument resolution and the magnification of the optical system. The response of the OMA to a deuterium lamp of known intensity was measured subsequent to the experiments with the lamp placed at the location of the Z-pinch.¹⁶⁴ The OMA measurement was 700 counts/channel in a time of 92 ms. The intensity of the deuterium lamp was 8.5×10^3 Watts/cm³sr.

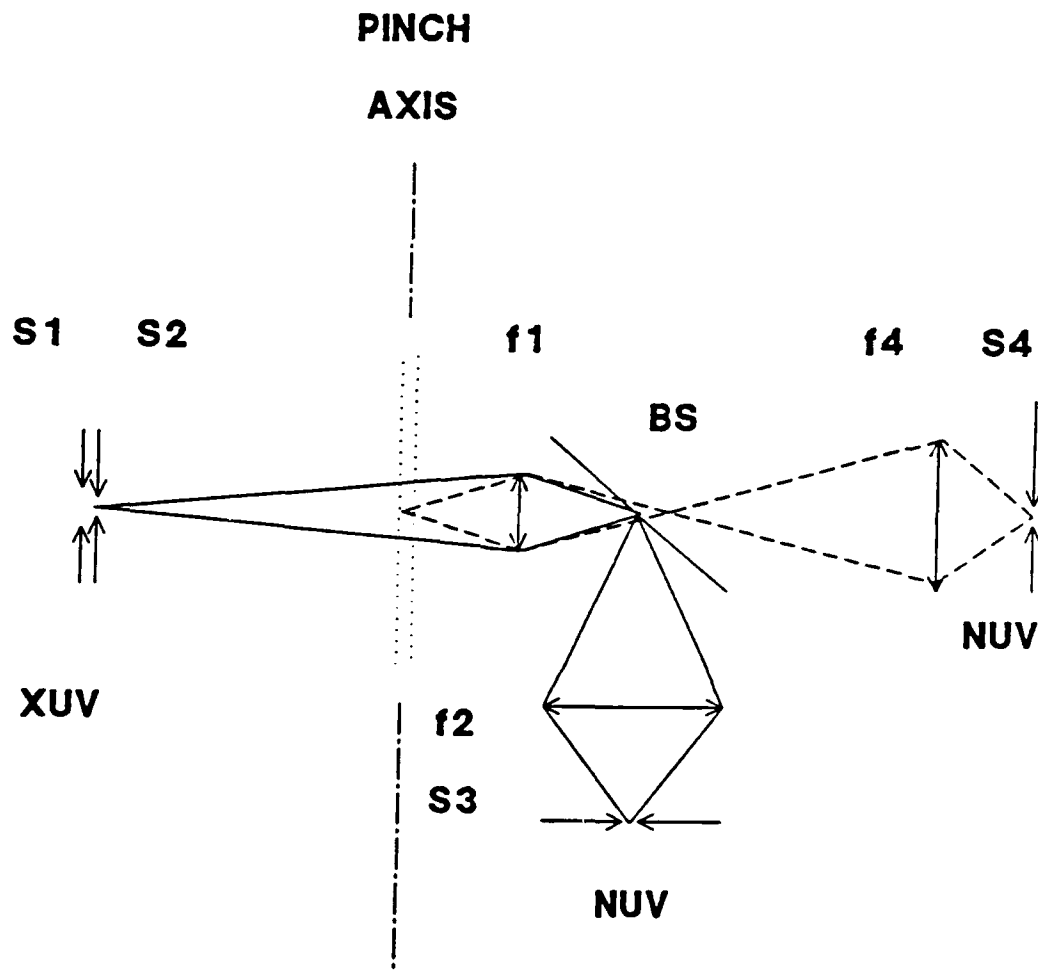


FIG. D.12. Optical arrangement (top view) for spatially resolved measurements with the OMA mounted on S4. The labels are identified in Fig. D.5.

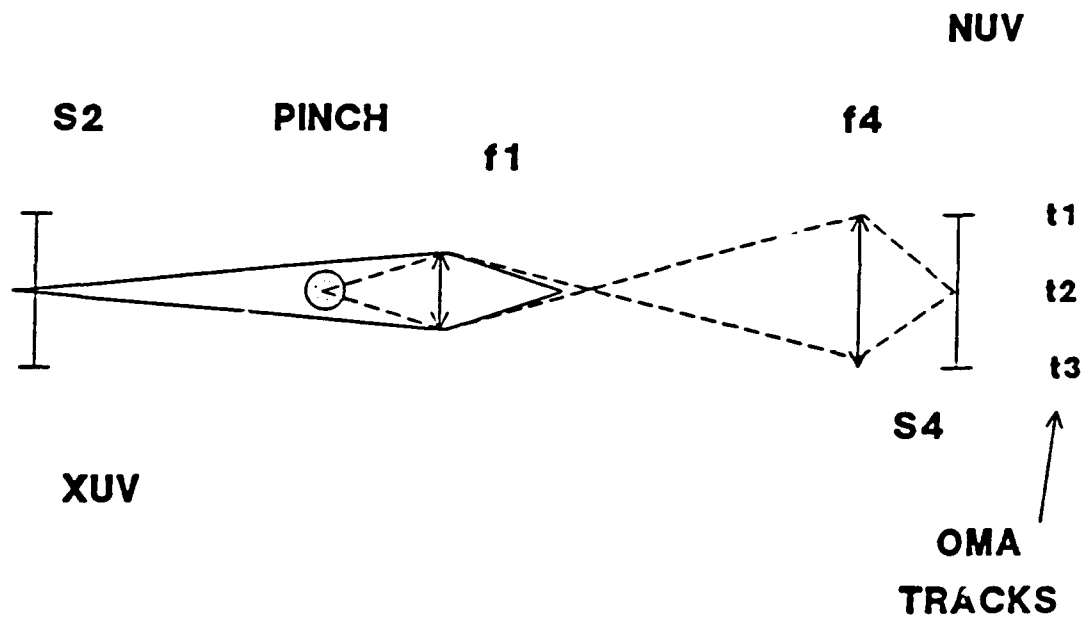


FIG. D.13. Optical arrangement (side view) for spatially resolved measurements with the OMA mounted on S4. Spectral tracks from the OMA correspond to different spatial locations along the diameter of the pinch.

Bibliography

- [1] Richard A. London, Mordecai D. Rosen, and James E. Trebes, Appl. Opt., 28, 3397 (1989).
- [2] A.V. Vinogradov, I.I. Sobel'man, and E.A. Yukov, Sov. J. Quantum Electron. 5, 59 (1975).
- [3] B.A. Norton, and N.J. Peacock, J. Phys. B 6, 989 (1975).
- [4] F.C. Young, S.J. Stephanakis, V.E. Sherrer, B.L. Welch, G. Melhman, P.G. Burkhalter, and J.P. Apruzese, Appl. Phys. Lett. 60, 3427 (1987).
- [5] S.J. Stephanakis, J.P. Apruzese, P.G. Burkhalter, G. Cooperstein, J. Davis, D.D. Hinshelwood, G. Melhman, D. Mosher, P.F. Ottinger, V.E. Sherrer, J.W. Thornhill, B.L. Welch, and F.C. Young, IEEE Trans. Plasma Sci. PS-16, 472 (1988).
- [6] J.P. Apruzese, J. Davis, and K.G. Whitney, J. Appl. Phys., 53, 4020 (1982).
- [7] R.C. Elton, X-ray Lasers (Academic Press, San Diego, 1990), p. 54.
- [8] D.L. Matthews, P.L. Hagelstein, M.D. Rosen, M.J. Eckart, N.M. Ceglio, A.U. Hazi, H. Medeck, B.J. MacGowan, J.E. Trebes, B.L. Whitten, E.M. Campbell, C.W. Hatcher, A.M. Hawryluk, R.L. Kauffman, L.D. Pleasance, G. Rambach, J. H. Scofield, G. Stone, and T.A. Weaver, Phys. Rev. Lett. 54, 110 (1985).
- [9] N.R. Pereira, and J. Davis, J. Appl. Phys., 64, R1 (1988).
- [10] J.P. Apruzese, G. Mehlman, J. Davis, J.E. Rogerson, V.E. Sherrer, S.J. Stephanakis, P.F. Ottinger, and F.C. Young, Phys. Rev. A 35, 4896 (1987).
- [11] G. Cooperstein and P.F. Ottinger, IEEE Trans. Plasma Sci. PS-15, 629 (1987).
- [12] F.C. Young, V.E. Sherrer, S.J. Stephanakis, D.D. Hinshelwood, P.J. Goodrich, G. Mehlman, D.A. Newman, and B.L. Welch, Proceedings of the International Conference on LASERS '88, edited by R.C. Sze and F.J. Duarte (STS Press, McLean, VA, 1989), p. 98.
- [13] C. Deeney, T. Nash, R.R. Prasad, M. Krishnan, D. Hinshelwood, and F.C. Young, Proceedings of the International Conference on LASERS '89, edited by E.G. Harris and T.M. Shay (STS Press, McLean, VA, 1990), p. 21.
- [14] C. Deeney, R.R. Prasad, T. Nash, and N. Knobel, Rev. Sci.

Instrum. 61, 1551 (1990).

- [15] M.K. Matzen, J.L. Porter, R.B. Spielman, B.A. Hammel, W.W. Hsing, T.W. Hussey, and E.J. McGuire, Proceedings of the International Conference on LASERS '89, edited by D.G. Harris and T.M. Shay (STS Press, McLean, VA, 1990), p. 86.
- [16] J.P. Apruzese, R.W. Clark, and J. Davis, Proc. Lasers '90, 39 (1990).
- [17] R.C. Elton, X-ray Lasers (Academic Press, San Diego, 1990), pp. 22-23.
- [18] R.C. Elton, X-ray Lasers (Academic Press, San Diego, 1990), p. 11.
- [19] R.W. Waynant and R.C. Elton, in Proceedings of the IEEE, 64, (IEEE, New York, 1976), p. 1059.
- [20] R.C. Elton, X-ray Lasers (Academic Press, San Diego, 1990), p. 157.
- [21] B.J. MacGowan, et al., J. Appl. Phys. 61, 5243 (1987).
- [22] C. Keane, et al., Bull. Am. Phys. Soc. 33, 2041 (1988).
- [23] T.N. Lee, E.A. McLean, and R.C. Elton, in Atomic Processes in Plasmas, AIP Conf. Proc. No. 168, A. Hauer and A.I. Merts, Eds., p. 125 (American Institute of Physics, New York, 1988).
- [24] T.N. Lee, E.A. McLean, J.A. Stamper, H.R. Griem, and C. Manka, Bull. Am. Phys. Soc. 33, 1920 (1988).
- [25] B.J. MacGowan, et al., Bull. Am. Phys. Soc. 33, 2042 (1988).
- [26] M.H. Key, C.L.S. Lewis, and M.J. Lamb, Opt. Commun. 28, 331 (1979).
- [27] D. Jacoby, G.J. Pert, S.A. Ramsden, L.D. Shorrock, and G.J. Tallents, Opt. Commun. 37, 193 (1981).
- [28] J.F. Seely, C.M. Brown, U. Feldman, M. Richardson, B. Yaakob, and W.E. Behring, Opt. Commun. 54, 289 (1985).
- [29] D.L. Matthews, E.M. Campbell, K. Estabrook, W. Hatcher, R.L. Kauffman, R.W. Lee, and C.L. Wang, Appl. Phys. Lett. 45, 226 (1984).
- [30] P.R. Herman, T. Tachi, K. Shihoyama, H. Shiraga, and Y. Kato, IEEE Trans. Plasma Sci. 16, 520 (1988).
- [31] C.L.S. Lewis, et al., Plasma Phys. and Controlled Fusion 30, 35 (1988).
- [32] O. Willi, et al., in Atomic Processes in Plasmas, AIP Conf.

- Proc. No. 168, A. Hauer and A.I. Merts, Eds., (American Institute of Physics, New York, 1988), p. 115.
- [33] H. Milchberg, J.L. Schwob, C.H. Skinner, S. Suckewer, and D. Voorhees, in Atomic Processes in Plasmas, AIP Conf. Proc. No. 168, A. Hauer and A.I. Merts, Eds., (American Institute of Physics, New York, 1988), p. 379.
 - [34] V.A. Bhagavatula and B. Yaakobi, *Opt. Commun.* 24, 331 (1978).
 - [35] P. Jaegle', G. Jamelot, A. Carillon, A. Klisnick, A. Sureau, H. Guennou, in Atomic Processes in Plasmas, AIP Conf. Proc. No. 168, A. Hauer and A.I. Merts, Eds., (American Institute of Physics, New York, 1988), p. 468.
 - [36] C.H. Skinner, D. Dicicco, D. Kim, L. Meixler, C.H. Nam, W. Tighe, and S. Suckewer, *IEEE Trans. Plasma Sci.* 16, 512 (1988).
 - [37] J. C. Moreno, H. R. Griem, S. Goldsmith and J. Knauer, *Phys. Rev. A* 39, 6033 (1989).
 - [38] G. Jamelot, P. Jaeglé, A. Carillon, F. Gadi, B. Gauthé, H. Guennou, A. Klisnick, C. Möller, and A. Sureau, *IEEE Trans. Plasma Sci.* 16, 497 (1988).
 - [39] S. Suckewer, C.H. Skinner, H. Milchberg, C. Keane, D. Voorhees, *Phys. Rev. Lett.* 55, 1753 (1985).
 - [40] P. Rabinowitz, S. Jacobs, and G. Gould, *Appl. Opt.* 1, 513 (1962).
 - [41] V.A. Bhagavatula, *J. Appl. Phys.* 47, 4535 (1976).
 - [42] J. Trebes and M. Krishnan, *Phys. Rev. Lett.* 50, 679 (1983).
 - [43] R.H. Dixon and R.C. Elton, *J. Opt. Soc. Am. B* 1, 232 (1984).
 - [44] F.L. Cochran, J. Davis, and J.P. Apruzese, *J. Appl. Phys.* 57, 27 (1985).
 - [45] J.P. Apruzese and J. Davis, *Phys. Rev. A* 31, 2976 (1985).
 - [46] J.P. Apruzese and J. Davis, *J. Appl. Phys.* 57, 4349 (1985).
 - [47] J. Davis, J.E. Rogerson, J.P. Apruzese, *NRL Memorandum Report* 5765, (1986).
 - [48] V.E. Jacobs, J. Davis, J.E. Rogerson, and M. Blaha, *Astrophys. J.* 230, 627 (1979).
 - [49] W.C. Martin (private communication). W.C. Martin, *Physica Scripta.* 24, 24 (1981).
 - [50] B. Schiff, C.L. Pekeris, and Y. Accad, *Phys. Rev. A* 4, 885 (1971).

- [51] P.L. Haglestein, Lawrence Livermore National Laboratory Report UCRL-53100 (1981).
- [52] F. E. Irons, J. Phys. B 8, 3044 (1975).
- [53] R.C. Elton, X-ray Lasers (Academic Press, San Diego, 1990), p. 38.
- [54] H.R. Griem, M. Blaha, and P. Kepple, Phys. Rev. A 41, 5600 (1990).
- [55] B. Yaakobi, D. Steel, E. Thoros, A. Hauer, and B. Perry, Phys. Rev. Lett. 39, 1526 (1977).
- [56] J.P. Apruzese, P.C. Kepple, J. Davis, and D. Duston, Phys. Rev. A 24, 1001 (1981).
- [57] J.C. Lunney, R.E. Corbett, M.J. Lamb, C.L.S. Lewis, P. McCavana, L.D. Shorrock, S.J. Rose, and F. Pinzong, Opt. Commun. 50, 367 (1984).
- [58] M.H. Key, Plasma Phys. and Controlled Fusion 26, 1383 (1984).
- [59] R.H. Dixon, J.L. Ford, T.N. Lee, and R.C. Elton, Rev. Sci. Instrum. 56, 471 (1985).
- [60] R.C. Elton, T.N. Lee, and W.A. Molander, Phys. Rev. A 33, 2817 (1986).
- [61] R.C. Elton, T.N. Lee, and P.G. Burkhalter, Nuclear Instrum. Methods in Phys. Res. B9, 753 (1985).
- [62] R.J. Commisso, G. Cooperstein, R.A. Meger, J.M. Neri, P.F. Ottinger, Opening Switches, edited by A. Guenther, M. Kristiansen, and T. Martin, (Plenum Publishing Corp., 1987), p. 149.
- [63] F.C. Young, S.J. Stephanakis, and D. Mosher, J. Appl. Phys. 48, 3642 (1977).
- [64] J.D. Sethian, A.E. Robson, K.A Gerber, and A.W. DeSilva, Phys. Rev. Lett. 59, 892 (1987).
- [65] J. Bailey, Y. Ettinger, A. Fisher, and N. Rostoker, Appl. Phys. Lett. 40, 460 (1982).
- [66] M. Coppins, D.J. Bond, and M.G. Haines, Phys. Fluids 27, 2886 (1984).
- [67] F. Böttcher, J. Musielok, and H.-J. Kunze, Phys. Rev. A 36, 2265 (1987).
- [68] J. Shilo, A. Fisher, and N. Rostoker, Phys. Rev. Lett. 40, 515 (1978).

- [69] P. Burkhalter, J. Davis, J. Rauch, W. Clark, G. Dalbacka, and R. Schneider, *J. Appl. Phys.* 50, 705 (1979).
- [70] J. D. Perez, L. F. Chase, R.E. McDonald, L. Tannenwald, and B.A. Watson, *J. Appl. Phys.* 52, 670 (1981).
- [71] J. H. Degan, R.E. Reinovsky, D.L. Honea, and R.D. Bengtson, *J. Appl. Phys.* 52, 6550 (1981).
- [72] M.K. Matzen, R.J. Dukart, B.A. Hammel, D.L. Hanson, W.W. Hsing, T.W. Hussey, E.J. McGuire, M.A. Palmer, and R.P. Spielman, in Multilayer Structures and Laboratory X-Ray Laser Research, SPIE Vol. 688, 61 (1986).
- [73] A.E. Dangor, *Plasma Phys. and Controlled Fusion* 28, 1931 (1986).
- [74] M. Choppins, *Plasma Phys. and Controlled Fusion* 30, 201 (1988).
- [75] N. Pereira, J. Davis, and N. Rostocker, Eds., Proceedings of the 2nd International Conference on Dense Z-Pinches, Laguna Beach, CA, 1989, (AIP, New York, 1989).
- [76] W. H. Bennett, *Phys. Rev.* 45, 890 (1934).
- [77] R.S. Pease, *Proc. Phys. Soc. London* B70, 11 (1957).
- [78] J.P. Apruzese and P.C. Kepple, in Proceedings of the 2nd International Conference on Dense Z-Pinches, Laguna Beach, CA, 1989, edited by N.R. Pereira, J. Davis, and N. Rostoker (AIP, New York, 1989), p. 108.
- [79] D.L. Book, *NRL Publication* 177-4405, 34 (1991).
- [80] S.W. McDonald and P.F. Ottinger, *NRL Memorandum Report* 5785, pp. 19-21 (1986).
- [81] D.E. Post, R.V. Jensen, C.B. Tarter, W.H. Grasberger, and W.A. Lokke, *Atomic Data and Nuclear Data Tables* 20, 397 (1977).
- [82] P.J. Turchi and W.L. Baker, *J. Appl. Phys.* 44, 4936 (1973).
- [83] J. Katzenstein, *J. Appl. Phys.* 52, 676 (1981).
- [84] M. Krishnan, C. Denney, T. Nash, P.D. LaPell, K. Childers, in Proceedings of the 2nd International Conference on Dense Z-Pinches, Laguna Beach, CA, 1989, edited by N.R. Pereira, J. Davis, and N. Rostoker (AIP, New York, 1989), p. 17.
- [85] N.R. Pereira, N. Rostoker, and J.S. Pearlman, *J. Appl. Phys.* 55, 704 (1984).
- [86] J. Nycander and C. Wahlberg, *Nucl. Fusion* 24, 1357 (1984).
- [87] F.C. Young, S.J. Stephanakis, V.E. Sherrer, *Rev. Sci. Instrum.*

57, 2174 (1986).

- [88] G. Mehlman, P.G. Burkhalter, S.J. Stephanakis, F.C. Young, and D.J. Nagel, J. Appl. Phys. 60, 3427 (1986).
- [89] S.J. Stephanakis, J.P. Apruzese, P.G. Burkhalter, J. Davis, R.A. Meger, S.W. McDonald, G. Mehlman, P.F. Ottinger, and F.C. Young, Appl. Phys. Lett. 48, 829 (1986).
- [90] J.W. Thornhill, K.G. Whitney, and J. Davis, J. Quant. Spectrosc. Radiat. Transfer 44, 251 (1990).
- [91] S.J. Stephanakis, S.W. McDonald, P.F. Ottinger, J.R. Boller, V.E. Sherrer, and F.C. Young, Bull. Am. Phys. Soc. 30, 1389 (1985).
- [92] S.W. McDonald, P.F. Ottinger, S.J. Stephanakis, and F.C. Young, Bull. Am. Phys. Soc. 30, 1389 (1985).
- [93] R. Rodenburg, S. Wong, L. Koppel, and L. Burr, "Neon Source Optimization on Double-EAGLE", 1985 IEEE International Conference on Plasma Sci., (Pittsburgh, PA. 3-5 June 1985), p. 92.
- [94] R.B. Spielman, R.J. Dukart, D.L. Hanson, B.A. Hammel, W.W. Hsing, M.K. Matzen, J.L. Porter, in Proceedings of the 2nd International Conference on Dense Z-Pinches, Laguna Beach, CA, 1989, edited by N.R. Pereira, J. Davis, and N. Rostoker (AIP, New York, 1989), p. 3.
- [95] B.L. Welch, F.C. Young, R.J. Comisso, D.D. Hinshelwood, D. Mosher, and B.V. Weber, J. Appl. Phys. 65, 2664 (1989).
- [96] F. C. Young, S.J. Stephanakis, V.E. Sherrer, B.L. Welch, G. Mehlman, P.G. Burkhalter, and J.P. Apruzese, Appl. Phys. Lett. 50, 1053 (1987).
- [97] P. G. Burkhalter, G. Mehlman, J.P. Apruzese, D.A. Newman, V.E. Sherrer, F.C. Young, S.J. Stephanakis, and D.D. Hinshelwood, J. Quant. Spectrosc. Radiat. Transfer 44, 495 (1990).
- [98] J.P. Apruzese, G. Mehlman, J. Davis, J.E. Rogerson, V.E. Sherrer, S.J. Stephanakis, P.F. Ottinger, and F.C. Young, Phys. Rev. A 35, 4896 (1987).
- [99] F.C. Young, D.D. Hinshelwood, J.P. Apruzese, C. Deeney, T. Nash, R.R. Prasad, J. Appl. Phys. 69, 7520 (1991).
- [100] C. Deeney, T. Nash, R.R. Prasad, L. Warren, and J.P. Apruzese, Appl. Phys. Lett. 58, 1021 (1991).
- [101] J. Nilsen and E. Chandler, Phys. Rev. A (to be published).
- [102] M. Gizaix, H.J. Doucet, B. Etlicher, J.P. Furtlehner, H. Lamain, C. Rouille, J. Appl. Phys. 56, 3209 (1984).

- [103] D.D. Hinshelwood, P.J. Goodrich, G. Melhman, V.E. Sherrer, S.J. Stephanakis, B.L. Welch, and F.C. Young, "Confined Discharge Plasma Sources for Z-Pinch Experiments", 1989 IEEE International Conference on Plasma Sci., (Buffalo, N.Y. 22-24 May 1989), p. 112.
- [104] J.P. Apruzese, P.G. Burkhalter, G. Cooperstein, J. Davis, D. Mosher, P.F. Ottinger, J.E. Rogerson, S.J. Stephanakis, V.E. Sherrer, J.W. Thornhill, F.C. Young, G. Melhman, and B.L. Welch, Proceedings of the International Conference on LASERS '87, edited by F.J. Duarte (STS Press, McLean, VA, 1988), p. 37.
- [105] J.P. Apruzese, R.J. Comisso, G. Cooperstein, J. Davis, G. Melhman, D. Mosher, P.F. Ottinger, J.E. Rogerson, S.J. Stephanakis, V.E. Sherrer, J.W. Thornhill, B.L. Welch, and F.C. Young, in Short and Ultrashort Wavelength Lasers, SPIE 875, 2 (1988).
- [106] J.P. Apruzese, R.W. Clark, J. Davis, J.L. Porter, R.B. Speilman, M.K. Matzen, S.F. Lopez, J.S. McGurn, L.E. Ruggles, M. Vargas, D.K. Derzon, T.W. Hussey, and E.J. McGuire, NRL Memorandum Report 6817, pp. 1-8 (1991).
- [107] D.D. Hinshelwood, J.R. Boller, R.J. Comisso, G. Cooperstein, R.A. Meger, J.M. Neri, P.F. Ottinger, and B.V. Weber, Appl. Phys. Lett. 49, 1635 (1986).
- [108] B.V. Weber, R.J. Comisso, G. Cooperstein, J.M. Grossmann, D.D. Hinshelwood, D. Mosher, J.M. Negri, P.F. Ottinger, and S.J. Stephanakis, IEEE Trans. Plasma Sci. PS-15, 635 (1987).
- [109] C.W. Mendel, Jr., D.M. Zagar, G.S. Mills, S. Humphries, Jr., and S.A. Goldstein, Rev. Sci. Instrum. 51, 1641 (1980).
- [110] S. Wong, P. Smiley, T. Sheridan, J. Levine, and V. Buck, Rev. Sci. Instrum. 57, 1684 (1986).
- [111] C. Silawatshananai, F.S.B. Anderson, M.H. Brennan, G. Durance, I.R. Jones, E.L. Murray, and J. Tendys, Aust. J. Phys. 33, 1001 (1980).
- [112] K.F. Finken and U. Ackermann, J. Phys. D 16, 773 (1983).
- [113] E. Ruden, H.U. Rahman, A. Fisher, N. Rostoker, J. Appl. Phys. 61, 1311 (1987).
- [114] V.A. Boiko, S.A. Pikuz, and A. Ya Faenov, J. Phys. B 12, 1889 (1979).
- [115] R.L. Kelly, J. Phys. Chem. Ref. Data 16, 156 (1987).
- [116] J.A.R. Samson, Techniques of Vacuum Ultraviolet Spectroscopy (Pied Publications, Lincoln, Nebraska, 1967), p. 10.

- [117] B.L. Henke, F.G. Fujiwara, M.A. Tester, C.H. Dittmore, and M.A. Palmer, J. Opt. Soc. Am. B 1, 828 (1984).
- [118] E. Hinnov and F.W. Hofmann, J. Opt. Soc. Am. 53, 1259 (1963).
- [119] W.D. Johnston III and H.-J. Kunze, Astrophys. J. 157, 1469 (1969).
- [120] J.Z. Klose and W.L. Wiese, J. Quant. Spectrosc. Radiat. Transfer 42, 337 (1989).
- [121] A. Denis, J. Desesquelles, and M. Dufay, J. Opt. Soc. Am. 59, 976 (1918).
- [122] T.L. de Bruin, Z. Physik 77, 505 (1932).
- [123] R.L. Kelly, NASA Technical Memorandum 80268, p. 280 (1979).
- [124] W.L. Wiese, in Plasma Diagnostic Techniques, R.H. Huddlestone and S.L. Leonard Eds., (Academic Press, New York, 1965), pp. 299-315.
- [125] H.C. van de Hulst and J.M. Reesinck, Astrophys. J. 106, 121 (1947).
- [126] N. Konjevic and W.L. Wiese, J. Phys. Chem. Ref. Data, (to be published).
- [127] F. Böttcher, P. Breger, J.D. Hey, and H.-J. Kunze, Phys. Rev. A 38, 2690 (1988).
- [128] H.R. Griem, Y.W. Huang, J.-S. Wang, and J.C. Moreno, Phys. of Fluids (to be published).
- [129] J.P. Apruzese (private communication).
- [130] F. Venneri, Bull. Am. Phys. Soc. 33, (post deadline) (1988).
- [131] J.D. Sethian (private communication).
- [132] P.C. Filbert and D.A. Kohler, J. Appl. Phys. 68, 3091 (1990).
- [133] J.D. Shipman, Jr. (private communication).
- [134] H.R. Griem, Plasma Spectroscopy (McGraw-Hill, New York, 1964).
- [135] R.H. Huddlestone and S.L. Leonard Eds., Plasma Diagnostic Techniques (Academic Press, New York, 1965).
- [136] H.R. Griem, Plasma Spectroscopy (McGraw-Hill, New York, 1964), pp. 147-151.
- [137] Ibid, pp. 140-142.
- [138] Ibid, pp. 136-139.

- [139] Ibid, p. 160.
- [140] Ibid, p. 166.
- [141] R.W.P. McWhirter, in Plasma Diagnostic Techniques, R.H. Huddleston and S.L. Leonard Eds., (Academic Press, New York, 1965), pp. 208-214.
- [142] T.F. Stratton, in Plasma Diagnostic Techniques, R.H. Huddleston and S.L. Leonard Eds., (Academic Press, New York, 1965), p. 390.
- [143] R.W.P. McWhirter, in Plasma Diagnostic Techniques, R.H. Huddleston and S.L. Leonard Eds., (Academic Press, New York, 1965), p. 209.
- [144] H.R. Griem, Plasma Spectroscopy (McGraw-Hill, New York, 1964), p. 147.
- [145] Ibid, p. 307.
- [146] Ibid, p. 176.
- [147] K. Bockasten, J. Opt. Soc. Am. 51, 943 (1961).
- [148] W.L. Wiese, in Plasma Diagnostic Techniques, R.H. Huddleston and S.L. Leonard Eds., (Academic Press, New York, 1965), p. 311.
- [149] H.R. Griem, Plasma Spectroscopy (McGraw-Hill, New York, 1964), p. 197.
- [150] Ibid, p. 101.
- [151] H.R. Griem, Spectral Line Broadening by Plasmas (Academic Press, New York, 1974).
- [152] W.L. Wiese and N. Konjevic, J. Quant. Spectrosc. Radiat. Transfer 28, 185 (1982).
- [153] H.R. Griem, Plasma Spectroscopy (McGraw-Hill, New York, 1964), p. 125.
- [154] Ibid, p. 116.
- [155] D.L. Book, NRL Publication 177-4405, 29 (1991).
- [156] R. Glass, J. Phys. B 12, 1633 (1979).
- [157] W.L. Wiese, M.W. Smith, and B.M. Glemmon, Atomic Transition Probabilities, 1, NSRDS-NBS4 (US Government Printing Office, Washington, DC, 1966).
- [158] D.G. Hammer and D.W. Norcross, Mon. Not. R. Astr. Soc. 168, 263 (1974).

- [159] J.-S. Wang, H.R. Griem, R. Hess, W.L. Rowan, and T.P. Kochanski, Phys. Rev. A 33, 4293 (1986).
- [160] H.-J. Kunze, A.H. Gabriel, and H.R. Griem, Phys. Rev. 165, 267 (1968).
- [161] J.A.R. Samson, Techniques of Vacuum Ultraviolet Spectroscopy, (Pied Publications, Lincoln, Nebraska, 1967), p 26.
- [162] Ibid, p. 10.
- [163] Ibid, p. 217